

Advances in Applied Mechanics

Volume 43

ADVANCES IN

APPLIED MECHANICS

Edited by

Hassan Aref

VIRGINIA TECH, BLACKSBURG, VA, USA

Erik van der Giessen

UNIVERSITY OF GRONINGEN
GRONINGEN, THE NETHERLANDS

VOLUME 43



ELSEVIER

AMSTERDAM • BOSTON • HEIDELBERG • LONDON
NEW YORK • OXFORD • PARIS • SAN DIEGO
SAN FRANCISCO • SINGAPORE • SYDNEY • TOKYO

Academic Press is an imprint of Elsevier



Academic Press is an imprint of Elsevier
525 B Street, Suite 1900, San Diego, CA 92101-4495, USA
30 Corporate Drive, Suite 400, Burlington, MA 01803, USA
84 Theobald's Road, London WC1X 8RR, UK
Radarweg 29, PO Box 211, 1000 AE Amsterdam, The Netherlands

First edition 2009

Copyright © 2009 Elsevier Inc. All rights reserved.

No part of this publication may be reproduced, stored in a retrieval system or transmitted in any form or by any means electronic, mechanical, photocopying, recording or otherwise without the prior written permission of the publisher.

Permissions may be sought directly from Elsevier's Science & Technology Rights Department in Oxford, UK: phone (+44) (0) 1865 843830; fax (+44) (0) 1865 853333; email: permissions@elsevier.com. Alternatively you can submit your request online by visiting the Elsevier website at <http://elsevier.com/locate/permissions>, and selecting *Obtaining permission to use Elsevier material*.

Notice

No responsibility is assumed by the publisher for any injury and/or damage to persons or property as a matter of products liability, negligence or otherwise, or from any use or operation of any methods, products, instructions or ideas contained in the material herein.

ISBN: 978-0-12-374813-3

ISSN: 0065-2156

For information on all Academic Press publications
visit our website at www.elsevierdirect.com

Printed and bound in USA

09 10 11 12 10 9 8 7 6 5 4 3 2 1

Working together to grow
libraries in developing countries

www.elsevier.com | www.bookaid.org | www.sabre.org

ELSEVIER

BOOK AID
International

Sabre Foundation

Contents

PREFACE	vii
-------------------	-----

A Shell Theory for Carbon Nanotubes Based on the Interatomic Potential and Atomic Structure

J. Wu, K. C. Hwang and Y. Huang

Abstract	2
1. Introduction	2
2. Interatomic Potentials	7
3. A Plate Theory for Graphene Based on the Interatomic Potential	10
4. A Linear Shell Theory for Carbon Nanotubes Based on the Interatomic Potential	18
5. Can a Single-Wall Carbon Nanotube Be Modeled as a Thin Shell?	25
6. A Nonlinear, Finite-Deformation Shell Theory for Carbon Nanotubes Based on the Interatomic Potential	34
7. Instability of Carbon Nanotubes	49
8. Concluding Remarks	62
Acknowledgments	63
A. The Incremental Form of Equilibrium Equation	63
B. The Symmetric Membrane Stress and Moment, and Covariant Derivatives	64
References	65

Tensegrity: 60 Years of Art, Science, and Engineering

C. Sultan

Abstract	70
1. Introduction	70
2. Tensegrity Origins: The Pioneers	71

3. From Abstract Art to Abstract Science	76
4. The Blossoming 1990s and Beyond	84
5. Advances in Statics Research	85
6. Advances in Dynamics Research	97
7. Deploying Tensegrity Structures	112
8. Controllable Tensegrity Structures	117
9. Tensegrity Structures in Biology	125
10. The Future	133
11. Challenges for Controllable Tensegrity Structures	134
12. Conclusions	138
Acknowledgments	139
References	139

Skin Biothermomechanics: Modeling and Experimental Characterization

F. Xu and T. J. Lu

Abstract	148
1. Introduction	148
2. Review of Related Studies	152
3. Modeling of Skin Biothermomechanics and Thermal Pain	162
4. Experimental Methodology	180
5. Biothermomechanical Behavior of Skin Tissue	196
6. Conclusions	229
Acknowledgments	234
References	234
SUBJECT INDEX	249

Preface

There are few areas in science and engineering where applied mechanics does not continue to make significant contributions. This volume of *Advances in Applied Mechanics* is proof of this by highlighting the role of solid mechanics in topics ranging from carbon nanotubes to the response of skin tissue.

Carbon nanotubes (CNTs) hold many promises, including improved mechanical behavior of materials based on or reinforced with CNTs. Predictive modeling of such properties requires that the CNT behavior can be cast in a continuum model. One of the challenges there is that the wall of a CNT is only one atom thick. The chapter by Wu, Hwang, and Huang shows how to systematically derive a continuum shell description of a CNT on the basis of its atomic structure and a state-of-the-art interatomic potential for carbon. The resulting CNT model is different from all existing shell theories, but can be reduced to it for specific CNTs when allowing for (known) relative errors. The finite-deformation version of this atomistic-based shell theory is used to study the instability of single-wall CNTs subject to structural loading states, such as compression and torsion.

The second chapter, by C. Sultan from Virginia Tech, also addresses structures but of a special type: tensegrity structures. While originating in the avant garde art of the twentieth century, the concept of a tensegrity structure has made its way into a variety of applications in engineering and is even recognized nowadays in applied sciences. Beside a broad historical overview of the evolution of tensegrity structures, this chapter provides a detailed yet concise summary of the fundamental mechanics that gives these frameworks their peculiar static and dynamical properties. Modern applications, for instance in the form of deployable structures for aeronautics, are discussed as well as the possible role of tensegrity in cell biology.

Biology, or perhaps medicine, is also the area of application for the third and final chapter of this volume, co-authored by the Cambridge–China team of Xu and Lu. This chapter provides an extensive outline of the interaction between heat conduction, thermal damage, and the mechanical response of skin in determining thermal pain sensations. An experimental methodology encompassing a variety of techniques is presented against the background of recent models for skin biothermomechanics and thermal pain. The results supplement knowledge of the mechanical properties of skin tissue under normal physiological conditions with detailed characterization of the changes in mechanical properties of skin tissue due to temperature changes and the corresponding thermal damage. The new insights and model parameters are expected to be crucial for thermal therapy in skin disease treatments.

**Hassan Aref
Erik van der Giessen**

A Shell Theory for Carbon Nanotubes Based on the Interatomic Potential and Atomic Structure

J. WU,^a K. C. HWANG,^a and Y. HUANG^b

^a*FML, Department of Engineering Mechanics, Tsinghua University, Beijing 100084, China*

^b*Departments of Civil and Environmental Engineering, and Mechanical Engineering, Northwestern University, Evanston, Illinois 60208, USA*

Abstract.....	2
1. Introduction.....	2
2. Interatomic Potentials.....	7
3. A Plate Theory for Graphene Based on the Interatomic Potential.....	10
4. A Linear Shell Theory for Carbon Nanotubes Based on the Interatomic Potential.....	18
4.1. Membrane Strains and Curvatures.....	18
4.2. Constitutive Relations.....	21
4.3. Equilibrium Equations.....	25
5. Can a Single-Wall Carbon Nanotube Be Modeled as a Thin Shell?	25
5.1. Order of Error (Δ/R) ³ : Not a Classical Linear Elastic Shell.....	26
5.2. Order of Error (Δ/R) ² : A Linear Elastic Orthotropic Shell.....	26
5.3. Order of Error (Δ/R): A Classical Linear Elastic Shell with a Universal Shell Thickness.....	31
6. A Nonlinear, Finite-Deformation Shell Theory for Carbon Nanotubes Based on the Interatomic Potential.....	34
6.1. General Description of a Curved Surface.....	34
6.2. Membrane Strains and Curvatures of a Deformed Surface.....	35
6.3. Deformation of a Single-Wall Carbon Nanotube.....	36
6.4. Membrane Stresses and Moments in a Carbon Nanotube.....	38
6.5. Equilibrium Equations for Membrane Stresses and Moments ..	39
6.6. Examples.....	42
7. Instability of Carbon Nanotubes.....	49
7.1. Instability of Carbon Nanotubes in Tension.....	50
7.2. Instability of Carbon Nanotubes in Compression.....	53
7.3. Instability of Carbon Nanotubes Subject to Internal Pressure. .	56
7.4. Instability of Carbon Nanotubes Subject to External Pressure..	58
7.5. Instability of Carbon Nanotubes in Torsion.....	60
8. Concluding Remarks.....	62
Acknowledgments.....	63

Appendix A The Incremental Form of Equilibrium Equation.	63
Appendix B The Symmetric Membrane Stress and Moment, and Covariant Derivatives.	64
References.	65

Abstract

A finite-deformation shell theory for single-wall carbon nanotubes (CNTs) is established directly from the atomic structure of CNT and the interatomic potential by accounting for the important effect of moment and curvature (of CNTs) in the Cauchy–Born rule. The theory incorporates the effect of bending moment and curvature for a curved surface, and accurately accounts for the nonlinear, multibody atomistic interactions, as well as the carbon nanotube chirality. It avoids the ambiguous definition of nanotube thickness, and provides the constitutive relations among stress, moment, strain, and curvature via the interatomic potential.

The constitutive behavior of a CNT is different from that of a classical shell, but its overall structural response at infinitesimal deformation may still be approximately represented by a linear elastic thin shell for some representative loadings such as tension, compression, bending, torsion, internal, and external pressure. The ratio of atomic spacing ($\Delta \approx 0.14$ nm) to CNT radius, Δ/R , is used to identify the order of error, where Δ/R ranges from zero (for graphene) to about 40% [for the (5,5) armchair CNT ($R = 0.35$ nm)]. For the order of error $O[(\Delta/R)^3]$ (as compared to unity), which is about 6% for the (5,5) armchair CNT, the structural response of a CNTs cannot be represented by any classical shell. For the order of error $O[(\Delta/R)^2]$, which is about 16% for the (5,5) armchair CNT, a CNT can be approximated by a linear elastic orthotropic thin shell. Only for the order of error $O(\Delta/R)$, which is about 40% for the (5,5) armchair CNT, a universal constant shell thickness and Young's modulus can be defined, and CNTs can be represented by an elastic isotropic thin shell.

The instability of single-wall CNTs subject to tension, compression, internal and external pressure, and torsion is studied.

1. Introduction

A single-wall carbon nanotube (CNT), as illustrated in Fig. 1.1, has a single layer of carbon atoms. It has a perfect hexagonal lattice structure, a diameter on the order of 1 nm and a length ranging from 1 to 100 μm (or even longer). The structure of a single-wall CNT can be conceptualized by wrapping a graphene (one-atom-thick layer of graphite) into a seamless cylinder. As shown in Fig. 1.2, the graphene sheet is wrapped in the circumferential direction $C_h = n\mathbf{a}_1 + m\mathbf{a}_2$ of CNT represented by a pair of indices (n, m) . The integers n and m denote the number of unit vectors \mathbf{a}_1 and \mathbf{a}_2 along two directions in the honeycomb crystal lattice of graphene. If $m = 0$, the nanotubes are called “zigzag.” If $n = m$, the nanotubes are called “armchair.” Otherwise, they are called “chiral.” The carbon atoms inside a graphene sheet are

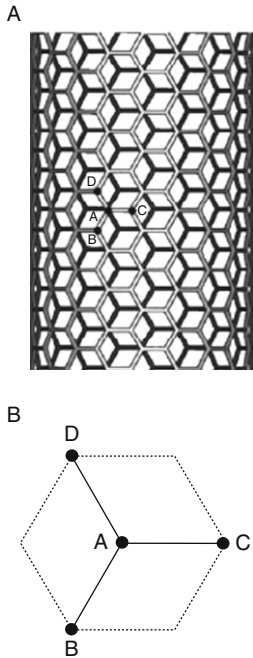


FIG. 1.1 A carbon nanotube (CNT) prior to deformation: (A) a CNT and (B) a representative atom (*A*) and its three nearest-neighbor atoms (*B*, *C*, and *D*).

covalently bonded through overlapping *s*-orbitals, making it the stiffest material known today in the absence of defects (Lee, Wei, Kysar, & Hone, 2008). The *p*-orbitals of graphene out of the plane start to interact for CNTs with small radius.

As compared to metals, carbon nanotubes have superior properties, such as low mass density ($\sim 1/6$ of steel mass density), high Young's modulus on the order of 1 TPa (~ 6 times steel modulus) (e.g., Lee et al., 2008; Qian, Wagner, Liu, Yu, & Ruoff, 2002; Srivastava, Menon, & Cho, 2001; Yakobson & Avouris, 2001), and therefore have many potential applications.

There are extensive atomistic studies of CNT mechanical behavior (e.g., Belytschko, Xiao, Schatz, & Ruoff, 2002; Samsonidze, Samsonidze, & Yakobson, 2002; Yakobson, Brabec, & Bernholc, 1996; Yakobson, Campbell, Brabec, & Bernholc, 1997). Atomistic simulations, in general, are limited in time scale (up to 1 ns) and size scale (up to 1 μm). The atomic-scale finite element method has been developed recently to extend the continuum finite element method to atomic scale by explicitly accounting for the nonlinear and multibody atomistic interactions (Liu, Huang, et al., 2004; Liu, Jiang, Huang, Qu, Yu, et al., 2005). It provides a seamless linkage between the molecular mechanics and continuum methods (at least at 0 K).

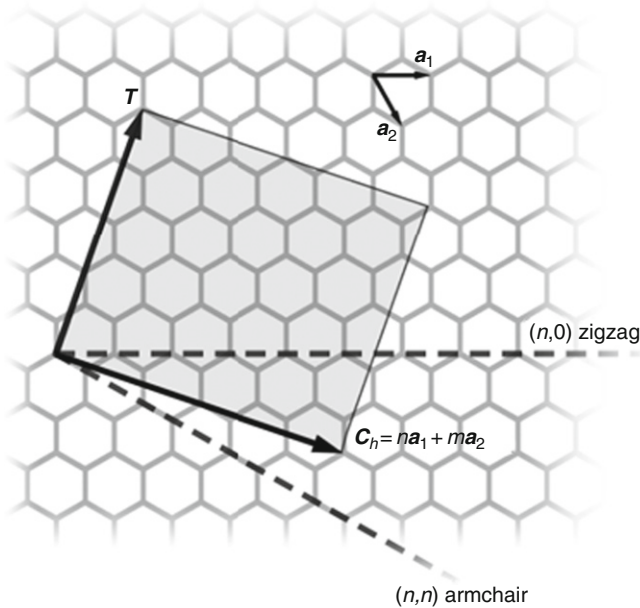


FIG. 1.2 A schematic diagram of graphene sheet wrapped seamlessly to a single carbon nanotube.

There also exist two types of continuum models for CNTs. The first is to model CNTs by continuum structural elements, such as spring, truss, beam, membrane, plate, and shell, and is called the type-I continuum model in this chapter. For a few representative loading cases (e.g., tension, bending), the material and geometric properties of continuum elements (e.g., elastic modulus, thickness) are determined by fitting the atomistic simulation results. For example, [Yakobson et al. \(1996\)](#) modeled CNTs as classical linear elastic isotropic shells, which have a strain energy

$$E = \frac{1}{2} \int \int \left\{ D \left[\left(\kappa_x + \kappa_y \right)^2 - 2(1-v)(\kappa_x \kappa_y - \kappa_{xy}^2) \right] + \frac{C}{1-v^2} \left[\left(\varepsilon_x + \varepsilon_y \right)^2 - 2(1-v)(\varepsilon_x \varepsilon_y - \varepsilon_{xy}^2) \right] \right\} dS, \quad (1.1)$$

where D and C are the bending and tension rigidities, respectively; v is the Poisson's ratio; κ_x , κ_y , and κ_{xy} are the curvatures; ε_x , ε_y , and ε_{xy} are the membrane strains; and the integration is over the CNT surface. By fitting the energy obtained from molecular dynamics simulations ([Robertson, Brenner, & Mintmire, 1992](#))

for CNTs in uniaxial tension and in bending (from a graphene sheet to a CNT), [Yakobson et al. \(1996\)](#) determined $D = 0.85 \text{ eV}$, $C = 59 \text{ eV/atom} = 360 \text{ J/m}^2$, and $v = 0.19$. Carbon nanotubes have also been modeled as Euler beams ([Govindjee & Sackman, 1999](#)), trusses and plates ([Odegard, Gates, Nicholson, & Wise, 2002](#)), trusses and torsion springs ([Chang & Gao, 2003; Nasdala & Ernst, 2005; Natsuki, Tantrakarn, & Endo, 2004](#)), cylinders ([Gao & Li, 2003](#)), beams with circular cross sections ([Li & Chou, 2003, 2004](#)), cylindrical shells ([Sears & Batra, 2004](#)), trusses between nearest and second nearest atoms ([Leung, Guo, He, & Kitipornchai, 2005](#)), trusses and torsion springs or membranes and torsion springs ([Wang, Zhang, & Lu, 2005](#)), and spatial trusses and shells ([Chen & Cao, 2006](#)). These types of continuum models rely on fitting the energy from atomistic simulations, and is restricted to linear elastic analysis (and often elastic isotropy).

Another type of continuum models is based on the interatomic potential and atomic structure of carbon nanotubes, and is called the type-II continuum model in this chapter. They incorporate the nonlinear, multibody interatomic potential for carbon directly into the continuum analysis (e.g., [Arroyo & Belytschko, 2002, 2004; Jiang et al., 2003; Zhang, Huang, Gao, & Hwang, 2002; Zhang, Huang, Geubelle, & Hwang, 2002; Zhang, Huang, Geubelle, Klein, & Hwang, 2002; Zhang, Jiang, Huang, Geubelle, & Hwang, 2004](#)) via the Born rule ([Born & Huang, 1959](#)), that is, to equate the continuum strain energy to energy in atomic bonds. [Arroyo & Belytschko \(2002, 2004\)](#) used the exponential Born rule and geodesic to study CNTs and graphene. The atomistic-based continuum theories of [Jiang et al. \(2003\)](#), [Zhang, Huang, Geubelle, Klein, et al. \(2002\)](#), and [Zhang et al. \(2004\)](#) account for the CNT chirality, and agree well with molecular dynamics simulations without any parameter fitting. Their theories have been extended to account for the effect of finite temperature (e.g., [Jiang, Huang, & Hwang, 2005; Jiang, Liu, et al., 2004](#)) and coupled electromechanical behavior (e.g., [Johnson, Liu, & Huang, 2004; Liu, Jiang, et al., 2004](#)), and to study defect nucleation in CNTs (e.g., [Jiang, Feng, et al., 2004; Song et al., 2006](#)). However, they are membrane theories that cannot account for the effect of graphene bending, which is important in the experimental determination of the CNT elastic modulus from their buckling ([Khang et al., 2008](#)), and in many applications such as CNT-based sensors (e.g., [Tombler et al., 2000](#)), oscillators (e.g., [Jiang, Yu, et al., 2004](#)), bio-inspired adhesion (e.g., [Zhou, Huang, Liu, Wu, Hwang, et al., 2007](#)), and CNT-reinforced composite materials (e.g., [Shi, Feng, Huang, & Hwang, 2004; Shi, Feng, Huang, Hwang, & Gao, 2004; Tan, Jiang, Huang, Liu, & Hwang, 2007](#)).

Recently [Wu, Hwang, and Huang \(2008\)](#) developed a finite-deformation shell theory directly from the interatomic potential for carbon via the modified Born rule. It belongs to the second type of continuum models discussed above but does account for the effect of moment and curvature. Its equilibrium equations and

boundary conditions are the same as the classical shell theories of Koiter (1966), Niordson (1985), and Sanders (1963) (see Wu, Hwang, Huang, & Song, 2008a). However, its constitutive model, which relates increments of second Piola-Kirchhoff membrane stress $\dot{\mathbf{T}}$ and moment $\dot{\mathbf{M}}$ to increments of Green strain $\dot{\mathbf{E}}$ and curvature $\dot{\mathbf{K}}$, is established from the interatomic potential and is very different from the linear elastic isotropic constitutive model in the following three aspects (see Wu, Peng, Hwang, Song, & Huang, 2008):

- (i) The constitutive model becomes nonlinear (with 2% tolerance) for strains beyond 1%.
- (ii) The constitutive model is anisotropic for CNTs with a diameter smaller than 1 nm. For CNTs with a diameter larger than 1 nm, the constitutive model also becomes anisotropic as deformation increases.
- (iii) The constitutive model has couplings between the membrane stress and curvature, and between the moment and membrane strain.

Even though the constitutive behavior of CNTs is not strictly linear elastic isotropic, is it possible that the overall structural response of CNTs be approximately represented by a linear elastic thin shell for some representative loadings such as tension, compression, bending, torsion, internal, and external pressure? In other words, can the structural response (global behavior) of CNTs be approximately represented by a type-I continuum model of linear elastic thin shell, even if the constitutive response (local behavior) cannot? If yes, how large is the error? What are the elastic modulus and shell thickness of CNTs? Is the thin shell elastically isotropic? Peng, Wu, Hwang, Song, and Huang (2008) answered these questions. Similar to Huang, Wu, and Hwang (2006) for graphene, they obtained the tension and bending rigidities (as well as the shear and torsion rigidities) of CNTs directly from the interatomic potential. The ratio of atomic spacing ($\Delta \approx 0.14$ nm) to CNT radius (R), Δ/R , was used to identify the error, which ranges from zero (for graphene) to about 40% [for a small (5,5) armchair CNT ($R = 0.35$ nm)]. The order of error in Wu, Hwang, and Huang's (2008) atomistic-based shell theory is $O[(\Delta/R)^3]$ (as compared to unity), which is about 6% for the (5,5) armchair CNT. The CNTs can be approximated by an elastic orthotropic thin shell at small strains, but the order of error then decreases to $O[(\Delta/R)^2]$ (i.e., larger error), which is about 16% for the (5,5) armchair CNT. Only when the order of the error decreases to $O(\Delta/R)$ (largest error in the present study), which is about 40% for the (5,5) armchair CNT, a universal constant shell thickness and Young's modulus can be defined, and CNTs can be represented by an isotropic elastic thin shell.

The purpose of this chapter is to review the continuum shell modeling of CNTs based on the interatomic potential and the atomic structure. It begins with a review of the Brenner (1990) interatomic potential and its second-generation

potential (Brenner, Shenderova, Harrison, Stuart, Ni, et al., 2002) in Section 2, though the proposed continuum shell model can be based on other interatomic potentials (see, e.g., Pettifor & Oleinik, 1999). The proposed approach to establish a continuum shell theory from the interatomic potential is illustrated in Section 3 for graphene, which is a single, planar layer of carbon atoms, and therefore avoids the complexity of the curved surface and the finite CNT radius. For such a single layer of atoms, the bending rigidity results from the multibody atomistic interactions, rather than from tension and compression on the opposite sides of the neutral plane as in the classical shell theory. Section 4 provides a linear shell theory for CNTs (subject to infinitesimal deformation). Its constitutive relation is derived directly from the interatomic potential without introducing any classical structure models (e.g., shell), nor fitting parameters (e.g., thickness, elastic modulus). The resulting constitutive relation is different from the classical shell theories since it involves couplings between the membrane stress and curvature, and between the moment and membrane strain. Furthermore, this atomistic-based shell theory does not need any shell thickness, nor Young's modulus. Based on this linear theory it is discussed in Section 5 whether the structural response of a CNT can be modeled by a classical linear elastic shell and the corresponding order of error. A nonlinear, finite-deformation shell theory is derived from the interatomic potential in Section 6. Once again it is different from the classical shell theories since it does not involve shell thickness, nor Young's modulus. The instability of CNTs subject to various loadings is studied in Section 7 (Wu, Hwang, Huang, & Song, 2008b).

2. Interatomic Potentials

Brenner (1990) established an interatomic potential, bond order for carbon from the Tersoff (1988) formalism as

$$V(i,j) = V_R(r_{ij}) - B_{ij}V_A(r_{ij}), \quad (2.1)$$

where r_{ij} is the distance between atoms i and j (no summation for Latin subscripts), V_R and V_A are the repulsive and attractive pair terms depending only on r_{ij}

$$V_R(r) = \frac{D^{(e)}}{S-1} \exp\left\{-\sqrt{2S}\beta(r - R^{(e)})\right\} f_c(r), \quad (2.2)$$

$$V_A(r) = \frac{D^{(e)}S}{S-1} \exp\left\{-\sqrt{2/S}\beta(r - R^{(e)})\right\} f_c(r), \quad (2.3)$$

$R^{(e)} = 0.1390$ nm is the equilibrium spacing between a pair of carbon atoms, $D^{(e)} = 6.00$ eV is the corresponding energy stored in the atomic bond, $S = 1.22$ is the ratio of attractive to repulsive bond energies, and $\beta = 21 \text{ nm}^{-1}$ characterizes how fast the energy decreases away from the equilibrium point,

$$f_c(r) = \begin{cases} 1 & r < R^{(1)} \\ \frac{1}{2} \left\{ 1 + \cos \left[\frac{\pi(r - R^{(1)})}{R^{(2)} - R^{(1)}} \right] \right\} & R^{(1)} \leq r \leq R^{(2)} \\ 0 & r > R^{(2)} \end{cases} \quad (2.4)$$

is a smooth cutoff function with $R^{(1)} = 0.17$ nm and $R^{(2)} = 0.2$ nm. For bond lengths beyond 0.2 nm, the above cutoff function suggests vanishing bond energy.

The multibody coupling term B_{ij} in Eq. (2.1) depends on atoms other than i and j :

$$B_{ij} = \left[1 + \sum_{k(\neq i,j)} G(\varphi_{ijk}) f_c(r_{ik}) \right]^{-1/2}, \quad (2.5)$$

where r_{ik} is the distance between atoms i and k ($k \neq i, j$), φ_{ijk} is angle between bonds $i-j$ and $i-k$, and

$$G(\varphi_{ijk}) = a_0 \left[1 + \frac{c_0^2}{d_0^2} - \frac{c_0^2}{d_0^2 + (1 + \cos \varphi_{ijk})^2} \right] \quad (2.6)$$

with $a_0 = 0.00020813$, $c_0 = 330$, and $d_0 = 3.5$.

Figure 2.1 shows (by the solid line) the interatomic potential V versus bond length r_{ij} for the fixed bond angle $\varphi_{ijk} = 120^\circ$. It reaches the minimum at the bond length $r_0 = 0.145$ nm, which is the equilibrium bond length for graphene to be discussed in Section 3.

Recently, Brenner et al. (2002) developed the second-generation interatomic potential for carbon. It includes both modified analytic functions for the intramolecular interactions and an expanded fitting database. It yields a much improved description of bond energies, lengths, and especially force constants for carbon–carbon bonds as compared to the earlier effort, and therefore has produced an improved fit to the elastic properties of diamond and graphite, which in turn yield better predictions for the energies of several surface reconstructions and interstitial defects. Forces associated with rotation about dihedral angles for carbon–carbon double bonds as well as angular interactions associated with hydrogen centers have also been modeled which were not included in the Brenner (1990)

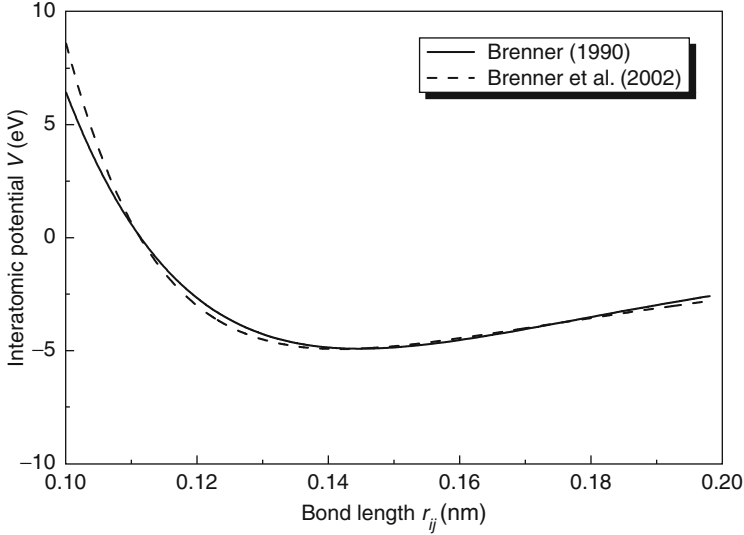


FIG. 2.1 The interatomic potential V according to Eq. (2.1) versus the bond length r_{ij} for fixed bond angle $\varphi_{ijk} = 120^\circ$.

potential. The pair terms in Eqs. (2.2) and (2.3) and multibody coupling term in Eq. (2.5) become

$$V_R(r) = \left(1 + \frac{Q}{r}\right) A e^{-\alpha r} f_c(r), \quad (2.7)$$

$$V_A(r) = \sum_{n=1}^3 B_n e^{-\beta_n r} f_c(r), \quad (2.8)$$

$$B_{ij} = \left[1 + \sum_{k(\neq i, j)} G(\varphi_{ijk}) f_c(r_{ik}) \right]^{-1/2}, \quad (2.9)$$

where the cutoff function is the same as Eq. (2.4); $A = 10,954$ eV, $\alpha = 47.465$ nm $^{-1}$, $Q = 0.031346$ nm, $B_1 = 12,389$ eV, $\beta_1 = 47.205$ nm $^{-1}$, $B_2 = 17.567$ eV, $\beta_2 = 14.332$ nm $^{-1}$, $B_3 = 30.715$ eV, $\beta_3 = 13.827$ nm $^{-1}$; and the function $G(\varphi_{ijk})$ becomes

$$\begin{aligned}
G(\varphi) &= 0.27186 + 0.48922 \cos \varphi - 0.43286 \cos^2 \varphi - 0.56140 \cos^3 \varphi \\
&\quad + 1.2711 \cos^4 \varphi - 0.037931 \cos^5 \varphi, \quad \text{for } 0^\circ \leq \varphi \leq 109.47^\circ, \\
&= 0.69669 + 5.5444 \cos \varphi + 23.432 \cos^2 \varphi + 55.948 \cos^3 \varphi \\
&\quad + 69.876 \cos^4 \varphi + 35.312 \cos^5 \varphi, \quad \text{for } 109.47^\circ < \varphi < 120^\circ, \\
&= 0.00260 - 1.0980 \cos \varphi - 4.3460 \cos^2 \varphi - 6.8300 \cos^3 \varphi \\
&\quad - 4.9280 \cos^4 \varphi - 1.3424 \cos^5 \varphi, \quad \text{for } 120^\circ \leq \varphi \leq 180^\circ.
\end{aligned} \tag{2.10}$$

[Figure 2.1](#) also shows (by the dashed line) the second-generation interatomic potential versus the bond length r_{ij} for the fixed bond angle $\varphi_{ijk} = 120^\circ$. It reaches a minimum at the bond length $r_0 = 0.142$ nm, which is slightly shorter than $r_0 = 0.145$ nm according to the [Brenner \(1990\)](#) potential. The two potentials are essentially the same near the initial equilibrium state, but the force constants (second-order derivatives) can be different.

To distinguish the results based on the [Brenner \(1990\)](#) potential and the second-generation interatomic potential ([Brenner et al., 2002](#)), we use solid and dashed lines for their predictions, respectively, throughout this chapter.

3. A Plate Theory for Graphene Based on the Interatomic Potential

[Huang et al. \(2006\)](#) developed a plate theory for graphene based on the interatomic potential. The bond angle is 120° for the initial state of graphene without deformation. The equilibrium bond length r_0 is obtained by minimizing the potential V at the bond angle 120° , that is, $\frac{\partial V}{\partial r_{ij}}|_{r_{ij}=r_0, \varphi_{ijk}=120^\circ} = 0$. For the [Brenner \(1990\)](#) potential given in Eqs. (2.1)–(2.6), $r_0 = R^{(e)} - \frac{1}{\beta} \frac{\sqrt{S/2}}{(S-1)}$ $\times \ln B_0 = 0.145$ nm, where $B_0 = 0.96$ is the multibody coupling term B_{ij} evaluated at $\varphi_{ijk} = 120^\circ$.

For the graphene subject to an infinitesimal in-plane membrane strain ε , the changes of bond length $r_{ij} - r_0$ and bond angle $\varphi_{ijk} - 120^\circ$ are also infinitesimal. The Taylor series expansion of the cosine of bond angle is $\cos \varphi_{ijk} = -\frac{1}{2} - \frac{\sqrt{3}}{2} \times (\varphi_{ijk} - 120^\circ) + \frac{1}{4} (\varphi_{ijk} - 120^\circ)^2 + \dots$, such that $\cos \varphi_{ijk} + \frac{1}{2}$ is infinitesimal. The interatomic potential in Eq. (2.1) can then be expanded in a Taylor series expansion as

$$\begin{aligned}
V &= V_0 + \sum_{k \neq i, j} \left(\frac{\partial V}{\partial \cos \varphi_{ijk}} \right)_0 \left(\cos \varphi_{ijk} + \frac{1}{2} \right) + \frac{1}{2} \left(\frac{\partial^2 V}{\partial r_{ij}^2} \right)_0 (r_{ij} - r_0)^2 \\
&\quad + \sum_{k \neq i, j} \left(\frac{\partial^2 V}{\partial r_{ij} \partial \cos \varphi_{ijk}} \right)_0 (r_{ij} - r_0) \left(\cos \varphi_{ijk} + \frac{1}{2} \right) \\
&\quad + \frac{1}{2} \sum_{k, l \neq i, j} \left(\frac{\partial^2 V}{\partial \cos \varphi_{ijk} \partial \cos \varphi_{ijl}} \right)_0 \left(\cos \varphi_{ijk} + \frac{1}{2} \right) \left(\cos \varphi_{ijl} + \frac{1}{2} \right),
\end{aligned} \tag{3.1}$$

where the subscript “0” denotes the initial, equilibrium state ($r_{ij} = r_0$ and $\varphi_{ijk} = 120^\circ$); the terms higher than the second order are neglected; and the first-order derivative $(\partial V / \partial r_{ij})_0$ vanishes. The above Taylor series is expanded with respect to $\cos \varphi_{ijk}$ (instead of φ_{ijk}) because the interatomic potentials in Section 2 depend on the bond angle via $\cos \varphi_{ijk}$ [see Eqs. (2.6) and (2.10)]. Equation (3.1) involves five constants, namely the first-order derivative $(\partial V / \partial \cos \varphi_{ijk})_0$, and second-order derivatives $(\partial^2 V / \partial r_{ij}^2)_0$, $(\partial^2 V / \partial r_{ij} \partial \cos \varphi_{ijk})_0$, $(\partial^2 V / \partial \cos \varphi_{ijk} \partial \cos \varphi_{ijk})_0$, and $(\partial^2 V / \partial \cos \varphi_{ijk} \partial \cos \varphi_{ijl})_0 (k \neq l)$, which can be obtained analytically. For example, for the Brenner (1990) potential given in Eqs. (2.1)–(2.6)

$$\left(\frac{\partial V}{\partial \cos \varphi_{ijk}} \right)_0 = \frac{D^{(e)} S}{S - 1} \delta a_0 c_0^2 \frac{1}{(d_0^2 + 1/4)^2} B_0^{[(\delta+1)/\delta] + [1/(S-1)]} = 1.841 \text{ eV},$$

$$\left(\frac{\partial^2 V}{\partial r_{ij}^2} \right)_0 = 2D^{(e)} \beta^2 B_0^{S/(S-1)} = 4337 \text{ eV/nm}^2,$$

$$\begin{aligned} \left(\frac{\partial^2 V}{\partial r_{ij} \partial \cos \varphi_{ijk}} \right)_0 &= -\frac{D^{(e)} \sqrt{2S}}{S - 1} \beta \delta a_0 c_0^2 \frac{1}{(d_0^2 + 1/4)^2} B_0^{[(\delta+1)/\delta] + [1/(S-1)]} \\ &= -49.49 \text{ eV/nm}, \end{aligned}$$

$$\begin{aligned} \left(\frac{\partial^2 V}{\partial \cos \varphi_{ijk} \partial \cos \varphi_{ijk}} \right)_0 &= \frac{D^{(e)} S}{S - 1} \delta a_0 c_0^2 \frac{1}{(d_0^2 + 1/4)^3} B_0^{[(\delta+1)/\delta] + [1/(S-1)]} \\ &\quad \times \left[2d_0^2 - \frac{3}{2} - \frac{(\delta+1) B_0^{1/\delta} a_0 c_0^2}{d_0^2 + 1/4} \right] = 3.014 \text{ eV}, \end{aligned}$$

and

$$\begin{aligned} \left(\frac{\partial^2 V}{\partial \cos \varphi_{ijk} \partial \cos \varphi_{ijl}} \right)_0 (k \neq l) &= -\frac{D^{(e)} S}{S - 1} \delta (\delta+1) a_0^2 c_0^4 \frac{1}{(d_0^2 + 1/4)^4} B_0^{[(\delta+2)/\delta] + [1/(S-1)]} = -0.3728 \text{ eV}. \end{aligned}$$

Here, the first-order derivative $(\partial V / \partial \cos \varphi_{ijk})_0$ reflects multibody atomistic interactions.

The Taylor series expansion in Eq. (3.1) holds for any multibody interatomic potential since it involves only derivatives at the initial, equilibrium state. For the second-generation interatomic potential (Brenner et al., 2002) given in Eqs. (2.7)–(2.10), these five constants and equilibrium bond length r_0 become 1.592 eV, 4356 eV/nm², −59.14 eV/nm, 3.099 eV, −0.3673 eV, and 0.142 nm, respectively.

The Cauchy–Born rule (Born & Huang, 1959) equates the energy stored in atomic bonds to strain energy at the continuum level. Atoms move according to a single mapping $\mathbf{F} = \partial\mathbf{x}/\partial\mathbf{X}$ from the initial to the current (deformed) configurations of the Bravais lattice, where \mathbf{X} and \mathbf{x} denote positions of the atom in these two configurations, respectively. A bond between a pair of atoms i and j in the initial configuration is described by the vector $\mathbf{r}_{ij}^{(0)} = r_0\mathbf{n}$, where r_0 is the initial bond length and \mathbf{n} is the unit vector along the initial bond direction. For a simple Bravais lattice, the deformed bond is $\mathbf{r}_{ij} = \mathbf{F} \cdot \mathbf{r}_{ij}^{(0)}$, which has the length $\mathbf{r}_{ij} = \sqrt{\mathbf{r}_{ij} \cdot \mathbf{r}_{ij}} = r_0 \left[1 + \mathbf{n} \cdot \boldsymbol{\varepsilon} \cdot \mathbf{n} - \frac{1}{2} (\mathbf{n} \cdot \boldsymbol{\varepsilon} \cdot \mathbf{n})^2 \right]$ for infinitesimal in-plane membrane strain $\boldsymbol{\varepsilon}$. The single mapping \mathbf{F} ensures equilibrium of atoms for a simple Bravais lattice.

Graphene, however, is a Bravais multilattice, for which a single mapping \mathbf{F} cannot ensure the equilibrium of atoms anymore (Zhang, Huang, Geubelle, Klein, et al., 2002). For uniform in-plane normal membrane strains ε_{11} and ε_{22} and shear strain ε_{12} (Fig. 3.1A), graphene can be decomposed to two simple Bravais sublattices (Zhang, Huang, Geubelle, Klein, et al., Zhang et al., 2004), as shown in Fig. 3.2 by the open and solid circles, respectively. Each sublattice follows the single mapping \mathbf{F} , but the two sublattices may have a shift $\boldsymbol{\zeta}$ to ensure the equilibrium of atoms. The deformed bond (between atoms from two different sublattices) then becomes $\mathbf{r}_{ij} = \mathbf{F} \cdot \mathbf{r}_{ij}^{(0)} + \boldsymbol{\zeta}$, which has the length r_{ij} given by $r_{ij}^2 = r_0^2(\delta_{\alpha\beta} + 2\varepsilon_{\alpha\beta})(n_\alpha + x_\alpha)(n_\beta + x_\beta)$, where $\delta_{\alpha\beta}$ is the second-order identity tensor, $\mathbf{x} = \frac{1}{r_0}\mathbf{F}^{-1} \cdot \boldsymbol{\zeta}$ is to be determined analytically via energy minimization (note the summation over Greek subscripts).

For the graphene subject to the combined in-plane membrane strain $\varepsilon_{\alpha\beta}$ ($\alpha, \beta = 1, 2$) and curvature κ_{11} , κ_{22} , and κ_{12} (Fig. 3.1B), which stretch and bend the graphene, respectively, the distance between two nearest-neighbor atoms (from *different* sublattices) becomes (Huang et al., 2006)

$$r_{ij}^2 = r_0^2(\delta_{\alpha\beta} + 2\varepsilon_{\alpha\beta})(n_\alpha + x_\alpha)(n_\beta + x_\beta) - \frac{r_0^4}{12} [\kappa_{\alpha\beta}(n_\alpha + x_\alpha)(n_\beta + x_\beta)]^2, \quad (3.2)$$

where the shift vector \mathbf{x} is to be determined analytically via energy minimization; the first term on the right-hand side is the leading term in bond length due to in-plane membrane strain, and the second term represents the leading term in bond length due to the curvature. Figure 3.3 illustrates this second term via a

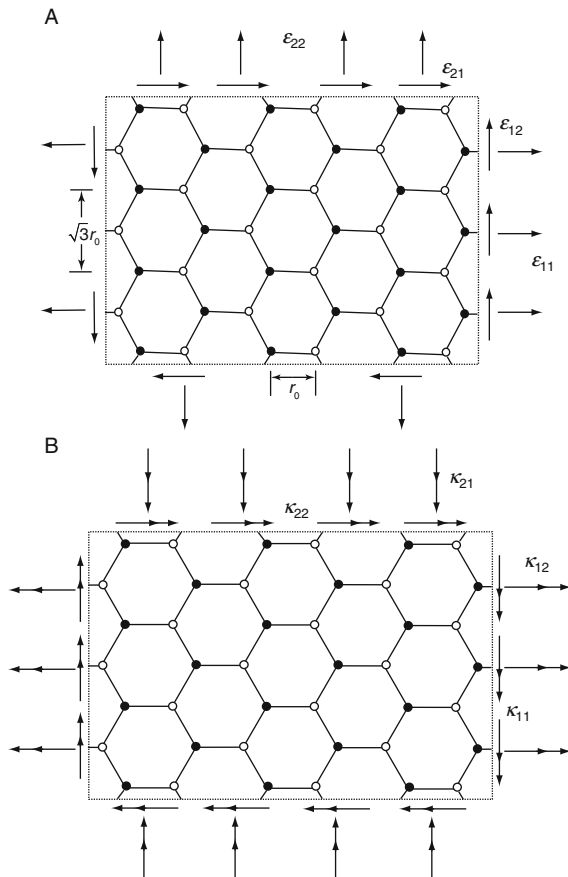


FIG. 3.1 Schematic diagram of a graphene sheet subject to (A) in-plane membrane strain and (B) curvature.

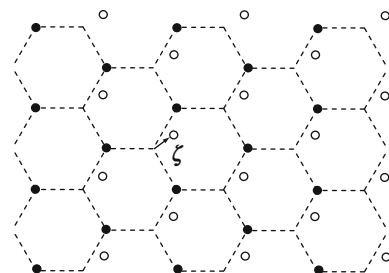


FIG. 3.2 A shift vector ζ between two sublattices is introduced to ensure the equilibrium of atoms.

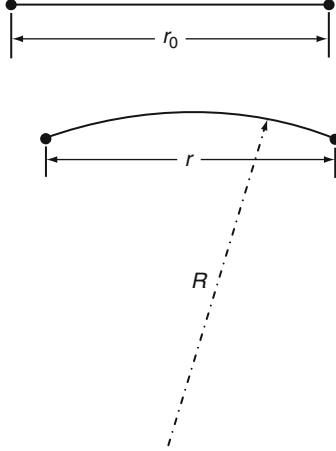


FIG. 3.3 A straight segment of length r_0 bent to a circular arc of radius R without stretch.

straight segment of length r_0 bent to a circular arc of radius R without stretch. The arc length is r_0 , and the straight length r between the two end points of the segment is $r = 2R \sin[r_0/(2R)]$. Its Taylor expansion for $r_0 \ll R$ gives $r = 2R \left[\frac{r_0}{2R} - \frac{1}{6} \left(\frac{r_0}{2R} \right)^3 + O\left(\frac{r_0}{R}\right)^5 \right]$, and therefore $r^2 = r_0^2 - \frac{r_0^4}{12R^2} + O\left(\frac{r_0^6}{R^4}\right)$, which is the same as Eq. (3.2) if the curvature κ is replaced by $1/R$.

The bond angle φ_{ijk} between bonds $i-j$ and $i-k$ can be similarly obtained as

$$\begin{aligned} \cos \varphi_{ijk} &= \frac{r_0^2}{r_{ij} r_{ik}} \left(n_\alpha^{(1)} + x_\alpha \right) \left(n_\lambda^{(2)} + x_\lambda \right) \\ &\times \left\{ \delta_{\alpha\lambda} + 2\varepsilon_{\alpha\lambda} + \frac{r_0^2}{12} \kappa_{\alpha\beta} \kappa_{\gamma\lambda} \left[3 \left(n_\beta^{(1)} + x_\beta \right) \left(n_\gamma^{(2)} + x_\gamma \right) \right. \right. \\ &\quad \left. \left. - 2 \left(n_\beta^{(2)} + x_\beta \right) \left(n_\gamma^{(2)} + x_\gamma \right) - 2 \left(n_\beta^{(1)} + x_\beta \right) \left(n_\gamma^{(1)} + x_\gamma \right) \right] \right\}, \quad (3.3) \end{aligned}$$

where $\mathbf{n}^{(1)}$ and $\mathbf{n}^{(2)}$ represent the directions of $i-j$ and $i-k$ bonds prior to deformation, respectively.

Substitution of Eqs. (3.2) and (3.3) into the Taylor expansion (3.1) gives the bond energy V as a quadratic function of membrane strain ε , shift vector \mathbf{x} , and curvature $\boldsymbol{\kappa}$. The energy associated with each atom is $\Phi = \frac{1}{2} \sum_{j=1}^3 V(r_{ij}; \cos \varphi_{ijk}, k \neq i, j)$, with the summation running over the three nearest-neighbor atoms, and the factor one half resulting from equipartition of bond energy. The shift vector is determined from energy minimization $\partial \Phi / \partial x_\lambda = 0$ as

$$x_\lambda = \frac{2}{3} A \varepsilon_{\alpha\beta} \sum_{j=1}^3 n_\alpha n_\beta n_\lambda, \quad (3.4)$$

which depends on the in-plane membrane strain ε but not on the curvature κ (and therefore no shift for curvature only), $\sum_{j=1}^3 n_\alpha n_\beta n_\lambda$ is the summation running over the three nearest-neighbor atoms, and A is given in terms of the five derivatives and equilibrium bond length r_0 by

$$A = 1 - \frac{8r_0^2 \left(\frac{\partial^2 V}{\partial r_{ij}^2} \right)_0 + 12r_0 \left(\frac{\partial^2 V}{\partial r_{ij} \partial \cos \varphi_{ijk}} \right)_0}{12 \left(\frac{\partial V}{\partial \cos \varphi_{ijk}} \right)_0 + 4r_0^2 \left(\frac{\partial^2 V}{\partial r_{ij}^2} \right)_0 + 18 \left(\frac{\partial^2 V}{\partial \cos \varphi_{ijk} \partial \cos \varphi_{ijl}} \right)_0 - 9 \left(\frac{\partial^2 V}{\partial \cos \varphi_{ijk} \partial \cos \varphi_{ijl}} \right)_0 + 12r_0 \left(\frac{\partial^2 V}{\partial r_{ij} \partial \cos \varphi_{ijk}} \right)_0}. \quad (3.5)$$

The strain energy density (energy per unit area of graphene) is $w = \Phi / S_0$, where $S_0 = 3\sqrt{3}r_0^2/4$ is the area per atom. It becomes the following quadratic function of ε and κ once the shift vector x is substituted by Eq. (3.4):

$$w = \frac{\sqrt{3}}{8} \left(\frac{\partial V}{\partial \cos \varphi_{ijk}} \right)_0 (\kappa_{11} + \kappa_{22})^2 + \frac{1}{4\sqrt{3}} \left(\frac{\partial^2 V}{\partial r_{ij}^2} \right)_0 (\varepsilon_{11} + \varepsilon_{22})^2 + \frac{B}{32\sqrt{3}} [(\varepsilon_{11} - \varepsilon_{22})^2 + 4\varepsilon_{12}^2], \quad (3.6)$$

where

$$B = \frac{3(1-A)^2}{r_0^2} \left[4 \left(\frac{\partial V}{\partial \cos \varphi_{ijk}} \right)_0 + 6 \left(\frac{\partial^2 V}{\partial \cos \varphi_{ijk} \partial \cos \varphi_{ijl}} \right)_0 - 3 \left(\frac{\partial^2 V}{\partial \cos \varphi_{ijk} \partial \cos \varphi_{ijl}} \right)_0 \right] + 4(1+A)^2 \left(\frac{\partial^2 V}{\partial r_{ij}^2} \right)_0 - 12 \frac{(1-A^2)}{r_0} \left(\frac{\partial^2 V}{\partial r_{ij} \partial \cos \varphi_{ijk}} \right)_0. \quad (3.7)$$

The strain energy density w depends on the curvature κ only via $\kappa_{11} + \kappa_{22}$, and is independent of $\kappa_{11} - \kappa_{22}$ and κ_{12} . For equibiaxial curvature $\kappa_{11} = \kappa_{22} = \kappa$ [and no membrane strain, which gives a vanishing shift vector in Eq. (3.4)], both the bond length in Eq. (3.2) and bond angle in Eq. (3.3) change according to $r_{ij}^2 = r_0^2(1 - \frac{1}{12}\kappa^2 r_0^2)$ and $\cos \varphi_{ijk} = -\frac{1}{2} + \frac{3}{8}\kappa^2 r_0^2$. For terms up to κ^2 , the bond length change does not contribute to the interatomic potential V in Eq. (3.1) since $(r_{ij} - r_0)^2$ is on the order $O(\kappa^4)$. The bond-angle change, however, contributes to V via $\sum_{k \neq i,j} \left(\frac{\partial V}{\partial \cos \varphi_{ijk}} \right)_0 \left(\cos \varphi_{ijk} + \frac{1}{2} \right)$. For $\kappa_{11} = \kappa$ and $\kappa_{22} = -\kappa$, that is, saddle

shape, it can be shown that the k -summation over the three bonds at each atom vanishes, and therefore does not contribute to the strain energy density.

The membrane stress (force per unit length) is the work conjugate of membrane strain, $\partial w/\partial \varepsilon_{\alpha\beta}$, and is given by

$$\begin{aligned} (\sigma_{11} + \sigma_{22})t &= \frac{1}{\sqrt{3}} \left(\frac{\partial^2 V}{\partial r_{ij}^2} \right)_0 (\varepsilon_{11} + \varepsilon_{22}), \\ \left\{ \begin{array}{c} (\sigma_{11} - \sigma_{22})t \\ \sigma_{12}t \end{array} \right\} &= \frac{B}{8\sqrt{3}} \left\{ \begin{array}{c} \varepsilon_{11} - \varepsilon_{22} \\ \varepsilon_{12} \end{array} \right\}. \end{aligned} \quad (3.8)$$

It is noted that the membrane stress naturally emerges as the product of “conventional membrane stress” $\sigma_{\alpha\beta}$ (force per unit area) and “thickness” t of the graphene because the strain energy density is the energy per unit area (instead of volume). The shear rigidity (ratio of $\sigma_{12}t$ to ε_{12}) is proportional to B , and the biaxial tension rigidity [ratio of $(\sigma_{11} + \sigma_{22})t$ to $(\varepsilon_{11} + \varepsilon_{22})$] is proportional to $(\partial^2 V / \partial r_{ij}^2)_0$.

The moment (bending/twisting moment per unit length) is the work conjugate of curvature, $\partial w/\partial \kappa_{\alpha\beta}$, and is given by

$$\begin{aligned} M_{11} + M_{22} &= \frac{\sqrt{3}}{2} \left(\frac{\partial V}{\partial \cos \varphi_{ijk}} \right)_0 (\kappa_{11} + \kappa_{22}), \\ \left\{ \begin{array}{c} M_{11} - M_{22} \\ M_{12} \end{array} \right\} &= 0. \end{aligned} \quad (3.9)$$

Its torsion rigidity vanishes at infinitesimal strain (since $M_{12} = 0$), and the biaxial bending rigidity [ratio of $(M_{11} + M_{22})$ to $(\kappa_{11} + \kappa_{22})$] is proportional to $(\partial V / \partial \cos \varphi_{ijk})_0$, which reflects multibody atomistic interactions. (A pair potential $V = V(r_{ij})$ would give vanishing bending rigidity for graphene.) The above moment–curvature relation is different from the classical linear elastic shell theory in the following aspects because the strain energy density in Eq. (3.6) depends on the curvature only via $\kappa_{11} + \kappa_{22}$:

- (i) The torque vanishes, $M_{12} = 0$, and the normal components of the moment are always equal, $M_{11} = M_{22}$.
- (ii) The moment is proportional to the sum of principal curvatures $\kappa_{11} + \kappa_{22}$, and is independent of deviatoric components of curvatures. For example, curvatures $\kappa_{11} = -\kappa_{22}$ give vanishing moments.

Comparison of strain energy density in Eq. (3.6) with the membrane energy density $\frac{C}{2(1-v^2)} \left[(\varepsilon_x + \varepsilon_y)^2 - 2(1-v)(\varepsilon_x \varepsilon_y - \varepsilon_{xy}^2) \right]$ in Eq. (1.1) for the classical

linear elastic thin shells suggests the identifications $\frac{C}{1-v} = \frac{1}{\sqrt{3}} \left(\frac{\partial^2 V}{\partial r_{ij}^2} \right)_0$ and $\frac{C}{1+v} = \frac{B}{8\sqrt{3}}$, which give

$$C = \frac{B}{4\sqrt{3}} \frac{\left(\frac{\partial^2 V}{\partial r_{ij}^2} \right)_0}{\left(\frac{\partial^2 V}{\partial r_{ij}^2} \right)_0 + \frac{B}{8}}, \quad v = \frac{\left(\frac{\partial^2 V}{\partial r_{ij}^2} \right)_0 - \frac{B}{8}}{\left(\frac{\partial^2 V}{\partial r_{ij}^2} \right)_0 + \frac{B}{8}}. \quad (3.10)$$

However, the comparison of strain energy density in [Eq. \(3.6\)](#) with the bending energy density $\frac{D}{2} [(\kappa_x + \kappa_y)^2 - 2(1-v)(\kappa_x \kappa_y - \kappa_{xy}^2)]$ in [Eq. \(1.1\)](#) for the classical linear elastic thin shells suggests $D(1+v) = \frac{\sqrt{3}}{2} (\partial V / \partial \cos \varphi_{ijk})_0$ and $D(1-v) = 0$, which give

$$D = \frac{\sqrt{3}}{4} \left(\frac{\partial V}{\partial \cos \varphi_{ijk}} \right)_0, \quad v = 1. \quad (3.11)$$

The Poisson's ratios in [Eqs. \(3.10\) and \(3.11\)](#) are contradictory. This is because in a classical linear elastic shell, the bending rigidity results from the tension and compression on opposite sides of the neutral plane. Consequently, its bending, tension, torsion, and shear rigidities satisfy

$$\frac{\text{bending rigidity}}{\text{tension rigidity}} = \frac{\text{torsion rigidity}}{\text{shear rigidity}}. \quad (3.12)$$

In graphene, the bending rigidity results from multibody atomistic interactions, as reflected from the bond-angle dependence $(\partial V / \partial \cos \varphi_{ijk})_0$ of the interatomic potential in [Eq. \(3.11\)](#), and is not directly related to the tension rigidity such that

$$\frac{\text{bending rigidity}}{\text{tension rigidity}} \neq \frac{\text{torsion rigidity}}{\text{shear rigidity}}. \quad (3.13)$$

In fact, the right-hand side in [Eq. \(3.13\)](#) is zero due to the vanishing torsion rigidity at infinitesimal strain in [Eq. \(3.9\)](#). The above inequality makes it impossible to define a single Poisson's ratio for both tension and bending.

[Equation \(3.12\)](#) is the basis for defining the shell thickness in the prior continuum shell modeling of CNTs ([Yakobson et al., 1996](#)) since the ratio of bending to tension rigidities equals $t^2/12$ in the classical linear elastic shell theory. Such defined thickness, however, does not give a constant value for graphene (and CNTs) and depends on the type of loading (e.g., uniaxial or biaxial

loadings), due to the inequality in Eq. (3.13) (Huang et al., 2006). In fact, the reported shell thickness varies from 0.062 to 0.089 nm (Kudin, Scuseria, & Yakobson, 2001; Tu et al., 2002; Wang, Zheng, Liu, & Jiang, 2005; Yakobson et al., 1996; Zhou, Zhou, & Ou-Yang, 2000), which may be partially due to this loading dependence.

4. A Linear Shell Theory for Carbon Nanotubes Based on the Interatomic Potential

4.1. MEMBRANE STRAINS AND CURVATURES

The linear shell theory in this section is the limit of infinitesimal deformation for the nonlinear, finite-deformation shell theory in Section 6. A point on the CNT is $\mathbf{P} = Re_R + Ze_Z$, where (R, θ, Z) are the cylindrical coordinates, R is the CNT radius, and the base vector \mathbf{e}_R varies with θ . For two nearby points on the CNT, \mathbf{P} and $\mathbf{P} + \Delta\mathbf{P}$ with coordinates (R, θ, Z) and $(R, \theta + \Delta\theta, Z + \Delta Z)$, the Taylor series expansion around the point \mathbf{P} gives

$$\begin{aligned}\Delta\mathbf{P} = & \frac{\partial\mathbf{P}}{\partial\theta}\Delta\theta + \frac{\partial\mathbf{P}}{\partial Z}\Delta Z + \frac{1}{2} \left[\frac{\partial^2\mathbf{P}}{\partial\theta^2}(\Delta\theta)^2 + 2\frac{\partial^2\mathbf{P}}{\partial\theta\partial Z}\Delta\theta\Delta Z + \frac{\partial^2\mathbf{P}}{\partial Z^2}(\Delta Z)^2 \right] \\ & + \frac{1}{6} \left[\frac{\partial^3\mathbf{P}}{\partial\theta^3}(\Delta\theta)^3 + 3\frac{\partial^3\mathbf{P}}{\partial\theta^2\partial Z}(\Delta\theta)^2\Delta Z + 3\frac{\partial^2\mathbf{P}}{\partial\theta\partial Z^2}\Delta\theta(\Delta Z)^2 + \frac{\partial^3\mathbf{P}}{\partial Z^3}(\Delta Z)^3 \right] \\ & + O(|\Delta\xi|^4) = \mathbf{e}_\theta R\Delta\theta + \mathbf{e}_Z\Delta Z - \frac{1}{2}\mathbf{e}_R R(\Delta\theta)^2 - \frac{1}{6}\mathbf{e}_\theta R(\Delta\theta)^3 + O(|\Delta\xi|^4),\end{aligned}\tag{4.1}$$

where $|\Delta\xi|$ is $R|\Delta\theta|$ or $|\Delta Z|$. The length of $\Delta\mathbf{P}$ is

$$|\Delta\mathbf{P}|^2 = R^2(\Delta\theta)^2 + (\Delta Z)^2 - \frac{1}{12}R^2(\Delta\theta)^4 + O(|\Delta\xi|^5).\tag{4.2}$$

The angle φ between two vectors $\Delta\mathbf{P}_{(1)}$ and $\Delta\mathbf{P}_{(2)}$, which is needed in the multibody interatomic potential for carbon in Section 2, is obtained from $\cos\varphi = \frac{\Delta\mathbf{P}_{(1)} \cdot \Delta\mathbf{P}_{(2)}}{|\Delta\mathbf{P}_{(1)}||\Delta\mathbf{P}_{(2)}|}$, where

$$\begin{aligned}\Delta\mathbf{P}_{(1)} \cdot \Delta\mathbf{P}_{(2)} = & R^2\Delta\theta_{(1)}\Delta\theta_{(2)} + \Delta Z_{(1)}\Delta Z_{(2)} \\ & + \frac{1}{12}R^2\Delta\theta_{(1)}\Delta\theta_{(2)} \left[3\Delta\theta_{(1)}\Delta\theta_{(2)} - 2(\Delta\theta_{(1)})^2 - 2(\Delta\theta_{(2)})^2 \right] + O(|\Delta\xi|^5).\end{aligned}\tag{4.3}$$

The point on the CNT $\mathbf{P} = Re_R + Ze_Z$ moves to $\mathbf{p} = \mathbf{P} + \mathbf{U} = (R + U_R)\mathbf{e}_R + U_\theta\mathbf{e}_\theta + (Z + U_Z)\mathbf{e}_Z$, where $\mathbf{U} = U_R\mathbf{e}_R + U_\theta\mathbf{e}_\theta + U_Z\mathbf{e}_Z$ is the

displacement, and its components U_R , U_θ , and U_Z are functions of θ and Z . The components of the membrane strain tensor are obtained from the derivatives of in-surface displacements U_θ and U_Z (see, e.g., [Niordson, 1985](#); [Timoshenko & Woinowsky-Krieger, 1959](#)):

$$\varepsilon_{\theta\theta} = \frac{1}{R} \frac{\partial U_\theta}{\partial \theta} + \frac{U_R}{R}, \quad 2\varepsilon_{\theta Z} = \frac{\partial U_\theta}{\partial Z} + \frac{1}{R} \frac{\partial U_Z}{\partial \theta}, \quad \varepsilon_{ZZ} = \frac{\partial U_Z}{\partial Z}. \quad (4.4)$$

The components of the curvature tensor $\kappa_{\alpha\beta}$ ($\alpha, \beta = \theta, Z$) are obtained from the derivatives of out-of-surface displacement U_R (e.g., [Niordson, 1985](#)):

$$\kappa_{\theta\theta} = \frac{1}{R^2} \left(\frac{\partial^2 U_R}{\partial \theta^2} - 2 \frac{\partial U_\theta}{\partial \theta} - U_R \right), \quad \kappa_{\theta Z} = \frac{1}{R} \left(\frac{\partial^2 U_R}{\partial \theta \partial Z} - \frac{\partial U_\theta}{\partial Z} \right), \quad \kappa_{ZZ} = \frac{\partial^2 U_R}{\partial Z^2}. \quad (4.5)$$

For two nearby points \mathbf{p} and $\mathbf{p} + \Delta\mathbf{p}$ on the deformed CNT, the Taylor series expansion around the point \mathbf{p} gives

$$\begin{aligned} \Delta\mathbf{p} = \Delta\mathbf{P} + \frac{\partial \mathbf{U}}{\partial \theta} \Delta\theta + \frac{\partial \mathbf{U}}{\partial Z} \Delta Z + \frac{1}{2} \left[\frac{\partial^2 \mathbf{U}}{\partial \theta^2} (\Delta\theta)^2 + 2 \frac{\partial^2 \mathbf{U}}{\partial \theta \partial Z} \Delta\theta \Delta Z + \frac{\partial^2 \mathbf{U}}{\partial Z^2} (\Delta Z)^2 \right] \\ + \frac{1}{6} \left[\frac{\partial^3 \mathbf{U}}{\partial \theta^3} (\Delta\theta)^3 + 3 \frac{\partial^3 \mathbf{U}}{\partial \theta^2 \partial Z} (\Delta\theta)^2 \Delta Z + 3 \frac{\partial^3 \mathbf{U}}{\partial \theta \partial Z^2} \Delta\theta (\Delta Z)^2 + \frac{\partial^3 \mathbf{U}}{\partial Z^3} (\Delta Z)^3 \right] + O(|\Delta\xi|^4). \end{aligned} \quad (4.6)$$

Its length, up to the order $O(|\mathbf{U}|^2)$, is given by

$$\begin{aligned} |\Delta\mathbf{p}|^2 = |\Delta\mathbf{P}|^2 + 2 \left[\varepsilon_{\theta\theta} (R\Delta\theta)^2 + 2\varepsilon_{\theta Z} R\Delta\theta \Delta Z + \varepsilon_{ZZ} (\Delta Z)^2 \right] \\ + \frac{1}{6} R(\Delta\theta)^2 \left[\kappa_{\theta\theta} (R\Delta\theta)^2 + 2\kappa_{\theta Z} R\Delta\theta \Delta Z + \kappa_{ZZ} (\Delta Z)^2 \right] + \dots, \end{aligned} \quad (4.7)$$

where \dots represents terms that are on the order of $|\Delta\xi|^5$, or $|\Delta\xi|^3$ with the coefficients that are linearly proportional to the gradient of membrane strains $|\nabla\boldsymbol{\varepsilon}|$, that is, $O(|\nabla\boldsymbol{\varepsilon}| \cdot |\Delta\xi|^3)$, which can also be written in terms of the characteristic length L of deformation as $O\left(\frac{|\boldsymbol{\varepsilon}|}{L} \cdot |\Delta\xi|^3\right)$. Any continuum theory holds only when the characteristic length L of deformation is much larger than the atomic spacing Δ (otherwise discrete, atomistic simulations should be used). Therefore, [Eq. \(4.7\)](#) can be written as

$$|\Delta \mathbf{p}|^2 = |\Delta \mathbf{P}|^2 + \left\{ \begin{array}{l} 2 \left[\varepsilon_{\theta\theta} (R\Delta\theta)^2 + 2\varepsilon_{\theta Z} R\Delta\theta\Delta Z + \varepsilon_{ZZ} (\Delta Z)^2 \right] \\ + \frac{1}{6} R(\Delta\theta)^2 \left[\kappa_{\theta\theta} (R\Delta\theta)^2 + 2\kappa_{\theta Z} R\Delta\theta\Delta Z + \kappa_{ZZ} (\Delta Z)^2 \right] \end{array} \right\} (4.8)$$

$$\times \left[1 + O\left(\frac{\Delta}{L}\right) \right],$$

that is, its order of error (as compared to unity) is $O(\Delta/L)$. Here, the curvature terms are essentially independent of membrane strains, as discussed before. The bond angle φ after deformation can be similarly obtained from $\cos\varphi = \frac{\Delta\mathbf{p}_{(1)} \cdot \Delta\mathbf{p}_{(2)}}{|\Delta\mathbf{p}_{(1)}||\Delta\mathbf{p}_{(2)}|}$, where

$$\Delta\mathbf{p}_{(1)} \cdot \Delta\mathbf{p}_{(2)} = \Delta\mathbf{P}_{(1)} \cdot \Delta\mathbf{P}_{(2)} + \left\{ \begin{array}{l} 2\varepsilon_{\theta\theta} R^2 \Delta\theta_{(1)} \Delta\theta_{(2)} + 2\varepsilon_{\theta Z} R (\Delta\theta_{(1)} \Delta Z_{(2)} + \Delta\theta_{(2)} \Delta Z_{(1)}) + 2\varepsilon_{ZZ} \Delta Z_{(1)} \Delta Z_{(2)} \\ - \frac{R}{4} \kappa_{z\beta} (\Delta\xi_{z(1)} \Delta\xi_{\beta(1)} \Delta\theta_{(2)}^2 + \Delta\xi_{z(2)} \Delta\xi_{\beta(2)} \Delta\theta_{(1)}^2) \\ + \frac{R}{6} \kappa_{z\beta} (\Delta\xi_{z(1)} \Delta\theta_{(2)} + \Delta\xi_{z(2)} \Delta\theta_{(1)}) (\Delta\xi_{\beta(1)} \Delta\theta_{(1)} + \Delta\xi_{\beta(2)} \Delta\theta_{(2)}) \end{array} \right\}$$

$$\times \left[1 + O\left(\frac{\Delta}{L}\right) \right]. \quad (4.9)$$

where $\Delta\xi_{\theta(1)} = R\Delta\theta_{(1)}$, $\Delta\xi_{Z(1)} = \Delta Z_{(1)}$, $\Delta\xi_{\theta(2)} = R\Delta\theta_{(2)}$, $\Delta\xi_{Z(2)} = \Delta Z_{(2)}$.

Similar to graphene, CNTs do not have a simple Bravais lattice, and their hexagonal lattice structure can be decomposed into two triangular sublattices (Fig. 3.2) that are shifted by the vector η to ensure the equilibrium of atoms. The shift vector η degenerates to $r_0\mathbf{x}$ for a graphene (Section 3), where r_0 is the initial bond length. The vector $\Delta\mathbf{P}$, with components $(R\Delta\theta, \Delta Z)$, between two atoms from different sublattices, becomes $\Delta\mathbf{p}$ after deformation and has the new coordinates:

$$R\Delta\bar{\theta} = R\Delta\theta + \eta_\theta, \quad \Delta\bar{Z} = \Delta Z + \eta_Z, \quad (4.10)$$

where η is to be determined. The bond length and angle in Eqs. (4.8) and (4.9) still hold once $(R\Delta\theta, \Delta Z)$ are replaced by $(R\Delta\bar{\theta}, \Delta\bar{Z})$:

$$|\Delta\mathbf{p}|^2 = |\Delta\mathbf{P}|^2 + \left[2\varepsilon_{z\beta} \Delta\bar{\xi}_z \Delta\bar{\xi}_\beta + \frac{1}{6} R(\Delta\bar{\theta})^2 \kappa_{z\beta} \Delta\bar{\xi}_z \Delta\bar{\xi}_\beta \right] \left[1 + O\left(\frac{\Delta}{L}\right) \right], \quad (4.11)$$

$$\Delta \mathbf{p}_{(1)} \cdot \Delta \mathbf{p}_{(2)} = \Delta \mathbf{P}_{(1)} \cdot \Delta \mathbf{P}_{(2)} + \left\{ \begin{array}{l} 2\varepsilon_{\alpha\beta} \Delta \bar{\xi}_{\alpha_{(1)}} \Delta \bar{\xi}_{\beta_{(2)}} - \frac{R}{4} \kappa_{\alpha\beta} \left(\Delta \bar{\xi}_{\alpha_{(1)}} \Delta \bar{\xi}_{\beta_{(1)}} \Delta \bar{\theta}_{(2)}^2 + \Delta \bar{\xi}_{\alpha_{(2)}} \Delta \bar{\xi}_{\beta_{(2)}} \Delta \bar{\theta}_{(1)}^2 \right) \\ + \frac{R}{6} \kappa_{\alpha\beta} \left(\Delta \bar{\xi}_{\alpha_{(1)}} \Delta \bar{\theta}_{(2)} + \Delta \bar{\xi}_{\alpha_{(2)}} \Delta \bar{\theta}_{(1)} \right) \left(\Delta \bar{\xi}_{\beta_{(1)}} \Delta \bar{\theta}_{(1)} + \Delta \bar{\xi}_{\beta_{(2)}} \Delta \bar{\theta}_{(2)} \right) \\ \times \left[1 + O\left(\frac{\Delta}{L}\right) \right], \end{array} \right\} \quad (4.12)$$

where $\Delta \bar{\xi}_\theta = R \Delta \bar{\theta}$ and $\Delta \bar{\xi}_Z = \Delta \bar{Z}$.

4.2. CONSTITUTIVE RELATIONS

The bond length and angle, and also the interatomic potential, now depend on membrane strains $\varepsilon_{\alpha\beta}$, curvatures $\kappa_{\alpha\beta}$, and shift vector η_λ :

$$r_{ij} = r_{ij}(\varepsilon_{\alpha\beta}, \kappa_{\alpha\beta}, \eta_\lambda), \quad \varphi_{ijk} = \varphi_{ijk}(\varepsilon_{\alpha\beta}, \kappa_{\alpha\beta}, \eta_\lambda); \quad V = V(r_{ij}, \varphi_{ijk}; k \neq i, j). \quad (4.13)$$

The strain energy density w is the energy (stored in atomic bonds) per unit area, and is given by

$$w(\varepsilon_{\alpha\beta}, \kappa_{\alpha\beta}, \eta_\lambda) = \frac{1}{2} \frac{\sum_{1 \leq j \leq 3} V(r_{ij}, \varphi_{ijk}; k \neq i, j)}{S_0}, \quad (4.14)$$

where the factor 1/2 results from the equal partition of bond energy between atoms, and S_0 is the average area per atom. The shift vector is determined by minimizing energy $\partial w / \partial \eta_\lambda = 0$ to ensure the equilibrium of atoms, which gives

$$\boldsymbol{\eta} = - \left[\left(\frac{\partial^2 w}{\partial \boldsymbol{\eta} \partial \boldsymbol{\eta}} \right)_0 \right]^{-1} \cdot \left[\left(\frac{\partial^2 w}{\partial \boldsymbol{\eta} \partial \boldsymbol{\epsilon}} \right)_0 : \boldsymbol{\epsilon} + \left(\frac{\partial^2 w}{\partial \boldsymbol{\eta} \partial \boldsymbol{\kappa}} \right)_0 : \boldsymbol{\kappa} \right] \quad (4.15)$$

for infinitesimal deformation, where the subscript “0” denotes the initial state of the CNT prior to deformation. For graphene at the initial configuration (same bond length r_0 and same bond angle 120°), it can be shown that the above $\boldsymbol{\eta}$ degenerates to $r_0 \boldsymbol{x}$ given in Eq. (3.4).

The strain energy density then becomes a function of membrane strains and curvatures, $w = w[\varepsilon_{\alpha\beta}, \kappa_{\alpha\beta}, \eta_\lambda(\varepsilon_{\alpha\beta}, \kappa_{\alpha\beta})]$. For infinitesimal deformations, it is a quadratic function

$$w = w_0 + \frac{1}{2} [\boldsymbol{\varepsilon} : \mathbf{L} : \boldsymbol{\varepsilon} + \boldsymbol{\kappa} : \mathbf{S} : \boldsymbol{\kappa} + \boldsymbol{\varepsilon} : \mathbf{H} : \boldsymbol{\kappa} + \boldsymbol{\kappa} : \mathbf{H}^T : \boldsymbol{\varepsilon}], \quad (4.16)$$

where

$$\begin{aligned} \mathbf{L} &= \left(\frac{\partial^2 w}{\partial \boldsymbol{\varepsilon} \partial \boldsymbol{\varepsilon}} \right)_0 - \left(\frac{\partial^2 w}{\partial \boldsymbol{\varepsilon} \partial \boldsymbol{\eta}} \right)_0 \cdot \left[\left(\frac{\partial^2 w}{\partial \boldsymbol{\eta} \partial \boldsymbol{\eta}} \right)_0 \right]^{-1} \cdot \left(\frac{\partial^2 w}{\partial \boldsymbol{\eta} \partial \boldsymbol{\varepsilon}} \right)_0, \\ \mathbf{S} &= \left(\frac{\partial^2 w}{\partial \boldsymbol{\kappa} \partial \boldsymbol{\kappa}} \right)_0 - \left(\frac{\partial^2 w}{\partial \boldsymbol{\kappa} \partial \boldsymbol{\eta}} \right)_0 \cdot \left[\left(\frac{\partial^2 w}{\partial \boldsymbol{\eta} \partial \boldsymbol{\eta}} \right)_0 \right]^{-1} \cdot \left(\frac{\partial^2 w}{\partial \boldsymbol{\eta} \partial \boldsymbol{\kappa}} \right)_0 \end{aligned} \quad (4.17)$$

are the tensile and bending rigidities, respectively, and

$$\begin{aligned} \mathbf{H} &= \left(\frac{\partial^2 w}{\partial \boldsymbol{\varepsilon} \partial \boldsymbol{\kappa}} \right)_0 - \left(\frac{\partial^2 w}{\partial \boldsymbol{\varepsilon} \partial \boldsymbol{\eta}} \right)_0 \cdot \left[\left(\frac{\partial^2 w}{\partial \boldsymbol{\eta} \partial \boldsymbol{\eta}} \right)_0 \right]^{-1} \cdot \left(\frac{\partial^2 w}{\partial \boldsymbol{\eta} \partial \boldsymbol{\kappa}} \right)_0, \\ \mathbf{H}^T &= \left(\frac{\partial^2 w}{\partial \boldsymbol{\kappa} \partial \boldsymbol{\varepsilon}} \right)_0 - \left(\frac{\partial^2 w}{\partial \boldsymbol{\kappa} \partial \boldsymbol{\eta}} \right)_0 \cdot \left[\left(\frac{\partial^2 w}{\partial \boldsymbol{\eta} \partial \boldsymbol{\eta}} \right)_0 \right]^{-1} \cdot \left(\frac{\partial^2 w}{\partial \boldsymbol{\eta} \partial \boldsymbol{\varepsilon}} \right)_0 \end{aligned} \quad (4.18)$$

are the coupling rigidities.

The membrane stress \mathbf{t} (force per unit length) and moment \mathbf{m} (bending/twisting moment per unit length) are the work conjugates of membrane strain $\boldsymbol{\varepsilon}$ and curvature $\boldsymbol{\kappa}$, respectively. The strain energy density in Eq. (4.16) gives the following linear constitutive relation¹:

$$\begin{aligned} \mathbf{t} &= \mathbf{L} : \boldsymbol{\varepsilon} + \mathbf{H} : \boldsymbol{\kappa}, \\ \mathbf{m} &= \mathbf{H}^T : \boldsymbol{\varepsilon} + \mathbf{S} : \boldsymbol{\kappa}. \end{aligned} \quad (4.19)$$

It is different from the constitutive models in the classical shell theories due to the membrane stress/curvature coupling via the coupling rigidity tensor \mathbf{H} and the moment/membrane strain coupling via \mathbf{H}^T . Wu, Peng, et al. (2008) defined the degree of coupling

$$D_H = \left(\frac{\|\mathbf{H}\| \|\mathbf{H}^T\|}{\|\mathbf{L}\| \|\mathbf{S}\|} \right)^{1/2}, \quad (4.20)$$

¹ The stress and moment defined here are the force and moment per unit length because the strain energy density defined in Eq. (4.14) is the energy per unit area (instead of volume).

which vanishes for the classical linear elastic shell as well as for graphene, where the norm of a fourth-order tensor is defined by $\|\mathbf{L}\| = (L_{\alpha\beta\gamma\delta}L_{\alpha\beta\gamma\delta})^{1/2}$. It is shown versus the CNT radius R in Fig. 4.1 for the second-generation interatomic potential (Brenner et al., 2002). It is essentially independent of the CNT chirality since the curves for armchair and zigzag CNTs are practically the same. However, it depends on the CNT radius. For a (5,5) armchair CNT ($R = 0.35$ nm), D_H is 42%, which suggests significant membrane stress/curvature and moment/membrane strain coupling. This coupling effect should be accounted for $R < 1.5$ nm since D_H is over 10% (but the classical shell theories do not). Most single-wall CNTs observed in experiments have radii less than 2.1 nm because larger CNTs may self-collapse due to van der Waals interactions (Liu, Yu, et al., 2004). It is therefore important to account for the coupling rigidity tensor.

Another difference with the classical linear elastic isotropic shell theories is that the tension and bending rigidity tensors \mathbf{L} and \mathbf{S} are anisotropic. This anisotropy results from the effect of CNT radius because the elastic behavior of graphene given in Eqs. (3.8) and (3.9) is isotropic. Wu, Peng, et al. (2008) introduced the degrees of anisotropy

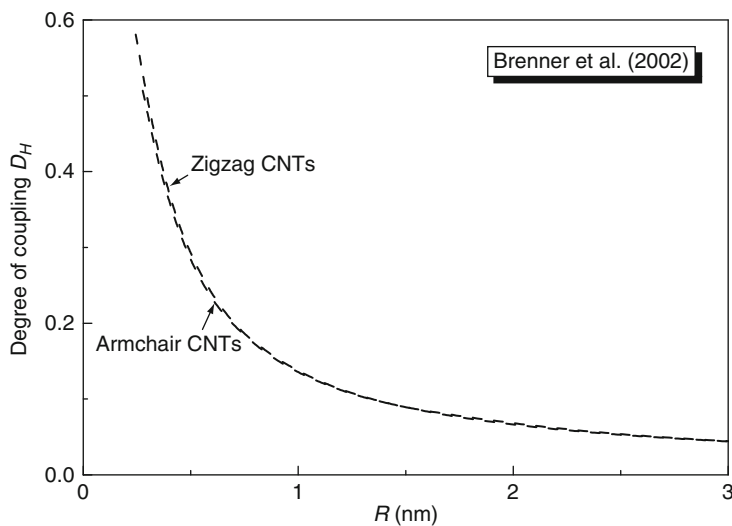


FIG. 4.1 The degree of coupling versus the radius of single-wall carbon nanotubes.

$$D_L = \frac{\|\mathbf{L} - \bar{\mathbf{L}}\|}{\|\mathbf{L}\|}, \quad D_S = \frac{\|\mathbf{S} - \bar{\mathbf{S}}\|}{\|\mathbf{S}\|}, \quad (4.21)$$

where $\bar{L}_{\alpha\beta\gamma\delta} = \bar{G}_L (\delta_{\alpha\gamma}\delta_{\beta\delta} + \delta_{\alpha\delta}\delta_{\beta\gamma} - \delta_{\alpha\beta}\delta_{\gamma\delta}) + \bar{K}_L \delta_{\alpha\beta}\delta_{\gamma\delta}$ ($\alpha, \beta, \gamma, \delta = \theta, Z$) is the isotropic tensor to approximate \mathbf{L} , and its shear rigidity $\bar{G}_L = \frac{1}{8}(L_{1111} + L_{2222} - 2L_{1122} + 4L_{1212})$ and in-surface bulk rigidity $\bar{K}_L = \frac{1}{4}(L_{1111} + L_{2222} + 2L_{1122})$ are obtained by minimizing $\|\mathbf{L} - \bar{\mathbf{L}}\|$; and the isotropic tensor $\bar{\mathbf{S}}$ can be obtained similarly. Figure 4.2 shows D_L and D_S versus the radius R of armchair CNTs for the second-generation interatomic potential (Brenner et al., 2002). For a (5,5) armchair CNT ($R = 0.35$ nm), $D_L = 7.8\%$ and $D_S = 13\%$, which suggests the important effect of anisotropy for small CNTs. However, D_L and D_S decrease rapidly as the CNT radius increases, and vanish for graphene. For a (10,10) armchair CNT ($R = 0.68$ nm), they are only 4.1% and 3.0%, respectively, such that large CNTs can be modeled as isotropic.

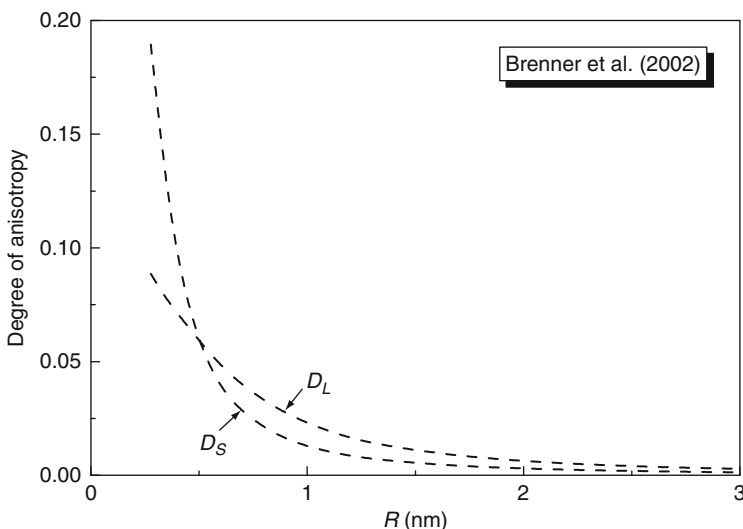


FIG. 4.2 The degree of anisotropy versus the radius of armchair single-wall carbon nanotubes, where D_L and D_S are for the tension and bending rigidity, respectively.

4.3. EQUILIBRIUM EQUATIONS

The equilibrium equations are (e.g., Niordson, 1985)²

$$\begin{aligned} \frac{1}{R} \frac{\partial t_{\theta\theta}}{\partial \theta} + \frac{\partial t_{\theta Z}}{\partial Z} - \frac{2}{R^2} \frac{\partial m_{\theta\theta}}{\partial \theta} - \frac{2}{R} \frac{\partial m_{\theta Z}}{\partial Z} + \bar{x}_\theta &= 0, \\ \frac{1}{R} \frac{\partial t_{\theta Z}}{\partial \theta} + \frac{\partial t_{ZZ}}{\partial Z} + \bar{x}_Z &= 0, \\ \frac{1}{R^2} \frac{\partial^2 m_{\theta\theta}}{\partial \theta^2} + \frac{\partial^2 m_{ZZ}}{\partial Z^2} + \frac{2}{R} \frac{\partial^2 m_{\theta Z}}{\partial \theta \partial Z} + \frac{t_{\theta\theta}}{R} - \frac{m_{\theta\theta}}{R^2} - p &= 0, \end{aligned} \quad (4.22)$$

where \bar{x}_θ and \bar{x}_Z are the in-surface area forces and p is the internal pressure. The traction boundary conditions are

$$\begin{aligned} t_{\theta Z} - \frac{2}{R} m_{\theta Z} &= \bar{t}_\theta + \frac{1}{R} \bar{m}_T, \\ t_{ZZ} &= \bar{t}_Z, \\ m_{ZZ} &= \bar{m}_B, \\ \frac{2}{R} \frac{\partial m_{Z\theta}}{\partial \theta} + \frac{\partial m_{ZZ}}{\partial Z} &= -\bar{t}_R - \frac{1}{R} \frac{\partial \bar{m}_T}{\partial \theta}, \end{aligned} \quad (4.23)$$

where \bar{t}_θ and \bar{t}_Z are the prescribed in-surface tractions, \bar{t}_R is the out-of-surface traction, and \bar{m}_B and \bar{m}_T are the prescribed bending moment and torque.

5. Can a Single-Wall Carbon Nanotube Be Modeled as a Thin Shell?

Let Δ denote the atomic spacing. Its ratio to the CNT radius, Δ/R , is used in this section to identify the order of errors to approximate a single-wall CNT by a thin shell. It will be shown that, while CNTs cannot be modeled as ordinary shells in general (Section 5.1), they can be viewed as special cases when one is willing to allow larger errors, such as a linear elastic orthotropic shell for the order of error $(\Delta/R)^2$ (Section 5.2), or an isotropic shell for the order of error (Δ/R) (Section 5.3).

² The effect of initial residual stress in the CNT is always negligibly small (Wu, Hwang, & Huang, 2008), and is therefore not accounted for here.

5.1. ORDER OF ERROR $(\Delta/R)^3$: NOT A CLASSICAL LINEAR ELASTIC SHELL

Let $[x]$ denote the order of magnitude of variable x . It can be shown that the rigidity tensors in Eqs. (4.17) and (4.18) are on the order of (Peng et al., 2008)

$$[\mathbf{L}] \sim \frac{[\nabla V]L}{S_0}, \quad [\mathbf{S}] \sim \frac{[\nabla V]L}{S_0} \Delta^2, \quad [\mathbf{H}] \sim \frac{[\nabla V]L}{S_0} \frac{\Delta^2}{R}, \quad (5.1)$$

where ∇V is the gradient of interatomic potential (locally averaged per atom), L is the characteristic length of deformation, S_0 is the area per atom on the CNT of radius R , and Δ is the atomic spacing. For a graphene ($R \rightarrow \infty$), $\mathbf{H} = 0$ such that there is no tension/bending coupling. For a CNT, these rigidity tensors have the following orders of magnitude with respect to Δ/R :

$$[\mathbf{S}]R^{-2} \sim [\mathbf{L}] \left(\frac{\Delta}{R} \right)^2, \quad [\mathbf{H}]R^{-1} \sim [\mathbf{L}] \left(\frac{\Delta}{R} \right)^2. \quad (5.2)$$

The order of magnitude of the coupling rigidity tensor can also be written as $[\mathbf{H}] \sim \sqrt{[\mathbf{L}][\mathbf{S}]} \frac{\Delta}{R}$.

The order of the error in Eqs. (4.2) and (4.3) is $O[(\Delta/R)^3]$. The coupling between membrane stress and curvature and between moment and membrane strain shown in Section 4 is important to the order of error $O[(\Delta/R)^3]$. Therefore, a CNT cannot be modeled as a classical linear elastic shell for the order of error $O[(\Delta/R)^3]$. For an atomic spacing of $\Delta = 0.14\text{nm}$ and the (5,5) armchair CNT ($R = 0.35\text{ nm}$), $(\Delta/R)^3$ is around 6%.

5.2. ORDER OF ERROR $(\Delta/R)^2$: A LINEAR ELASTIC ORTHOTROPIC SHELL

Peng et al. (2008) used the constitutive model in Eq. (4.19) to determine the linear elastic structural response of a CNT subject to the following simple loadings:³

- (i) *Uniaxial tension (or compression).* The ratio of axial force F_Z to axial strain ε_{ZZ} is

$$\frac{F_Z}{\varepsilon_{ZZ}} = 2\pi R \left[L_{ZZZZ} - \frac{(L_{\theta\theta ZZ} - H_{ZZ\theta\theta}R^{-1})^2}{L_{\theta\theta\theta\theta} - 2H_{\theta\theta\theta\theta}R^{-1} + S_{\theta\theta\theta\theta}R^{-2}} \right] \left\{ 1 + O\left[\left(\frac{\Delta}{R}\right)^3\right] \right\}. \quad (5.3)$$

³ The effect of initial residual stress in the CNT is not accounted for since it is negligibly small (Peng et al., 2008).

The ratio of circumferential strain to axial strain is

$$\frac{\varepsilon_{\theta\theta}}{\varepsilon_{ZZ}} = -\frac{L_{\theta\theta ZZ} - H_{ZZ\theta\theta}R^{-1}}{L_{\theta\theta\theta\theta} - 2H_{\theta\theta\theta\theta}R^{-1} + S_{\theta\theta\theta\theta}R^{-2}} \left\{ 1 + O\left[\left(\frac{\Delta}{R}\right)^3\right] \right\}. \quad (5.4)$$

As indicated, the order of the error in Eqs. (5.3) and (5.4) is $O[(\Delta/R)^3]$, the same as Section 4.

(ii) *Torsion.* The ratio of torque T to twist κ (rotation angle per unit length) is

$$\frac{T}{\kappa} = 2\pi R^3 (L_{\theta Z \theta Z} - 4H_{\theta Z \theta Z}R^{-1} + 4S_{\theta Z \theta Z}R^{-2}) \left\{ 1 + O\left[\left(\frac{\Delta}{R}\right)^3\right] \right\}. \quad (5.5)$$

(iii) *Internal (or external) pressure.* The circumferential membrane stress $t_{\theta\theta}$ (per unit length) and strain $\varepsilon_{\theta\theta}$, axial strain ε_{ZZ} , and internal pressure p are related by

$$t_{\theta\theta} = [(L_{\theta\theta\theta\theta} - H_{\theta\theta\theta\theta}R^{-1})\varepsilon_{\theta\theta} + L_{\theta\theta ZZ}\varepsilon_{ZZ}] \left\{ 1 + O\left[\left(\frac{\Delta}{R}\right)^3\right] \right\}, \quad (5.6)$$

$$p = \frac{1}{R} [(L_{\theta\theta\theta\theta} - 2H_{\theta\theta\theta\theta}R^{-1} + S_{\theta\theta\theta\theta}R^{-2})\varepsilon_{\theta\theta} + (L_{\theta\theta ZZ} - H_{ZZ\theta\theta}R^{-1})\varepsilon_{ZZ}] \times \left\{ 1 + O\left[\left(\frac{\Delta}{R}\right)^3\right] \right\}, \quad (5.7)$$

$$\frac{\varepsilon_{ZZ}}{\varepsilon_{\theta\theta}} = -\frac{L_{ZZ\theta\theta} - H_{ZZ\theta\theta}R^{-1}}{L_{ZZZZ}} \left\{ 1 + O\left[\left(\frac{\Delta}{R}\right)^3\right] \right\}. \quad (5.8)$$

(iv) *Bending.* The displacements in the CNT are $u_\theta = -\frac{k}{2}(L^2 - Z^2)\sin\theta$, $u_Z = kRZ\cos\theta$, and $u_R = \frac{k}{2}(L^2 - Z^2 - 2\lambda R^2)\cos\theta$, where k is the curvature, L is the beam length, and λ is to be determined. These give the membrane strains and curvatures as $\varepsilon_{\theta\theta} = -k\lambda R\cos\theta$, $\varepsilon_{ZZ} = kR\cos\theta$, $\varepsilon_{\theta Z} = 0$, $\kappa_{\theta\theta} = 2k\lambda\cos\theta$, $\kappa_{ZZ} = -k\cos\theta$, and $\kappa_{\theta Z} = 0$. The membrane stresses and moments are obtained from the constitutive relation (4.19). The equilibrium equation (4.22) gives

$$\lambda = \frac{L_{00ZZ} - R^{-1}H_{00ZZ} - 2R^{-1}H_{ZZ00} + 2R^{-2}S_{00ZZ}}{L_{0000} - 4R^{-1}H_{0000} + 4R^{-2}S_{0000}}.$$

The ratio of bending moment M to curvature k is

$$\frac{M}{k} = \pi R^3 \left[L_{ZZZZ} - H_{ZZZZ}R^{-1} - \frac{L_{00ZZ} - 2H_{ZZ00}R^{-1} - H_{00ZZ}R^{-1} + 2S_{00ZZ}R^{-2}}{L_{0000} - 4H_{0000}R^{-1} + 4S_{0000}R^{-2}} \right. \\ \times \left. (L_{ZZ00} - 2H_{ZZ00}R^{-1}) \right] \left\{ 1 + O\left[\left(\frac{\Delta}{R}\right)^3\right] \right\}. \quad (5.9)$$

The ratio of strains in the circumferential direction to axial direction at each point is

$$\frac{\varepsilon_{\theta\theta}}{\varepsilon_{ZZ}} = -\frac{L_{00ZZ} - 2H_{ZZ00}R^{-1} - H_{00ZZ}R^{-1} + 2S_{00ZZ}R^{-2}}{L_{0000} - 4H_{0000}R^{-1} + 4S_{0000}R^{-2}} \left\{ 1 + O\left[\left(\frac{\Delta}{R}\right)^3\right] \right\}. \quad (5.10)$$

Even though the constitutive relation (4.19) does not fit any classical linear elastic shell theory, it is possible that the above structural response of CNT can be represented by an orthotropic thin shell, which involves four independent elastic properties, namely the shear stiffness $G_{12}h$, tension stiffness E_2h along the axial direction and the corresponding Poisson's ratio ν_{12} ; the tension stiffness E_1h along the circumferential direction and the corresponding Poisson's ratio ν_{21} , which satisfy

$$\frac{\nu_{21}}{E_1h} = \frac{\nu_{12}}{E_2h}. \quad (5.11)$$

The torque-twist relation (5.5) gives the shear stiffness

$$G_{12}h = (L_{\theta Z \theta Z} - 4H_{\theta Z \theta Z}R^{-1} + 4S_{\theta Z \theta Z}R^{-2}) \left\{ 1 + O\left[\left(\frac{\Delta}{R}\right)^3\right] \right\}. \quad (5.12)$$

The uniaxial tension relations (5.3) and (5.4) give the tension stiffness E_2h along the axial direction and the corresponding Poisson's ratio ν_{12} :

$$E_2h = \left[L_{ZZZZ} - \frac{(L_{00ZZ} - H_{ZZ00}R^{-1})^2}{L_{0000} - 2H_{0000}R^{-1} + S_{0000}R^{-2}} \right] \left\{ 1 + O\left[\left(\frac{\Delta}{R}\right)^3\right] \right\}, \quad (5.13)$$

$$\nu_{12} = \frac{L_{\theta\theta ZZ} - H_{ZZ\theta\theta}R^{-1}}{L_{\theta\theta\theta\theta} - 2H_{\theta\theta\theta\theta}R^{-1} + S_{\theta\theta\theta\theta}R^{-2}} \left\{ 1 + O\left[\left(\frac{\Delta}{R}\right)^3\right] \right\}. \quad (5.14)$$

The internal pressure relations (5.6)–(5.8) give the tension stiffness $E_1 h$ along the circumferential direction and the corresponding Poisson's ratio ν_{21} :

$$E_1 h = \left[L_{\theta\theta\theta\theta} - H_{\theta\theta\theta\theta}R^{-1} - \frac{L_{\theta\theta ZZ}(L_{ZZ\theta\theta} - H_{ZZ\theta\theta}R^{-1})}{L_{ZZZZ}} \right] \left\{ 1 + O\left[\left(\frac{\Delta}{R}\right)^3\right] \right\}, \quad (5.15)$$

$$\nu_{21} = \frac{L_{ZZ\theta\theta} - H_{ZZ\theta\theta}R^{-1}}{L_{ZZZZ}} \left\{ 1 + O\left[\left(\frac{\Delta}{R}\right)^3\right] \right\}. \quad (5.16)$$

However, it is straightforward to verify that the tension stiffness and Poisson's ratios defined in Eqs. (5.13)–(5.16) do not satisfy the requirement in Eq. (5.11) for an orthotropic thin shell.

The bending relations (5.9) and (5.10) also give the tension stiffness $E'_2 h$ along the axial direction and the corresponding Poisson's ratio ν'_{12} :

$$E'_2 h = \left[L_{ZZZZ} - H_{ZZZZ}R^{-1} - \frac{L_{\theta\theta ZZ} - 2H_{ZZ\theta\theta}R^{-1} - H_{\theta\theta ZZ}R^{-1} + 2S_{\theta\theta ZZ}R^{-2}}{L_{\theta\theta\theta\theta} - 4H_{\theta\theta\theta\theta}R^{-1} + 4S_{\theta\theta\theta\theta}R^{-2}} \right. \\ \times \left. (L_{ZZ\theta\theta} - 2H_{ZZ\theta\theta}R^{-1}) \right] \left\{ 1 + O\left[\left(\frac{\Delta}{R}\right)^3\right] \right\}, \quad (5.17)$$

$$\nu'_{12} = \frac{L_{\theta\theta ZZ} - 2H_{ZZ\theta\theta}R^{-1} - H_{\theta\theta ZZ}R^{-1} + 2S_{\theta\theta ZZ}R^{-2}}{L_{\theta\theta\theta\theta} - 4H_{\theta\theta\theta\theta}R^{-1} + 4S_{\theta\theta\theta\theta}R^{-2}} \left\{ 1 + O\left[\left(\frac{\Delta}{R}\right)^3\right] \right\}. \quad (5.18)$$

The tension stiffness and Poisson's ratios obtained from Eqs. (5.17) and (5.18) for bending are not the same as their counterparts in Eqs. (5.13) and (5.14) for tension. Therefore, the structural response of a CNT *cannot* be represented by a thin shell for the order of error $O[(\Delta/R)^3]$.

However, if one is willing to accept a larger error, $O[(\Delta/R)^2]$, the above stiffness and Poisson's ratios take a much simpler form:

$$G_{12}h = L_{\theta Z \theta Z} \left\{ 1 + O \left[\left(\frac{\Delta}{R} \right)^2 \right] \right\}, \quad (5.12a)$$

$$E_2 h = \left(L_{ZZZZ} - \frac{L_{\theta\theta ZZ}^2}{L_{\theta\theta\theta\theta}} \right) \left\{ 1 + O \left[\left(\frac{\Delta}{R} \right)^2 \right] \right\}, \quad (5.13a)$$

$$v_{12} = \frac{L_{\theta\theta ZZ}}{L_{\theta\theta\theta\theta}} \left\{ 1 + O \left[\left(\frac{\Delta}{R} \right)^2 \right] \right\}, \quad (5.14a)$$

$$E_1 h = \left(L_{\theta\theta\theta\theta} - \frac{L_{\theta\theta ZZ}^2}{L_{ZZZZ}} \right) \left\{ 1 + O \left[\left(\frac{\Delta}{R} \right)^2 \right] \right\}, \quad (5.15a)$$

$$v_{21} = \frac{L_{\theta\theta ZZ}}{L_{ZZZZ}} \left\{ 1 + O \left[\left(\frac{\Delta}{R} \right)^2 \right] \right\}, \quad (5.16a)$$

$$E'_2 h = \left(L_{ZZZZ} - \frac{L_{\theta\theta ZZ}^2}{L_{\theta\theta\theta\theta}} \right) \left\{ 1 + O \left[\left(\frac{\Delta}{R} \right)^2 \right] \right\}, \quad (5.17a)$$

$$v'_{12} = \frac{L_{\theta\theta ZZ}}{L_{\theta\theta\theta\theta}} \left\{ 1 + O \left[\left(\frac{\Delta}{R} \right)^2 \right] \right\}. \quad (5.18a)$$

They satisfy the requirement in Eq. (5.11) for an orthotropic thin shell, and the tension stiffness and Poisson's ratios obtained from bending are the same as their counterparts in tension, but their order of error decreases to $O[(\Delta/R)^2]$ (i.e., larger error), which is around 16% for the (5,5) armchair CNT. Therefore, for the order of error $O[(\Delta/R)^2]$, the CNT can be modeled as a linear elastic orthotropic thin shell (as far as the linear elastic structural response is concerned).

5.3. ORDER OF ERROR (Δ/R): A CLASSICAL LINEAR ELASTIC SHELL WITH A UNIVERSAL SHELL THICKNESS

The previous section is limited to linear elasticity. A nonlinear problem, namely buckling of a CNT, is studied in the following to explore whether a CNT can be modeled by a linear elastic orthotropic thin shell with a universal shell thickness. The loading cases include the compression, torsion, and external pressure:

- (i) *Uniaxial compression.* For a CNT of radius R and length L subject to a uniaxial compressive load P , the deformation is uniform prior to buckling. The velocity (or perturbation of the displacement field) becomes nonuniform at the onset of buckling, and can be expressed as

$$v_\theta = V_{\theta 0} \sin n\theta \cos \frac{m\pi Z}{L}, \quad v_Z = V_{Z 0} \cos n\theta \sin \frac{m\pi Z}{L}, \quad v_R = V_{R 0} \cos n\theta \cos \frac{m\pi Z}{L}, \quad (5.19)$$

where $n (=1, 2, 3, \dots)$ and $m (=1, 2, 3, \dots)$ denote the wave numbers in the circumferential and axial directions, respectively, and the coefficients $V_{\theta 0}, V_{Z 0}, V_{R 0}$ are to be determined. The rates of membrane strain and curvature are obtained from Eqs. (4.4) and (4.5) by replacing the displacement \mathbf{U} with the velocity in Eq. (5.19). The constitutive relation (4.19) then gives the rates of membrane stress and moment. Their substitution into the incremental form of equilibrium equation (4.22), given in Appendix A, yields the linear algebraic equations for $V_{\theta 0}, V_{Z 0}, V_{R 0}$. The vanishing of its determinant gives a cubic equation for the buckling force P_{critical} . Its solution, to order $O[(\Delta/R)^2]$, has been obtained by Peng et al. (2008) and is a rather long expression. However, when the order of error decreases to $O(\Delta/R)$ (i.e., larger error), the critical buckling force (for each pair of wave numbers n and m) simplifies to

$$P_{\text{critical}} = 2\pi R \left[\frac{1 - v_{12}v_{21}}{n^2(n^2 + 1)} L_{ZZZZ} \left(\frac{m\pi R}{L} \right)^2 + \frac{n^2(n^2 - 1)^2}{(n^2 + 1)} \frac{S_{\theta\theta\theta\theta}}{R^2} \left(\frac{L}{m\pi R} \right)^2 \right] \times \left[1 + O\left(\frac{\Delta}{R}\right) \right]. \quad (5.20)$$

It depends on the bending rigidity tensor S only via a single component, $S_{\theta\theta\theta\theta}$.

- (ii) *Torsion.* For a CNT of radius R and length L subject to a torque T , the velocity at the onset of buckling is nonuniform, and can be expressed as

$$v_\theta = V_{\theta 0} \cos\left(\frac{m\pi Z}{L} - n\theta\right), \quad v_Z = V_{Z 0} \cos\left(\frac{m\pi Z}{L} - n\theta\right), \quad v_R = V_{R 0} \sin\left(\frac{m\pi Z}{L} - n\theta\right), \quad (5.21)$$

where $n = 1, 2, 3, \dots, m = 1, 2, 3, \dots$, and the coefficients $V_{\theta 0}, V_{Z 0}, V_{R 0}$ are to be determined. The substitution of above velocity into the incremental equilibrium equation yields the linear algebraic equations for $V_{\theta 0}, V_{Z 0}, V_{R 0}$. The vanishing of its determinant gives the governing equation for the critical buckling torque T_{critical} . Its solution, to the order of error $O[(\Delta/R)^2]$, is obtained by Peng et al. (2008). Once the order of error decreases to $O(\Delta/R)$ (i.e., larger error), the critical buckling torque simplifies to

$$T_{\text{critical}} = \pi R^2 \left[\frac{1 - v_{12} v_{21}}{n^3(n^2 - 1)} L_{ZZZZ} \left(\frac{m\pi R}{L} \right)^3 + n(n^2 - 1) \frac{S_{0000}}{R^2} \left(\frac{L}{m\pi R} \right) \right] \left[1 + O\left(\frac{\Delta}{R}\right) \right], \quad (5.22)$$

which also depends on the bending rigidity tensor S only via a single component, S_{0000} .

(iii) *External pressure.* For a CNT of radius R and length L subject to an external pressure p , the velocity at the onset of buckling is also given by Eq. (5.19). Its substitution into the incremental equilibrium equation yields linear algebraic equations for $V_{\theta 0}, V_{Z 0}, V_{R 0}$. The vanishing of its determinant gives the governing equation for the critical buckling pressure p_{critical} . Its solution, to the order of error $O[(\Delta/R)^2]$, is obtained by Peng et al. (2008). If the order of error decreases to $O(\Delta/R)$ (i.e., larger error), the critical buckling pressure is simplified to

$$p_{\text{critical}} = \left[\frac{1 - v_{12} v_{21}}{n^4(n^2 - 1)} \frac{L_{ZZZZ}}{R} \left(\frac{m\pi R}{L} \right)^4 + (n^2 - 1) \frac{S_{0000}}{R^3} \right] \left[1 + O\left(\frac{\Delta}{R}\right) \right], \quad (5.23)$$

which once again depends on the bending rigidity tensor S only via a single component, S_{0000} .

The above critical buckling loads of a CNT are compared to their counterparts for a classical linear elastic orthotropic thin shell (Timoshenko & Gere, 1961) in order to explore whether a constant thickness can be chosen to represent the CNT by a linear elastic shell. The comparison of critical buckling torque in Eq. (5.22) with that for an orthotropic thin shell

$$T_{\text{critical}} = \pi R^2 \left[\frac{E_2 h}{n^3(n^2 - 1)} \left(\frac{m\pi R}{L} \right)^3 + n(n^2 - 1) \frac{h^2}{12R^2} \frac{E_1 h}{1 - v_{12}v_{21}} \left(\frac{L}{m\pi R} \right) \right]$$

gives effective shell thickness:

$$h = \sqrt{\frac{12S_{0000}}{L_{0000}}} \left[1 + O\left(\frac{\Delta}{R}\right) \right]. \quad (5.24)$$

Its order of error is $O(\Delta/R)$, rather than $O[(\Delta/R)^2]$ as in [Section 5.2](#).

The comparison of the uniaxial compression buckling force in [Eq. \(5.20\)](#) with that for an orthotropic thin shell

$$P_{\text{critical}} = 2\pi R \left[\frac{E_2 h}{n^2(n^2 + 1)} \left(\frac{m\pi R}{L} \right)^2 + \frac{n^2(n^2 - 1)^2}{(n^2 + 1)} \frac{h^2}{12R^2} \frac{E_1 h}{1 - v_{12}v_{21}} \left(\frac{L}{m\pi R} \right)^2 \right]$$

gives the same thickness in [Eq. \(5.24\)](#). The comparison of the external buckling pressure in [Eq. \(5.23\)](#) with that for an orthotropic thin shell

$$p_{\text{critical}} = \left[\frac{E_2 h}{n^4(n^2 - 1)R} \left(\frac{m\pi R}{L} \right)^4 + (n^2 - 1) \frac{h^2}{12R^2} \frac{E_1 h}{(1 - v_{12}v_{21})R} \right]$$

also gives the same thickness in [Eq. \(5.24\)](#). This is mainly because all buckling loads depend on the bending rigidity tensor S only via a single component S_{0000} . Thus, a universal constant shell thickness $h = \sqrt{12S_{0000}/L_{0000}}$ can be defined, albeit for a positively large error of order $O(\Delta/R)$ [around 40% for the (5,5) armchair CNT]. For the order of error $O[(\Delta/R)^2]$ [around 16% for the (5,5) armchair CNT], [Peng et al. \(2008\)](#) showed that the thickness obtained from the critical buckling loads for compression, torsion, and external pressure are different such that a universal constant thickness cannot be defined for the order of error $O[(\Delta/R)^2]$.

Based on the order of tension, bending and coupling rigidities in [Eq. \(5.1\)](#), the membrane energy $\frac{1}{2}\boldsymbol{\epsilon} : \mathbf{L} : \boldsymbol{\epsilon}$, bending energy $\frac{1}{2}\boldsymbol{\kappa} : \mathbf{S} : \boldsymbol{\kappa}$ and coupling energy $\boldsymbol{\epsilon} : \mathbf{H} : \boldsymbol{\kappa}$ are on the order of $\frac{|\nabla V|L}{S_0} [\boldsymbol{\epsilon}]^2$, $\frac{|\nabla V|L}{S_0} [\boldsymbol{\kappa}\Delta]^2$ and $\frac{|\nabla V|L}{S_0} [\boldsymbol{\epsilon}][\boldsymbol{\kappa}\Delta]\frac{\Delta}{R}$, respectively. Because of $2[\boldsymbol{\epsilon}][\boldsymbol{\kappa}\Delta] \leq [\boldsymbol{\epsilon}]^2 + [\boldsymbol{\kappa}\Delta]^2$, the coupling energy is (less than) Δ/R multiplied by the sum of membrane energy and bending energy. At an order of error $O(\Delta/R)$, the coupling energy is then negligible compared to the sum of the membrane energy and bending energy such that the membrane stress/curvature

and moment/membrane strain coupling can be neglected. Furthermore, the tension and bending rigidity tensors \mathbf{L} and \mathbf{S} in the constitutive model (4.19) become isotropic for the order of error $O(\Delta/R)$ (as the case for graphene, $R \rightarrow \infty$) such that the CNT can be modeled as a linear elastic isotropic thin shell as far as its buckling is concerned.

6. A Nonlinear, Finite-Deformation Shell Theory for Carbon Nanotubes Based on the Interatomic Potential

6.1. GENERAL DESCRIPTION OF A CURVED SURFACE

A point \mathbf{P} on a curved surface can be represented by

$$\mathbf{P} = \mathbf{P}(\xi^1, \xi^2), \quad (6.1)$$

where (ξ^1, ξ^2) are curvilinear coordinates on the surface (e.g., cylindrical coordinates $R\Theta$ and Z on a CNT with R being the initial radius of the CNT prior to loading). The covariant base vectors $\mathbf{A}_\alpha = \partial\mathbf{P}/\partial\xi^\alpha (\alpha = 1, 2)$ are in the tangent plane of the surface. The covariant base vectors give the coefficients of the first fundamental form as

$$A_{\alpha\beta} = \mathbf{A}_\alpha \cdot \mathbf{A}_\beta. \quad (6.2)$$

The unit normal to the surface is $\mathbf{N} = \frac{\mathbf{A}_1 \times \mathbf{A}_2}{|\mathbf{A}_1 \times \mathbf{A}_2|}$. The coefficients of the second fundamental form, which characterize the curvatures of the surface, are

$$B_{\alpha\beta} = \mathbf{N} \cdot \frac{\partial^2 \mathbf{P}}{\partial \xi^\alpha \partial \xi^\beta}. \quad (6.3)$$

For two points on the surface, $\mathbf{P}(\xi^1, \xi^2)$ and $\mathbf{P} + \Delta\mathbf{P}$ with coordinates ξ^α and $\xi^\alpha + \Delta\xi^\alpha$, the Taylor series expansion around the point \mathbf{P} gives

$$\Delta\mathbf{P} = \frac{\partial \mathbf{P}}{\partial \xi^\alpha} \Delta\xi^\alpha + \frac{1}{2!} \frac{\partial^2 \mathbf{P}}{\partial \xi^\alpha \partial \xi^\beta} \Delta\xi^\alpha \Delta\xi^\beta + \frac{1}{3!} \frac{\partial^3 \mathbf{P}}{\partial \xi^\alpha \partial \xi^\beta \partial \xi^\gamma} \Delta\xi^\alpha \Delta\xi^\beta \Delta\xi^\gamma + O(|\Delta\xi|^4), \quad (6.4)$$

where $\partial\mathbf{P}/\partial\xi^\alpha = \mathbf{A}_\alpha$, and the second and third order derivatives of \mathbf{P} involve the coefficients $A_{\alpha\beta}$, $B_{\alpha\beta}$, and their derivatives (Eisenhart, 1947). Any continuum theory that represents the collective behavior of atoms holds only when the characteristic length L of deformation is much larger than the atomic spacing Δ ,

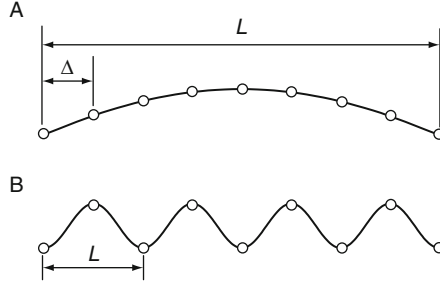


FIG. 6.1 Schematic diagram of the characteristic length L of deformation pattern and the atomic spacing Δ . (A) $L \gg \Delta$ such that the collective behavior of atoms can be represented by a continuum. (B) $L \sim \Delta$ such that a continuum description is not applicable.

as schematically illustrated in Fig. 6.1. For \mathbf{P} and $\mathbf{P} + \Delta\mathbf{P}$ representing two neighbor atoms on the surface, the Taylor series expansion (6.4) (for the order of error $O[(\Delta/L), (\Delta/R)^3]$ as in Section 4) then becomes (Wu, Hwang, & Huang, 2008)

$$\Delta\mathbf{P} = \left(\Delta\xi^\alpha - \frac{1}{6} B_{\beta\lambda} B_{\gamma\mu} A^{\alpha\mu} \Delta\xi^\beta \Delta\xi^\gamma \Delta\xi^\lambda \right) \mathbf{A}_\alpha + \frac{1}{2} B_{\alpha\beta} \Delta\xi^\alpha \Delta\xi^\beta \mathbf{N}, \quad (6.5)$$

where $A^{\alpha\mu}$ is the inverse of $A_{\alpha\mu}$.

The length of $\Delta\mathbf{P}$ is given by

$$|\Delta\mathbf{P}|^2 = A_{\alpha\beta} \Delta\xi^\alpha \Delta\xi^\beta - \frac{1}{12} (B_{\alpha\beta} \Delta\xi^\alpha \Delta\xi^\beta)^2. \quad (6.6)$$

The angle φ between two vectors $\Delta\mathbf{P}_{(1)}$ and $\Delta\mathbf{P}_{(2)}$, which is needed in the multibody interatomic potential for carbon (e.g., Section 2), is given by $\cos\varphi = \frac{\Delta\mathbf{P}_{(1)} \cdot \Delta\mathbf{P}_{(2)}}{|\Delta\mathbf{P}_{(1)}||\Delta\mathbf{P}_{(2)}|}$, where

$$\begin{aligned} \Delta\mathbf{P}_{(1)} \cdot \Delta\mathbf{P}_{(2)} &= A_{\alpha\beta} \Delta\xi_{(1)}^\alpha \Delta\xi_{(2)}^\beta + \frac{1}{12} B_{\alpha\beta} B_{\gamma\lambda} \Delta\xi_{(1)}^\alpha \Delta\xi_{(2)}^\lambda \\ &\times \left(3\Delta\xi_{(1)}^\beta \Delta\xi_{(2)}^\gamma - 2\Delta\xi_{(2)}^\beta \Delta\xi_{(2)}^\gamma - 2\Delta\xi_{(1)}^\beta \Delta\xi_{(1)}^\gamma \right). \end{aligned} \quad (6.7)$$

6.2. MEMBRANE STRAINS AND CURVATURES OF A DEFORMED SURFACE

The surface $\mathbf{P}(\xi^1, \xi^2)$ deforms to a new surface $\mathbf{p}(\xi^1, \xi^2)$. The base vectors for the deformed surface are $\mathbf{a}_\alpha = \partial\mathbf{p}/\partial\xi^\alpha$; the unit normal is $\mathbf{n} = \frac{\mathbf{a}_1 \times \mathbf{a}_2}{|\mathbf{a}_1 \times \mathbf{a}_2|}$; and the coefficients of the first and second fundamental forms are $a_{\alpha\beta} = \mathbf{a}_\alpha \cdot \mathbf{a}_\beta$ and $b_{\alpha\beta} = \mathbf{n} \cdot \frac{\partial^2 \mathbf{p}}{\partial \xi^\alpha \partial \xi^\beta}$, respectively.

Two points \mathbf{P} and $\mathbf{P} + \Delta\mathbf{P}$ on the surface deform to \mathbf{p} and $\mathbf{p} + \Delta\mathbf{p}$, where $\Delta\mathbf{p}$ can be obtained from Eq. (6.5) by replacing A_α , N , $A_{\alpha\beta}$, and $B_{\alpha\beta}$ with a_α , n , $a_{\alpha\beta}$, and $b_{\alpha\beta}$, respectively. Its length and angle with neighbor bond can be similarly obtained from Eqs. (6.6) and (6.7).

The components of the Green strain are the difference between the coefficients of the first fundamental form before and after the deformation, that is,

$$E_{\alpha\beta} = \frac{1}{2}(a_{\alpha\beta} - A_{\alpha\beta}). \quad (6.8)$$

Similarly, the curvatures are the difference between the coefficients of the second fundamental form:

$$K_{\alpha\beta} = b_{\alpha\beta} - B_{\alpha\beta}. \quad (6.9)$$

The length of $\Delta\mathbf{p}$ and its angle with the neighbor bond are then related to the components of Green strain and curvatures by

$$|\Delta\mathbf{p}|^2 = (A_{\alpha\beta} + 2E_{\alpha\beta})\Delta\xi^\alpha\Delta\xi^\beta - \frac{1}{12}[(B_{\alpha\beta} + K_{\alpha\beta})\Delta\xi^\alpha\Delta\xi^\beta]^2, \quad (6.10)$$

$$\cos\varphi = \frac{\Delta\mathbf{p}_{(1)} \cdot \Delta\mathbf{p}_{(2)}}{|\Delta\mathbf{p}_{(1)}||\Delta\mathbf{p}_{(2)}|},$$

and

$$\begin{aligned} \Delta\mathbf{p}_{(1)} \cdot \Delta\mathbf{p}_{(2)} &= (A_{\alpha\beta} + 2E_{\alpha\beta})\Delta\xi_{(1)}^\alpha\Delta\xi_{(2)}^\beta + \frac{1}{12}(B_{\alpha\beta} + K_{\alpha\beta})(B_{\gamma\lambda} + K_{\gamma\lambda})\Delta\xi_{(1)}^\alpha\Delta\xi_{(2)}^\lambda \\ &\times \left(3\Delta\xi_{(1)}^\beta\Delta\xi_{(2)}^\gamma - 2\Delta\xi_{(2)}^\beta\Delta\xi_{(2)}^\gamma - 2\Delta\xi_{(1)}^\beta\Delta\xi_{(1)}^\gamma\right). \end{aligned} \quad (6.11)$$

6.3. DEFORMATION OF A SINGLE-WALL CARBON NANOTUBE

As discussed in Section 3, CNTs do not have simple Bravais lattice since their hexagonal lattice structure can be decomposed to two triangular, sublattices marked by open and solid circles in Fig. 3.2. The two sublattices undergo a shift vector η to minimize the energy and ensure the equilibrium of atoms. The vector $\Delta\mathbf{P}$ between two atoms from different sublattices has coordinates $\Delta\xi^\alpha$ on the CNT prior to deformation. It becomes $\Delta\mathbf{p}$ on the deformed CNT, and has the new coordinates

$$\Delta\bar{\xi}^\alpha = \Delta\xi^\alpha + \eta^\alpha, \quad (6.12)$$

where η^α are to be determined. The bond length and angle in Eqs. (6.10) and (6.11) are obtained by replacing $\Delta\xi^\alpha$ by $\Delta\bar{\xi}^\alpha$:

$$|\Delta\mathbf{p}|^2 = (A_{\alpha\beta} + 2E_{\alpha\beta})\Delta\bar{\xi}^\alpha\Delta\bar{\xi}^\beta - \frac{1}{12}\left[(B_{\alpha\beta} + K_{\alpha\beta})\Delta\bar{\xi}^\alpha\Delta\bar{\xi}^\beta\right]^2, \quad (6.13)$$

$$\cos\varphi = \frac{\Delta\mathbf{p}_{(1)} \cdot \Delta\mathbf{p}_{(2)}}{|\Delta\mathbf{p}_{(1)}||\Delta\mathbf{p}_{(2)}|},$$

and

$$\begin{aligned} \Delta\mathbf{p}_{(1)} \cdot \Delta\mathbf{p}_{(2)} &= (A_{\alpha\beta} + 2E_{\alpha\beta})\Delta\bar{\xi}_{(1)}^\alpha\Delta\bar{\xi}_{(2)}^\beta \\ &\quad + \frac{1}{12}(B_{\alpha\beta} + K_{\alpha\beta})(B_{\gamma\lambda} + K_{\gamma\lambda})\Delta\bar{\xi}_{(1)}^\alpha\Delta\bar{\xi}_{(2)}^\lambda \\ &\quad \times \left(3\Delta\bar{\xi}_{(1)}^\beta\Delta\bar{\xi}_{(2)}^\gamma - 2\Delta\bar{\xi}_{(2)}^\beta\Delta\bar{\xi}_{(2)}^\gamma - 2\Delta\bar{\xi}_{(1)}^\beta\Delta\bar{\xi}_{(1)}^\gamma\right). \end{aligned} \quad (6.14)$$

The bond length and angle, and also the interatomic potential, depend on the components of Green strain $E_{\alpha\beta}$, curvatures $K_{\alpha\beta}$, and shift vector η^λ :

$$r_{ij} = r_{ij}(E_{\alpha\beta}, K_{\alpha\beta}, \eta^\lambda), \varphi_{ijk} = \varphi_{ijk}(E_{\alpha\beta}, K_{\alpha\beta}, \eta^\lambda); V = V(r_{ij}, \varphi_{ijk}; k \neq i, j). \quad (6.15)$$

The strain energy density w is the energy (stored in atomic bonds) per initial unit area, and is given by

$$w(E_{\alpha\beta}, K_{\alpha\beta}, \eta^\lambda) = \frac{1}{2} \frac{\sum_{1 \leq j \leq 3} V(r_{ij}, \varphi_{ijk}; k \neq i, j)}{S_0}, \quad (6.16)$$

where $S_0 = \iint \sqrt{A_{11}A_{22} - A_{12}^2} d\xi^1 d\xi^2$ is the average area per atom. The shift vector is determined by minimizing energy to ensure the equilibrium of atoms, that is,

$$\frac{\partial w}{\partial \eta^\lambda} = 0, \quad (6.17)$$

which gives η^λ in terms of $E_{\alpha\beta}$ and $K_{\alpha\beta}$:

$$\eta^\lambda = \eta^\lambda(E_{\alpha\beta}, K_{\alpha\beta}). \quad (6.18)$$

The strain energy density in Eq. (6.16) then becomes the function of Green strain $E_{\alpha\beta}$ and curvature $K_{\alpha\beta}$:

$$w = w[E_{\alpha\beta}, K_{\alpha\beta}, \eta^\lambda(E_{\alpha\beta}, K_{\alpha\beta})]. \quad (6.19)$$

6.4. MEMBRANE STRESSES AND MOMENTS IN A CARBON NANOTUBE

The membrane strain tensor, whose components are $E_{\alpha\beta}$, is $\mathbf{E} = E_{\alpha\beta} A^\alpha A^\beta$, where A^α is the contravariant base vector related to the covariant base vector A_α by $A^\alpha = A^{\alpha\beta} A_\beta$. The reciprocal pair of base vectors satisfy $A^\alpha \cdot A_\alpha = 1$ (no sum over α) and $A^\alpha \cdot A_\beta = 0$ ($\alpha \neq \beta$). Similarly, the curvature tensor is $\mathbf{K} = K_{\alpha\beta} A^\alpha A^\beta$.

The second Piola–Kirchhoff membrane stress tensor \mathbf{T} is the work conjugate of the Green strain tensor \mathbf{E} :

$$\mathbf{T} = \frac{Dw}{DE} = \frac{\partial w}{\partial E} + \frac{\partial w}{\partial \eta} \cdot \frac{\partial \eta}{\partial E} = \frac{\partial w}{\partial E}, \quad (6.20)$$

where $\partial w / \partial \eta = 0$ in Eq. (6.17) has been used. The components of Eq. (6.20) are

$$T^{\alpha\beta} = \frac{\partial w}{\partial E_{\alpha\beta}}, \quad (6.21)$$

where $T^{\alpha\beta}$ are the contravariant components of \mathbf{T} , that is, $\mathbf{T} = T^{\alpha\beta} A_\alpha A_\beta$. It is important to distinguish the covariant and contravariant components and base vectors for curvilinear coordinates.

The moment tensor \mathbf{M} is the work conjugate of the curvature tensor \mathbf{K} :

$$\mathbf{M} = \frac{Dw}{DK} = \frac{\partial w}{\partial K} + \frac{\partial w}{\partial \eta} \cdot \frac{\partial \eta}{\partial K} = \frac{\partial w}{\partial K}. \quad (6.22)$$

Its contravariant components are

$$M^{\alpha\beta} = \frac{\partial w}{\partial K_{\alpha\beta}}, \quad (6.23)$$

with $\mathbf{M} = M^{\alpha\beta} A_\alpha A_\beta$.

Equations (6.20) and (6.22) give the constitutive relation for CNTs. Their incremental form is given by

$$\begin{aligned}\dot{\mathbf{T}} &= \mathbf{L} : \dot{\mathbf{E}} + \mathbf{H} : \dot{\mathbf{K}}, \\ \dot{\mathbf{M}} &= \mathbf{H}^T : \dot{\mathbf{E}} + \mathbf{S} : \dot{\mathbf{K}},\end{aligned}\quad (6.24)$$

where $\mathbf{L} = \mathbf{L}^T$ and $\mathbf{S} = \mathbf{S}^T$ are the symmetric tension and bending rigidities given by

$$\begin{aligned}\mathbf{L} &= \frac{D}{DE} \left(\frac{\partial w}{\partial E} \right) = \frac{\partial^2 w}{\partial E \partial E} - \frac{\partial^2 w}{\partial E \partial \eta} \cdot \left(\frac{\partial^2 w}{\partial \eta \partial \eta} \right)^{-1} \cdot \frac{\partial^2 w}{\partial \eta \partial E}, \\ \mathbf{S} &= \frac{D}{DK} \left(\frac{\partial w}{\partial K} \right) = \frac{\partial^2 w}{\partial K \partial K} - \frac{\partial^2 w}{\partial K \partial \eta} \cdot \left(\frac{\partial^2 w}{\partial \eta \partial \eta} \right)^{-1} \cdot \frac{\partial^2 w}{\partial \eta \partial K},\end{aligned}\quad (6.25)$$

and $\partial w / \partial \eta = 0$ in Eq. (6.17) has been used, \mathbf{H} and \mathbf{H}^T are the coupled tension/bending rigidities given by

$$\begin{aligned}\mathbf{H} &= \frac{D}{DK} \left(\frac{\partial w}{\partial E} \right) = \frac{\partial^2 w}{\partial E \partial K} - \frac{\partial^2 w}{\partial E \partial \eta} \cdot \left(\frac{\partial^2 w}{\partial \eta \partial \eta} \right)^{-1} \cdot \frac{\partial^2 w}{\partial \eta \partial K}, \\ \mathbf{H}^T &= \frac{D}{DE} \left(\frac{\partial w}{\partial K} \right) = \frac{\partial^2 w}{\partial K \partial E} - \frac{\partial^2 w}{\partial K \partial \eta} \cdot \left(\frac{\partial^2 w}{\partial \eta \partial \eta} \right)^{-1} \cdot \frac{\partial^2 w}{\partial \eta \partial E},\end{aligned}\quad (6.26)$$

which represent the coupling between membrane stresses and curvatures (or between moments and membrane strains) for a curved surface.

6.5. EQUILIBRIUM EQUATIONS FOR MEMBRANE STRESSES AND MOMENTS

The Cauchy membrane stress tensor \mathbf{t} , defined for the deformed configuration, is related to the second Piola–Kirchhoff membrane stress \mathbf{T} by

$$\mathbf{t} = \frac{1}{J} \mathbf{F} \cdot \mathbf{T} \cdot \mathbf{F}^T, \quad (6.27)$$

where

$$\mathbf{F} = \mathbf{a}_1 \mathbf{A}^1 + \mathbf{a}_2 \mathbf{A}^2 \quad (6.28)$$

is the deformation gradient tensor which maps an infinitesimal element $d\mathbf{P} = d\xi^1 \mathbf{A}_1 + d\xi^2 \mathbf{A}_2$ of the CNT prior to deformation to $d\mathbf{p} = \mathbf{F} \cdot d\mathbf{P} = d\xi^1 \mathbf{a}_1 + d\xi^2 \mathbf{a}_2$ of the deformed CNT, \mathbf{a}_1 and \mathbf{a}_2 are the code-formed base vectors for the deformed CNT, $\mathbf{F}^T = \mathbf{A}^1 \mathbf{a}_1 + \mathbf{A}^2 \mathbf{a}_2$ and $J = \sqrt{a_{11}a_{22} - (a_{12})^2}$ are the transpose and Jacobian of \mathbf{F} , respectively.

The Cauchy membrane stress is then obtained from Eqs. (6.27) and (6.28) as $\mathbf{t} = \frac{1}{J}[T^{11}\mathbf{a}_1\mathbf{a}_1 + T^{22}\mathbf{a}_2\mathbf{a}_2 + T^{12}(\mathbf{a}_1\mathbf{a}_2 + \mathbf{a}_2\mathbf{a}_1)]$, which has the same components $T^{\alpha\beta}$ as the second Piola–Kirchhoff membrane stress (except the factor $1/J$) but on different base vectors, and $J\mathbf{t}$ is called the contravariant “pushforward” of \mathbf{T} .

Similarly, the moment tensor \mathbf{m} for the deformed configuration is

$$\mathbf{m} = \frac{1}{J}\mathbf{F} \cdot \mathbf{M} \cdot \mathbf{F}^T, \quad (6.29)$$

which gives $\mathbf{m} = \frac{1}{J}[M^{11}\mathbf{a}_1\mathbf{a}_1 + M^{22}\mathbf{a}_2\mathbf{a}_2 + M^{12}(\mathbf{a}_1\mathbf{a}_2 + \mathbf{a}_2\mathbf{a}_1)]$, and has the same components as the moment tensor \mathbf{M} (except the factor $1/J$) but different base vectors, $Jm^{\alpha\beta} = M^{\alpha\beta}$, and $J\mathbf{m}$ is called the contravariant “pushforward” of \mathbf{M} . Wu et al. (2008a) discussed the relations among \mathbf{t} , \mathbf{m} , and asymmetric membrane stress and moment tensors in most shell theories, which are given in Appendix B.

In the current, deformed configuration, the constitutive relation (6.24) can be expressed via the Oldroyd rate as

$$\begin{aligned} (J\mathbf{t})^{\text{Oldr}} &= \mathcal{L} : \mathbf{d} + \mathcal{H} : \boldsymbol{\kappa}, & \frac{d}{dt}(Jt^{\alpha\beta}) &= \mathcal{S}^{\alpha\beta\lambda\gamma}d_{\lambda\gamma} + \mathcal{K}^{\alpha\beta\lambda\gamma}K_{\lambda\gamma}, \\ (J\mathbf{m})^{\text{Oldr}} &= \mathcal{H}^T : \mathbf{d} + \mathcal{S} : \boldsymbol{\kappa}, & \frac{d}{dt}(Jm^{\alpha\beta}) &= \mathcal{K}^{\lambda\gamma\alpha\beta}d_{\lambda\gamma} + \mathcal{S}^{\alpha\beta\lambda\gamma}K_{\lambda\gamma}, \end{aligned} \quad (6.30)$$

where \mathbf{d} and $\boldsymbol{\kappa}$ are related to the rates of Green strain $\dot{\mathbf{E}}$ and curvature tensor $\dot{\mathbf{K}}$ by

$$\mathbf{d} = \mathbf{F}^{-T} \cdot \dot{\mathbf{E}} \cdot \mathbf{F}^{-1} = \dot{E}_{11}\mathbf{a}^1\mathbf{a}^1 + \dot{E}_{22}\mathbf{a}^2\mathbf{a}^2 + \dot{E}_{12}(\mathbf{a}^1\mathbf{a}^2 + \mathbf{a}^2\mathbf{a}^1), \quad (6.31)$$

$$\boldsymbol{\kappa} = \mathbf{F}^{-T} \cdot \dot{\mathbf{K}} \cdot \mathbf{F}^{-1} = \dot{K}_{11}\mathbf{a}^1\mathbf{a}^1 + \dot{K}_{22}\mathbf{a}^2\mathbf{a}^2 + \dot{K}_{12}(\mathbf{a}^1\mathbf{a}^2 + \mathbf{a}^2\mathbf{a}^1), \quad (6.32)$$

which have the same components as $\dot{E}_{\alpha\beta}$ and $\dot{K}_{\alpha\beta}$ but different base vectors, that is, they are the covariant “pushforward” of $\dot{\mathbf{E}}$ and $\dot{\mathbf{K}}$, respectively. Their components are related to the covariant and contravariant components, v_α and v^α ($\alpha = 1, 2$), of the velocity \mathbf{v} and the component $v_3 = v^3$ normal to the CNT surface by (Niordson, 1985)

$$d_{\alpha\beta} = \dot{E}_{\alpha\beta} = \frac{1}{2}(v_{\alpha;\beta} + v_{\beta;\alpha}) - v_3 b_{\alpha\beta}, \quad (6.33)$$

$$\kappa_{\alpha\beta} = \dot{K}_{\alpha\beta} = v_{;\beta}^3 b_{\alpha\beta} + v_{;\beta}^\lambda b_{\lambda\alpha} + v_{;\alpha}^\lambda b_{\lambda\beta} + v^\lambda b_{\lambda\alpha;\beta} - v_3 b_{\alpha\lambda} b_{\beta}^\lambda, \quad (6.34)$$

where $b_{\beta}^\lambda = a^{\lambda\alpha}b_{\alpha\beta}$, $a^{\lambda\alpha}$ is the inverse of $a_{\lambda\alpha}$, and is related to $a_{\lambda\alpha}$ by $\begin{pmatrix} a^{11} & a^{12} \\ a^{21} & a^{22} \end{pmatrix} = \begin{pmatrix} a_{11} & a_{12} \\ a_{21} & a_{22} \end{pmatrix}^{-1}$; and “;” denotes the covariant derivatives given in Appendix B.

The tension, bending, and coupling rigidities in the current, deformed configuration in Eq. (6.30) are related to their counterparts in the initial configuration by

$$\mathcal{L} = (\underset{*}{\mathbf{FFFF}})^* \underset{*}{\mathbf{L}}, \quad \mathcal{S} = (\underset{*}{\mathbf{FFFF}})^* \underset{*}{\mathbf{S}}, \quad (6.35)$$

$$\mathcal{H} = (\underset{*}{\mathbf{FFFF}})^* \underset{*}{\mathbf{H}}, \quad \mathcal{H}^T = (\underset{*}{\mathbf{FFFF}})^* \underset{*}{\mathbf{H}}^T, \quad (6.36)$$

and they have the same contravariant components, $\mathcal{L}^{\alpha\beta\lambda\gamma} = L^{\alpha\beta\lambda\gamma}$, $\mathcal{S}^{\alpha\beta\lambda\gamma} = S^{\alpha\beta\lambda\gamma}$, and $\mathcal{H}^{\alpha\beta\lambda\gamma} = H^{\alpha\beta\lambda\gamma}$, but again on different base vectors (the quad-dot product between \mathbf{FFFF} and any fourth-order tensor simply changes the base vectors from the initial configuration to the current, deformed configuration).

The equilibrium equations in the finite-deformation shell theory can be written in terms of \mathbf{t} and \mathbf{m} as (e.g., Niordson, 1985)

$$t^{\alpha\beta}_{;\beta} + 2b_{\cdot\beta}^{\alpha} m^{\beta\lambda}_{;\lambda} + b_{\cdot\lambda;\beta}^{\alpha} m^{\lambda\beta} + \bar{x}^{\alpha} = 0 \quad (\alpha = 1, 2), \quad (6.37)$$

$$b_{\alpha\beta} t^{\alpha\beta} + b_{\alpha\beta} b_{\cdot\lambda}^{\beta} m^{\alpha\lambda} - m^{\beta\lambda}_{;\beta\lambda} + \bar{x}^3 = 0, \quad (6.38)$$

where \bar{x}^{α} and \bar{x}^3 are the effective in-surface and out-of-surface area forces (applied force per current unit area), respectively, $t^{\alpha\beta}$, $m^{\alpha\beta}$ are the contravariant components of \mathbf{t} and \mathbf{m} , respectively.

The traction boundary conditions are (Niordson, 1985)

$$(t^{\alpha\beta} + 2b_{\cdot\lambda}^{\alpha} m^{\lambda\beta}) v_{\beta} = \bar{t}^{\alpha} + b_{\cdot\lambda}^{\alpha} \bar{m}^{\lambda} \quad (\alpha = 1, 2), \quad (6.39)$$

$$m^{\alpha\beta}_{;\alpha} v_{\beta} + \frac{\partial}{\partial s} (m^{\alpha\beta} v_{\alpha} s_{\beta}) = -\bar{t}^3 + \frac{\partial \bar{m}_T}{\partial s}, \quad (6.40)$$

$$m^{\alpha\beta} v_{\alpha} v_{\beta} = \bar{m}_B, \quad (6.41)$$

where \bar{t}^{α} and \bar{t}^3 are the prescribed effective in-surface and out-of-surface tractions, \bar{m}_B and \bar{m}_T are the prescribed bending moment and torque, s is the unit vector along the boundary, and $\mathbf{v} = \mathbf{s} \times \mathbf{n}$ is the in-surface unit normal, $\partial/\partial s$ is the directional derivative along the direction of s , \bar{m}^{λ} is the component of boundary moment $\bar{\mathbf{m}} = \bar{m}^1 \mathbf{a}_1 + \bar{m}^2 \mathbf{a}_2 = \bar{m}_T s + \bar{m}_B \mathbf{v}$.

The incremental equilibrium equations, which are needed in the instability analysis in [Section 7](#), are

$$\frac{d}{dt} (P^{\alpha\beta}_{;\beta}) + 2 \frac{d}{dt} (b^z_{\beta} m^{\beta\lambda}_{;\lambda}) + \frac{d}{dt} (b^z_{\lambda;\beta} m^{\lambda\beta}) + \frac{d\bar{x}^\alpha}{dt} = 0 \quad (\alpha = 1, 2), \quad (6.42)$$

$$\frac{d}{dt} (b_{\alpha\beta} t^{\alpha\beta}) + \frac{d}{dt} (b_{\alpha\beta} b^z_{;\lambda} m^{\alpha\lambda}) - \frac{d}{dt} (m^{\beta\lambda}_{;\lambda\beta}) + \frac{d\bar{x}^3}{dt} = 0. \quad (6.43)$$

6.6. EXAMPLES

The second-generation potential for carbon ([Brenner et al., 2002](#)) is used in the following examples.

6.6.1. Bending Rigidity of Graphene

[Yakobson et al. \(1996\)](#) calculated the bending rigidity of graphene to determine the nanotube thickness. They used molecular dynamics to obtain the difference in energy (per atom), ΔU , between single-wall CNTs and graphene. Under the assumption that the bending rigidity EI is the same for graphene and for a CNT layer, this energy difference is related to the CNT radius by $\Delta U = EIS_0/(2R^2)$, where $S_0 = (3\sqrt{3}/4)r_0^2$ is the area of graphene per atom. [Yakobson et al. \(1996\)](#) then obtained the bending rigidity EI by fitting the molecular dynamics results to the $\Delta U = EIS_0/(2R^2)$ relation.

We study the rolling of a graphene sheet into a CNT in order to validate the above expression $\Delta U = EIS_0/(2R^2)$. Let ξ^1 and ξ^2 be the Cartesian coordinates on the (undeformed) graphene, which is rolled to a CNT along ξ^1 (and therefore ξ^2 is along the CNT axis). The coefficients of the first and second fundamental forms are $A_{\alpha\beta} = \delta_{\alpha\beta}$ and $B_{\alpha\beta} = 0$. Let ε_1 and ε_2 denote the engineering strains to be determined in the circumferential and axial directions (ξ^1 and ξ^2) during rolling of the graphene to the CNT.⁴ The point $\mathbf{P}(\xi^1, \xi^2)$ on the graphene becomes $\mathbf{p} = Re_R + (1 + \varepsilon_2)\xi^2 \mathbf{e}_Z$ on the CNT, where R is the CNT radius, and \mathbf{e}_R and \mathbf{e}_Z are the unit vectors along the radial and axial directions. The polar angle is $\Theta = [(1 + \varepsilon_1)\xi^1]/R$. The base vectors are $\mathbf{a}_1 = \partial\mathbf{p}/\partial\xi^1 = (1 + \varepsilon_1)\mathbf{e}_\Theta$ and $\mathbf{a}_2 = \partial\mathbf{p}/\partial\xi^2 = (1 + \varepsilon_2)\mathbf{e}_Z$, where \mathbf{e}_Θ is the unit vector in the circumferential direction. The nonvanishing coefficients of the first and second fundamental forms become $a_{11} = (1 + \varepsilon_1)^2$, $a_{22} = (1 + \varepsilon_2)^2$, and $b_{11} = -\frac{(1+\varepsilon_1)^2}{R}$, which give

⁴ Only armchair and zigzag CNTs are studied such that there is no shear.

the nonvanishing components of the Green strain and curvature tensors $E_{11} = \varepsilon_1 + (1/2)\varepsilon_1^2$, $E_{22} = \varepsilon_2 + \frac{1}{2}\varepsilon_2^2$, and $K_{11} = -(1 + \varepsilon_1)^2/R$.

The strain energy density w becomes a function of ε_1 and ε_2 (and shift vector η_1 and η_2). Since the CNT is not subject to any externally applied strain during the rolling from the graphene, ε_1 and ε_2 are determined by minimizing the strain energy, that is, $\partial w/\partial\varepsilon_1 = \partial w/\partial\varepsilon_2 = 0$.

[Figure 6.2](#) shows the energy (per atom) versus the CNT radius R for armchair and zigzag CNTs. The relation $\Delta U = EIS_0/(2R^2)$ is also shown, with the bending rigidity $EI = M_{11}/\kappa_{11} = (\sqrt{3}/4)(\partial V/\partial \cos \varphi_{ijk})_0$ for graphene under uniaxial curvature κ_{11} ($\kappa_{22} = 0$). The present analysis agrees very well with the relation $\Delta U = EIS_0/(2R^2)$.

6.6.2. Tension of Carbon Nanotubes

An armchair or zigzag CNT is subject to simple tension with the (engineering) axial strain $\varepsilon_{\text{axial}}$ (at finite deformation, which is different from the linear analysis in [Section 5.2](#)). The strain $\varepsilon_{\text{lateral}}$ in the circumferential direction due to lateral contraction is to be determined. Let $\xi^1 = R\Theta$ and $\xi^2 = Z$, where Θ and Z are the cylindrical coordinates, and the initial radius R of the CNT prior to tension is used to scale Θ such that ξ^1 has the length dimension. The nonvanishing coefficients of the first and second fundamental forms are $A_{11} = 1$, $A_{22} = 1$, and $B_{11} = -1/R$. The point $P = Re_R + Ze_Z$ on the CNT prior to tension becomes

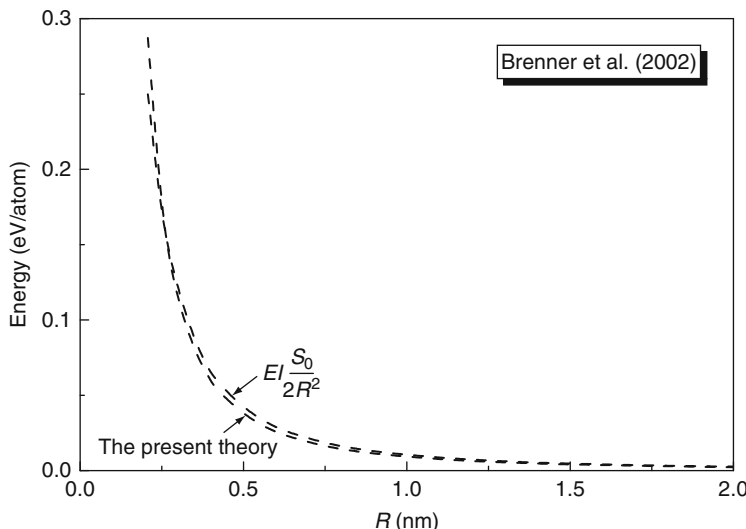


FIG. 6.2 Dependence of the energy according to the present theory and of $EIS_0/(2R^2)$ on the carbon nanotube radius R .

$\mathbf{p} = R(1 + \varepsilon_{\text{lateral}})\mathbf{e}_R + Z(1 + \varepsilon_{\text{axial}})\mathbf{e}_Z$ on the deformed CNT. The base vectors $\mathbf{a}_1 = \partial\mathbf{p}/\partial\xi^1 = (1 + \varepsilon_{\text{lateral}})\mathbf{e}_\Theta$ and $\mathbf{a}_2 = \partial\mathbf{p}/\partial\xi^2 = (1 + \varepsilon_{\text{axial}})\mathbf{e}_Z$ give the non-vanishing coefficients of the first and second fundamental forms $a_{11} = (1 + \varepsilon_{\text{lateral}})^2$, $a_{22} = (1 + \varepsilon_{\text{axial}})^2$, and $b_{11} = -(1 + \varepsilon_{\text{lateral}})/R$. The nonvanishing components of the Green strain and curvature tensors are $E_{11} = \varepsilon_{\text{lateral}} + (1/2)\varepsilon_{\text{lateral}}^2$, $E_{22} = \varepsilon_{\text{axial}} + (1/2)\varepsilon_{\text{axial}}^2$, and $K_{11} = -\varepsilon_{\text{lateral}}/R$. The nonvanishing components of second Piola–Kirchhoff membrane stress and moment tensors are obtained from Eqs. (6.21) and (6.23). The equilibrium equations become $T_{11} - M_{11}/[R(1 + \varepsilon_{\text{lateral}})] = 0$, which gives the strain $\varepsilon_{\text{lateral}}$ in the circumferential direction in terms of the axial strain $\varepsilon_{\text{axial}}$, that is, $\varepsilon_{\text{lateral}} = \varepsilon_{\text{lateral}}(\varepsilon_{\text{axial}})$.

Figure 6.3A shows the axial force, normalized by the CNT circumference $2\pi R$ prior to tension, versus the axial strain for several armchair and zigzag CNTs. The curves do not depend strongly on the CNT radius R , but the chirality has a strong effect. At the limit of strain approaching zero, the force/strain ratio is given analytically as $2\pi[R(L_{2222} - v_{12}L_{2211}) + v_{12}H_{2211}]$, where $v_{12} = (R^2L_{1122} - RH_{2211})/(R^2L_{1111} - 2RH_{1111} + S_{1111} + RM_{11}^{(0)})$ is the Poisson ratio, and the superscript “(0)” denotes the initial residual membrane stress and moment in the CNT. Figure 6.3B shows the force/strain ratio (for the infinitesimal strain), normalized by $2\pi R$, versus the CNT radius for armchair and zigzag CNTs. The force/strain ratio depends weakly on the CNT chirality since the

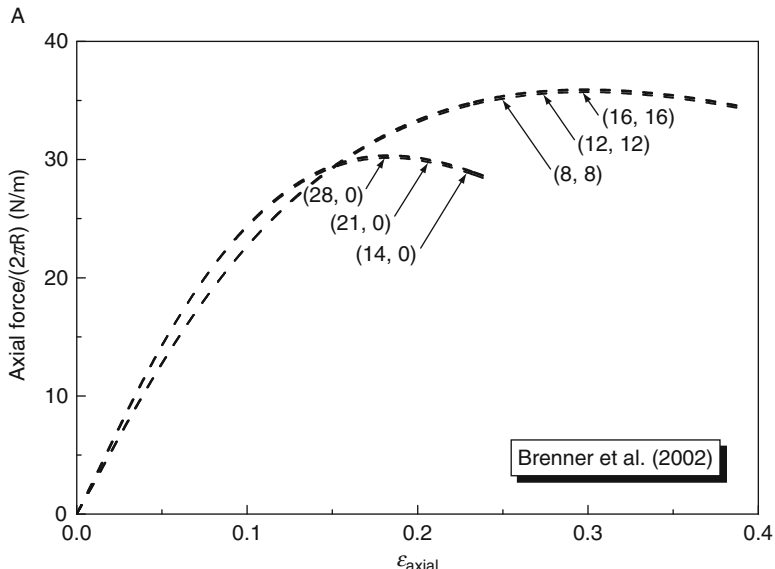


FIG. 6.3 (Continued)

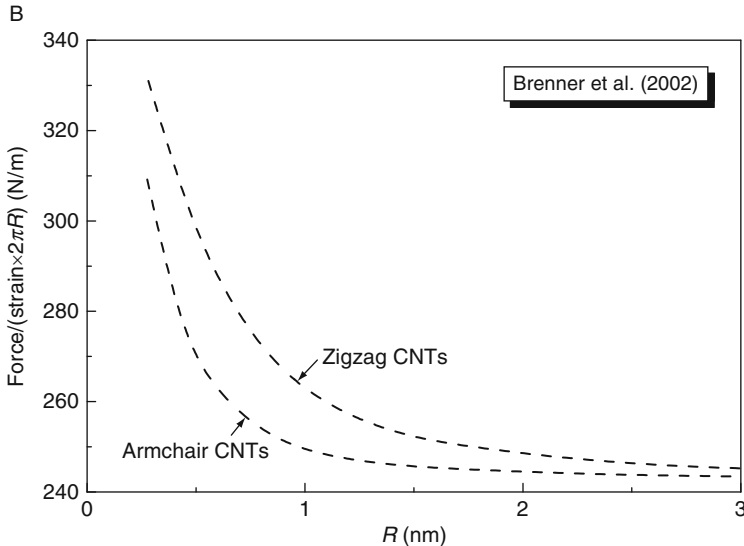


FIG. 6.3 (A) The axial force, normalized by the carbon nanotube circumference $2\pi R$ prior to deformation, versus the engineering strain $\varepsilon_{\text{axial}}$ for several armchair and zigzag carbon nanotubes in simple tension. (B) The force/strain ratio at the vanishing strain versus the radius of armchair and zigzag carbon nanotubes.

curves for armchair and zigzag are rather close. Furthermore, after normalization by $2\pi R$, the force/strain ratio becomes a constant once the CNT radius exceeds 1 nm.

6.6.3. Pressure of Carbon Nanotubes

For an armchair or zigzag CNT of radius R subject to internal pressure P^{int} (force per initial unit area), the deformation is uniform and axisymmetric prior to bifurcation. The analysis in Section 6.6.2 still holds except that the equilibrium equation becomes $T_{11} - M_{11}/[R(1 + \varepsilon_{\text{lateral}})] = P^{\text{int}}R/(1 + \varepsilon_{\text{lateral}})$ when finite-deformation effects are taken into account. The traction-free condition at the end of CNT requires $T_{22} = 0$. These two equations give the strains $\varepsilon_{\text{axial}}$ and $\varepsilon_{\text{lateral}}$ in the axial and circumferential directions in terms of the internal pressure P^{int} .

Figure 6.4A shows the internal pressure, multiplied by the initial radius R of the CNT, versus the lateral strain for several armchair and zigzag CNTs. Similar to Fig. 6.3A, the curves do not depend strongly on the CNT radius R , but the chirality (armchair versus zigzag) has a strong effect. At the limit of internal pressure approaching zero, the pressure/strain ratio is given analytically as $R^{-3}(R^2L_{1111} - v_{21}R^2L_{1122} - 2RH_{1111} + v_{21}RH_{2211} + S_{1111} + RM_{11}^{(0)})$, where

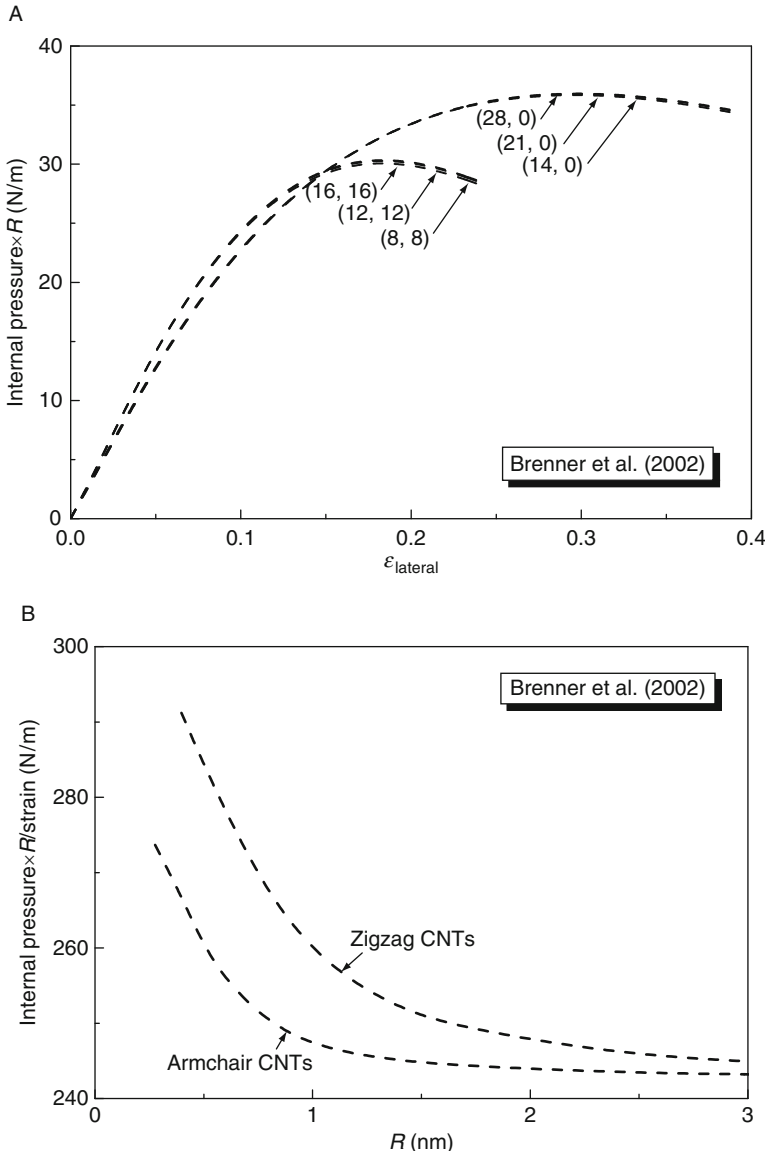


FIG. 6.4 (A) The internal pressure, multiplied by the initial radius R , versus the engineering strain $\varepsilon_{\text{lateral}}$ for several armchair and zigzag carbon nanotubes in internal pressure. (B) The internal pressure/strain ratio at small strains versus the radius of armchair and zigzag carbon nanotubes.

$v_{21} = (RL_{2211} - H_{2211})/(RL_{2222})$ is the corresponding Poisson's ratio. [Figure 6.4B](#) shows the pressure/strain ratio (at the infinitesimal strain), multiplied by R , versus the CNT radius for armchair and zigzag CNTs. The pressure/strain ratio depends weakly on the chirality since the curves for armchair and zigzag CNTs are rather close. The pressure/strain ratio, multiplied by R , becomes a constant once the CNT radius exceeds 2 nm.

6.6.4. Torsion of Carbon Nanotubes

An armchair or zigzag CNT is subject to torsion, and the twist (rotation per unit initial length) is denoted by κ . For $\xi^1 = R\Theta$ and $\xi^2 = Z$, the nonvanishing coefficients of first and second fundamental forms are $A_{11} = 1$, $A_{22} = 1$, and $B_{11} = -1/R$, where R is the CNT radius prior to torsion. The point $P = Re_R + Ze_Z$ prior to torsion moves to $p = R(1 + \varepsilon_{\text{lateral}})\mathbf{e}_r + Z(1 + \varepsilon_{\text{axial}})\mathbf{e}_Z$, where the initial unit vectors \mathbf{e}_R and \mathbf{e}_Θ distort during torsion to become $\mathbf{e}_r = \mathbf{e}_R \cos \kappa Z + \mathbf{e}_\Theta \sin \kappa Z$ and $\mathbf{e}_\theta = -\mathbf{e}_R \sin \kappa Z + \mathbf{e}_\Theta \cos \kappa Z$ since the polar angle Θ becomes $\theta = \Theta + \kappa Z$. The strains $\varepsilon_{\text{lateral}}$ and $\varepsilon_{\text{axial}}$ in the circumferential and axial directions due to finite torsion are to be determined. The base vectors after the torsion are $\mathbf{a}_1 = \partial p / \partial \xi^1 = (1 + \varepsilon_{\text{lateral}})\mathbf{e}_\theta$ and $\mathbf{a}_2 = \partial p / \partial \xi^2 = (1 + \varepsilon_{\text{lateral}})R\kappa\mathbf{e}_\theta + (1 + \varepsilon_{\text{axial}})\mathbf{e}_Z$, which give the coefficients of first and second fundamental forms:

$$\begin{pmatrix} a_{11} & a_{12} \\ a_{21} & a_{22} \end{pmatrix} = \begin{bmatrix} (1 + \varepsilon_{\text{lateral}})^2 & (1 + \varepsilon_{\text{lateral}})^2 R\kappa \\ (1 + \varepsilon_{\text{lateral}})^2 R\kappa & (1 + \varepsilon_{\text{lateral}})^2 R^2 \kappa^2 + (1 + \varepsilon_{\text{axial}})^2 \end{bmatrix}, \quad (6.44)$$

$$\begin{pmatrix} b_{11} & b_{12} \\ b_{21} & b_{22} \end{pmatrix} = \begin{bmatrix} -\frac{1 + \varepsilon_{\text{lateral}}}{R} & -(1 + \varepsilon_{\text{lateral}})\kappa \\ -(1 + \varepsilon_{\text{lateral}})\kappa & -(1 + \varepsilon_{\text{lateral}})R\kappa^2 \end{bmatrix}. \quad (6.45)$$

The components of Green strain and curvature tensors are

$$\begin{pmatrix} E_{11} & E_{12} \\ E_{21} & E_{22} \end{pmatrix} = \begin{bmatrix} \varepsilon_{\text{lateral}} + \frac{1}{2}\varepsilon_{\text{lateral}}^2 & \frac{1}{2}(1 + \varepsilon_{\text{lateral}})^2 R\kappa \\ \frac{1}{2}(1 + \varepsilon_{\text{lateral}})^2 R\kappa & \varepsilon_{\text{axial}} + \frac{1}{2}\varepsilon_{\text{axial}}^2 + \frac{1}{2}(1 + \varepsilon_{\text{lateral}})^2 R^2 \kappa^2 \end{bmatrix}, \quad (6.46)$$

$$\begin{pmatrix} K_{11} & K_{12} \\ K_{21} & K_{22} \end{pmatrix} = \begin{bmatrix} -\frac{\varepsilon_{\text{lateral}}}{R} & -(1 + \varepsilon_{\text{lateral}})\kappa \\ -(1 + \varepsilon_{\text{lateral}})\kappa & -(1 + \varepsilon_{\text{lateral}})R\kappa^2 \end{bmatrix}. \quad (6.47)$$

The components of second Piola–Kirchhoff membrane stress and moment are obtained from Eqs. (6.21) and (6.23). The equilibrium equations become $T_{11} + 2\kappa R T_{12} - (M_{11} + 2\kappa R M_{12} + \kappa^2 R^2 M_{22})/[R(1 + \varepsilon_{\text{lateral}})] = 0$. The boundary conditions for pure torsion require $T_{22} = 0$. These two equations give the strains $\varepsilon_{\text{axial}}$ and $\varepsilon_{\text{lateral}}$ in the axial and circumferential directions in terms of the twist κ .

Figure 6.5A shows the torque, normalized by $2\pi R^2$, versus the normalized twist κR for several armchair and zigzag CNTs. Similar to Figs. 6.3A and 6.4A, the CNT radius has little effect, but the chirality has a strong influence since the curves for armchair CNTs are far above the zigzag CNTs. At the limit of twist approaching zero, the torque/twist ratio is given analytically as $2\pi R(R^2 L_{1212} - 4RH_{1212} + 4S_{1212} - 2RM_{22}^{(0)})$. Figure 6.5B shows the torque/twist ratio (at infinitesimal twist), normalized by $2\pi R^3$, versus the CNT radius for armchair and zigzag CNTs, which once again depends weakly on the CNT chirality. The normalized torque/twist ratio also becomes a constant once the CNT radius exceeds 2 nm.

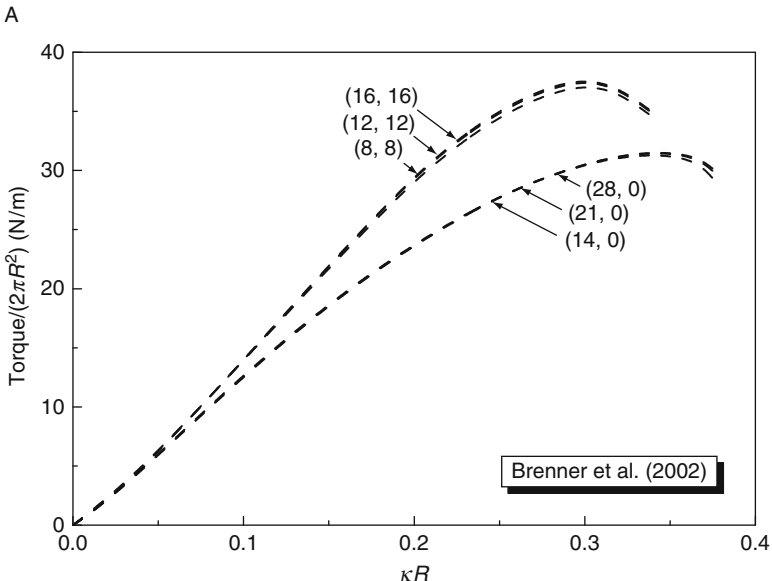


FIG. 6.5 (Continued)

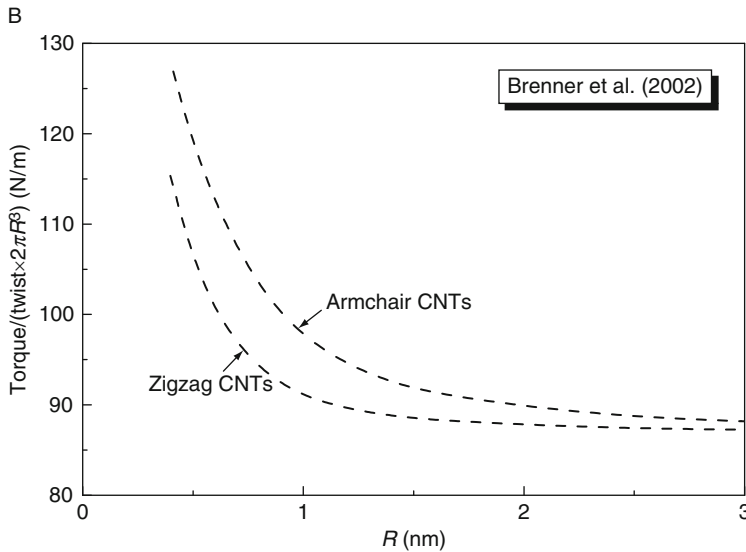


FIG. 6.5 (A) The torque, normalized by $2\pi R^2$ prior to deformation, versus the normalized twist κR for several armchair and zigzag carbon nanotubes in pure torsion. (B) The torque/twist ratio at vanishing twist versus the nanotube radius.

6.6.5. Bending of Carbon Nanotubes

The cross section of a CNT subject to bending is not circular anymore, as shown by the displacement field given in [Section 5.2](#). Here, the effect of initial residual membrane stress and moment in the CNT is accounted for, which is different from [Section 5.2](#). For an armchair or zigzag CNT subject to infinitesimal curvature k , the ratio of bending moment to curvature is obtained analytically as $\pi R^2 (RL_{2222} - R\lambda L_{2211} + 2\lambda H_{2211} - H_{2222} - M_{22}^{(0)})$, where $\lambda = (R^2 L_{1122} - RH_{1122} - 2RH_{2211} + 2S_{1122} + RM_{22}^{(0)}) / (R^2 L_{1111} - 4RH_{1111} + 4S_{1111} - RM_{11}^{(0)})$. [Figure 6.6](#) shows this bending moment/curvature ratio, normalized by πR^3 , versus the radius for armchair and zigzag CNTs, which is approximately constant once the CNT radius exceeds 1 nm.

7. Instability of Carbon Nanotubes

For a CNT subject to tension/compression, internal/external pressure, and torsion, the deformation is uniform prior to instability, as given in [Section 6](#).

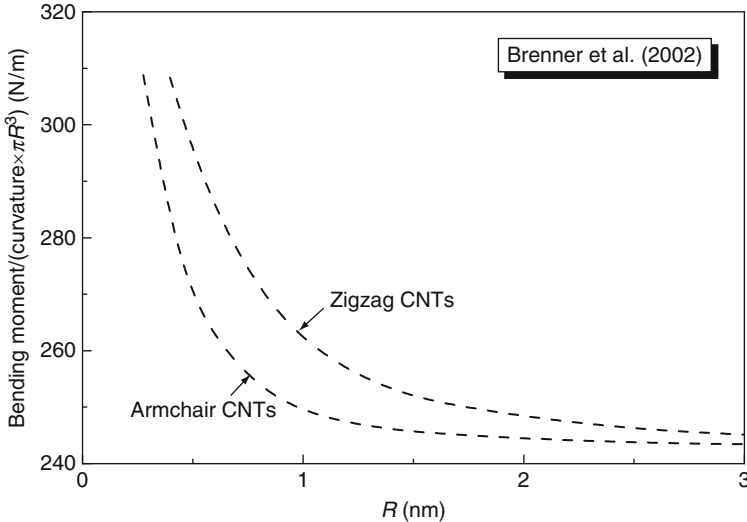


FIG. 6.6 The bending moment/curvature ratio at the vanishing curvature, normalized by πR^3 , versus the radius for armchair and zigzag carbon nanotubes.

7.1. INSTABILITY OF CARBON NANOTUBES IN TENSION

The increment (rate) of deformation becomes nonuniform at the onset of bifurcation. Let $v = \dot{U}$ denote the velocity with the covariant components $v_\Theta = v_1$, $v_Z = v_2$, and $v_R = v_3$. For a CNT of length L subject to the axial force but no shear at two ends $Z = 0$ and L , the velocity (prior to and) at the onset of bifurcation satisfies (Zhang et al., 2004)

$$v_Z = \frac{\partial v_\Theta}{\partial Z} = \frac{\partial v_R}{\partial Z} = 0 \quad \text{at } Z = 0, L. \quad (7.1)$$

We first consider axisymmetric bifurcation. The axisymmetric velocity field, satisfying the incremental equilibrium equations (6.42) and (6.43) and boundary condition Eq. (7.1), is given by

$$v_\Theta = 0, \quad v_Z = V_{Z0} \sin \frac{m\pi Z}{L}, \quad v_R = V_{R0} \cos \frac{m\pi Z}{L}, \quad (7.2)$$

where $m = 1, 2, 3, \dots$ is the eigenmode number, and (V_{Z0}, V_{R0}) is the corresponding eigenvector satisfying the following homogeneous algebraic equation:

$$\begin{pmatrix} Q_{ZZ} & Q_{ZR} \\ Q_{RZ} & Q_{RR} \end{pmatrix} \begin{pmatrix} V_{Z0} \\ V_{R0} \end{pmatrix} = 0. \quad (7.3)$$

The coefficients Q_{IJ} are given in terms of the incremental tension, bending, and coupled tension/bending rigidity tensors \mathbf{L} , \mathbf{S} , and \mathbf{H} [Eqs. (6.25) and (6.26)] and the membrane stress and moment tensors \mathbf{T} and \mathbf{M} by

$$\begin{aligned} Q_{ZZ} &= - \left[L_{2222} + \frac{T_{22}}{(1 + \varepsilon_{\text{axial}})^2} \right] \left(\frac{m\pi}{L} \right)^2, \\ Q_{ZR} = Q_{RZ} &= - \frac{1 + \varepsilon_{\text{lateral}}}{R} \left[L_{2211} - \frac{H_{2211}}{R(1 + \varepsilon_{\text{lateral}})} \right] \frac{m\pi}{L} \\ &\quad + \left[H_{2222} + \frac{M_{22}}{(1 + \varepsilon_{\text{axial}})^2} \right] \left(\frac{m\pi}{L} \right)^3, \\ Q_{RR} &= - \frac{(1 + \varepsilon_{\text{lateral}})^2}{R^2} \\ &\quad \times \left[L_{1111} - \frac{2H_{1111}}{R(1 + \varepsilon_{\text{lateral}})} + \frac{S_{1111}}{R^2(1 + \varepsilon_{\text{lateral}})^2} + \frac{M_{11}}{R(1 + \varepsilon_{\text{lateral}})^3} \right] \\ &\quad + \left[\frac{2(1 + \varepsilon_{\text{lateral}})}{R} H_{1122} - \frac{2}{R^2} S_{1122} - T_{22} - \frac{1 + \varepsilon_{\text{lateral}}}{R(1 + \varepsilon_{\text{axial}})^2} M_{11} \right] \\ &\quad \times \left(\frac{m\pi}{L} \right)^2 - S_{2222} \left(\frac{m\pi}{L} \right)^4. \end{aligned} \quad (7.4)$$

To have a nontrivial solution, the determinant of the 2×2 matrix in Eq. (7.3) must vanish. The smallest axial strain $\varepsilon_{\text{axial}}$ that satisfies this condition is the critical strain for bifurcation in tension, and is denoted by $\varepsilon_{\text{cr}}^{\text{tension}}$. Figure 7.1 shows $\varepsilon_{\text{cr}}^{\text{tension}}$ based on the Brenner (1990) potential versus mR/L for (8,8), (12,12) and (16,16) armchair CNTs and (14,0), (21,0) and (28,0) zigzag CNTs, where $m (= 1, 2, 3, \dots)$ is the eigen mode number, and R and L are the CNT radius and length, respectively. The CNT radius has essentially no effect on the critical strain for bifurcation in tension since the curves for armchair CNTs are almost identical, and so are the ones for zigzag CNTs. The CNT chirality, however, has a significant influence on the bifurcation in tension. For example, the (8,8) armchair and (14,0) zigzag CNTs have approximately the same radius, but the critical strain for the (14,0) zigzag CNT is lower than that for the (8,8) armchair CNT.

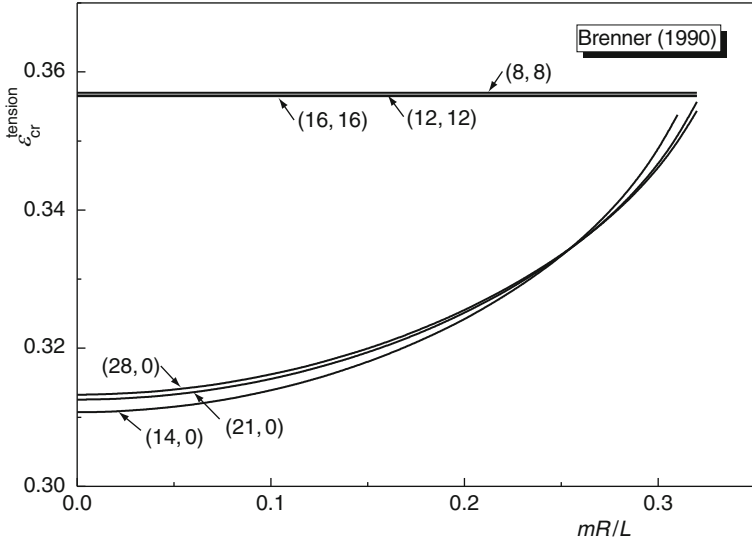


FIG. 7.1 The critical strain for axisymmetric bifurcation in tension based on the [Brenner \(1990\)](#) potential versus mR/L for (8,8), (12,12) and (16,16) armchair carbon nanotubes and (14,0), (21,0) and (28,0) zigzag carbon nanotubes, where $m (=1, 2, 3, \dots)$ is the bifurcation mode number, R and L are radius and length of the carbon nanotube, respectively.

This critical strain is identical to the one given by the membrane theory of CNT ([Zhang et al., 2004](#)) based on the same interatomic potential ([Brenner, 1990](#)). The identical result given by the shell theory and membrane theory suggests that the CNT bending rigidity has essentially no effect on bifurcation in tension. This is because bifurcation in tension is a material instability, and not a structure instability as for buckling in compression ([Wu, Hwang, Song, & Huang, 2008](#)).

For nonaxisymmetric bifurcation, the velocity field, satisfying the incremental equilibrium [equations \(6.42\) and \(6.43\)](#) and boundary condition [Eq. \(7.1\)](#), is given by

$$v_\Theta = V_{\Theta 0} \sin n\Theta \cos \frac{m\pi Z}{L}, \quad v_Z = V_{Z0} \cos n\Theta \sin \frac{m\pi Z}{L}, \quad v_R = V_{R0} \cos n\Theta \cos \frac{m\pi Z}{L}, \quad (7.5)$$

where $n = 1, 2, 3, \dots$, $n = 0$ degenerates to the axisymmetric bifurcation [Eq. \(7.2\)](#), and the eigenvector $(V_{\Theta 0}, V_{Z0}, V_{R0})$ satisfies a set of homogeneous algebraic equations. The vanishing of the determinant of coefficient matrix gives the condition for nonaxisymmetric bifurcation. [Figure 7.2](#) shows the critical strain $\epsilon_{cr}^{tension}$ for axisymmetric and non-axisymmetric bifurcation ($n = 0, 1, 2, 3, \dots$) of the (8,8) armchair CNT in tension. The critical strain for non-axisymmetric

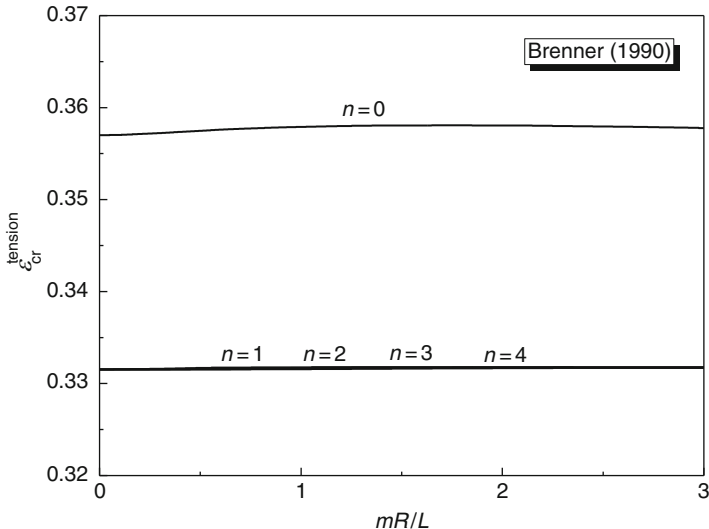


FIG. 7.2 The critical strain for bifurcation in tension based on the [Brenner \(1990\)](#) potential versus mR/L for the (8,8) armchair carbon nanotube, where $n = 0$ represents axisymmetric bifurcation, while $n = 1, 2, 3, \dots$ is for non-axisymmetric bifurcation.

bifurcation ($n = 1, 2, 3, \dots$) is essentially a constant (i.e., independent of n), 0.332, and is always smaller than its axisymmetric counterpart. This is very different from classical linear elastic thin shells, which have no bifurcation under tension.

[Figure 7.3](#) shows the critical strain $\varepsilon_{cr}^{tension}$ for bifurcation in tension based on the second-generation potential ([Brenner et al., 2002](#)). Similar to [Fig. 7.2](#) for the [Brenner \(1990\)](#) potential, the critical strain for non-axisymmetric bifurcation ($n = 1, 2, 3, \dots$) is always smaller than its axisymmetric counterpart, but it is not a constant anymore and is dependant on both n and mR/L .

7.2. INSTABILITY OF CARBON NANOTUBES IN COMPRESSION

Even though the membrane theory and shell theory for CNTs give the same critical strain for bifurcation in tension in [Section 7.1](#), the membrane theory is not applicable to instability of CNTs in compression since it does not have bending rigidity. We use the finite-deformation shell theory formulated in [Section 6](#) to study the instability of CNTs in compression. The deformation is uniform prior to bifurcation, and is the same as that in [Section 6.6.2](#) except for the axial strain $\varepsilon_{axial} < 0$. Once the compressive strain reaches a critical value, $-\varepsilon_{cr}^{compression}$, bifurcation occurs. In the following $\varepsilon_{cr}^{compression}$ is called the buckling strain.

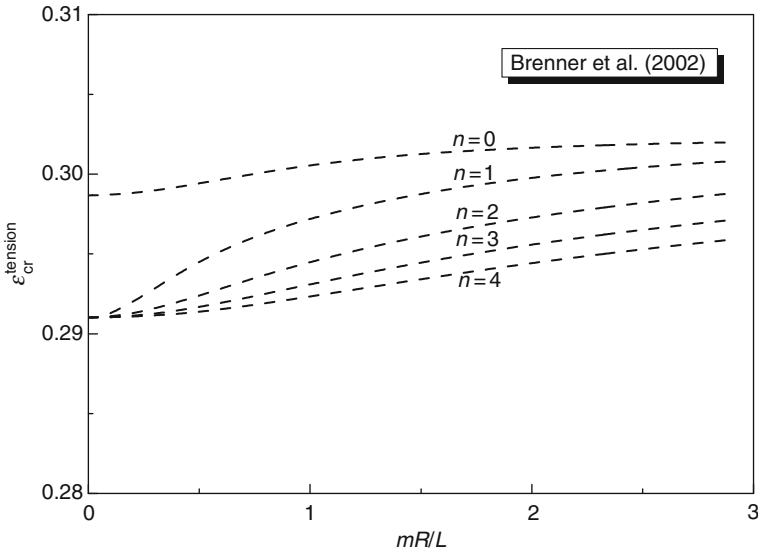


FIG. 7.3 The critical strain for bifurcation in tension based on the second-generation interatomic potential (Brenner et al., 2002) versus mR/L for the (8,8) armchair carbon nanotube.

The onset of bifurcation is governed by the analysis in Section 7.1, except that $\varepsilon_{\text{axial}} < 0$. Figure 7.4 shows the buckling strain $\varepsilon_{\text{cr}}^{\text{compression}}$ based on the Brenner (1990) potential versus $L/(mR)$ for the (8,8) armchair CNT in compression, where $m (= 1, 2, 3, \dots)$ is the eigenmode number. Both axisymmetric ($n = 0$) and nonaxisymmetric bifurcations ($n = 1, 2, 3, \dots$) are considered, where the velocity field for $n = 1$ is identical to that for the Euler beam buckling. For long CNTs $L/(mR) > 6.9$, $n = 1$ (Euler beam buckling) gives the smallest buckling strain $\varepsilon_{\text{cr}}^{\text{compression}}$. For relatively short CNTs $L/(mR) < 6.9$, $n = 2$ gives the smallest $\varepsilon_{\text{cr}}^{\text{compression}}$. Axisymmetric bifurcation ($n = 0$) never occurs in compression.

Figure 7.5 shows the buckling strain $\varepsilon_{\text{cr}}^{\text{compression}}$ based on the second-generation interatomic potential (Brenner et al., 2002) for the (8,8) armchair CNT in compression. The curves look similar to those in Fig. 7.4, but the buckling strain is smaller. The difference once again originates from different functions and parameters used in two potentials.

Figure 7.6 shows the buckling strain based on the Brenner (1990) potential for the (8,8), (12,12), and (16,16) armchair CNTs in compression. For long CNTs [large $L/(mR)$], all curves coincide and give the same buckling strain $\varepsilon_{\text{cr}}^{\text{compression}}$ corresponding to Euler beam buckling $n = 1$. For relatively short CNTs, other buckling modes appear, such as $n = 2$ for the (8,8) armchair CNT, and $n = 2$ and

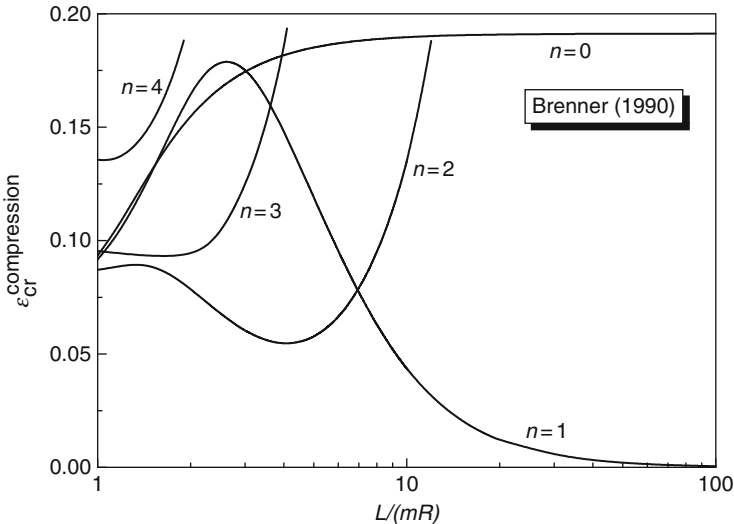


FIG. 7.4 The critical strain for bifurcation in compression based on the [Brenner \(1990\)](#) potential versus $L/(mR)$ for the (8,8) armchair carbon nanotube.

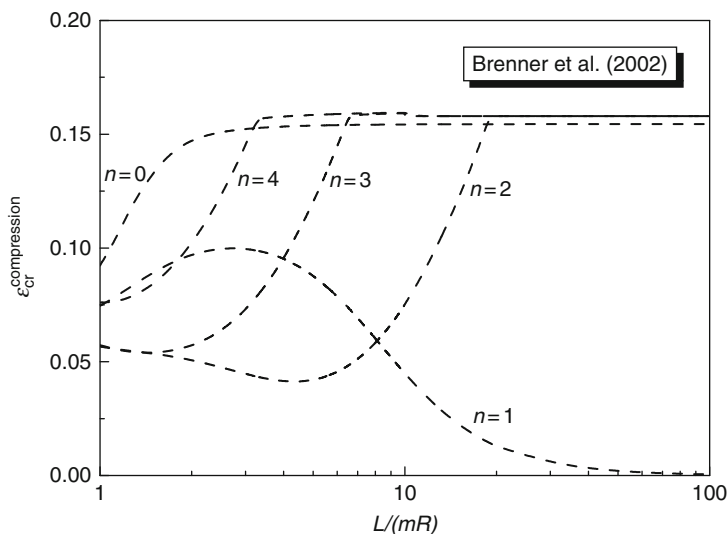


FIG. 7.5 The critical strain for bifurcation in compression based on the second-generation interatomic potential ([Brenner et al., 2002](#)) versus $L/(mR)$ for the (8,8) armchair carbon nanotube.

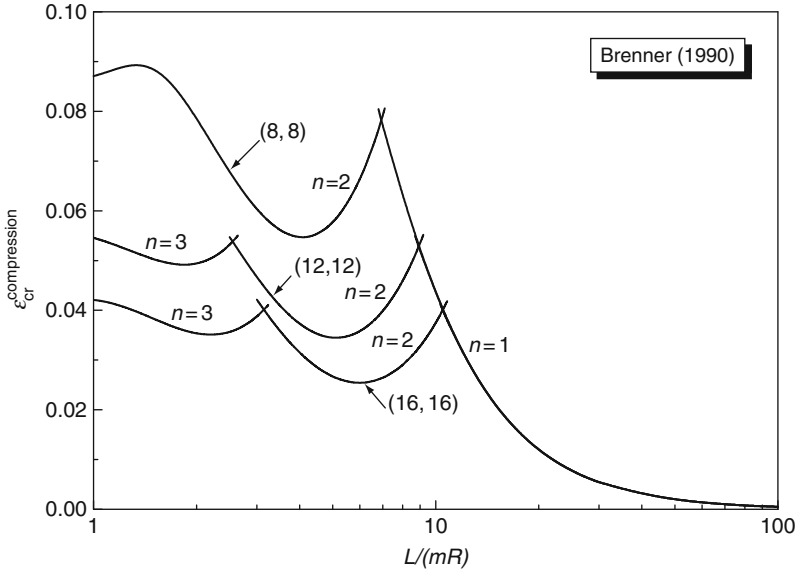


FIG. 7.6 The critical strain for bifurcation in compression based on the [Brenner \(1990\)](#) potential versus $L/(mR)$ for the (8,8), (12,12), and (16,16) armchair carbon nanotubes.

$n = 3$ for (12,12) and (16,16) armchair CNTs. This strong dependence on the CNT radius was not observed in tension bifurcation ([Section 7.1](#)).

7.3. INSTABILITY OF CARBON NANOTUBES SUBJECT TO INTERNAL PRESSURE

Similar to [Section 6.6.3](#), the deformation is still uniform at the onset of bifurcation, but its increment (rate) is not, and is given by [Eq. \(7.5\)](#). The incremental equilibrium [equations \(6.42\) and \(6.43\)](#) then give a homogeneous algebraic equation for $(V_{\Theta 0}, V_{Z0}, V_{R0})$:

$$\begin{pmatrix} Q_{\Theta\Theta} & Q_{\Theta Z} & Q_{\Theta R} \\ Q_{Z\Theta} & Q_{ZZ} & Q_{ZR} \\ Q_{R\Theta} & Q_{RZ} & Q_{RR} \end{pmatrix} \begin{pmatrix} V_{\Theta 0} \\ V_{Z0} \\ V_{R0} \end{pmatrix} = 0, \quad (7.6)$$

where, similar to [Eq. \(7.4\)](#), the coefficients Q_{IJ} are given analytically in terms of the incremental rigidity tensors \mathbf{L} , \mathbf{S} , and \mathbf{H} , and the membrane stress and moment tensors \mathbf{T} and \mathbf{M} . To have a nontrivial solution, the determinant of the 3×3 matrix in [Eq. \(7.6\)](#) must vanish, which gives the critical condition for bifurcation of CNTs subject to internal pressure.

Figure 7.7 shows the critical internal pressure for bifurcation, $P_{\text{cr}}^{\text{int}}$, based on the Brenner (1990) potential versus L/mR for the (8,8), (12,12), and (16,16) armchair CNT, where $m (= 1, 2, 3, \dots)$ is the eigenmode number, and R and L are the CNT radius and length, respectively. The bifurcation mode always corresponds to $n = 1$ (the same mode as the Euler beam buckling). The CNT radius has little effect on the critical internal pressure for bifurcation since the curves in Fig. 7.7 are close. This is similar to the bifurcation in tension (Section 7.1) since the membrane stress state is also in tension for the CNT subject to the internal pressure. The critical internal pressure for bifurcation $P_{\text{cr}}^{\text{int}}$ decreases monotonically with increasing CNT length L (and does not approach an asymptote). For a CNT length/radius ratio of $L/(mR) = 200$, $P_{\text{cr}}^{\text{int}}$ is about 100 MPa. This is very different from classical linear elastic thin shells, which have no bifurcation under internal pressure.

Figure 7.8 shows the critical internal pressure for bifurcation, $P_{\text{cr}}^{\text{int}}$, based on the second-generation interatomic potential (Brenner et al., 2002) for (8,8), (12,12), and (16,16) armchair CNTs. The bifurcation mode corresponds to $n = 1$ (the same mode as Euler beam buckling). The curves in Fig. 7.8 are rather similar to those in Fig. 7.7.

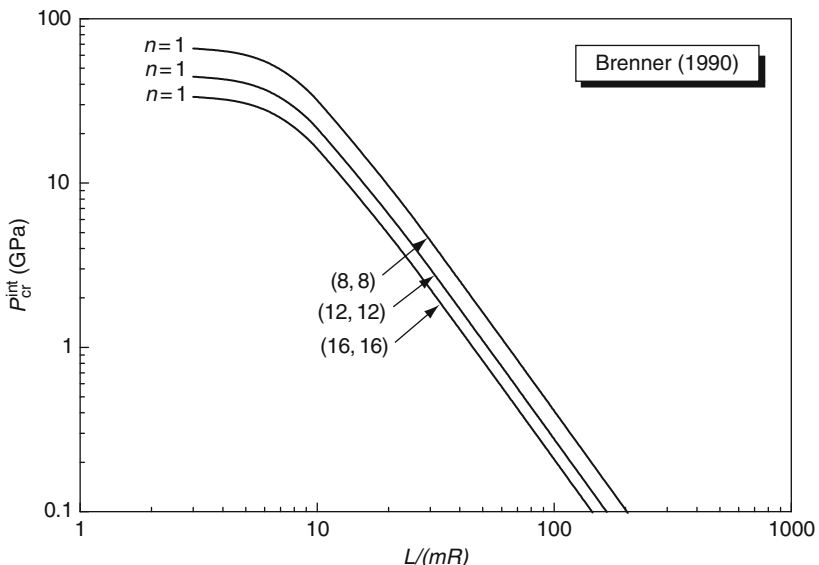


FIG. 7.7 The critical internal pressure for bifurcation based on the Brenner (1990) potential versus $L/(mR)$ for the (8,8), (12,12), and (16,16) armchair carbon nanotubes. The bifurcation corresponds to $n = 1$ (nonaxisymmetric mode).

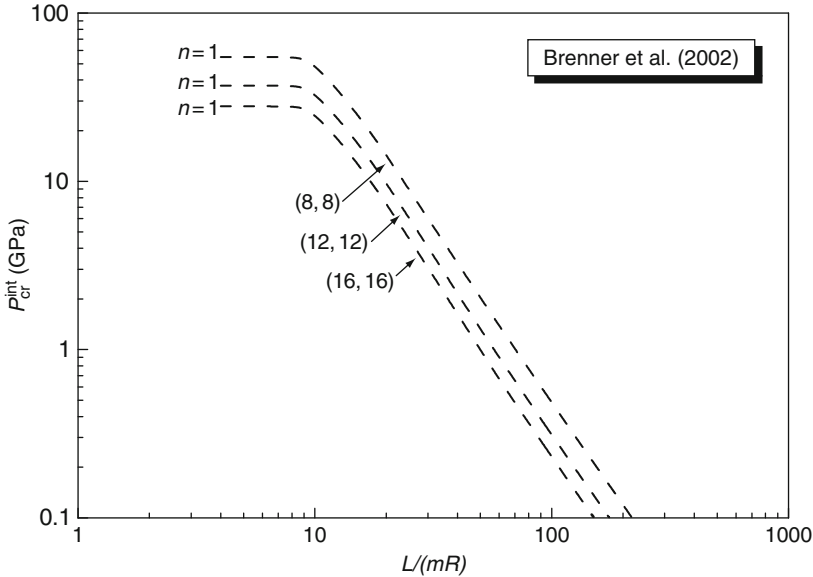


FIG. 7.8 The critical internal pressure for bifurcation based on the second-generation interatomic potential (Brenner et al., 2002) versus $L/(mR)$ for the (8,8), (12,12), and (16,16) armchair carbon nanotubes. The bifurcation corresponds to $n = 1$ (nonaxisymmetric mode).

7.4. INSTABILITY OF CARBON NANOTUBES SUBJECT TO EXTERNAL PRESSURE

For an armchair or zigzag CNT of radius R subject to external pressure P^{ext} , the deformation is uniform and axisymmetric prior to bifurcation. The analysis in Section 7.3 still holds except that the internal pressure P^{int} is replaced by $-P^{\text{ext}}$. Equation (7.6) also gives the critical condition for bifurcation into the modes according to Eq. (7.5) under external pressure (if P^{int} is replaced by $-P^{\text{ext}}$).

Figure 7.9 shows the critical external pressure for bifurcation, $P_{\text{cr}}^{\text{ext}}$, based on the Brenner (1990) potential versus $L/(mR)$ for the (8,8) armchair CNT, where $m (= 1, 2, 3, \dots)$ is the eigenmode number, and R and L are the CNT radius and length, respectively. Both the axisymmetric ($n = 0$) and nonaxisymmetric bifurcations ($n = 1, 2, 3, \dots$) are considered. For CNT lengths $L/(mR) > 3.3$, $n = 2$ gives the lowest critical external pressure $P_{\text{cr}}^{\text{ext}}$. For very short CNTs $L/(mR) < 3.3$, other bifurcation modes ($n = 3, 4, \dots$) appear, but the axisymmetric bifurcation ($n = 0$) or nonaxisymmetric bifurcation with $n = 1$ never occur. The bifurcation modes ($n = 2, 3, 4, \dots$) for the external pressure are completely different from that for the internal pressure ($n = 1$) in Section 7.3.

Figure 7.10 shows the critical external pressure for bifurcation, $P_{\text{cr}}^{\text{ext}}$, based on the second-generation interatomic potential (Brenner et al., 2002) for the (8,8)

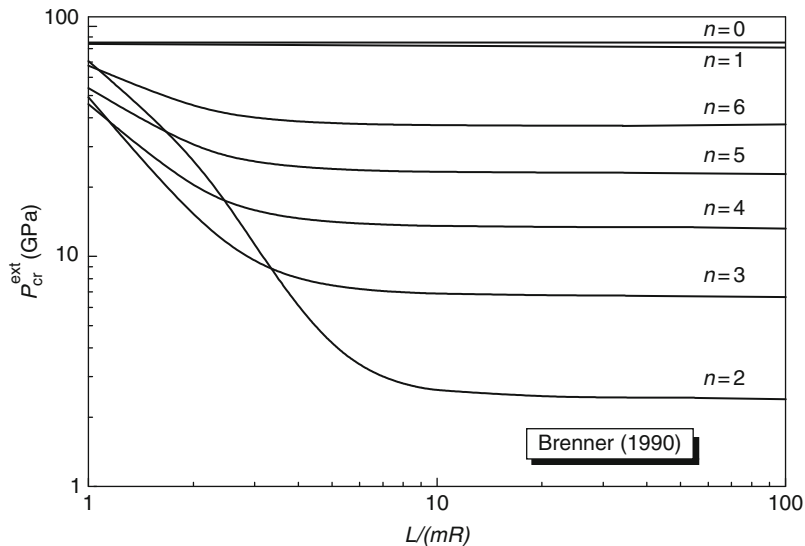


FIG. 7.9 The critical external pressure for bifurcation based on the [Brenner \(1990\)](#) potential versus $L/(mR)$ for the (8,8) armchair carbon nanotube.

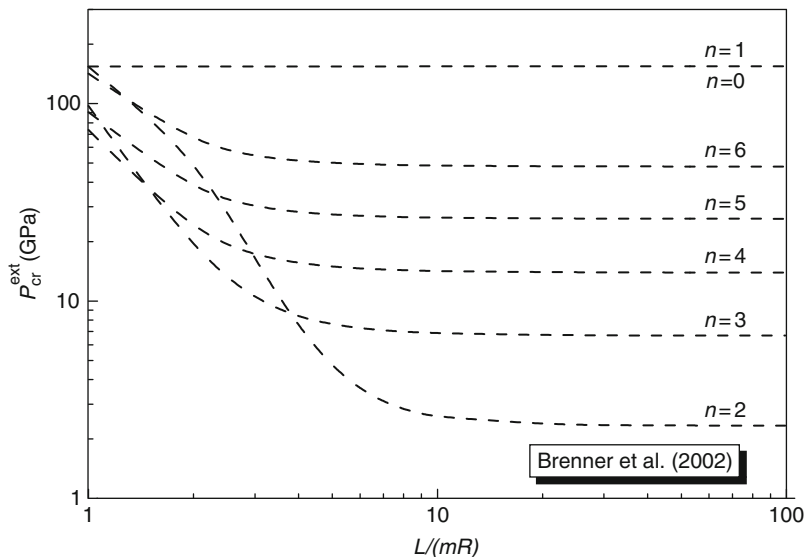


FIG. 7.10 The critical external pressure for bifurcation based on the second-generation interatomic potential ([Brenner et al., 2002](#)) versus $L/(mR)$ for the (8,8) armchair carbon nanotube.

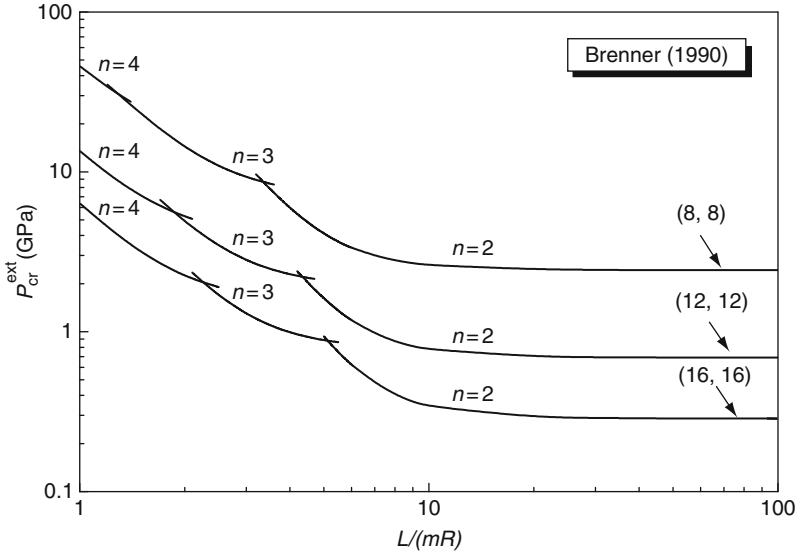


FIG. 7.11 The critical external pressure for bifurcation based on the [Brenner \(1990\)](#) potential versus $L/(mR)$ for the (8,8), (12,12), and (16,16) armchair carbon nanotubes.

armchair CNT. The results are somewhat different from those in [Fig. 7.9](#) for the [Brenner \(1990\)](#) potential, reflecting the difference between the two potentials.

[Figure 7.11](#) shows the critical external pressure for bifurcation, $P_{\text{cr}}^{\text{ext}}$, based on the [Brenner \(1990\)](#) potential for the (8,8), (12,12), and (16,16) armchair CNTs. Similar to [Fig. 7.9](#), the bifurcation mode corresponds to $n = 2$ for long CNTs [large $L/(mR)$] and to $n = 3, 4, \dots$ for shorter CNTs, and never to $n = 0$ (axisymmetric bifurcation) or $n = 1$. The critical external pressure for bifurcation decreases rapidly as the CNT radius increases since $P_{\text{cr}}^{\text{ext}}$ for the (16,16) armchair CNT is much smaller than that for the (8,8) armchair CNT.

7.5. INSTABILITY OF CARBON NANOTUBES IN TORSION

The deformation is still uniform at the onset of bifurcation, but its increment (rate) is not. Let $\mathbf{v} = \dot{\mathbf{U}}$, with components v_R , v_Θ , and v_Z denote the velocity away from the homogeneous solution. The velocity field in the CNT can be expressed as

$$\begin{aligned} v_\Theta &= V_{\Theta 0} \cos\left(\frac{m\pi Z}{L} - n\Theta\right), \\ v_Z &= V_{Z 0} \cos\left(\frac{m\pi Z}{L} - n\Theta\right), \\ v_R &= V_{R 0} \sin\left(\frac{m\pi Z}{L} - n\Theta\right), \end{aligned} \quad (7.7)$$

where $n = 0, 1, 2, 3, \dots, m$ ($= 1, 2, 3, \dots$) are the eigenmode numbers, and $(V_{\Theta 0}, V_{Z0}, V_{R0})$ is the corresponding eigenvector. Substitution of Eq. (7.7) into the incremental equilibrium equations (6.42) and (6.43) yields a set of homogeneous algebraic equations for $(V_{\Theta 0}, V_{Z0}, V_{R0})$. The vanishing of determinant of the coefficient matrix gives the condition for the critical twist κ_{cr} at which the torsional bifurcation takes place.

Figure 7.12 shows $\kappa_{cr}R$ based on the Brenner (1990) potential versus $L/(mR)$ for the (8,8), (12,12), and (16,16) armchair CNTs, where m ($= 1, 2, 3, \dots$) is the eigenmode number, and R and L are the CNT radius and length, respectively. For long CNTs [large $L/(mR)$], the bifurcation mode is always $n = 2$. The corresponding critical twist for bifurcation κ_{cr} approaches a constant value for each CNT as $L/(mR)$ increases. For relatively short CNTs, other bifurcation modes $n = 3, 4, \dots$ appear, but $n = 0$ and $n = 1$ never occur.

Figure 7.13 shows the critical twist for bifurcation, $\kappa_{cr}R$, based on the second-generation interatomic potential (Brenner et al., 2002). The trend is similar to that in Fig. 7.12 based on the Brenner (1990) potential, but the two potentials give noticeably different critical twist values for bifurcation in torsion.

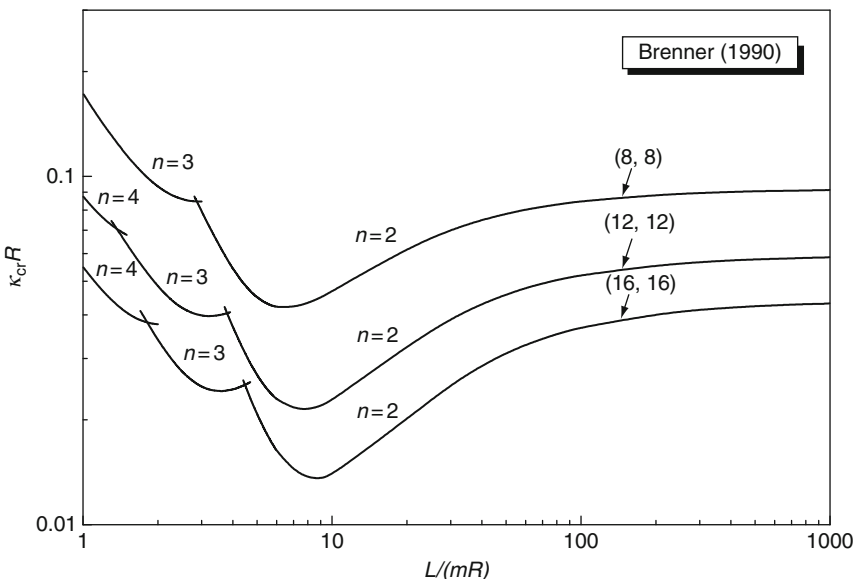


FIG. 7.12 The critical twist κ_{cr} for bifurcation based on the Brenner (1990) potential versus $L/(mR)$ for the (8,8), (12,12), and (16,16) armchair carbon nanotubes.

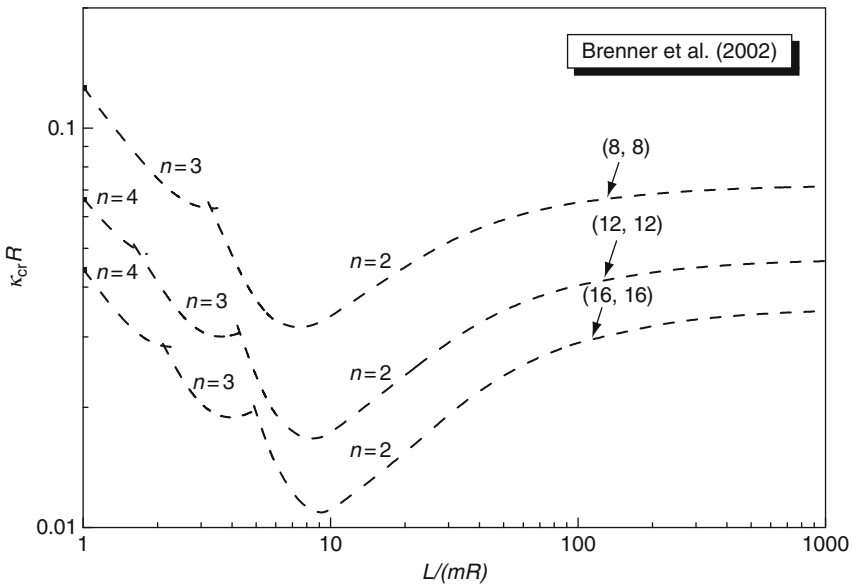


FIG. 7.13 The critical twist κ_{cr} for bifurcation based on the second-generation interatomic potential (Brenner et al., 2002) versus $L/(mR)$ for the (8,8), (12,12), and (16,16) armchair carbon nanotubes.

8. Concluding Remarks

A finite-deformation shell theory for single-wall CNTs is established directly from the atomic structure of CNT and the interatomic potential. It is different from all existing shell theories because of the coupling in the constitutive model between the membrane stress and curvature, and between moment and membrane strain. It is also different from the classical Cauchy–Born rule linking atomistic models to the three-dimensional continuum theory since it accounts for the important effect of moment and curvature (of CNTs).

For graphene, this atomistic-based shell theory degenerates to a plate theory, but it is different from any classical plate theories because the bending rigidity in a classical plate results from the tension and compression on opposite sides of the neutral plane, while the bending rigidity of graphene, which has a single layer of atoms, results from the multibody atomistic interactions (i.e., from the bond-angle dependence in the interatomic potential).

Even though the constitutive behavior of a CNT is different from that of a classical shell, its overall structural response for infinitesimal deformation may still be approximately represented by a linear elastic thin shell for some representative loadings such as tension, compression, bending, torsion, internal and external pressure. The ratio of atomic spacing ($\Delta \approx 0.14\text{nm}$) to CNT radius, Δ/R , is

used to identify the order of error for such an approximation, where Δ/R ranges from zero (for graphene) to about 40% [for the (5,5) armchair CNT ($R = 0.35\text{nm}$)]. For the order of error $O[(\Delta/R)^3]$ (as compared to unity), which is about 6% for the (5,5) armchair CNT, the structural response of a CNTs cannot be represented by any classical shell. For the order of error $O[(\Delta/R)^2]$, which is about 16% for the (5,5) armchair CNT, a CNT can be approximated by a linear elastic orthotropic thin shell. Only for the order of error $O(\Delta/R)$, which is about 40% for the (5,5) armchair CNT, a universal constant shell thickness and Young's modulus can be defined, and CNTs can be represented by an elastic isotropic thin shell.

The atomistic-based finite-deformation shell theory is used to study the instability of single-wall CNTs subject to tension, compression, internal and external pressure, and torsion.

Acknowledgments

Y.H. acknowledges the supports from the NSF through Nano-CEMMS (grant no. DMI03-28162) at the University of Illinois and ONR Composites for Marine Structures Program (grant N00014-01-1-0205, Program Manager Dr. Y. D. S. Rajapakse). The authors also acknowledge the supports from the NSFC and Ministry of Education of China. K. C. Hwang also acknowledges the support from National Basic Research Program of China (973 Program) (grant no. 2007CB936803).

Appendix A The Incremental Form of Equilibrium Equation

The incremental form of equilibrium [equation \(4.22\)](#) is

$$\begin{aligned} & \frac{1}{R} \frac{\partial}{\partial \theta} \left(\frac{dt_{\theta\theta}}{dt} \right) + \frac{\partial}{\partial Z} \left(\frac{dt_{\theta Z}}{dt} \right) - \frac{2}{R^2} \frac{\partial}{\partial \theta} \left(\frac{dm_{\theta\theta}}{dt} \right) - \frac{2}{R} \frac{\partial}{\partial Z} \left(\frac{dm_{\theta Z}}{dt} \right) \\ & + t_{\theta Z} \frac{\partial}{\partial Z} \left(3 \frac{v_R}{R} + \frac{3}{R} \frac{\partial v_\theta}{\partial \theta} + \frac{\partial v_Z}{\partial Z} \right) + t_{ZZ} \frac{\partial^2 v_\theta}{\partial Z^2} \\ & + m_{\theta\theta} \frac{1}{R^2} \frac{\partial}{\partial \theta} \left(\frac{1}{R} \frac{\partial^2 v_R}{\partial \theta^2} - \frac{v_R}{R} - \frac{2}{R} \frac{\partial v_\theta}{\partial \theta} - \frac{\partial v_Z}{\partial Z} \right) \\ & + m_{\theta Z} \frac{2}{R} \frac{\partial}{\partial Z} \left(\frac{1}{R} \frac{\partial^2 v_R}{\partial \theta^2} - 2 \frac{v_R}{R} - \frac{3}{R} \frac{\partial v_\theta}{\partial \theta} - \frac{\partial v_Z}{\partial Z} \right) + m_{ZZ} \frac{1}{R} \frac{\partial^2}{\partial Z^2} \left(\frac{\partial v_R}{\partial \theta} - 2v_\theta \right) = 0, \end{aligned} \quad (\text{A.1})$$

$$\begin{aligned}
& \frac{1}{R} \frac{\partial}{\partial \theta} \left(\frac{dt_{\theta Z}}{dt} \right) + \frac{\partial}{\partial Z} \left(\frac{dt_{ZZ}}{dt} \right) + t_{\theta \theta} \frac{1}{R^2} \frac{\partial^2 v_Z}{\partial \theta^2} \\
& + t_{\theta Z} \frac{1}{R} \frac{\partial}{\partial \theta} \left(\frac{v_R}{R} + \frac{1}{R} \frac{\partial v_\theta}{\partial \theta} + 3 \frac{\partial v_Z}{\partial Z} \right) + t_{ZZ} \frac{\partial}{\partial Z} \left(\frac{v_R}{R} + \frac{1}{R} \frac{\partial v_\theta}{\partial \theta} + 2 \frac{\partial v_Z}{\partial Z} \right) \\
& + m_{\theta \theta} \frac{1}{R^2} \frac{\partial^3 v_R}{\partial \theta^2 \partial Z} + m_{\theta Z} \frac{2}{R} \frac{\partial^3 v_R}{\partial \theta \partial Z^2} + m_{ZZ} \frac{\partial^3 v_R}{\partial Z^3} = 0,
\end{aligned} \tag{A.2}$$

$$\begin{aligned}
& \frac{1}{R^2} \frac{\partial^2}{\partial \theta^2} \left(\frac{dm_{\theta \theta}}{dt} \right) - \frac{1}{R^2} \frac{dm_{\theta \theta}}{dt} + \frac{2}{R} \frac{\partial^2}{\partial \theta \partial Z} \left(\frac{dm_{\theta Z}}{dt} \right) + \frac{\partial^2}{\partial Z^2} \left(\frac{dm_{ZZ}}{dt} \right) \\
& + \frac{1}{R} \frac{dt_{\theta \theta}}{dt} - 2t_{\theta Z} \frac{1}{R} \frac{\partial}{\partial Z} \left(\frac{\partial v_R}{\partial \theta} - v_\theta \right) - t_{ZZ} \frac{\partial^2 v_R}{\partial Z^2} \\
& + m_{\theta \theta} \frac{1}{R} \left(\frac{3}{R^2} \frac{\partial^2 v_R}{\partial \theta^2} - \frac{\partial^2 v_R}{\partial Z^2} - \frac{v_R}{R^2} + \frac{2}{R^2} \frac{\partial^3 v_\theta}{\partial \theta^3} + \frac{2}{R} \frac{\partial^3 v_Z}{\partial \theta^2 \partial Z} \right) \\
& + m_{\theta Z} \frac{2}{R} \frac{\partial}{\partial Z} \left(\frac{3}{R} \frac{\partial v_R}{\partial \theta} + \frac{2}{R} \frac{\partial^2 v_\theta}{\partial \theta^2} - \frac{v_\theta}{R} + 2 \frac{\partial^2 v_Z}{\partial \theta \partial Z} \right) \\
& + m_{ZZ} \frac{\partial^2}{\partial Z^2} \left(\frac{v_R}{R} + \frac{2}{R} \frac{\partial v_\theta}{\partial \theta} + 2 \frac{\partial v_Z}{\partial Z} \right) = 0,
\end{aligned} \tag{A.3}$$

where $t_{\alpha\beta}, m_{\alpha\beta}$ ($\alpha, \beta = \theta, Z$) denote the membrane stress and moment at the onset of bifurcation.

Appendix B The Symmetric Membrane Stress and Moment, and Covariant Derivatives

The asymmetric membrane stress tensor t_{asym} and moment \mathbf{m}_{asym} in exiting shell theories satisfy three force equilibrium equations and three moment equilibrium equations (Niordson, 1985):

$$t_{\text{asym}}^{\alpha\beta}_{;\beta} - b_{\alpha\beta}^{\alpha} t_{\text{asym}}^{\beta\beta} + X^\alpha = 0 \quad (\alpha = 1, 2), \tag{B.1}$$

$$t_{\text{asym}}^{\alpha\beta}_{;\beta} + b_{\lambda\beta}^{\alpha} t_{\text{asym}}^{\lambda\beta} + X^3 = 0, \tag{B.2}$$

$$m_{\text{asym}}{}^{\alpha\beta}_{;\beta} + t_{\text{asym}}{}^{3\alpha} + M^\alpha = 0 \quad (\alpha = 1, 2), \quad (\text{B.3})$$

$$c_{\alpha\beta} \left(t_{\text{asym}}{}^{\alpha\beta} + b_{\gamma}^{\beta} m_{\text{asym}}{}^{\alpha\gamma} \right) = 0, \quad (\text{B.4})$$

where $c_{\alpha\beta} = J e_{\alpha\beta}$ and $e_{\alpha\beta}$ is the two-dimensional permutation tensor ($e_{11} = e_{22} = 0$, $e_{12} = -e_{21} = 1$). The substitution of out-of-surface shear membrane stress $t_{\text{asym}}{}^{3\beta}$ in Eq. (B.3) into Eqs. (B.1) and (B.2) yields three equilibrium equations (6.37) and (6.38). The symmetric moment \mathbf{m} in Eqs. (6.37) and (6.38) is the symmetric part of the above asymmetric moment \mathbf{m}_{asym} :

$$\mathbf{m} = \frac{1}{2} (\mathbf{m}_{\text{asym}} + \mathbf{m}_{\text{asym}}^T). \quad (\text{B.5})$$

The symmetric membrane stress is given by

$$\mathbf{t} = \dot{\mathbf{t}}_{\text{asym}} - \mathbf{b} \cdot \mathbf{m}_{\text{asym}}^T = \dot{\mathbf{t}}_{\text{asym}}^T - \mathbf{m}_{\text{asym}} \cdot \mathbf{b} = \mathbf{t}^T, \quad (\text{B.6})$$

which is symmetric due to Eq. (B.4), where $\dot{\mathbf{t}}_{\text{asym}}$ is the in-surface part of the \mathbf{t}_{asym} .

The covariant derivatives of vector and tensor are

$$S^\alpha_{;\lambda} = \frac{\partial S^\alpha}{\partial \xi^\lambda} + S^\mu \gamma^\alpha_{\mu\lambda}, \quad (\text{B.7})$$

$$S^\alpha_{\cdot\beta;\lambda} = \frac{\partial S^\alpha_{\cdot\beta}}{\partial \xi^\lambda} + S^\mu_{\cdot\beta} \gamma^\alpha_{\mu\lambda} - S^\alpha_{\cdot\mu} \gamma^\mu_{\beta\lambda}, \quad (\text{B.8})$$

$$S^\alpha_\beta{}^{\lambda} = \frac{\partial S^\alpha_\beta}{\partial \xi^\lambda} + S^\mu_\beta \gamma^\alpha_{\mu\lambda} + S^\alpha_\mu \gamma^\beta_{\mu\lambda}, \quad (\text{B.9})$$

where $\gamma^\alpha_{\mu\lambda}$ is the Christoffel symbol for the deformed CNT.

References

- Arroyo, M., & Belytschko, T. (2002). An atomistic-based finite deformation membrane for single layer crystalline films. *Journal of the Mechanics and Physics of Solids*, 50, 1941–1977.
- Arroyo, M., & Belytschko, T. (2004). Finite crystal elasticity of carbon nanotubes based on the exponential Cauchy–Born rule. *Physical Review B*, 69, 115415.
- Belytschko, T., Xiao, S. P., Schatz, G. C., & Ruoff, R. S. (2002). Atomistic simulations of nanotube fracture. *Physical Review B*, 65, 235430.
- Born, M., & Huang, K. (1959). *Dynamical theory of crystal lattices*. Oxford: Oxford University Press.

- Brenner, D. W. (1990). Empirical potential for hydrocarbons for use in simulating the chemical vapor deposition of diamond films. *Physical Review B*, *42*, 9458–9471.
- Brenner, D. W., Shenderova, O. A., Harrison, J. A., Stuart, S. J., Ni, B., & Sinnott, S. B. (2002). A second-generation reactive empirical bond order (REBO) potential energy expression for hydrocarbons. *Journal of Physics: Condensed Matter*, *14*, 783–802.
- Chang, T., & Gao, H. (2003). Size-dependent elastic properties of a single-walled carbon nanotube via a molecular mechanics model. *Journal of the Mechanics and Physics of Solids*, *51*, 1059–1074.
- Chen, X., & Cao, G. (2006). A structural mechanics study of single-walled carbon nanotubes generalized from atomistic simulation. *Nanotechnology*, *17*, 1004–1015.
- Eisenhart, L. P. (1947). *An introduction to differential geometry: With use of the tensor calculus*. Princeton/London: Princeton University Press/Geoffrey Cumberlege, Oxford University Press.
- Gao, X. L., & Li, K. (2003). Finite deformation continuum model for single-walled carbon nanotubes. *International Journal of Solids and Structures*, *40*, 7329–7337.
- Govindjee, S., & Sackman, J. L. (1999). On the use of continuum mechanics to estimate the properties of nanotubes. *Solid State Communications*, *110*, 227–230.
- Huang, Y., Wu, J., & Hwang, K. C. (2006). Thickness of graphene and single-wall carbon nanotubes. *Physical Review B*, *74*, 245413.
- Jiang, H., Feng, X. Q., Huang, Y., Hwang, K. C., & Wu, P. D. (2004). Defect nucleation in carbon nanotubes under tension and torsion: Stone–Wales transformation. *Computer Methods in Applied Mechanics and Engineering*, *193*, 3419–3429.
- Jiang, H., Huang, Y., & Hwang, K. C. (2005). A finite-temperature continuum theory based on interatomic potentials. *Journal of Engineering Materials and Technology*, *127*, 408–416.
- Jiang, H., Liu, B., Huang, Y., & Hwang, K. C. (2004). Thermal expansion of single wall carbon nanotubes. *Journal of Engineering Materials and Technology*, *126*, 265–270.
- Jiang, H., Yu, M.-F., Liu, B., & Huang, Y. (2004). Intrinsic energy loss mechanisms in a cantilevered carbon nanotube beam oscillator. *Physical Review Letters*, *93*, 185501.
- Jiang, H., Zhang, P., Liu, B., Huang, Y., Geubelle, P. H., Gao, H., et al. (2003). The effect of nanotube radius on the constitutive model for carbon nanotubes. *Computational Materials Science*, *28*, 429–442.
- Johnson, H. T., Liu, B., & Huang, Y. (2004). Electron transport in deformed carbon nanotubes. *Journal of Engineering Materials and Technology*, *126*, 222–229.
- Khang, D. Y., Xiao, J., Kocabas, C., MacLaren, S., Banks, T., Jiang, H., et al. (2008). Molecular scale buckling mechanics in individual, aligned single-wall carbon nanotubes on elastomeric substrates. *Nano Letters*, *8*, 124–130.
- Koiter, W. T. (1966). On the nonlinear theory of thin elastic shells, I, II, III. *Proceedings of the Koninklijke Nederlandse Akademie van Wetenschappen, Series B*, *69*, 1–54.
- Kudin, K. N., Scuseria, G. E., & Yakobson, B. I. (2001). C2F, BN, and C nanoshell elasticity from ab initio computations. *Physical Review B*, *64*, 235406.
- Lee, C. G., Wei, X. D., Kysar, J. W., & Hone, J. (2008). Measurement of the elastic properties and intrinsic strength of monolayer graphene. *Science*, *321*, 385–388.
- Leung, A. Y. T., Guo, X., He, X. Q., & Kitipornchai, S. (2005). A continuum model for zigzag single-walled carbon nanotubes. *Applied Physics Letters*, *86*, 083110.
- Li, C., & Chou, T. W. (2003). A structural mechanics approach for the analysis of carbon. *International Journal of Solids and Structures*, *40*, 2487–2499.
- Li, C., & Chou, T. W. (2004). Modeling of elastic buckling of carbon nanotubes by molecular structural mechanics approach. *Mechanics of Materials*, *36*, 1047–1055.
- Liu, B., Huang, Y., Jiang, H., Qu, S., & Hwang, K. C. (2004). The atomic-scale finite element method. *Computer Methods in Applied Mechanics and Engineering*, *193*, 1849–1864.
- Liu, B., Jiang, H., Huang, Y., Qu, S., Yu, M. F., & Hwang, K. C. (2005). Atomic-scale finite element method in multiscale computation with applications to carbon nanotubes. *Physical Review B*, *72*, 035435.

- Liu, B., Jiang, H., Johnson, H. T., & Huang, Y. (2004). The influence of mechanical deformation on the electrical properties of single wall carbon nanotubes. *Journal of the Mechanics and Physics of Solids*, 52, 1–26.
- Liu, B., Yu, M.-F., & Huang, Y. (2004). Role of lattice registry in the full collapse and twist formation of carbon nanotubes. *Physical Review B*, 70, 161402.
- Nasdala, L., & Ernst, G. (2005). Development of a 4-node finite element for the computation of nano-structured materials. *Computational Materials Science*, 33, 443–458.
- Natsuki, T., Tantrakarn, K., & Endo, M. (2004). Prediction of elastic properties for single-walled carbon nanotubes. *Carbon*, 42, 39–45.
- Niordson, F. (1985). *Shell theory (North-Holland series in applied mathematics and mechanics)* (Vol. 29). New York: North-Holland.
- Odegard, G. M., Gates, T. S., Nicholson, L. M., & Wise, K. E. (2002). Equivalent-continuum modeling of nano-structured materials. *Composites Science and Technology*, 62, 1869–1880.
- Peng, J., Wu, J., Hwang, K. C., Song, J., & Huang, Y. (2008). Can a single-wall carbon nanotube be modeled as a thin shell? *Journal of the Mechanics and Physics of Solids*, 56, 2213–2234.
- Pettifor, D. G., & Oleinik, I. I. (1999). Analytic bond-order potentials beyond Tersoff–Brenner. I. Theory. *Physical Review B*, 59, 8487.
- Qian, D., Wagner, G. J., Liu, W. K., Yu, M.-F., & Ruoff, R. S. (2002). Mechanics of carbon nanotubes. *Applied Mechanics Reviews*, 55, 495–533.
- Robertson, D. H., Brenner, D. W., & Mintmire, J. W. (1992). Energetics of nanoscale graphitic tubules. *Physical Review B*, 45, 12592–12595.
- Samsonidze, Ge. G., Samsonidze, G. G., & Yakobson, B. I. (2002). Energetics of Stone–Wales defects in deformations of monoatomic hexagonal layers. *Computational Materials Science*, 23, 62–72.
- Sanders, J. L. (1963). Nonlinear theories for thin shells. *Quarterly of Applied Mathematics*, 21, 21–36.
- Sears, A., & Batra, R. C. (2004). Macroscopic properties of carbon nanotubes from molecular-mechanics simulations. *Physical Review B*, 69, 235406.
- Shi, D. L., Feng, X. Q., Huang, Y., & Hwang, K. C. (2004). Critical evaluation of the stiffening effect of carbon nanotubes in composites. *Key Engineering Materials*, 261, 1487–1492.
- Shi, D. L., Feng, X. Q., Huang, Y., Hwang, K. C., & Gao, H. (2004). The effect of nanotube waviness and agglomeration on the elastic property of carbon nanotube-reinforced composites. *Journal of Engineering Materials and Technology (ASME Transactions)*, 126, 250–257.
- Song, J., Jiang, H., Shi, D. L., Feng, X. Q., Huang, Y., Yu, M. F., et al. (2006). Stone–Wales transformation: Precursor of fracture in carbon nanotubes. *International Journal of Mechanical Sciences*, 48, 1464–1470.
- Srivastava, D., Menon, M., & Cho, K. J. (2001). Computational nanotechnology with carbon nanotubes and fullerenes. *Computational Science and Engineering*, 3, 42–55.
- Tan, H., Jiang, L. Y., Huang, Y., Liu, B., & Hwang, K. C. (2007). The effect of van der Waals-based interface cohesive law on carbon nanotube-reinforced composite materials. *Composites Science and Technology*, 67, 2941–2946.
- Tersoff, J. (1988). New empirical approach for the structure and energy of covalent systems. *Physical Review B*, 37, 6991–7000.
- Timoshenko, S., & Gere, J. (1961). *Theory of elastic stability*. New York: McGraw-Hill.
- Timoshenko, S., & Woinowsky-Krieger, S. (1959). *Theory of plates and shells*. New York: McGraw-Hill.
- Tombler, T. W., Zhou, C. W., Alexseyev, L., Kong, J., Dai, H. J., Lei, L., et al. (2000). Reversible electromechanical characteristics of carbon nanotubes under local-probe manipulation. *Nature*, 405, 769–772.
- Tu, Z., & Ou-Yang, Z. C. (2002). Single-walled and multiwalled carbon nanotubes viewed as elastic tubes with the effective Young's moduli dependent on layer number. *Physical Review B*, 65, 233407.
- Wang, M., Zhang, X., & Lu, M. W. (2005). Nonlinear membrane-spring model for carbon nanotubes. *Physical Review B*, 72, 205403.

- Wang, L., Zheng, Q., Liu, J. Z., & Jiang, Q. (2005). Size dependence of the thin-shell model for carbon nanotubes. *Physical Review Letters*, 95, 105501.
- Wu, J., Hwang, K. C., & Huang, Y. (2008). An atomistic-based finite-deformation shell theory for single-wall carbon nanotubes. *Journal of the Mechanics and Physics of Solids*, 56, 279–292.
- Wu, J., Hwang, K. C., Huang, Y., & Song, J. (2008a). A finite-deformation shell theory for carbon nanotubes based on the interatomic potential. Part I: Basic theory. *Journal of Applied Mechanics*, 75, 061006.
- Wu, J., Hwang, K. C., Huang, Y., & Song, J. (2008b). A finite-deformation shell theory for carbon nanotubes based on the interatomic potential. Part II: Instability analysis. *Journal of Applied Mechanics*, 75, 061007.
- Wu, J., Hwang, K. C., Song, J., & Huang, Y. (2008). Material and structural instabilities of single-wall carbon nanotubes. *Acta Mechanica Sinica*, 24, 285–288.
- Wu, J., Peng, J., Hwang, K. C., Song, J., & Huang, Y. (2008). The intrinsic stiffness of single-wall carbon nanotubes. *Mechanics Research Communications*, 35, 2–9.
- Yakobson, B. I., & Avouris, P. (2001). Mechanical properties of carbon nanotubes. In M. S. Dresselhaus, G. Dresselhaus & P. Avouris (Eds.), *Carbon nanotubes*. Topics in applied physics, Vol. 80 (pp. 287–329). Berlin: Springer-Verlag.
- Yakobson, B. I., Brabec, C. J., & Bernholc, J. (1996). Nanomechanics of carbon tubes: instabilities beyond linear response. *Physical Review Letters*, 76, 2511–2514.
- Yakobson, B. I., Campbell, M. P., Brabec, C. J., & Bernholc, J. (1997). High strain rate fracture and C-chain unraveling in carbon nanotubes. *Computational Materials Science*, 8, 341–348.
- Zhang, P., Huang, Y., Gao, H., & Hwang, K. C. (2002). Fracture nucleation in single-wall carbon nanotubes under tension: A continuum analysis incorporating interatomic potentials. *Journal of Applied Mechanics—Transactions of the ASME*, 69, 454–458.
- Zhang, P., Huang, Y. G., Geubelle, P. H., & Hwang, K. C. (2002). On the continuum modeling of carbon nanotubes. *Acta Mechanica Sinica*, 18, 528–536.
- Zhang, P., Huang, Y., Geubelle, P. H., Klein, P. A., & Hwang, K. C. (2002). The elastic modulus of single-walled carbon nanotubes: A continuum analysis incorporating interatomic potentials. *International Journal of Solids and Structures*, 39, 3893–3906.
- Zhang, P., Jiang, H., Huang, Y., Geubelle, P. H., & Hwang, K. C. (2004). An atomistic-based continuum theory for carbon nanotubes: Analysis of fracture nucleation. *Journal of the Mechanics and Physics of Solids*, 52, 977–998.
- Zhou, W., Huang, Y., Liu, B., Wu, J., Hwang, K. C., & Wei, B. Q. (2007). Adhesion between carbon nanotubes and substrate: Mimicking the Gecko Foothair. *NANO*, 2, 175–179.
- Zhou, X., Zhou, J. J., & Ou-Yang, Z. C. (2000). Strain energy and Young's modulus of single-wall carbon nanotubes calculated from electronic energy-band theory. *Physical Review B*, 62, 13692.

Tensegrity: 60 Years of Art, Science, and Engineering

C. SULTAN

*Aerospace and Ocean Engineering Department, Virginia Polytechnic
Institute and State University, Blacksburg, Virginia 24060, USA*

Abstract	70
1. Introduction	70
2. Tensegrity Origins: The Pioneers.....	71
2.1. The Birth of the Tensegrity Sculpture.....	71
2.2. The Birth of the Tensegrity Concept.....	74
3. From Abstract Art to Abstract Science.....	76
3.1. Kenner and Tensegrity.....	76
3.2. Pioneering Structural Engineering Research in Tensegrity.....	76
3.3. Mathematics Research in Tensegrity Frameworks.....	82
3.4. Pioneering Research in Tensegrity Dynamics.....	83
4. The Blossoming 1990s and Beyond.....	84
5. Advances in Statics Research.....	85
5.1. Form-Finding: The Prestressability Problem.....	85
5.2. Static Response.....	95
6. Advances in Dynamics Research.....	97
6.1. Nonlinear Equations of Motion.....	97
6.2. Damping, Stiffness, and Stability Properties.....	100
6.3. Vibration Properties.....	104
6.4. Clustered Natural Frequencies in Tensegrity Structures.....	106
7. Deploying Tensegrity Structures.....	112
8. Controllable Tensegrity Structures.....	117
8.1. Tensegrity Structures and Control Design.....	117
8.2. Research in Tensegrity Structures Control.....	118
8.3. A Tensegrity Flight Simulator.....	120
9. Tensegrity Structures in Biology.....	125
10. The Future.....	133
11. Challenges for Controllable Tensegrity Structures.....	134
11.1. Servomotors.....	135
11.2. Shape Memory Alloys.....	136
11.3. Electroactive Polymers.....	136
11.4. Piezoactuators and Magnetostrictive Actuators.....	137

12. Conclusions	138
Acknowledgments.....	139
References.....	139

Abstract

This chapter traces down the roots of the first man-made objects which resemble what are nowadays known as tensegrity structures. It then shows how the tensegrity concept evolved, finding increasingly large audience in engineering, mathematics, and biology. The history of tensegrity structures research is presented including references to the most important discoveries and examples of the author's contributions. Some of the current challenges these structures face in the area of practical applications conclude the chapter.

1. Introduction

Sixty years have passed since the first tensegrity *sculpture* originated from Kenneth Snelson's skillful hands ([Snelson, 1965, 1996](#)) and much has happened to the original, toy-like object and the associated tension–integrity concept. The interest in these fascinating sculptures slowly migrated from the intuitive, inspirational world of art into the systematic and rigorous world of science, to recently blossom in applied areas of science and engineering. Nowadays, tensegrity *structures* are emerging as the “structural systems for the future” ([Motro, 2003](#)) and are perceived as potential solutions to many practical problems. In aerospace engineering they are regarded as promising deployable structures ([Sultan & Skelton, 1998b, 2003b](#)), which will enable various applications like adaptive space telescopes ([Sultan, Corless, & Skelton, 1999](#)), flight simulators ([Sultan, Corless, & Skelton, 2000](#)), antennas ([Djouadi, Motro, Pons, & Crosnier, 1998; Knight, Duffy, Crane, & Rooney, 2000; Tibert & Pellegrino, 2002](#)), morphing structures ([Moored & Bart-Smith, 2007](#)), and robots ([Aldrich, Skelton, & Kreutz-Delgado, 2003; Paul, Valero-Cuevas, & Lipson, 2006](#)). In civil engineering, tensegrity structures have a relatively long history, having been proposed for various applications including shelters, domes ([Fuller, 1962; Hanaor, 1992; Marks & Fuller, 1973; Motro, 1990; Pellegrino, 1992](#)), or bridges ([Micheletti, Nicotra, Podio-Guidugli, & Stucchi, 2005](#)). In biology, tensegrity structures enjoy considerable success as models for the structural mechanisms through which cells are organized and function ([Canadas, Laurent, Oddou, Isabey, & Wendling, 2002; Ingber, 1993; Lazopoulos, 2004; Lazopoulos & Lazapoulou, 2005; Stamenovic & Coughlin, 2000; Sultan, Stamenovic, & Ingber, 2004; Volokh, Vilnay, & Belsky, 2000; Wendling, Canadas, & Chabrand, 2003](#)). Mathematical investigation of these structures also led to fundamental discoveries in the theory of rigidity and

stability of frameworks (Connelly & Back, 1998; Connelly & Whiteley, 1992). More recently, tensegrity structures have been proposed for applications in the emerging field of aquaculture (Jensen, Wroldsen, Lader, Fredheim, & Heide, 2007) and as energy-harvesting devices (Scruggs & Skelton, 2006).

This review of the evolution of tensegrity structures from their beginnings in the avant-garde art of the early twentieth century to the science and engineering of the twenty-first century presents the major milestones in tensegrity structures research and the developments around the tensegrity concept. Firstly, the origins of tensegrity structures in the world of abstract art are investigated. Then the evolution of the tensegrity concept is presented, with references to the main research directions and applications. The most important contributions, which led to significant advances, are reviewed and fundamental properties of these structures, as reflected by various researchers, are identified. Examples of some of the author's contributions are included. Lastly, several challenges tensegrity structures research and implementation face are presented, along with considerations regarding their future.

2. Tensegrity Origins: The Pioneers

2.1. THE BIRTH OF THE TENSEGRITY SCULPTURE

The twentieth century was a sublime as well as a tragic adventure of the human spirit. Its beginnings witnessed the birth of a new Europe from the ashes of disintegrating empires, a world in which homogeneity and uniformity was no longer the rule and in which the individual was trying to establish himself as the driving force of the social system he belonged to. This evolution toward a fragmentary, multifaceted society could not pass without influencing and being reflected in the artistic circles. In parallel with the social revolution, the art world experienced its own emancipation, as it migrated from the rigid, well-structured patron system, to a flexible system of autonomous artists living of their own exploits and characterized by an increased freedom of expression. The transition from realism (1850) to impressionism (1874), and then to the fundamental revolution brought along by cubism (1908) is representative for this evolution toward an increased level of *abstractization*. At the turn of the twentieth century Picasso's and Braque's cubism was mirroring the fragmentation of the society, and the avant-garde movement, from which surrealists will later emerge, was flourishing.

In this context *constructivism*, which vaguely refers to the abstract art that emerged from the Russian avant-garde, came along. Constructivist art is geometric, experimental, and reductive, focused on the representation of basic elements

and illustrating forms which are believed to have universal meaning. Examining the well-known tensegrity sculpture of Snelson, the Needle Tower exhibited at the Hirshhorn Museum and Sculpture Garden in Washington, D.C. (Fig. 2.1), one cannot help to notice how this work of art fits the above discussion on constructivism. It is very abstract, geometric, reduced to a set of simple basic elements, bars, and cables. Needless to say that at the time it was built (1968), theoretical investigation of tensegrity structures of this complexity was simply missing. Hence it is purely experimental.

The roots of tensegrity structures were placed in the constructivist art world by [Emmerich \(1988\)](#) and [Motro \(1996\)](#) who pointed out that the first sculpture which resembles a tensegrity structure, a “proto-tensegrity,” was built by a truly constructivist artist, Karl Ioganson, in 1920 and exhibited in Moscow in 1921, under the title of “Study in Balance.” This sculpture, which was reconstituted



FIG. 2.1 The “Needle Tower” built by Kenneth Snelson in 1968.

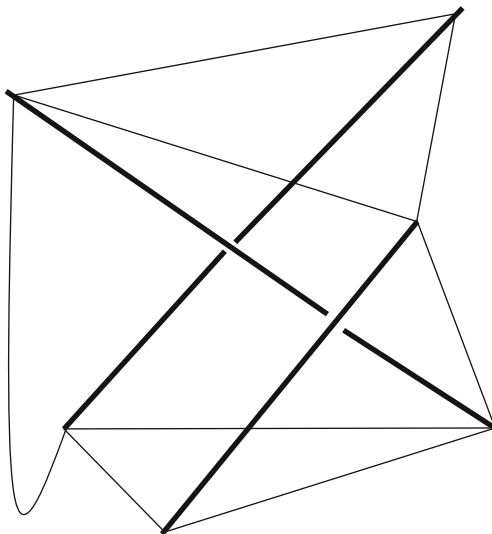


FIG. 2.2 The “proto-tensegrity” sculpture built by Loganson in 1920.

from photographs, consisted of three bars and seven cables and was manipulable through another cable (Fig. 2.2 shows a sketch of the sculpture). Loganson’s sculpture falls short of meeting one of the main requirements for a tensegrity structure: that it yields a *stiff equilibrium configuration under no external force and moment* and with *all cables in tension*. As one can see, external forces must be applied to Loganson’s structure in order to keep it in equilibrium with all cables in tension: the slack cable must be acted upon by an external pull force to put it in tension and give stiffness to the structure. It is not clear (at least to the author of this chapter) if Loganson ever surmounted this difficulty and built a tensegrity sculpture.

The first reported tensegrity sculpture was built in 1948 by Kenneth Snelson who, while studying at the Black Mountain College in North Carolina (Snelson, 1996), succeeded in creating the object shown in Fig. 2.3. This sculpture, a simple unit consisting of two X-shaped bars and 14 cables, is indeed in a stiff equilibrium configuration under no external actions and with all cables in tension. Snelson later defined tensegrity as a closed structural system composed of a set of three or more compression struts within a network of cables in tension, combined in such a way that the struts do not touch one another, but press outwardly against nodal points in the tension network to form a firm, triangulated, prestressed, tension and compression unit (see Sadao, 1996; Snelson, 1996).



FIG. 2.3 The first tensegrity sculpture built by Snelson in 1948.

2.2. THE BIRTH OF THE TENSEGRITY CONCEPT

Snelson's accomplishment caught the attention of R. Buckminster Fuller who saw in Snelson's sculpture the most crystalline representation of the *tension-integrity* principle, which he was mentally experimenting with at the time. This principle states that structural integrity is maintained through the interaction between continuous tension elements and compressive, isolated ones. If Snelson invented the *object*, Fuller was the one to name it, creating the *word* tensegrity. Through this picturesque, yet inspirational denomination, Fuller pointed out that the tension members are crucial in maintaining the structural shape, which explains the acronym tensegrity = tension + integrity, with no room for a single syllable indicating compression.

However, Fuller did not limit his definition to structures, calling tensegrity a structural-relationship *principle*. According to [Sadao \(1996\)](#) for Fuller tensegrity

is nature's grand structural strategy: at the cosmic level Fuller imagined that the “spherical astro-islands of compression of the solar system are continuously controlled in their progressive repositioning in respect to one another by comprehensive tension of the system which Newton called gravity,” whereas at the atomic level he noticed that “man's probing within the atom disclosed the same kind of discontinuous-compression, discontinuous-tension apparently governing the atom's structure.” To make a clear distinction between Fuller's tensegrity principle and Snellen's sculptures, the denomination tensegrity structures is used in reference to all physical objects encountered in engineering, architecture, or biology, which resemble Snellen's sculptures.

Fuller did not invent the object “tensegrity structure.” The credit for doing this definitely goes to Snellen, as several articles published in the International Journal of Space Structures ([Emmerich, 1996](#); [Sadao, 1996](#); [Snellen, 1996](#)) clearly settled the controversy; however, Fuller can rightfully be credited with popularizing the tensegrity concept and object through his inspirational lectures, which used to draw very large and heterogeneous audiences. As it will be shown later, it was due to these lectures that the tensegrity concept transcended from the world of abstract art into the world of abstract science.

Before closing this section, it is important to mention that another pioneer in tensegrity structures was David Georges Emmerich, who in 1958, apparently unaware of Snellen's and Fuller's work, built several tensegrity structures, which he called self-tensioning structures ([Motro, 1992](#)). As he points out in his last publication ([Emmerich, 1996](#)), ironically and appropriately, the event took place while Emmerich was treating his ailing joints affected by arthrosis. Hence, he was definitely for *joints-free structures*, which is one of the major advantages of many tensegrity structures: they can be built with no rigid-to-rigid joints (i.e., no bars in contact). Emmerich acknowledged that tensioned cables are essential in these structures, in agreement with Fuller's tensegrity principle, and limited the discussion to assemblies of cables and rectilinear bars.

In summary, tensegrity structures emerged in the early-mid-twentieth century as an artistic trend, rather than as an attempt to develop load-bearing structures. With respect to these structures practicality the pioneers were assuming totally opposite attitudes: they were either very skeptical (Snellen) or very enthusiastic (Fuller). In the early years of tensegrity structures (1950s–1960s) Fuller, Snellen, and Emmerich used their intuition to point out some of these structures particularities, but except for crude geometrical studies and patent applications ([Fuller, 1962](#); [Snellen, 1965](#)) none of them truly embarked on the rigorous path of systematic research. Surprisingly enough, the person who ushered tensegrity from the world of abstract art into the world of abstract science was the celebrated modernist literary critic of the last century, Hugh Kenner.

3. From Abstract Art to Abstract Science

3.1. KENNER AND TENSEGRITY

The frenzy of the space exploration era of the 1960s created the need for lightweight structures for space construction. In this context Fuller became an adamant advocate for the use of tensegrity structures due to their *flexibility*, potential for *deployment*, and *lightness*. So fascinated was Kenner by Fuller's popularizing lectures, that, while a Professor of Humanities at John Hopkins University, he took time aside from his studies on Ezra Pound and others of the like, to write a book ([Kenner, 1976](#)) in which he initiated the systematic study of tensegrity structures. The book introduces Newtonian analysis into tensegrity structures statics, treating them as diagrams of equilibrated forces, and uses simple geometry to find equilibrium configurations. For example, Kenner uses node equilibrium conditions and symmetry arguments to find the prestressable configuration of the expandable octahedron, thus analytically solving the pre-stressability problem, which consists of finding equilibrium configurations with all cables in tension and under no external force and moment. At the same time, [Pugh \(1976\)](#) wrote a book on practical rules for building simple tensegrity structures. The major merit of these works is that they raised the level of awareness in tensegrity structures and set the stage for the developments to follow.

3.2. PIONEERING STRUCTURAL ENGINEERING RESEARCH IN TENSEGRITY

These developments followed suit very soon. [Calladine \(1978\)](#) of Cambridge University wrote an article pointing out a very interesting fact: configurations of the tensegrity type have been predicted theoretically as far back as in 1864. In his paper "On the Calculation of the Equilibrium and Stiffness of Frames" ([Maxwell, 1864](#)), Maxwell defines a frame as "a system of lines connecting a number of points" and a stiff frame as "one in which the distance between any two points cannot be altered without changing the length of one or more of the connecting lines of the frame." Maxwell's corresponding rule states that a frame having j points requires in general $3j$ lines, excluding the points and lines which belong to a fixed foundation, to render it simply stiff. [Maxwell \(1864\)](#) states that a simply stiff frame is statically determinate, which means that the force in each member of the frame sustaining any arbitrary external loading is uniquely determined from the equations of equilibrium. [Calladine \(1978\)](#) remarks that

some of the tensegrity structures popularized by Fuller have fewer members than are necessary to satisfy Maxwell's rule; hence, they should not be stiff. However, they are not mechanisms either, as one might expect. Maxwell anticipated such exceptions to his rule, stating that when a frame with a smaller number of lines is stiff, certain conditions must be fulfilled, rendering the case of a maximum or minimum value of one or more of its lines. However, the stiffness of the frame is of an inferior order, because a small disturbing force may produce a displacement infinite in comparison to itself. The conditions under which Maxwell's rule is violated also permit at least one state of self-stress (or prestress) in the frame. Thus, tensegrity structures, idealized as pin-jointed frames, can be placed in the class of statically and kinematically indeterminate structures with infinitesimal mechanisms. A frame is kinematically indeterminate if the location of the joints is not uniquely determined by the length of the members, or, equivalently, if the kinematic equations cannot be uniquely solved for the nodal displacements in terms of the member extensions. The terminology “infinitesimal mechanisms” means that the structure can undergo *infinitesimal* change of shape with no change in the length of the members. Calladine (1978) remarks that, in general, the existence of an infinitesimal mechanism in a frame that satisfies Maxwell's rule implies a corresponding state of self-stress and in the absence of prestress the mechanism thus obtained has zero stiffness. Importantly, he points out that the infinitesimal mechanisms of tensegrity structures are stiffened by prestress.

Calladine's analysis was developed using the following equilibrium and kinematic equations:

$$GF_i = F_e, \quad G^T \Delta n = \Delta e, \quad (3.1)$$

where G is the equilibrium matrix, F_i and F_e are vectors of internal and external forces, whereas Δn and Δe are vectors of *small* nodal displacements and structural member extensions, respectively. The static and kinematic determinacy concepts as well as infinitesimal and finite mechanisms and their relation to the equilibrium matrix are illustrated next using these equations and the examples in Fig. 3.1.

Consider the three-dimensional structure shown in Fig. 3.1A, which is composed of three bars, OA , OB , OC such that the joints (A , B , C , O) allow only relative rotational motion but no translation. An orthonormal dextral reference frame, $Oxyz$, is introduced, with origin at the common joint, O (for simplicity the Oz -axis is not shown). The coordinates of the nodal points in this reference frame are indicated in the figure. The equilibrium matrix is

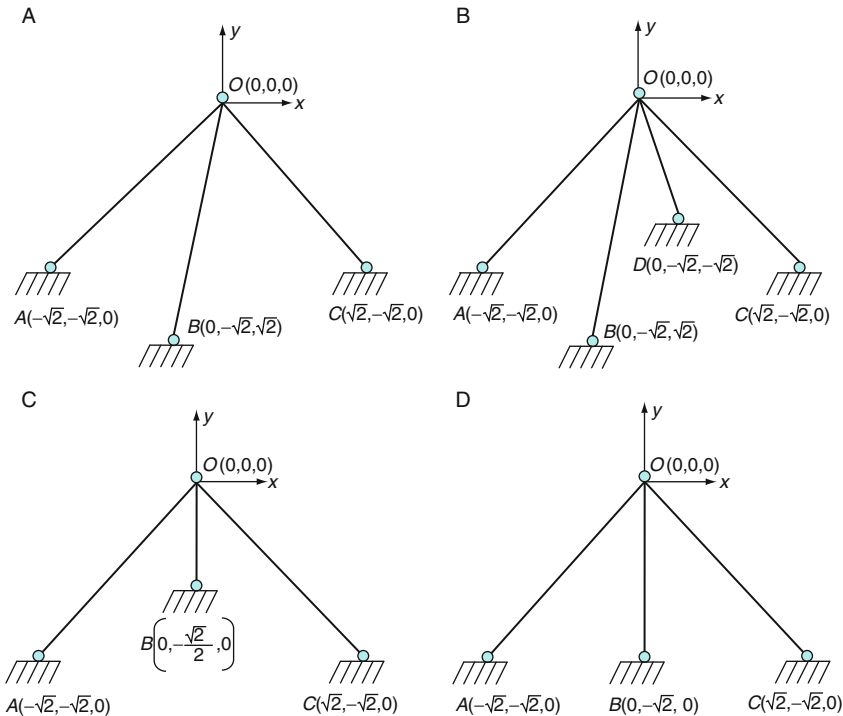


FIG. 3.1 Illustration of static and kinematic indeterminacy. (A) Statically and kinematically determined structure. (B) Statically indetermined and kinematically determined structure. (C) Statically and kinematically indetermined structure with an infinitesimal mechanism. (D) Statically and kinematically indetermined structure with a finite mechanism.

$$G = \begin{bmatrix} -\frac{\sqrt{2}}{2} & 0 & \frac{\sqrt{2}}{2} \\ -\frac{\sqrt{2}}{2} & -\frac{\sqrt{2}}{2} & -\frac{\sqrt{2}}{2} \\ 0 & \frac{\sqrt{2}}{2} & 0 \end{bmatrix} \quad (3.2)$$

and the structure is clearly statically and kinematically determined because G is invertible. If an extra bar (OD) is added, as shown in Fig. 3.1B, the equilibrium matrix becomes

$$G = \begin{bmatrix} -\frac{\sqrt{2}}{2} & 0 & \frac{\sqrt{2}}{2} & 0 \\ -\frac{\sqrt{2}}{2} & -\frac{\sqrt{2}}{2} & -\frac{\sqrt{2}}{2} & -\frac{\sqrt{2}}{2} \\ 0 & \frac{\sqrt{2}}{2} & 0 & -\frac{\sqrt{2}}{2} \end{bmatrix}. \quad (3.3)$$

Now, the rank of G is three but the structure is statically indeterminate because the internal force vector, F_i , can be completely determined only up to an arbitrary, multiplicative scalar. The structure is prestressable and has a single state of self-stress (or prestress), represented by this multiplicative scalar. The structure is kinematically determined because G^T has rank three and the kinematic equations can be uniquely solved for Δn . However, the components of Δe cannot be specified independently because G^T has an extra row. Consider now the structures shown in Fig. 3.1C and D, in which, unlike in Fig. 3.1A, all bars are in the same plane. Additionally, in Fig. 3.1D the fixed end points (A , B , and C) are collinear. The equilibrium matrix is the same for these two structures:

$$G = \begin{bmatrix} -\frac{\sqrt{2}}{2} & 0 & \frac{\sqrt{2}}{2} \\ -\frac{\sqrt{2}}{2} & -1 & -\frac{\sqrt{2}}{2} \\ 0 & 0 & 0 \end{bmatrix}. \quad (3.4)$$

Both frames satisfy Maxwell's rule, are statically and kinematically indeterminate, and, because the rank of G is two, allow for one state of prestress and one inextensional mechanism. However, their kinematic behavior is *quantitatively* different: the structure in Fig. 3.1C has an *infinitesimal* mechanism whereas the one in Fig. 3.1D has a *finite* mechanism. Indeed, for the structure in Fig. 3.1C, if the common joint (O) moves *slightly* in the direction perpendicular to the plane of the bars (OAC), the bars exhibit changes in their lengths that are of higher order in terms of the displacement of the joint O . On the other hand, for the structure in Fig. 3.1D, the joint O can experience *large* movement without any variation in the lengths of the bars. The difference between the two mechanisms can be easily understood and visualized by considering the circle obtained by intersecting the two spheres centered at A and C and of radii equal to $AO = CO$. For the structure in Fig. 3.1D this circle belongs to the sphere centered at B and of radius equal to the middle bar length, BO , and the middle bar does not prohibit large movement

of the common joint, O , along this circle. Thus, a finite mechanism is obtained. On the other hand, in Fig. 3.1C the aforementioned circle is just tangent to the sphere centered at B and of radius BO . Thus only infinitesimal displacements can be tolerated and only an infinitesimal mechanism exists. Clearly, this example indicates a major limitation of an analysis that uses only the equilibrium matrix in Eq. (3.1): one cannot distinguish between finite and infinitesimal mechanisms.

Calladine's pioneering work was continued by Pellegrino, Tarnai, and Hanaor who investigated tensegrity structures along the same lines, as members of the class of pin-jointed frames. Tarnai (1980) discovered geometries which result in static and kinematic indeterminacy of certain pin-jointed cylindrical truss structures by enforcing the condition that the determinant of the equilibrium matrix is zero. Some of these structures have infinitesimal mechanisms whereas others have finite mechanisms. Through further analysis of the kernel of the equilibrium matrix for the structures with infinitesimal mechanisms he indicates which members can be replaced by cables in a given equilibrium configuration, namely those members that are in tension. This method can be used to discover tensegrity structures and to find analytical solutions to the prestressability problem. Pellegrino and Calladine (1986) developed matrix-based methods that can be used for the segregation of the inextensional deformation modes of a pin-jointed frame into rigid body modes and internal mechanisms, and for detecting when a state of self-stress imparts first-order stiffness to an inextensional mode of deformation. The two authors perfected the method of segregating first-order mechanisms from higher-order mechanisms, including finite ones (Calladine & Pellegrino, 1991). The analysis requires the computation of N_s quadratic forms in N_m variables, where N_s is the number of independent states of self-stress (or prestress) and N_m is the number of independent mechanisms. If any linear combination of these quadratic forms is sign definite the mechanisms are first-order infinitesimal. The connections between mechanisms, prestressability, stiffness, geometry, and stability have been further explored by other researchers (e.g., Guest & Fowler, 2007; Murakami, 2001b; Schenk, Guest, & Herder, 2007; Vassart, Laporte, & Motro, 2000).

Working along similar lines, Hanaor (1988) presented a classification of pin-jointed skeletal structures composed of bars and cables, which is summarized in Fig. 3.2. He identifies two major subclasses, of “not prestressable” and “prestressable” structures. The “not prestressable” subclass contains statically determinate structures and mechanisms whereas the “prestressable” subclass has two branches. The first branch contains statically indeterminate and kinematically determinate structures. In such a structure prestress is achieved by means of lack of fit (e.g., Fig. 3.1B). The second branch contains statically and kinematically

Pin-jointed			
Not prestressable		Prestressable	
Statically determinate	Mechanisms	Statically indeterminate kinematically determinate	Statically indeterminate kinematically indeterminate Tensegrity

FIG. 3.2 Classification of pin-jointed structures according to Hanaor (1988).

indeterminate structures with infinitesimal mechanisms that depend on prestress for their geometric integrity (e.g., Fig. 3.1C). This is where Hanaor places tensegrity structures, idealized as pin-jointed frames. In his initial work, Hanaor (1988) considers that the bars in a tensegrity structure are discontinuous (i.e., there are no rigid-to-rigid articulated joints), but in a later paper devoted to form-finding and static load response of double layer tensegrity domes (Hanaor, 1992), he remarks that the generalization of the tensegrity concept might include bars connected at the joints.

Several features are common to the work of the aforementioned pioneers in structural analysis of tensegrity. Firstly, tensegrity structures are treated as particular instantiations of *pin-jointed frames*. Secondly, the analysis is limited by the *small displacement* and *geometrically linear* behavior assumption underlying Eq. (3.1). The shortcomings of such an analysis were well known at the time the first scientific articles on structural analysis of tensegrity structures were published (see, e.g., Besseling, Ernst, Van der Werff, De Koning, & Riks, 1979). Thirdly, the methods and tools used to carry out the analysis are from *linear algebra*. Last but not least, the focus of the analysis is the *statics* of tensegrity structures and static applications only (e.g., domes) are investigated.

At this point, it is worth to remark that, based on Maxwell's observation that the maximum or minimum value of one or more of the frame's members is attained at equilibrium, Pellegrino (1986) developed a numerical approach aimed at finding prestressable configurations of tensegrity structures. He reduced this problem to solving a constrained minimization problem, and illustrated it on two tensegrity configurations, the triangular prism and the truncated tetrahedron. Unfortunately, as noticed by the author, such an approach is not feasible for more complex structures because the number of constraints increases dramatically with the number of members.

3.3. MATHEMATICS RESEARCH IN TENSEGRITY FRAMEWORKS

The early 1980s represented another major step forward in tensegrity structures research, as these fascinating structures caught the attention of several mathematicians like Connelly, Roth, and Whiteley (Connelly, 1980; Roth & Whiteley, 1981). Inspired by Snelson's tensegrity structures, these researchers extended the concept to a class of mathematical objects which they called "tensegrity frameworks." In their studies, a tensegrity framework is an ordered finite collection of points in the Euclidean space, with certain pairs of these points, called cables, constrained not to get farther apart, certain pairs, called struts, constrained not to get closer together, and certain pairs, called bars, constrained to stay the same distance apart (Roth & Whiteley, 1981). The concept of tensegrity frameworks includes only rectilinear, one-dimensional members such as bars, struts, and cables. However, it allows for bars in contact at a vertex through articulations that permit relative rotations between the bars, as well as for frameworks composed only of cables (e.g., spider web-like networks).

Mathematics research in tensegrity frameworks led to important results in the general theory of rigidity and stability of frameworks. Several notions like *first- and second-order rigidity*, *prestress stability*, and *rigidity* were introduced and rigorously analyzed (see Connelly, 1982; Connelly & Whiteley, 1996; Roth & Whiteley, 1981). Thus, a framework is:

- first-order rigid (or infinitesimally rigid) if the only smooth motion of the vertices for which the first time derivative of each member length is consistent with the constraints has its derivative at time zero equal to that of the restriction of a congruent motion of the Euclidean space;
- second-order rigid if every smooth motion of the vertices that does not violate any member constraint in the first and second derivative has its first derivative trivial (i.e., its first derivative is the derivative of a one parameter family of congruent motions);
- prestress stable if it has a proper strict self-stress such that a certain energy function, defined in terms of the stress and defined for all configurations, has a local minimum at the given configuration, which is a *strict* local minimum up to congruence of the whole framework. Note that in this context a proper strict self-stress means that the stress in each cable is positive and the strut stresses are negative, with no condition on the bars;
- rigid if each continuous motion of the points satisfying all the constraints is the restriction of a rigid motion of the ambient Euclidean space.

An important result derived by Connelly and Whiteley (1996) and illustrated in Fig. 3.3 is a hierarchical classification of frameworks with respect to rigidity

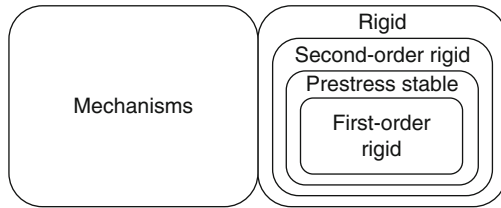


FIG. 3.3 Classification of frameworks with respect to rigidity properties (Connelly & Whiteley, 1996).

properties as follows: first-order rigidity implies prestress stability, which implies second-order rigidity, which at its turn implies rigidity, with none of these implications being reversible.

Later, Connelly and coworkers introduced the concept of a *superstable* tensegrity framework as a framework for which any comparable configuration (i.e., a configuration with the same number of vertices and connected by struts and cables in the same way) either violates one of the distance constraints or is congruent to the original framework (Connelly & Back, 1998). Superstability implies prestress stability, but it does not imply first-order rigidity. However, increasing prestress stiffens a superstable structure. The interested reader is referred to [Connelly and Back \(1998\)](#) for details and numerous examples.

The methods used to investigate tensegrity frameworks involve graph theory and energy functions (e.g., quadratic forms). Researchers relied heavily on group and representation theory that led to a complete catalogue of prestressable configurations of tensegrity frameworks with prescribed symmetries, which is one of their most important discoveries (Connelly & Back, 1998). One key characteristic of the models used in the analysis of tensegrity frameworks is that they are simplified (e.g., geometry-based models) such that they allow proving theorems and drawing general conclusions. For example, damping is not considered in the analysis and neither is the dynamics of these structures investigated.

3.4. PIONEERING RESEARCH IN TENSEGRITY DYNAMICS

As remarked shortly after their invention, apart from their ethereal appearance, tensegrity structures display an amazing flexibility, being *capable of large displacement*. This particularity makes them ideal for dynamical applications, which require that the structures experience significant change in their geometry, like robotic manipulators, deployable structures, or morphing structures. Moreover, it unmistakably differentiates tensegrity structures from most classical

structures, which are intended for operation in static conditions and designed accordingly. A structure intended for dynamical applications should be designed to meet dynamic specifications related, for example, to the time of response, overshoot, natural frequencies, and damping ratio.

A critical enabler for dynamic design of tensegrity structures is the dynamics research pioneered at the University of Montpellier, by Rene Motro. In the mid-1980s, Motro made a big step forward in tensegrity structures research by setting up a laboratory aimed at conducting both theoretical and experimental studies. In a paper published in 1986 ([Motro, Najari, & Jouanna, 1986](#)), Motro and coworkers reported experimental results on the dynamics of a tensegrity structure composed of three bars and nine cables. Moreover, experimentally obtained frequency response measurements were used along with analytical tools from harmonic analysis to identify linear models of this structure's dynamics. In [Motro et al. \(1986\)](#), nonlinear static experimental results were also published for the first time. The importance of this work cannot be overestimated because it shifted the focus from linear statics to nonlinear statics and dynamics research. The former is appropriate for structures that experience only small deformations and operate in static conditions, whereas the latter is what is necessary for structures that are capable of large deformations and intended to operate in dynamic conditions, like tensegrity.

At about the same time, [Motro \(1984\)](#) initiated numerical form-finding for tensegrity structures using the dynamical relaxation method. The key idea is that, for a structure acted upon by external forces, the equilibrium can be found by integrating the fictitious equations:

$$M\Delta\ddot{n} + C\Delta\dot{n} + K\Delta n = F_e, \quad (3.5)$$

where M is a mass matrix, C a damping matrix, K a stiffness matrix, F_e the vector of external forces, and Δn , $\Delta\dot{n}$, $\Delta\ddot{n}$ are the vectors of displacement, velocity, and acceleration, respectively. These equations are integrated until convergence to an equilibrium is obtained. [Motro \(1984\)](#) applied this method to find prestressable configurations of the triangular tensegrity prism. As it will be discussed later, the relaxation method experiences a very recent revival process because of its potential to find irregular (i.e., highly nonsymmetric) equilibrium shapes.

4. The Blossoming 1990s and Beyond

The pioneering contributions of the 1970s and 1980s in the linear and nonlinear statics, dynamics, and experimental analysis of tensegrity structures set the stage for the impressive, multidisciplinary developments to follow during the 1990s and 2000s. The last 15 years witnessed extraordinary growth and diversification in tensegrity structures research.

There are several reasons for this evolution. First and foremost, there was the acknowledgment that these structures might not be only objects of passive contemplation, but they might actually provide solutions to a variety of practical problems. Tensegrity structures were initially met with skepticism because they were looked upon mostly as static structures and as solutions to the old problem of mankind of providing shelter. Yet, there were already better solutions to this problem. As soon as the necessity to develop *dynamical structures capable of large displacement* was brought into light by the space exploration era, the interest in tensegrity structures increased considerably. A growing market for applications never encountered before, like deployable space antennas for satellites, adaptive space telescopes, robotic manipulators for future space stations, morphing structures was emerging, and tensegrity structures came across as prime candidate solutions.

Apart from these “market”-related considerations, there were computational and technological advances that facilitated substantial progress in tensegrity structures research. The 1980s and 1990s witnessed unprecedented improvement in computational capabilities, both at the algorithm development and at the hardware level (i.e., more powerful computers). The advances were not only in the development of reliable numerical tools but, even more importantly, in symbolical computational programs (Maple, Mathematica), which were employed in automated mathematical modeling, as well as in finding closed form solutions to a variety of problems (Sultan, 1999; Sultan, Corless, & Skelton, 2001; Sultan & Skelton, 2003a). As a consequence, sophisticated and closer to reality models were developed and used in the design and analysis of tensegrity structures of complexity never imagined before. On the technological side, advances in signal processing and microprocessors made real-time, online computation a reality, whereas embedded optic fibers became feasible solutions for sensing mechanisms in tensegrity structures (Sultan & Skelton, 1998a, 2004). Advances in miniature, energy efficient actuators like brushless servomotors, shape memory alloys, as well as electroactive polymers, turned these devices into potential solutions for tensegrity structures actuation. All these developments took tensegrity research to the next level and fully integrated, controllable tensegrity structures, moved closer to reality.

5. Advances in Statics Research

5.1. FORM-FINDING: THE PRESTRESSABILITY PROBLEM

As previously mentioned, the crucial issue in tensegrity statics is the *prestressability problem*, which consists of finding equilibrium configurations with all cables in tension when no external force and moment act on the structure. The first approaches to solving the prestressability problem were analytical,

researchers being interested in finding closed form solutions. As mentioned before, [Kenner \(1976\)](#) and [Tarnai \(1980\)](#) were able to find analytical solutions for simple symmetric geometries, while [Connelly and Back \(1998\)](#) subsequently managed to generate a catalogue of symmetric tensegrity frameworks.

In an attempt at generalization, [Sultan \(1999\)](#) formulated the prestressability problem for an arbitrary tensegrity structure composed of E elastic cables and R rigid bodies in which the joints are affected by kinetic friction and the cables are affected by kinetic damping. Kinetic friction means that the friction moment/force at a joint is zero when the relative angular/linear velocity between the members in contact is zero and kinetic damping means that the cable damping force is zero when the time derivative of its elongation is zero.

All external actions, including those due to external force fields (e.g., gravity), are neglected and the virtual work principle provides the prestressability conditions as a set of nonlinear equations *and* inequalities:

$$A(q)T = 0, \quad T_j > 0, \quad (5.1)$$

where $A_{ij} = \partial l_j / \partial q_i$, $i = 1, \dots, N$, $j = 1, \dots, E$, l_j is the length of cable j , T_j is the force in cable j , and q_i is the i th independent generalized coordinate. It is important to remark that $A(q)$ depends only on the generalized coordinates used to describe the structure's configuration and that the inequalities on the cable forces are essential since they enforce the condition that all cables are in tension. In addition, [Eq. \(5.1\)](#) can be directly used for assemblies including three-dimensional rigid bodies (see [Sultan, 1999](#); [Sultan et al., 2001](#) for details).

Note that the link between the equilibrium matrix, G , in [Eq. \(3.1\)](#) and $A(q)$ in [Eq. \(5.1\)](#) can be easily derived using the relations between the coordinates of the nodal points (joints) and the generalized coordinates, q_i , $i = 1, \dots, N$. However, in [Eq. \(5.1\)](#) only the elastic cables are considered; the rigid members (e.g., bars) are not included. Hence, by solving [Eq. \(5.1\)](#), one will obtain the values of the generalized coordinates and the cable forces at a prestressable configuration. The internal forces acting on the rigid members can be obtained by adequate postprocessing of the force balance equations as shown, for example, in [Sultan et al. \(2001\)](#). The formulation of the prestressability conditions, [Eq. \(5.1\)](#), adds to the complexity of the statics problem since nonlinear equalities *and* inequalities must simultaneously be solved for.

If $N < E$ the kernel of $A(q)$ is guaranteed to be nonzero, otherwise the necessary and sufficient condition for [Eq. \(5.1\)](#) to have nonzero solutions is

$$\det(A^T(q)A(q)) = 0, \text{ if } N > E, \quad \text{or} \quad \det(A(q)) = 0, \text{ if } N = E. \quad (5.2)$$

However, [Eq. \(5.2\)](#) guarantees only the existence of nonzero solutions of $A(q)T = 0$. Further analysis of the kernel of $A(q)$ at a solution of [Eq. \(5.2\)](#) must be

performed to find the conditions under which the cable forces are all positive such that the cables are in tension.

An important research goal is to solve the prestressability problem, Eq. (5.1), for a *continuous set* of solutions, called an *equilibrium manifold*, rather than for isolated solutions. As it will be shown later, such a manifold can be used to reliably deploy tensegrity structures. To solve Eq. (5.1) for an equilibrium manifold a methodology has been developed that uses numeric and symbolic computation (see Sultan, 1999; Sultan & Skelton, 2003a; Sultan et al., 2001). The key idea is to parameterize the class of configurations of interest using a small number of parameters, such that significantly simpler conditions are obtained that can be solved analytically, or numerically very easily. Usage of symmetries is of the essence in this methodology, as it will be clear from the next example.

Consider the two-stage “SVD” tensegrity structure depicted in Fig. 5.1. Note that this representative structure and some of its derivatives will be used throughout this chapter to illustrate important results and fundamental properties of tensegrity structures. The structure consists of a top ($B_{12}B_{22}B_{32}$), three bars ($A_{12}B_{12}$, $A_{22}B_{22}$, $A_{32}B_{32}$) attached to the top, three bars ($A_{11}B_{11}$, $A_{21}B_{21}$, $A_{31}B_{31}$) attached to a base ($A_{11}A_{21}A_{31}$), and 18 cables as follows: $B_{i1}A_{j2}$ are referred to as “Saddle” cables, $A_{j1}B_{i1}$ and $A_{j2}B_{i2}$ as “Vertical” cables, and $A_{j1}A_{i2}$ and $B_{j1}B_{i2}$ as “Diagonal” cables (hence the “SVD” denomination). Stage j is composed of bars with the second index j ; for example, stage 2 contains bars $A_{12}B_{12}$, $A_{22}B_{22}$, $A_{32}B_{32}$. Triangles $A_{11}A_{21}A_{31}$ and $B_{12}B_{22}B_{32}$ are congruent

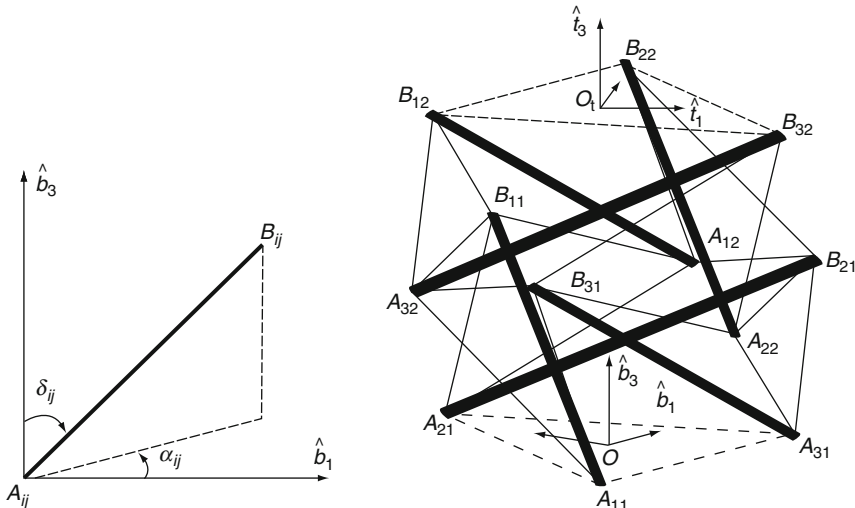


FIG. 5.1 Two-stage SVD tensegrity structure.

equilateral triangles of side length b . The bars are all identical, of length l , and are attached to the top and base via spherical joints, which allow only rotational motion. For the formulation of the prestressability conditions the cables are labeled as follows:

$$\begin{aligned} 1 &= A_{11}A_{32}, 2 = A_{11}B_{31}, 3 = A_{21}A_{12}, 4 = A_{21}B_{11}, 5 = A_{31}A_{22}, \\ 6 &= A_{31}B_{21}, 7 = A_{12}B_{21}, 8 = A_{12}B_{11}, 9 = A_{22}B_{31}, 10 = A_{22}B_{21}, \\ 11 &= A_{32}B_{11}, 12 = A_{32}B_{31}, 13 = A_{32}B_{12}, 14 = B_{11}B_{12}, 15 = A_{12}B_{22}, \\ 16 &= B_{21}B_{22}, 17 = A_{22}B_{32}, 18 = B_{31}B_{32}. \end{aligned} \quad (5.3)$$

The assumptions made for mathematical modeling are: the top and the base are rigid bodies, the bars are rigid and for each bar the rotational degree of freedom around the longitudinal axis, $A_{ij}B_{ij}$, is neglected. The last assumption is frequently used in preliminary analysis of structures and it can be justified, for example, if the thickness of the bar is negligible, or if the attachments of the bar to the top, base, and cables are such that no torsion moment on the bar is generated. Lastly, the joints and cables may be affected by kinetic friction and damping, respectively.

Two orthonormal dextral reference frames are introduced as shown in Fig. 5.1: a base frame, $\hat{b}_1, \hat{b}_2, \hat{b}_3$, which is assumed inertial and whose origin coincides with O , the center of triangle $A_{11}A_{21}A_{31}$, with \hat{b}_1 parallel to $A_{11}A_{31}$ and \hat{b}_3 perpendicular onto $A_{11}A_{21}A_{31}$, and a top reference frame, $\hat{t}_1, \hat{t}_2, \hat{t}_3$, with origin at O_t , the center of triangle $B_{12}B_{22}B_{32}$, such that \hat{t}_1 is parallel to $B_{12}B_{32}$ and \hat{t}_3 is perpendicular onto $B_{12}B_{22}B_{32}$. The independent generalized coordinates necessary to describe the configuration of the system are: the Euler angles for a 3–1–2 sequence, ψ, ϕ, θ , which characterize the orientation of the top reference frame with respect to the inertial frame, the inertial Cartesian coordinates, X, Y, Z , of O_t , and for each bar, $A_{ij}B_{ij}$, two angles, the declination, δ_{ij} , and the azimuth, α_{ij} , defined as follows. The declination is the angle made by $A_{ij}B_{ij}$ with \hat{b}_3 and the azimuth is the angle made by the projection of $A_{ij}B_{ij}$ onto $A_{11}A_{21}A_{31}$ with \hat{b}_1 (see Fig. 5.1). Thus, the vector of generalized coordinates is

$$q = [\delta_{11} \alpha_{11} \delta_{21} \alpha_{21} \delta_{31} \alpha_{31} \delta_{12} \alpha_{12} \delta_{22} \alpha_{22} \delta_{32} \alpha_{32} \psi \phi \theta X Y Z]^T. \quad (5.4)$$

After the generalized coordinates have been selected, symbolic computational software (Maple) is used for the derivation of matrix $A(q)$ in Eq. (5.1). Then, a class of configurations of interest is defined and its geometry parameterized using substantially fewer quantities than the number of generalized coordinates. At this point, introduction of geometric symmetries is crucial to simplify the prestressability conditions given by Eq. (5.1). For example, for the two-stage SVD structure, the class of “symmetrical configurations” is defined as follows: all bars

have the same declination, let it be called δ , the vertical projections of A_{i2}, B_{i1} , onto the base make a regular hexagon, and planes $A_{11}A_{21}A_{31}$ and $B_{12}B_{22}B_{32}$ are parallel. A typical symmetrical configuration is depicted in Fig. 5.2.

The geometry of symmetrical configurations is completely parameterized by only three independent quantities: α , the azimuth of bar $A_{11}B_{11}$, δ , and h , the overlap, defined as the distance between $B_{11}B_{21}B_{31}$ and $A_{12}A_{22}A_{32}$ and considered

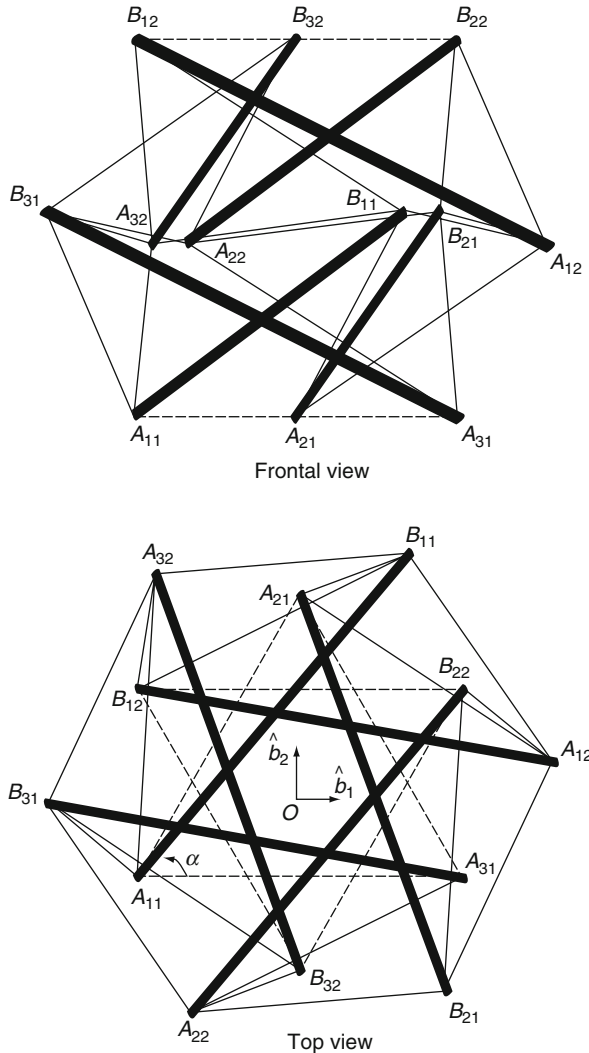


FIG. 5.2 Symmetrical configuration of a two-stage SVD tensegrity structure.

positive if the distance between $B_{11}B_{21}B_{31}$ and $A_{11}A_{21}A_{31}$ is greater than the distance between $A_{12}A_{22}A_{32}$ and $A_{11}A_{21}A_{31}$. The generalized coordinates corresponding to symmetrical configurations are easily expressed as $q = q(\alpha, \delta, h)$ and substituted into the general prestressability conditions given by Eq. (5.1) to obtain a simpler set of conditions:

$$A(\alpha, \delta, h)T = 0, \quad T_j > 0, j = 1, \dots, 18. \quad (5.5)$$

These conditions, even though much simpler than those directly obtained from Eq. (5.1), cannot be solved analytically and a numerical procedure must be used to find solutions. Since $N = E$, that is, $A(\alpha, \delta, h)$ is square, the condition for Eq. (5.5) to have nonzero solutions is $\det(A(\alpha, \delta, h)) = 0$. This is a polynomial equation in h , which is easily solved numerically after l , b , α , and δ have been fixed. After a solution of this equation for h is found, the kernel of the corresponding matrix $A(\alpha, \delta, h)$ is computed. If all the elements of this kernel can be simultaneously positive, a solution to the prestressability conditions has been found, otherwise the search must continue. More importantly, the structure of this kernel reveals a certain pattern in the distribution of cable forces due to the geometrical symmetries. For symmetrical configurations of the two-stage SVD structure, this pattern is characterized as follows: the tensions in all saddle, vertical, and diagonal cables are, respectively, the same, let them be called T_S , T_V , and T_D (see Sultan et al., 2001 for details). At the next step, a continuation principle is applied: if a solution to Eq. (5.5) has been found which displays such a pattern for the internal forces, then it is expected that this pattern is preserved in a neighborhood of the solution. As a consequence, the vector T is assumed to have the corresponding structure, which, for the example considered here, is

$$T = [T_D \ T_V \ T_D \ T_V \ T_D \ T_V \ T_S \ T_S \ T_S \ T_S \ T_S \ T_S \ T_V \ T_D \ T_V \ T_D \ T_V \ T_D]^T. \quad (5.6)$$

This formula for T is substituted *symbolically* into the prestressability conditions given by Eq. (5.5) and a smaller set of conditions is generated. This procedure leads to tremendous reduction of the size of the problem: for the two-stage SVD structure, from the original 18 nonlinear equations and 18 inequalities given by the general prestressability conditions of Eq. (5.1), down to a set of three equations and three inequalities. For this smaller set of conditions closed form solutions have been found, leading to the following result (see Sultan et al., 2001).

Theorem. For fixed $\alpha \in [0, 2\pi)$ and $\delta \in (0, \pi/2)$ the two-stage SVD tensegrity structure yields at most one symmetrical prestressable configuration for which the tensions in the saddle, vertical, and diagonal cables are, respectively, equal. Necessary and sufficient conditions for such a configuration to occur are given by

$$\frac{\pi}{6} < \alpha < \frac{\pi}{2}, \quad 0 < \delta < \frac{\pi}{2}, \quad l \left| \cos\left(\alpha + \frac{\pi}{6}\right) \right| \sin(\delta) < \frac{b}{2\sqrt{3}}, \quad (5.7)$$

and $\sin\left(\alpha + \frac{\pi}{6}\right) < \frac{3l \sin(\delta)}{2b}$.

The value of the corresponding overlap for such a configuration is given by

$$h = \begin{cases} \frac{\cos(\delta)}{2\gamma} \left(l\gamma + \sqrt{\frac{b^2}{3} - 3l^2\gamma^2} \right) - \frac{b}{\sqrt{3}} & \text{if } \alpha \neq \frac{\pi}{3}, \\ \frac{l \cos(\delta)}{2} & \text{if } \alpha = \frac{\pi}{3}, \end{cases} \quad (5.8)$$

where $\gamma = \sin(\delta) \cos(\alpha + (\pi/6))$. At such a configuration the rank of $A(\alpha, \delta, h)$ is 17 and only one state of prestress exists, the tensions being given by

$$[T_S \ T_V \ T_D] = P[T_{0S} \ T_{0V} \ T_{0D}]. \quad (5.9)$$

Here, P is an arbitrary positive scalar called the pretension coefficient and

$$[T_{0S} \ T_{0V} \ T_{0D}] = \frac{1}{\sqrt{6}} \frac{[T_S^r \ T_V^r \ T_D^r]}{\|[T_S^r \ T_V^r \ T_D^r]\|}, \quad (5.10)$$

where

$$T_S^r = \begin{cases} \frac{S}{D} \left(\frac{l \cos(\delta)}{h} - 1 \right) & \text{if } \alpha \neq \frac{\pi}{3}, \\ 1 & \text{if } \alpha = \frac{\pi}{3}, \end{cases} \quad (5.11)$$

$$T_V^r = \begin{cases} \frac{V}{D} \frac{1}{\sqrt{3} \cos\left(\alpha + \frac{\pi}{6}\right)} \left(\frac{l \cos(\delta)}{h} - 1 \right) \left(\sin\left(\alpha - \frac{\pi}{6}\right) - \cos(\alpha) \right) & \text{if } \alpha \neq \frac{\pi}{3}, \\ \frac{V}{D} \left(\frac{3l}{2b} \sin(\delta) - 1 \right) & \text{if } \alpha = \frac{\pi}{3}, \end{cases} \quad (5.12)$$

$$T_D^r = 1. \quad (5.13)$$

In the above, $\|\cdot\|$ denotes the Euclidean norm of a vector and S , V , and D are the lengths of the saddle, vertical, and diagonal cables at a symmetrical configuration, being given by

$$S = \sqrt{h^2 + \frac{b^2}{3} + l^2 \sin^2(\delta) - \frac{2}{\sqrt{3}} lb \sin(\delta) \cos\left(\alpha - \frac{\pi}{6}\right)}, \quad (5.14)$$

$$V = \sqrt{b^2 + l^2 - 2lb \sin(\delta) \sin\left(\alpha + \frac{\pi}{6}\right)}, \quad (5.15)$$

$$D = \sqrt{h^2 + \frac{b^2}{3} + l^2 - \frac{2}{\sqrt{3}} lb \sin(\delta) \sin(\alpha) - 2lh \cos(\delta)}. \quad (5.16)$$

The cable rest lengths corresponding to these equilibrium configurations will be further referred to as the “equilibrium controls” and can be easily computed in terms of the pretension coefficient, P , using the constitutive laws of the cables. For example, if the cables are linearly elastic, the force in cable j is

$$T_j = k_j \frac{l_j - l_{0j}}{l_{0j}}, \quad j = 1, \dots, 18, \quad (5.17)$$

where k_j is the cable’s stiffness, which here is defined as the product between the cross-section area and Young’s modulus, and l_{0j} its rest length. Then the equilibrium controls can be computed as

$$S_0 = \frac{k_S S}{P T_{0S} + k_S}, \quad V_0 = \frac{k_V V}{P T_{0V} + k_V}, \quad D_0 = \frac{k_D D}{P T_{0D} + k_D}. \quad (5.18)$$

Here, S_0 , V_0 , and D_0 denote the rest lengths of the saddle, vertical, and diagonal cables, respectively.

For $l = 4$ m and $b = 0.27$ m, the set of solutions given by Eqs. (5.7) and (5.8), that is, the “equilibrium manifold,” is represented in the three-dimensional space of α , δ , and h by the surface shown in Fig. 5.3. On this surface two curves are depicted, corresponding to configurations for which all the nodal points, A_{ij} , B_{ij} , $i = 1, 2$, $j = 1, 2$, lie on the surface of a sphere or a cylinder.

In Sultan et al. (2001) several tensegrity structures derived from the two-stage SVD type were analyzed as follows: the two-stage SVDT type obtained by

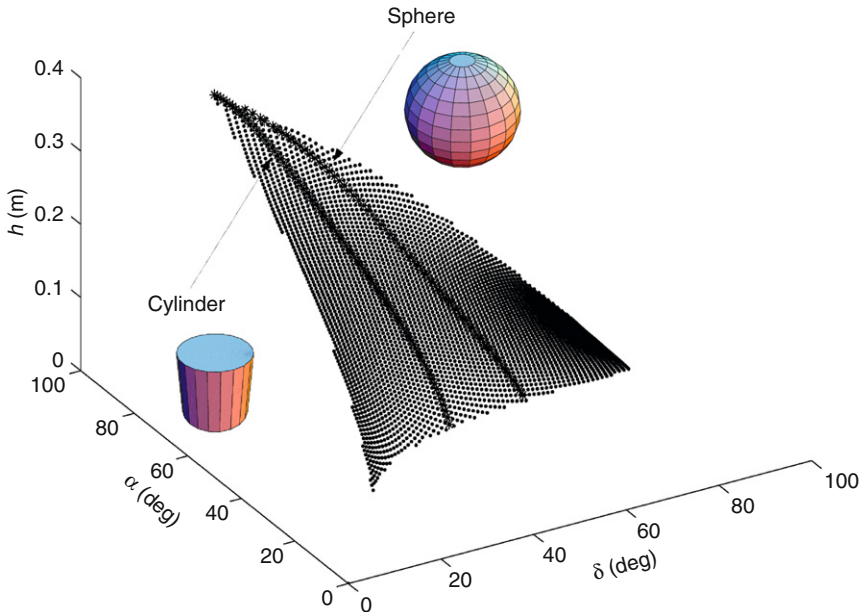


FIG. 5.3 Equilibrium manifold for the two-stage SVD structure.

replacing the rigid top with three “Top” elastic cables, $B_{12}B_{22}$, $B_{22}B_{32}$, $B_{12}B_{32}$, the SVDB type, obtained by replacing the “Base” and “Top” with six cables, the SD, SDB, SDT types obtained from the SVD, SVDB, SVDT types, respectively, by eliminating the vertical cables. It has been proven in [Sultan et al. \(2001\)](#) that the solution to the prestressability problem for the SVDB and SVDT types for symmetrical configurations is identical to the solution for the SVD type and that solutions to the prestressability problem for symmetrical configurations of the SD, SDB, SDT types can be obtained as limit cases of the corresponding solutions for the SVD, SVDB, SVDT types, respectively. [Sultan and Skelton \(2003a\)](#) later used this methodology for the investigation of the prestressability conditions for more complex structures called tensegrity towers having up to 10 stages (i.e., 30 bars and 138 cables), and built continuous sets of solutions that were used in deployment procedures ([Sultan & Skelton, 2003b](#)). Following similar ideas, [Murakami and Nishimura \(2001a,b\)](#) and [Nishimura and Murakami \(2001\)](#) investigated the prestressability problem for other symmetric tensegrity structures like icosahedral, dodecahedral modules, and cyclic tensegrity towers, being also able to find closed form solutions.

As it can be easily ascertained, the major issue with the analytical approaches is that they rely heavily on *exploiting symmetries* to achieve substantial

simplification of the prestressability conditions. Hence, they cannot be used to find arbitrary, nonregular prestressable configurations. For this purpose one has to employ numerical solvers. As already mentioned, general purpose numerical techniques were first used to find prestressable configurations by [Motro \(1984\)](#) and [Pellegrino \(1986\)](#), but these nonlinear solvers performed well only on small size problems. In the late 1990s a powerful numerical approach called the *force-density method*, was introduced in the study of tensegrity structures statics by [Vassart and Motro \(1999\)](#). This method is advantageous because the nonlinear equations of equilibrium are transformed into linear ones using the force to length ratios. Hence, only linear equations are solved in a numerical iterative scheme. In their review article of tensegrity form-finding (to which the interested reader is referred for more details), [Tibert and Pellegrino \(2003a\)](#) concluded that the major deficiency of the force-density method is that it does not provide control over the length of the members of the structure. Thus, shape constraints cannot be included in the classical force-density method. [Masic, Skelton, and Gill \(2005\)](#) addressed this issue and extended the force-density method to include shape as well as symmetry constraints. The ensuing procedure performed very well on large-scale tensegrity structures, including plates and shell-class tensegrity towers, with the number of structural elements in the hundreds. For example, a tensegrity plate with 270 elements and 96 nodes resulted in a problem with 282 variables and 360 constraints that was successfully solved in 27 iterations.

Recently, [Zhang and Ohsaki \(2006\)](#) developed an adaptive force-density method that uses eigenvalue analysis and spectral decomposition of the equilibrium matrix to find configurations for which the equilibrium matrix is rank deficient. However, this method does not consider geometrical (e.g., shape) constraints, hence retaining the deficiency observed by [Tibert and Pellegrino \(2003a\)](#). To include geometrical as well as internal force distribution constraints in an effective numerical procedure for finding prestressable configurations, [Zhang, Ohsaki, and Kanno \(2006\)](#) developed a method in which independent sets of axial forces and nodal locations are specified consecutively. The procedure is very efficient because only linear algebraic equations have to be solved and it is exemplified on several tensegrity structures. However, as the number of variables increases it is advisable to extensively use geometrical constraints that include symmetries. [Estrada, Bungartz, and Mohrdieck \(2006\)](#) proposed a versatile numerical procedure that includes a condition on the maximum rank of the force-density matrix and minimal member length. Only limited knowledge of the structure's topology is required (which members are cables and which bars) and the method can find arbitrary prestressable configurations. Neither force nor symmetry or shape constraints are included in this procedure.

Lastly, it is worth to mention that, prompted by advances in computational algorithms and the advent of powerful computers, recent efforts have been devoted to the revival of the dynamic relaxation method, primarily due to its capability to find highly irregular prestressable configurations. For example, [Zhang, Maurin, and Motro \(2006\)](#) successfully used it to find nonsymmetrical prestressable configurations for tensegrity structures having up to 8 bars and 36 cables.

5.2. STATIC RESPONSE

The static response of tensegrity structures to external loading has been investigated by many researchers ([Kebiche, Kazi-Aoual, & Motro, 1999](#); [Murakami, 2001b](#); [Quirant, Kazi-Aoul, & Motro, 2003](#); [Stamenovic, Fredberg, Wang, Butler, & Ingber, 1996](#); [Sultan & Skelton, 1998a](#)) for different purposes ranging from the study of cell mechanics to the design of tensegrity sensors ([Sultan & Skelton, 1998a, 2004](#)). A key characteristic is that, due to the intrinsic flexibility of tensegrity structures, static response studies require *nonlinear techniques*.

The importance of nonlinear static response analysis cannot be overestimated. First and foremost, these studies revealed the *emergent properties* and the *strong anisotropy* (see [Kebiche et al., 1999](#); [Stamenovic et al., 1996](#)) of tensegrity structures. Tensegrity structures may display nonlinear spring characteristics of various shapes, depending on the direction and type of the external applied load (see [Stamenovic et al., 1996](#); [Sultan & Skelton, 1998a, 2004](#)). As an example, consider the two-stage SVD structure previously investigated for prestressability. The structure is initially in a symmetrical prestressable configuration characterized by $\alpha = 50^\circ$, $\delta = 30^\circ$. The static response is obtained by numerically solving the equilibrium equations:

$$A(q)T(q, l_0) + H(q)F = 0, \quad (5.19)$$

where l_0 is the vector of cable rest lengths corresponding to the initial symmetrical prestressable configuration and computed using [Eq. \(5.18\)](#). The vector F contains the external forces and moments acting on the structure and $H(q)$ is a matrix of appropriate dimensions. Consider two scenarios, one in which only an external force, F_z , is applied to the rigid top along \hat{t}_3 and the second scenario in which only a moment, M_z , is applied to the top along \hat{t}_3 . [Figures 5.4 and 5.5](#) show the static response for several values of the pretension coefficient and certain material properties (see [Sultan & Skelton, 2004](#) for details). At all points on these curves all cables are in tension and the maximum forces in cables and bars are below the structural integrity limits. It can be easily ascertained that both static responses display strong nonlinearity and anisotropy, especially for small

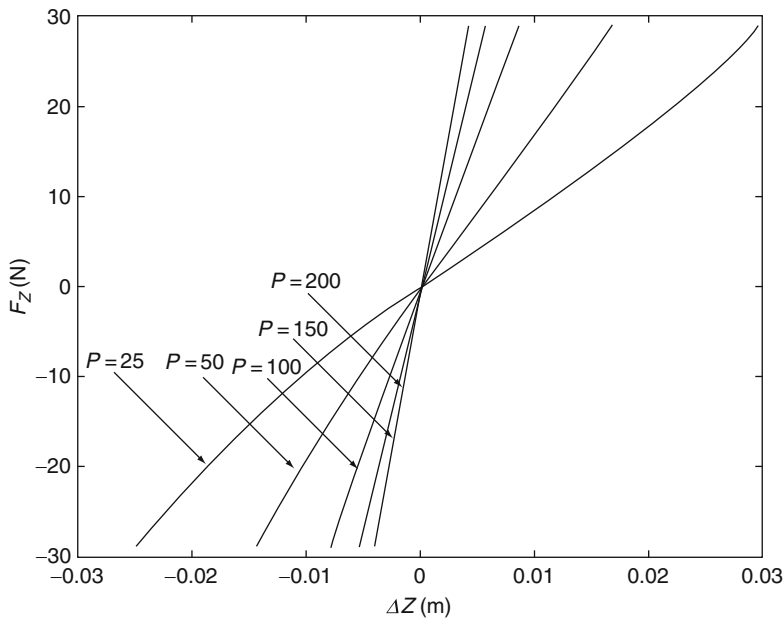


FIG. 5.4 Load-displacement characteristic of the two-stage SVD structure.

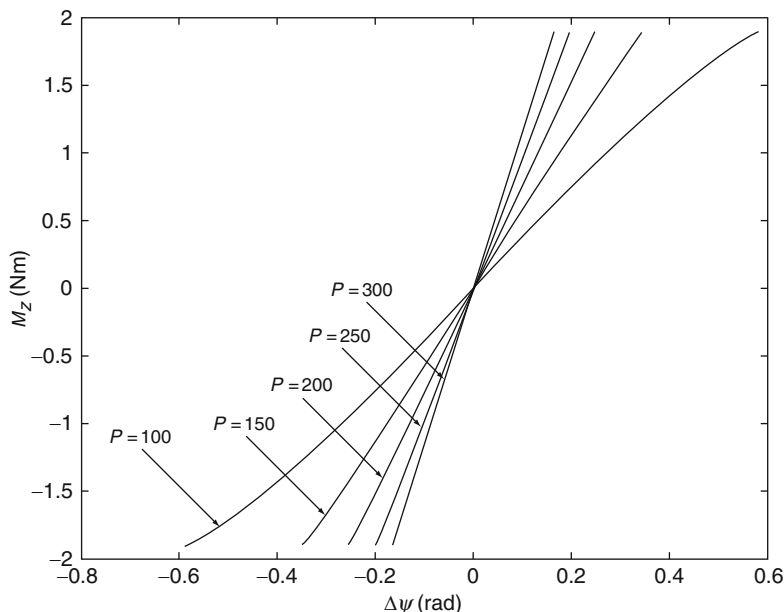


FIG. 5.5 Torque-twist characteristic of the two-stage SVD structure.

pretension. The load–deflection curve (F_z vs ΔZ) indicates a hardening characteristic, whereas the torque–twist curve (M_z vs $\Delta \Psi$) indicates a softening characteristic. Note that the responses are not inversion symmetric. It is evident from these figures that the structure becomes stiffer when pretension increases. It is also important to remark here that, using a simpler tensegrity structure composed of three bars, three linearly elastic cables, and three inextensible cables, [Oppenheim and Williams \(2000\)](#) were able to explain these characteristics of tensegrity structures, which were also observed experimentally, via closed form solutions.

Before closing this section, it is worth to mention several other efforts in the area of nonlinear static analysis as follows. [Masic, Skelton, and Gill \(2006\)](#) developed procedures to optimize the stiffness to mass ratio of symmetric and asymmetric tensegrity structures for several static loading scenarios. [Wang and Liu \(1996\)](#) investigated the static design of double layer tensegrity grids and extrapolated ideas related to tensegrity as pin-jointed structures to cable-strut systems (see also [Wang, 1998, 2004](#)), thus leveraging knowledge gained from tensegrity research into more general structural systems. Lastly, [Kahla and Kebiche \(2000\)](#) conducted an elastoplastic analysis of a certain tensegrity beam structure taking into account geometric and material nonlinearities and indicated that for this design some cables might break before bars experience buckling. The interested reader is also referred to a recent review on static analysis of tensegrity structures by [Juan and Tur \(2008\)](#).

6. Advances in Dynamics Research

6.1. NONLINEAR EQUATIONS OF MOTION

On the path of enabling applications of tensegrity structures, analysis of their dynamic properties is necessary and derivation of the nonlinear equations of motion is crucial ([Murakami, 2001a; Skelton, Pinaud, & Mingori, 2001; Sultan, 1999; Sultan, Corless, & Skelton, 2002a](#)). These equations can be obtained from the general equations that describe the dynamic behavior of elastic truss structures under large deformation, as has been done by [Murakami \(2001a\)](#). A different approach ([Sultan, 1999; Sultan et al., 2002a](#)), which has the advantage of providing direct insight into the structure of these equations, is to employ at the beginning of the modeling process the observation that tensegrity structures are constructed using members with very different characteristics: some of these members can be modeled as “soft,” massless elastic elements (e.g., cables), and the others as “hard,” rigid bodies. Because of this clear separation, for the

derivation of the equations of motion the system can be represented as a set of rigid bodies subjected to the potential elastic field of the massless, “soft” elements. Other potential fields (e.g., gravitational) as well as nonconservative forces and moments can be easily included and the analytical mechanics (e.g., Lagrange) formalism can be used to obtain the nonlinear equations of motion. This approach produces a mathematical model composed of a *finite* number of *ordinary* differential equations (ODEs). As it is well known, ODEs are much easier to deal with, numerically as well as analytically, than *partial* differential equations (PDEs).

On the other hand, for many types of flexible structures, such as conventional truss structures composed only of bars, clear separation between the properties of their members is not possible and, if accurate modeling is desired, the aforementioned modeling assumptions cannot be made. In this situation, application of the physical principles leads to an *infinitely* dimensional system of PDEs that describe the structure’s dynamics. As remarked in the previous paragraph, this is not the case with tensegrity structures, which are flexible structures that can be accurately described by a finite set of ODEs. This is a major advantage of tensegrity structures over conventional flexible structures.

In the following, the derivation of the nonlinear equations of motion for a tensegrity structure composed of E elastic and massless cables and R rigid bodies is illustrated. All the constraints are holonomic, scleronomic, and bilateral, and the external constraint forces and moments are workless, which means that they do not do work through a virtual displacement consistent with the geometric constraints. The influence of other potential fields (e.g., the gravitational field) is neglected. Let q be the N -dimensional vector of independent generalized coordinates that describe the configuration of the system with respect to an inertial reference frame. Application of the Lagrangean formalism requires the derivation of the kinetic and potential energies and of the nonconservative generalized forces. Since the cables are massless, the kinetic energy, $E_k(q, \dot{q})$, is only due to the rigid bodies:

$$E_k(q, \dot{q}) = \frac{1}{2} \dot{q}^T M(q) \dot{q}, \quad (6.1)$$

where $M(q)$ is the mass matrix. The potential energy, $E_p(q)$, is due to the elastic cables:

$$E_p(q) = \sum_{j=1}^E \int_0^{e_j} T_j d\epsilon_j, \quad (6.2)$$

where ε_j is the elongation of the j th cable, T_j its tension, which is positive if the cable is in tension and zero otherwise, and the differential element is $d\varepsilon_j = dl_j = \sum_{i=1}^N (\partial l_j / \partial q_i) dq_i$, where l_j is the length of the j th cable. Thus, the potential energy becomes

$$E_p(q) = \sum_{j=1}^E \int_{q_0}^q T_j \sum_{i=1}^N \frac{\partial l_j}{\partial q_i} dq_i, \quad (6.3)$$

where q_0 is the independent generalized coordinates vector corresponding to a configuration for which the cable elongations are zero (such a configuration is, e.g., a prestressable configuration with zero pretension). The nonconservative generalized force associated with the i th generalized coordinate can be expressed as

$$Q_i = \sum_{j=1}^R \left(\vec{F}_j \cdot \frac{\partial \vec{v}_j}{\partial \dot{q}_i} + \vec{M}_j \cdot \frac{\partial \vec{\omega}_j}{\partial \dot{q}_i} \right), \quad i = 1, \dots, N, \quad (6.4)$$

where \vec{F}_j and \vec{M}_j are the resultant nonconservative force and moment applied to rigid body j , whereas \vec{v}_j and $\vec{\omega}_j$ are the linear velocity of the center of mass and the angular velocity of the j th rigid body, respectively. Lagrange equations then yield N second-order nonlinear ODEs:

$$M(q)\ddot{q} + c(q, \dot{q}) + A(q)T = Q, \quad (6.5)$$

where Q is the vector of nonconservative generalized forces, $A(q)$ is the matrix which appears in the previously exposed static studies (e.g., Eq. (5.1)), T is the vector of cable forces, and the elements of $c(q, \dot{q})$ are given by

$$c_i = \sum_{j=1}^N \sum_{n=1}^N \left(\frac{\partial M_{ij}}{\partial q_n} - \frac{1}{2} \frac{\partial M_{jn}}{\partial q_i} \right) \dot{q}_j \dot{q}_n, \quad i = 1, \dots, N. \quad (6.6)$$

A particular case of interest is when the nonconservative forces and moments can be separated in two types. The first type is that of linear kinetic friction forces and moments at the joints of the structure and linear kinetic damping forces in the cables. Recall that a linear kinetic friction force or moment is proportional to the relative linear or angular velocity, respectively, between the members in contact at the joint, whereas a linear kinetic damping force in a cable is proportional to the time derivative of the cable's elongation. The second type is of external—but not friction or damping—forces and moments applied to the rigid bodies. For example, an external pure couple applied to a bar is of the second type. Similarly, external moments and forces applied to the top of the two-stage SVD

structure considered before are also of the second type (see Sultan et al., 2002a for more details). Because linear kinetic friction and damping forces and moments are linear in the angular and linear velocities, which, at their turn, are linear in the generalized velocities, \dot{q} , it follows from Eq. (6.4) that the corresponding generalized forces are also linear in the generalized velocities. Likewise, from Eq. (6.4) the generalized forces due to the forces and moments of the second type are linear in these external actions, represented by the vector F . Thus, the vector of generalized forces can be expressed as

$$Q = -C(q)\dot{q} - H(q)F, \quad (6.7)$$

where the term $-C(q)\dot{q}$ is due to the first type, that is, friction and damping effects, whereas the term $-H(q)F$ is due to the second type of nonconservative forces and moments. For a given topology of the structure matrices $C(q)$ and $H(q)$, called the damping and disturbance matrices, respectively, can be derived from Eq. (6.4) using simple operations. Note that whereas the damping matrix is square, the size of the disturbance matrix depends on the number of external forces and moments of the second type acting on the structure. For example, for the two-stage SVD structure, if these forces and moments act only on the top, $F = [M_x \ M_y \ M_z \ F_x \ F_y \ F_z]^T$ and $H(q)$ is a 18×6 matrix. Note that this matrix was also encountered in the static response studies (see Eq. (5.19)).

From Eqs. (6.5) and (6.7), the equations of motion are readily obtained as

$$M(q)\ddot{q} + c(q, \dot{q}) + C(q)\dot{q} + A(q)T + H(q)F = 0. \quad (6.8)$$

The energy-based formulation of the equations of motion has two big advantages. Firstly, it can be easily employed in the automated derivation, implementation, and analytical manipulation of the equations of motion using symbolic computational tools such as Maple and Mathematica. Sultan (1999) gives many details and examples, including formulas for all the terms in Eq. (6.8) for the two-stage SVD structure. Thus, the energy-based approach facilitates investigation of increasingly complex tensegrity structures. Secondly, as it will be shown shortly, the energy approach can be easily used to analyze important nonlinear damping and vibration properties of tensegrity structures.

6.2. DAMPING, STIFFNESS, AND STABILITY PROPERTIES

Tensegrity structures particularities result in very interesting damping properties. For example, using an energy formulation for the dynamics of a tensegrity structure composed of three rigid bars, three inextensible cables, and three linearly elastic cables, Oppenheim and Williams (2001a,b) showed that if only

the cables are affected by linear kinetic damping, then, along motions associated with an infinitesimal mechanism the decay rate of the system's energy is lower than the exponential rate characteristic to a linearly damped system. The two authors also showed that linear kinetic friction at the joints is more effective in dissipating the energy of the structure, resulting in an exponential rate of decay. These results are important because they relate previous work focused on kinematic properties like infinitesimal mechanisms (e.g., Hanaor, 1988; Pellegrino & Calladine, 1986) to dynamical properties of tensegrity structures, while also indicating a simple technological method to increase energy dissipation in these structures: by adding friction at the joints instead of using heavily damped cables. The fact that friction at the joints is effective in dissipating the energy of the structure was also confirmed using more sophisticated models by Sultan, Corless, and Skelton (2002b) and Sultan and Skelton (2003b). In the following paragraph, the two-stage SVD structure example is used to show that linear friction at the joints is sufficient to guarantee that the symmetrical prestressable configurations previously discovered and characterized by Eqs. (5.7) and (5.8) are locally stable and even exponentially stable.

Consider the structure depicted in Fig. 5.1 in which only the six joints that connect the bars to the base and rigid top are affected by linear kinetic friction. This means that the friction moment at joint j exerted by member a on member b is given by $\vec{M}_j = d(\vec{\omega}_b - \vec{\omega}_a)$ where $\vec{\omega}_*$ is the angular velocity of member “*” (here a is either the base or the rigid top and b one of the bars). The scalar $d < 0$ is the coefficient of friction, which is considered the same for all joints. The linearized equations of motion around an arbitrary symmetrical prestressable configuration characterized by α and δ and described by Eqs. (5.7) and (5.8), are easily derived from Eq. (6.8) as

$$M(\alpha, \delta)\ddot{\tilde{q}} + C(\alpha)\dot{\tilde{q}} + K(\alpha, \delta)\tilde{q} + H(\alpha, \delta)F = 0, \quad \tilde{q} = q - q_e, \quad (6.9)$$

where q_e represents the generalized coordinates vector for a symmetrical prestressable configuration. The mass matrix, $M(\alpha, \delta)$, which is too complicated to be reproduced here, is positive definite (see Sultan et al., 2002b for details). The damping matrix, $C(\alpha)$, has a particular structure that can be used to prove that it is positive semidefinite using Schur complements. Indeed,

$$C(\alpha) = \begin{bmatrix} -dI_6 & 0 & 0 \\ 0 & -dI_6 & C_a \\ 0 & C_a^T & C_b \end{bmatrix}, \quad (6.10)$$

where

$$C_a = -d \begin{bmatrix} 0 & -\sin(\alpha) & \cos(\alpha) & 0 & 0 & 0 \\ -1 & 0 & 0 & 0 & 0 & 0 \\ 0 & \cos\left(\alpha - \frac{\pi}{6}\right) & \sin\left(\alpha - \frac{\pi}{6}\right) & 0 & 0 & 0 \\ -1 & 0 & 0 & 0 & 0 & 0 \\ 0 & -\cos\left(\alpha + \frac{\pi}{6}\right) & -\sin\left(\alpha + \frac{\pi}{6}\right) & 0 & 0 & 0 \\ -1 & 0 & 0 & 0 & 0 & 0 \end{bmatrix}, \quad C_b = \begin{bmatrix} -3dI_3 & 0 \\ 0 & 0 \end{bmatrix}, \quad (6.11)$$

and I_* is the identity matrix of dimension *. The inequality $C(\alpha) \geq 0$ can be successively expressed using Schur complements as follows:

$$\begin{aligned} C(\alpha) \geq 0 &\Leftrightarrow \begin{bmatrix} -dI_6 & 0 & 0 \\ 0 & -dI_6 & C_a \\ 0 & C_a & C_b \end{bmatrix} \Leftrightarrow C_b + \frac{1}{d} C_a^T C_a \geq 0 \\ &\Leftrightarrow \begin{bmatrix} 3 - \|w\|^2 & v^T w \\ wv^T & 3 - \|v\|^2 \end{bmatrix} \geq 0, \end{aligned} \quad (6.12)$$

where

$$\begin{aligned} v &= \left[\cos\alpha \sin\left(\alpha - \frac{\pi}{6}\right) \sin\left(\alpha + \frac{\pi}{6}\right) \right]^T, \\ w &= \left[\sin\alpha - \cos\left(\alpha - \frac{\pi}{6}\right) \cos\left(\alpha + \frac{\pi}{6}\right) \right]^T. \end{aligned} \quad (6.13)$$

Since $3 - \|w\|^2 > 0$, Eq. (6.12) is equivalent to $\|v\|^2 \|w\|^2 - (v^T w)^2 \geq 0$ which is the well-known Schwartz inequality. This proves that $C(\alpha) \geq 0$.

The most complicated term in Eq. (6.9) is the tangent stiffness matrix, $K(\alpha, \delta)$, which is the Hessian of the potential energy at a symmetrical prestressable configuration. If the cables are linearly elastic, that is, the tension in cable j is given by Eq. (5.17), then the tangent stiffness matrix can be expressed as a sum of two parts, one that is proportional to pretension and the other that depends on the cable stiffnesses:

$$K(\alpha, \delta) = PK_P(\alpha, \delta) + K_0(\alpha, \delta), \quad (6.14)$$

where

$$K_0(\alpha, \delta) = k_S K_S(\alpha, \delta) + k_V K_V(\alpha, \delta) + k_D K_D(\alpha, \delta). \quad (6.15)$$

Matrices $K_S(\alpha, \delta), K_V(\alpha, \delta), K_D(\alpha, \delta)$ are only positive *semidefinite* and $K_P(\alpha, \delta)$ is positive *definite* (see Sultan et al., 2002b for details). The scalars k_S , k_V , and k_D are the stiffnesses of the saddle, vertical, and diagonal cables, respectively, used in Eq. (5.18). Thus, for positive pretension ($P > 0$), the tangent stiffness matrix is positive definite.

The fact that the mass and tangent stiffness matrices are positive definite and the damping matrix is positive semidefinite implies linearized stability of the symmetrical prestressable configurations. Moreover, by investigating the first-order system, $\dot{x} = A_p x$, where $x = [\tilde{q}^T \dot{\tilde{q}}^T]^T$ and

$$A_p = \begin{bmatrix} 0_{18} & I_{18} \\ -M(\alpha, \delta)^{-1} K(\alpha, \delta) & -M(\alpha, \delta)^{-1} C(\alpha) \end{bmatrix}, \quad (6.16)$$

it has been numerically ascertained that the eigenvalues of A_p have negative real parts across the entire equilibrium manifold presented in Fig. 5.3. This shows that *all* of the points of this equilibrium manifold are locally *exponentially* stable equilibria for the *nonlinear* equations of motion. Hence strong stability of these equilibria is achieved only with linear kinetic friction at the joints.

At this point it is important to make several observations related to the aforementioned results on the tangent stiffness matrix. Firstly, $K_0(\alpha, \delta)$ can also be expressed as

$$K_0(\alpha, \delta) = A(\alpha, \delta) \Sigma A(\alpha, \delta)^T, \quad (6.17)$$

where $A(\alpha, \delta)$ is the equilibrium matrix obtained after substitution of h given by Eq. (5.8) in $A(\alpha, \delta, h)$ of Eq. (5.5), whereas $\Sigma > 0$ is a diagonal matrix with the diagonal elements equal to the ratios between the cable stiffnesses and their lengths, that is, k_S/S , k_V/V , and k_D/D (see Sultan et al., 2002b). The infinitesimal mechanisms are directions of semidefiniteness for $K_0(\alpha, \delta)$. Indeed, if Δq is an infinitesimal mechanism at the prestressable configuration characterized by α and δ , then $A(\alpha, \delta)^T \Delta q = 0$ and

$$\Delta q^T K_0(\alpha, \delta) \Delta q = \Delta q^T A(\alpha, \delta) \Sigma A(\alpha, \delta)^T \Delta q = 0. \quad (6.18)$$

Equations (6.14) and (6.18) show that for $P = 0$, the infinitesimal mechanisms are directions of zero stiffness. However, because $K_P(\alpha, \delta) > 0$, as soon as pretension is applied, the tangent stiffness matrix, $K(\alpha, \delta)$, becomes positive

definite. This observation reflects the fundamental property of tensegrity structures, that they are stiffened as soon as pretension is applied—or, as other researchers put it, that their infinitesimal mechanisms are stiffened by prestress (see, e.g., [Calladine, 1978](#))—expressed using the tangent stiffness matrix.

Secondly, the stiffness of the structure increases with increasing pretension, P , in agreement with the static responses shown in [Figs. 5.4](#) and [5.5](#). Thirdly, since $K(\alpha, \delta)$ is the Jacobian—evaluated at a symmetrical prestressable configuration—of the left-hand side of [Eq. \(5.19\)](#), which defines the static response, $A(q)T(q, l_0) + H(q)F = 0$, then, by the implicit function theorem, it follows that in the neighborhood of each symmetrical prestressable configuration the solution of the static problem, that is, [Eq. \(5.19\)](#), can be expressed as a function of the external forces and moments, F . Thus, static bifurcations are not possible. Lastly, because $K_P(\alpha, \delta) > 0$, increasing pretension is expected to result in increasing natural frequencies. This is in accordance with general observations referred to in the next section.

6.3. VIBRATION PROPERTIES

Linearized dynamical models can be easily obtained, as shown before, from the nonlinear equations of motion and used for modal analysis studies. Such studies have been reported in many publications (e.g., [Furuya, 1992](#); [Lazzari, Vitaliani, Majowiecki, & Saetta, 2003](#); [Murakami & Nishimura, 2001a,b](#); [Nishimura & Murakami, 2001](#); [Tibert & Pellegrino, 2003b](#)) and led to several important conclusions described next.

Numerical studies carried out by Murakami and Nishimura on several tensegrity structures with symmetries such as cyclic cylindrical towers, regular truncated dodecahedral and icosahedral modules indicated that the lower natural frequencies increase approximately in proportion with the square root of the level of prestress in the structure (see, e.g., [Murakami & Nishimura, 2001a,b](#); [Nishimura & Murakami, 2001](#)). One may easily notice the similarity between this dependency and the one observed in strings of musical instruments such as guitars, violins, etc. The authors associate the lower natural frequencies with inextensional infinitesimal mechanisms modes and make the observation that for higher natural frequencies, which they associate with deformation modes, the variation with prestress is less significant.

[Sultan et al. \(2002b\)](#) enlarged the scope of modal analysis studies and investigated the combined effect of friction and pretension on the modal frequencies and damping ratios for several tensegrity structures. Consider, for example, a two-stage SVDT tensegrity structure that is affected only by linear friction moments at the three joints between the bars and the base. In [Fig. 5.1](#) these joints

are A_{j1} , $j = 1, 2, 3$ (note that Fig. 5.1 represents a two-stage SVDT structure if $B_{12}B_{22}$, $B_{22}B_{32}$, $B_{12}B_{32}$ are considered cables). The friction moment at joint j is given by $\bar{M}_j = d\vec{\omega}_j$ where $\vec{\omega}_j$ is the angular velocity of bar j , $j = 1, 2, 3$, and $d < 0$ is the friction coefficient, considered the same for all joints. The structure is characterized by the following parameters: $l = 0.4$ m, $b = 0.27$ m, the mass of the bars, $m = 0.8$ kg, the longitudinal moment of inertia of the bars, $J = 1.2$ kg m², and the stiffness of all cables, $k_j = 500$ N, $j = 1, \dots, 21$. The structure is in a symmetrical prestressable configuration for which $\alpha = \delta = 60^\circ$. Figure 6.1 shows the variation of the maximum modal frequency with the coefficients of pretension and friction. The curve obtained for $d = 0$ represents the variation of the minimum natural frequency with pretension. It clearly indicates a square-root dependency, in agreement with the observations of Murakami and Nishimura. One can also ascertain that, if the friction at the joints increases, the minimum modal damping becomes zero at low pretension. This corresponds to a purely damped, exponentially decaying mode. Figure 6.2 shows the dependency of the maximum modal frequency with the pretension and friction coefficients, indicating that the variation with pretension of the maximum natural frequency relative to the nominal value of the natural frequency is less pronounced. However, regardless of the values of the pretension and friction coefficients, the maximum modal damping is always nonzero, corresponding to an oscillatory decaying mode. It is also apparent from Fig. 6.2 that the frequency of this mode is not affected by friction. Additional numerical studies, conducted on both the

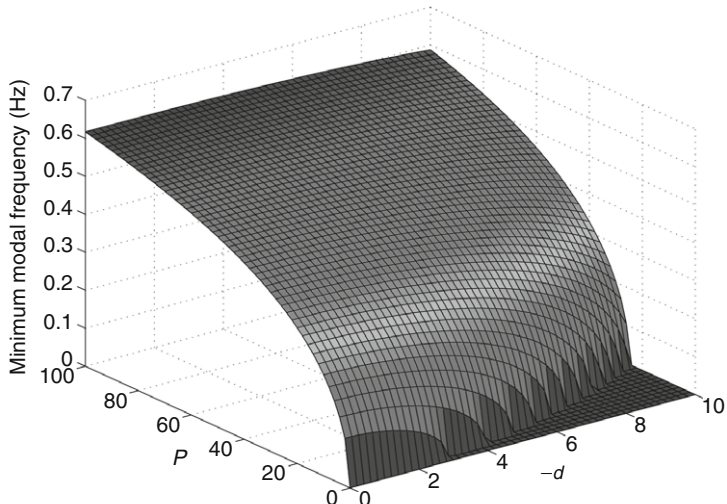


FIG. 6.1 Minimum modal frequency variation for the SVDT structure.

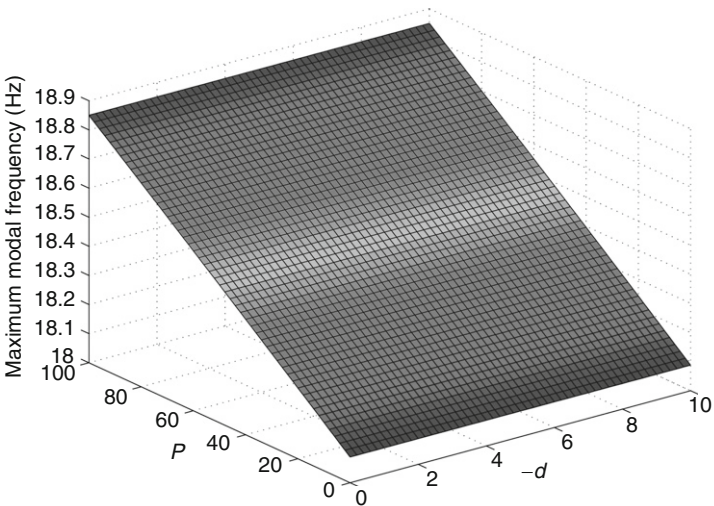


FIG. 6.2 Maximum modal frequency variation for the SVDT structure.

two-stage SVD and SVDT structures, showed that the modal dynamic range, defined as the difference between the maximum and minimum modal frequencies, increases with pretension and the range of modal damping, defined as the difference between the maximum and minimum modal damping, increases with the friction at the joints (see Sultan et al., 2002b for details).

6.4. CLUSTERED NATURAL FREQUENCIES IN TENSEGRITY STRUCTURES

A very important observation is that in tensegrity structures that have symmetries the occurrence of *multiple* or *clustered* natural frequencies is the rule rather than the exception (see Murakami & Nishimura, 2001a,b; Nishimura & Murakami, 2001; Sultan, 2009). The fact that increasing the degree of symmetry in a structure leads to multiple natural frequencies is due to the particular features of the corresponding mass and stiffness matrices, induced primarily by the geometrical symmetries and to a lesser extent by homogeneous material properties.

Repeated or even clustered natural frequencies are not desirable for several reasons. For example, the sensitivities of repeated natural frequencies and of the associated eigenvectors with respect to various parameters are difficult to compute, both analytically and numerically. It is also well known that repeated natural frequencies might lead to accumulation and propagation of numerical errors. Moreover, it has become generally accepted that clustered natural

frequencies are detrimental to proportional damping approximation, which, on the other hand, is very beneficial to the control as well as to the computational research community (see [Adhikari, 2004](#); [Gawronski, 2004](#); [Gawronski & Sawicki, 1997](#)). For proportional damping approximation a transformation from the “physical” coordinates, \tilde{q} , of the linearized system, [Eq. \(6.9\)](#), to the “modal” (q_m) coordinates is performed using the modal matrix, W , such that the modal system is obtained. For zero external actions, F , the modal system is

$$\ddot{q}_m + C_m \dot{q}_m + \Omega^2 q_m = 0, \quad (6.19)$$

where C_m is the modal damping matrix and Ω is the diagonal matrix of natural frequencies. Then, in the most popular approach to proportional damping approximation, the off-diagonal terms in the modal damping matrix are neglected (see [Gawronski, 2004](#)). Writing $C_p = \text{diag}(C_m)$ the proportionally damped model is then

$$\ddot{q}_p + C_p \dot{q}_p + \Omega^2 q_p = 0. \quad (6.20)$$

For accurate approximation the modal error, $\varepsilon_m = q_p - q_m$, and the physical error, computed as $\varepsilon(t) = W\varepsilon_m(t)$, should be negligible.

It is very important to remark here that experiments carried out by [Kono, Choong, Shimada, and Kunieda \(1999\)](#) indicated that, indeed, proportional damping approximation for tensegrity structures might lead to erroneous results. Kono and coworkers built a double layer tensegrity grid on which they performed physical dynamical experiments and finite element analysis. Comparison of these results showed that mass proportional Rayleigh damping model approximation, which is a particular case of the proportional damping approximation, is not appropriate for modeling damping in this structure: the proportionally damped model yields acceptable results only for low frequencies.

Last but not least, for a tensegrity structure clustered or repeated natural frequencies pose additional difficulties because, as previously mentioned, the existence of infinitesimal mechanisms has two important consequences. Firstly, the structure is flexible and prone to exhibiting large deformations. Secondly, if tendon damping is the main source of damping, along infinitesimal mechanisms the energy dissipation is low, that is, the structure is lightly damped. On the other hand, resonance phenomena lead to large deformations that are amplified in lightly damped structures with clustered/repeated natural frequencies ([Park, Kim, & Ma, 1994](#)). Thus, resonance phenomena are more dangerous in tensegrity structures with clustered natural frequencies than in structures in which these frequencies are separated.

The above discussion leads to the conclusion that separation of the natural frequencies must be considered as an important design criterion for tensegrity structures. Recent research indicated that such separation can be easily achieved, even in tensegrity structures with geometrical symmetries, by adequate selection of the elastic and inertia properties of the structure (Sultan, 2009). For illustration consider a two-stage SVD tensegrity at a symmetrical prestressable configuration characterized by $l = 1$ m, $b = 0.67$ m, $\alpha = \delta = 60^\circ$. The cables are linearly elastic as shown in Eq. (5.17) and affected by linear kinetic damping. For simplicity the damping coefficients in all cables are assumed the same, that is, the damping force in tendon j is $\vec{F}_j = c_1 \vec{l}_j$ with $c_1 < 0$. The mass, damping, and stiffness matrices are linear in the inertial, damping, and elastic parameters of the structure and are expressed as

$$M = \sum_{i=1}^6 m_i M_i, \quad C = c_1 C_1, \quad K = \sum_{i=1}^4 k_i K_i, \quad (6.21)$$

where m_1 represents the mass of the top, m_{2-4} its principal moments of inertia, $m_{5,6}$ the mass and longitudinal moment of inertia of a bar, k_{1-3} the stiffness of the saddle, vertical, and diagonal cables, respectively, k_4 the pretension coefficient, and c_1 the damping coefficient of the cables. Note that K_i , $i = 1, \dots, 4$, denote the matrices K_S , K_V , K_D , K_P in Eqs. (6.14) and (6.15) evaluated at the configuration of interest while k_{1-3} correspond to the scalars k_S , k_V , k_D in Eq. (6.15). Matrices M_i , C_1 , K_i have been computed using the general formulas given in Sultan (1999). The pretension coefficient has been included in the “elastic” properties because it is associated with the elastic cables.

The natural frequencies separation problem consists of selecting appropriate values for the 11 design parameters, that is, m_{1-6} , c_1 , and k_{1-4} , such that prescribed separations between the natural frequencies, ω_{ij} , are achieved, namely

$$|\omega_i - \omega_j| > \omega_{ij}, \quad i = 1, \dots, 17, \quad j = i + 1, \dots, 18, \quad (6.22)$$

where the natural frequencies are obtained by solving the generalized eigenvalue problem $\det(K - \omega_i^2 M) = 0$. In addition, upper and lower bound constraints on the natural frequencies are imposed:

$$\omega_{\min} < \omega_i < \omega_{\max}, \quad i = 1, \dots, 18. \quad (6.23)$$

These constraints are justified as follows. It is frequently desired to measure the modal frequencies of the structure using certain sensors. On the other hand, to capture the highest frequency, the sampling rate of the sensors must be at least twice this frequency. However, the sampling rate is limited and thus the highest

modal frequency should be limited. Lastly, since the modal frequencies are directly related to the natural frequencies, an upper bound constraint on the maximum natural frequency appears as natural. The minimum natural frequency is lower bounded to avoid slow modes. Low values of the natural frequencies correspond to a very “soft” (i.e., not sufficiently stiff) structure, which in many applications is not desirable.

Consider first the following *ad hoc* values for the design parameters, which correspond to a design further referred to as the “arbitrary” design:

$$\begin{aligned} k_{1-4} &= 1, \quad m_1 = 1, \quad m_2 = 3, \quad m_3 = 4, \\ m_4 &= 5, \quad m_5 = 1, \quad m_6 = 1, \quad c_1 = -1. \end{aligned} \quad (6.24)$$

All quantities are given in SI units. The natural frequencies distribution, shown in Fig. 6.3, indicates regions in which these frequencies are clustered: for eight pairs of neighboring natural frequencies the separation is less than 0.02 rad/s. This is not a good dynamic design. For example, if the responses to initial conditions of the nonproportionally, Eq. (6.19), and proportionally, Eq. (6.20), damped

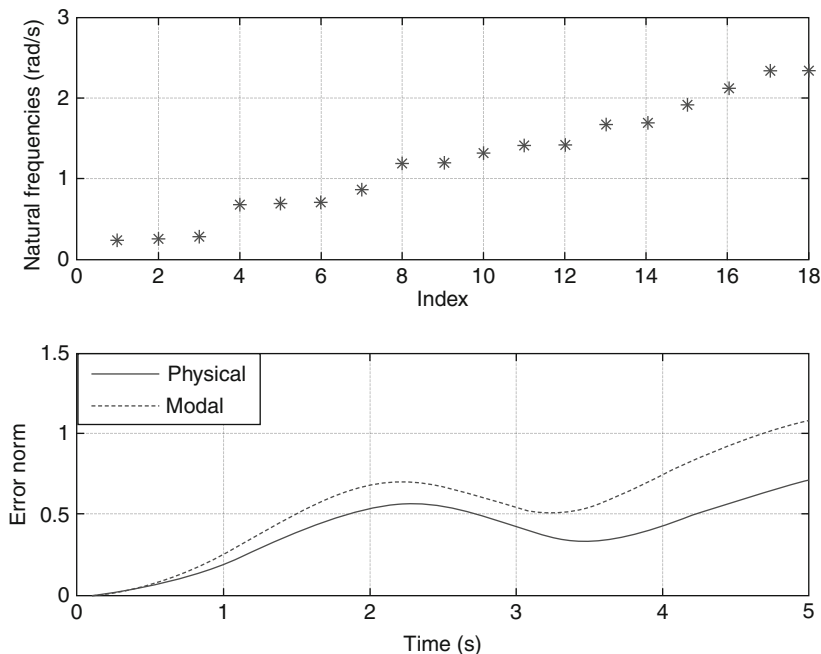


FIG. 6.3 Clustered natural frequencies lead to large proportional damping approximation errors for the “arbitrary” design.

models, are computed, the approximation errors are unacceptably large. Figure 6.3 shows the Euclidean norms of the modal, $\varepsilon_m(t)$, and physical, $\varepsilon(t)$, errors for the following initial conditions: $q_{m0} = q_{p0} = 0.4$, $\dot{q}_{m0} = \dot{q}_{p0} = 0.2$ (SI units). Clearly, redesign of the structure to achieve separation of the natural frequencies is imperative.

A fast algorithm which solves the natural frequencies separation problem has been developed and its application to the two-stage SVD structure for $\omega_{ij} = 0.2$, $\omega_{\min} = 0.8$, and $\omega_{\max} = 10$ (rad/s), led to the results shown in Fig. 6.4 (see Sultan, 2009 for details on the algorithm and numerical values of the corresponding design parameters). Analysis of the responses to initial conditions confirms that the proportional damping approximation can be applied. Figure 6.4 gives the errors for $q_{m0} = q_{p0} = 0.4$, $\dot{q}_{m0} = \dot{q}_{p0} = 0.2$ but similar patterns were observed for other initial conditions (see Sultan, 2009).

The next result reveals very interesting features. Firstly, even if the prescribed separation is large it may so happen that the results are worse than the results obtained for a smaller separation. Figure 6.5 corresponds to such a design, for which $\omega_{ij} = 0.4$, $\omega_{\min} = 2$, and $\omega_{\max} = 18$ (see Sultan, 2009 for numerical

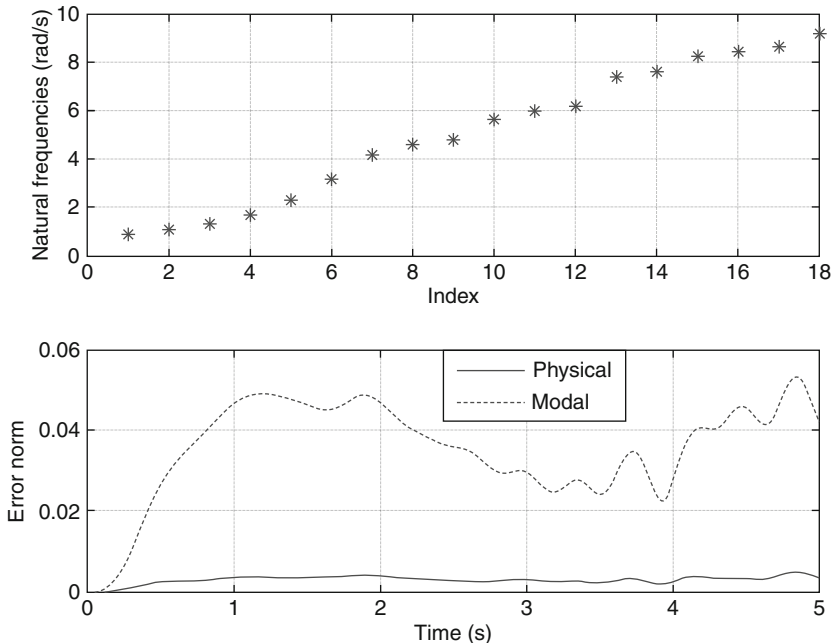


FIG. 6.4 Separated natural frequencies lead to negligible proportional damping approximation errors for a design corresponding to a minimum separation of $\omega_{ij} = 0.2$ rad/s.

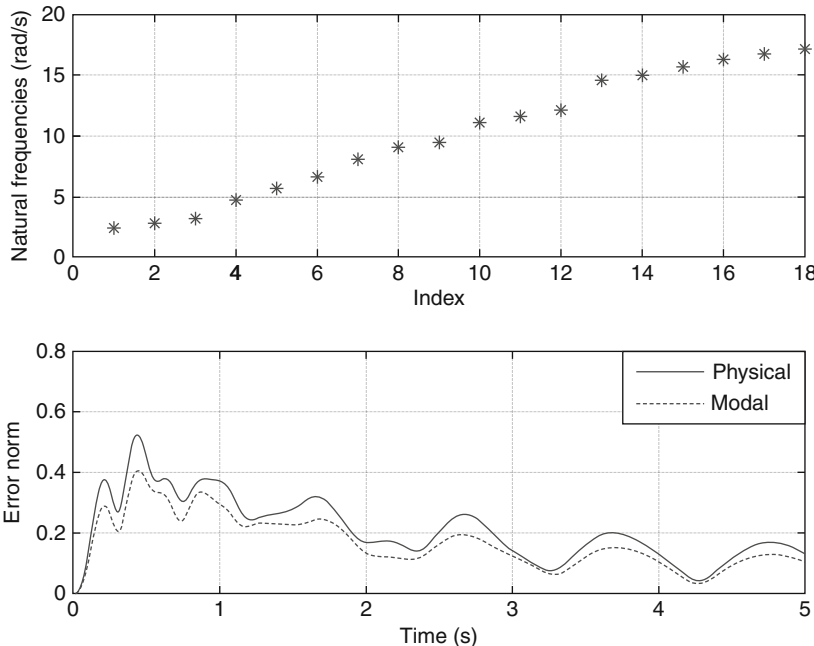


FIG. 6.5 Separated natural frequencies lead to large proportional damping approximation errors for a design corresponding to a minimum separation of $\omega_{ij} = 0.4$ rad/s.

values of the design parameters). Note that the initial conditions used in Fig. 6.5 are the same as before. It can be easily ascertained that the error in modal coordinates is much larger than the one in Fig. 6.4, despite the fact that the minimum separation between the natural frequencies is two times bigger than the one corresponding to the results in Fig. 6.4. Note that the relative separation corresponding to Fig. 6.5—defined as the minimum separation divided by the range of natural frequencies—is also bigger than the one corresponding to Fig. 6.4. Secondly, the error in the physical space is hugely amplified because the maximum singular value of the modal matrix is $\bar{\sigma}(W) = 1.55$. This is not a good design if proportional damping approximation is thought after. However, it may qualify as an acceptable dynamic design for other purposes because sufficient separation between the natural frequencies is achieved.

The results shown in Figs. 6.4 and 6.5 indicate that separation between natural frequencies might be a misleading criterion for accurate proportional damping approximation and that other criteria must be considered when the design objective is proportional damping approximation.

7. Deploying Tensegrity Structures

The accumulation of knowledge in the statics and dynamics of tensegrity structures led to a significant breakthrough: the development of a deployment procedure. Tensegrity structures deployment is particularly difficult because many constraints must be simultaneously satisfied during the process. Firstly, the integrity of the structural members must be guaranteed by placing constraints on their stress levels. Secondly, internal collision/contact must be avoided by guaranteeing sufficient clearance between the members of the structure. Thirdly, the cables should be in tension because slack cables may lead to entanglement and reduced stiffness of the structure. In addition, some performance index (energy consumption, time of deployment, etc.) should be optimized. Thus, in its complete formulation, the deployment problem is a nonlinear, path constrained optimization problem with a very large number of constraints. Because of this complexity, tensegrity structures deployment was, for a long time, attempted only conceptually (see, e.g., [Duffy, Roney, Knight, & Crane, 2000](#); [Furuya, 1992](#); [Hanaor, 1993](#)). A major development occurred in the late 1990s, when a deployment procedure which uses equilibrium manifolds to guarantee that all of the above requirements are met was developed (see [Sultan, 1999](#); [Sultan & Skelton, 1998b, 2003b](#)). The key idea is to control the motion of the structure such that the corresponding state space trajectory, called the deployment path, is *close to an equilibrium manifold*. In the following, this procedure will be exemplified using the two-stage SVD tensegrity structure.

Consider that the two-stage SVD structure ([Fig. 5.1](#)) is initially in a folded (undeployed) symmetrical prestressable configuration characterized by $\alpha_u = 69^\circ$, $\delta_u = 85^\circ$ and it must be deployed to reach a fully erected (deployed) symmetrical prestressable configuration characterized by $\alpha_d = 50^\circ$, $\delta_d = 55^\circ$. These configurations represent the “undeployed” and “deployed” configurations, respectively, shown in [Fig. 7.1](#), which depicts a deployment sequence that will be discussed shortly. Both configurations belong to the equilibrium manifold shown in [Fig. 5.3](#). The deployment method presented herein was introduced in [Sultan and Skelton \(1998b\)](#) and it requires that the rest lengths of the cables (or, equivalently, their active lengths) are controlled such that the deployment path is close to the equilibrium manifold. Then, due to the proximity of the deployment path to the equilibrium manifold, the successive configurations the structure passes through are close to equilibrium ones. Consequently, some properties of these equilibrium configurations (e.g., properties that are continuous in the generalized coordinates) are transferred to the intermediate configurations the

structure passes through during deployment. For example, geometrical properties are continuous functions of the generalized coordinates; thus, satisfaction of the clearance constraints across the entire equilibrium manifold is easily transferred to the configurations achieved during deployment. It is important to stress that this is true *only* if the deployment path is sufficiently close to the equilibrium manifold.

To facilitate satisfaction of the condition that the deployment path is close to the equilibrium manifold, the controls are required to vary in the equilibrium manifold's control set. In other words the controls are allowed to take *only* values that correspond to configurations in the equilibrium manifold, referred to as “equilibrium controls.” For the two-stage SVD structure the equilibrium controls are the saddle, vertical, and diagonal cable rest lengths. These have been derived in [Section 5.1](#), assuming linearly elastic cables, and are repeated here for convenience:

$$S_0 = \frac{k_S S}{PT_{0S} + k_S}, \quad V_0 = \frac{k_V V}{PT_{0V} + k_V}, \quad D_0 = \frac{k_D D}{PT_{0D} + k_D}, \quad (7.1)$$

respectively (see [Eq. \(5.18\)](#)). Because T_{0S} , T_{0V} , T_{0D} are functions of α and δ (see [Eqs. \(5.10\)–\(5.16\)](#)), the equilibrium controls are parameterized by these two angles (α and δ), which uniquely define a point in the equilibrium manifold. This deployment strategy requires that throughout the motion of the structure the six saddle cable rest lengths vary according to the function $S_0(\alpha, \delta)$, the six vertical cable rest lengths according to $V_0(\alpha, \delta)$, and the six diagonal cable rest lengths according to $D_0(\alpha, \delta)$. To indicate the fact that α and δ are related to the equilibrium manifold, the subscript “e” will be used. Thus, the control vector dependency on α and δ is formally written as $l_0 = l_0(\alpha_e, \delta_e)$. Next, α_e and δ_e are parameterized using functions of time, $\alpha_e = \alpha_e(t, p_\alpha)$, $\delta_e = \delta_e(t, p_\delta)$, and the system

$$M(q)\ddot{q} + c(q, \dot{q}) + C(q)\dot{q} + A(q)T(q, l_0) = 0, \quad (7.2)$$

obtained from [Eq. \(6.8\)](#) for $F = 0$, is driven by the corresponding time varying controls, $l_0 = l_0(t, p_\alpha, p_\delta)$. Note that p_α and p_δ are real-valued constant vectors. For example, if polynomial parameterizations are used, p_α and p_δ represent the coefficients of these polynomials. The parameterization $\alpha_e = \alpha_e(t, p_\alpha)$, $\delta_e = \delta_e(t, p_\delta)$ defines a curve in the equilibrium manifold which will be referred to as “the equilibrium path.”

At this point, it is important to make several observations. Firstly, by enforcing the controls to vary *only* in the equilibrium manifold's control set, the cables can be maintained in tension, thus avoiding entanglement and maintaining the structure stiff during deployment. This is so because the cable forces are continuous

functions of the controls (the rest lengths) and the generalized coordinates. Hence, if the deployment path is sufficiently close to the equilibrium manifold, the property that the tensions are positive across the entire equilibrium manifold will be transferred to the neighboring configurations achieved during deployment. Secondly, as shown in [Section 6.2](#), analysis of the linearized models concluded that each point of the equilibrium manifold is locally exponentially stable if the six joints between the bars and the base and the top are affected by linear kinetic friction. This strong stability property *and* the fact that, during deployment, the controls take values in the equilibrium manifold's control set, result in a crucial practical advantage: the deployment is fault tolerant. Indeed, if during deployment the controls are frozen to some intermediate values *and* the current state of the system is within the region of attraction of the point in the equilibrium manifold that corresponds to these values of the controls, the system will settle down asymptotically in time to this equilibrium, from which the deployment can be later restarted. Thirdly, if the deployment can be conducted in a quasistationary manner (which means that the generalized velocities and accelerations are negligible), the forces and moments experienced by the members of the structure during deployment will be close to the ones experienced at configurations in the equilibrium manifold. Hence, if the structure is designed using upper bounds on the stresses experienced at equilibria across the entire equilibrium manifold, satisfaction of the structural integrity constraints is guaranteed. Lastly, conditions under which the deployment path can be made *arbitrarily* close to the equilibrium manifold are strongly related to the stability properties of this manifold. For example, if the stability is exponential and uniform in the controls, then the deployment path can be made *arbitrarily* close to the equilibrium path using continuously differentiable and sufficiently slowly varying controls (see [Sultan, 2008](#)). Actually, arbitrarily close deployment and equilibrium paths can be achieved even if the stability is asymptotical and only piecewise constant controls are used (see [Sultan, 2008](#)). This is an important practical advantage because piecewise constant controls are easy to generate using digital technology. However, even these conditions may be too stringent because it is not necessary to make the deployment and equilibrium paths *arbitrarily* but *sufficiently* close. Hence practical solutions to the deployment problem using this methodology can be obtained even under milder stability conditions.

Returning to the example of the two-stage SVD structure deployment, an optimal control problem can be formulated and numerically solved for p_x and p_δ such that the time of deployment is minimized, subject to the constraints that the equilibrium and deployment paths are sufficiently close and the generalized velocities and accelerations are sufficiently small (see [Sultan & Skelton, 2003b](#)

for details on the numerical solution). For example for a structure with $l = 4$ m and $b = 0.27$ m, for a pretension coefficient $P = 300$ a deployment time of 13.14 s was obtained using quadratic polynomials in time for $\alpha_e = \alpha_e(t, p_\alpha)$, $\delta_e = \delta_e(t, p_\delta)$, that is,

$$\alpha_e = p_{\alpha 0} + p_{\alpha 1}t + p_{\alpha 2}t^2, \quad \delta_e = p_{\delta 0} + p_{\delta 1}t + p_{\delta 2}t^2. \quad (7.3)$$

The sequence of intermediate configurations is depicted in Fig. 7.1 and the corresponding variation of the controls in Fig. 7.2 (τ is the time normalized by the deployment time). Note that when τ reaches 1 the controls are fixed at the values corresponding to the final, desired deployed configuration, and indicated by the subscript “e.” The conditions that all cables are in tension, the clearance conditions as well as the structural integrity conditions were satisfied throughout the deployment (see Sultan & Skelton, 2003b). Note that the process is reversible, which is another advantage of this methodology: the structure can be folded back into the original configuration by reversing the variation of the controls.

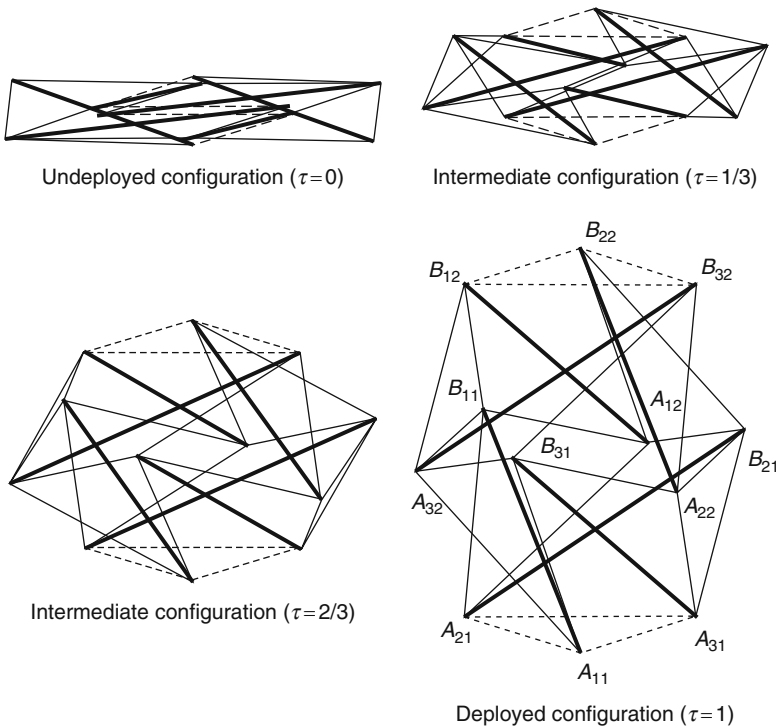


FIG. 7.1 Deployment sequence for the SVD structure.

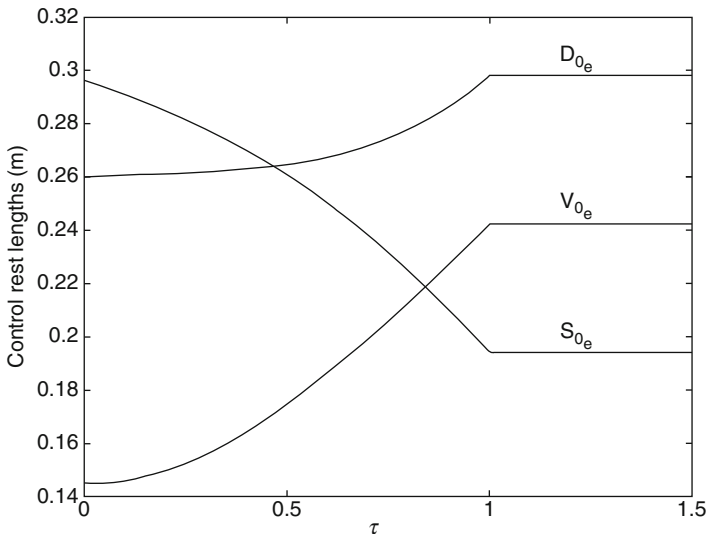


FIG. 7.2 Variation of the controls during deployment.

In [Sultan and Skelton \(2003b\)](#), the previous methodology was also illustrated on a more complex structure, a tensegrity tower with 9 bars and 33 cables and smoother controls (i.e., functions of class C^1 on the entire real axis of time) were used. Smoother controls are recommended because they reduce and may even eliminate the risk of exciting vibrations of high frequency in the structure. Skelton and coworkers later applied this deployment procedure to very complex tensegrity systems ([Masic & Skelton, 2005](#)).

There is an important disadvantage associated with the deployment procedure that uses equilibrium manifolds: it requires that many members of the structure are actively controlled. For example, in the previous example, all cables must be controlled using, for example, servomotors. The procedure can, of course, be applied using telescopic struts, or a combination of telescopic struts and controlled cables, but the number of members that must be controlled to ensure proximity to the equilibrium manifold might be prohibitive for practical implementation. To deal with this issue, later research conducted by [Tibert and Pellegrino \(2003b\)](#) focused on using *only one* central telescopic strut for deployment at the expense of reducing the space of achievable configurations and having to deal with the risk of cable entanglement. The major drawback of the procedure of Tibert and Pellegrino is that during deployment the structure has no

stiffness because cables are slack until the structure reaches the fully erected configuration. A second motor is used to stiffen the structure in the fully deployed configuration.

8. Controllable Tensegrity Structures

8.1. TENSEGRITY STRUCTURES AND CONTROL DESIGN

The 1990s meant a big step forward for tensegrity structures on the path of applications as dynamical structures. With advances in modern control theory, which enabled multivariable control for complex systems, introduction of control technology into these structures became possible. Tensegrity structures are ideal candidates for controllable structures for several reasons.

Firstly, as discussed in [Section 6.1](#), because of the clear distinction between the mechanical properties of their members (e.g., “soft,” massless elastic cables vs “hard,” rigid bodies), direct application of the physics principles to tensegrity structures leads to accurate dynamic models composed of *finite* sets of ODEs (see [Eqs. \(6.5\)](#) and [\(6.8\)](#)). This is a tremendous advantage for control design because it facilitates the direct use of modern, multivariable control theory tools. Modern control system design relies heavily on state space representations of the system’s dynamics, which are readily obtained from ODEs. On the other hand, for PDEs, which, as discussed previously ([Section 6.1](#)) are used to describe the dynamics of many conventional structures, the situation is different. For example, the separation of variables method is applied in some cases (e.g., if the equations are linear) to obtain an infinite set of ODEs and a set of PDEs with boundary values. Then, for control design, only several ODEs are retained, usually selected to capture the modes that are considered relevant for the control design problem of interest. Thus, qualitative *and* quantitative alteration of the original mathematical model is performed in the process. Moreover, this procedure complicates the verification and validation of the control system.

Secondly, tensegrity structures lend themselves naturally to integrated structure and control design ([Sultan & Skelton, 1997](#)), since their members can act as actuators or/and sensors while also serving as load carrying elements. Thirdly, since each member can act as a sensor or an actuator, tensegrity structures provide excellent opportunities for robust, fault tolerant, and redundant control architecture design. Last but not least, cables offer a very promising solution for actuation via servomotors or emerging concepts like shape memory alloys and electroactive polymers. The traditional solution for actuation of structures is to

use telescopic struts, which are plagued by well-known deficiencies such as significant wear and the difficulties associated with hydraulic actuation, including large cooling systems (see [Sultan et al., 2000](#) for more details).

8.2. RESEARCH IN TENSEGRITY STRUCTURES CONTROL

Various control and estimation techniques, ranging from linear to nonlinear ones have been successfully demonstrated on tensegrity structures. For example, in the first two papers devoted to tensegrity structures control ([Skelton & Sultan, 1997](#); [Sultan & Skelton, 1997](#)) the two-stage SVD structure depicted in Fig. 5.1 was analyzed. In the first publication ([Skelton & Sultan, 1997](#)) applications in vibration isolation and accurately pointing systems were targeted. Thus, the controlled outputs were the inertial position of the rigid top and its attitude, while the actuators were some of the cables. Linear dynamical feedback controllers were designed such that output variance constraints were satisfied, while either the control energy was minimized or input variance constraints were satisfied. Integrated structure and control design was investigated, leading to the conclusion that better performance is obtained if the structure and the control system are designed simultaneously than if they are designed sequentially (see [Sultan & Skelton, 1997](#)).

Shortly after, [Djouadi et al. \(1998\)](#) reported studies on an actively controlled tensegrity antenna composed of 27 cables and 12 struts. The goal of the control design problem was to reduce vibrations in such a system and for this purpose optimal controllers with three or six actuators were designed. The performance index that was minimized was quadratic in the nodal displacements, velocities, and in the control effort represented by actuator forces. Numerical simulations indicated that substantial reduction in the structure's vibrations can be achieved with such controllers.

[Sultan et al. \(1999\)](#) introduced linear matrix inequalities (LMIs) techniques in the design of a peak-to-peak controller for a tensegrity space telescope. Briefly, a peak-to-peak controller minimizes the ratio between the peak value of the norm of the output vector and that of the input vector. If the output vector is represented by pointing and alignment errors of a telescope and the input vector by external perturbations, then such a controller minimizes the effect of perturbations on the accuracy of the telescope. Simulations presented in [Sultan et al. \(1999\)](#) demonstrated the feasibility of such a control design for accurate pointing of a tensegrity telescope. [Sultan et al. \(2000\)](#) also demonstrated the feasibility of tensegrity structures in motion simulation by designing a nonlinear and robust tracking controller for a flight simulator. The key idea in such a system is to replace the conventional Stewart platform actuated using telescopic struts with a cable

controlled tensegrity structure. This simulator will be discussed in detail in the next section.

Later, [Kanchanasaratoor and Williamson \(2002\)](#) used the constrained particle dynamics technique to develop models for a general class of tensegrity structures. They constructed the linearized model of a three-bar tensegrity structure and used it for the design of optimal linear quadratic controllers aimed at continuously modifying the lengths of the bars in order to regulate the structure's configuration with respect to a prescribed equilibrium configuration.

[Shea, Fest, and Smith \(2002\)](#) took a new approach to tensegrity structures control design by introducing stochastic search methods. The authors point out that, due to the highly nonlinear and coupled behavior of tensegrity structures, changes in the length of a member (be it cable or telescopic strut) will affect the overall shape of the structure. Then they show how global shape control can be achieved via a combination of simulated annealing search and dynamic relaxation and using telescopic struts for actuation. Later, the same team ([Fest, Shea, & Smith, 2004](#)) used a different stochastic search algorithm combined with dynamic relaxation to identify good control commands for a complex tensegrity structure in which 10 telescopic struts are used for actuation. The goal was to maintain a prescribed slope of a plane situated in the upper level of the structure when the structure is subjected to certain perturbations. A prototype was built and successfully tested against 25 load cases, indicating good robustness properties.

Controllable tensegrity structures were also proposed for flexible robots. For example, [Aldrich et al. \(2003\)](#) solved a minimum time path following problem with saturation constraints for tensegrity used in robotics applications. Later, [Paul et al. \(2006\)](#) introduced land locomotor robots based on tensegrity. They studied the feasibility of two simple tensegrity robots and implemented automated design of controllers for forward locomotion using evolutionary techniques like genetic algorithms. The authors showed via simulations that actuator damage in a tensegrity robot can be accommodated, leading to graceful performance degradation. A tensegrity robot was also built as a proof of concept, demonstrating the ability to produce forward locomotion and showing that tensegrity structures can provide the basis for lightweight fault tolerant locomotion robots.

Recently, [Moored and Bart-Smith \(2007\)](#) used a tensegrity structure as the structural foundation for biomimetic morphing wings. In their work an optimization form-finding method is used to match biological displacements. The method assumes that the cables and struts can change their lengths. Thus, in a dynamic implementation actuation of all individual elements is required. The preliminary work reported in [Moored and Bart Smith \(2007\)](#) does not include control design but this is the next logical step for morphing structures.

In the following, an application of an actively controlled tensegrity structure in the field of flight simulation is presented.

8.3. A TENSEGRITY FLIGHT SIMULATOR

The most popular motion base for flight simulators is the Stewart platform ([Medeuil, 1988](#)), which is a complex and expensive mechanism due to the telescopic struts that are used to control the motion of the cabin. These actuators create major difficulties, especially when large accelerations and displacements must be generated. In these situations, large and rapid excursions of the telescopic struts are required, resulting in significant loads of both an inertial and dissipative nature that lead to a design including a heavy structure and a large cooling system. The life of a telescopic strut is also limited due to the considerable wearing that occurs during its operation.

A flight simulator in which the motion base is a tensegrity structure eliminates the aforementioned deficiencies by using cables for motion control instead of telescopic struts. Such a simulator can be obtained from the two-stage SVD structure depicted in [Fig. 5.1](#) as follows. Bars $A_{j1}B_{j1}$ and $A_{j2}B_{j2}$, $j = 1, 2, 3$, are rigidly attached to the base and top, respectively, and the structure has only 12 cables, the saddle and diagonal ones (see [Fig. 8.1](#)). The base is fixed, the cabin is attached to the top, and the motion is controlled using some of the cables. The bars are identical, of length l , they make the same angle with the perpendicular to the base or top, and the base and top triangles are equilateral of side length b . For simplicity, it is assumed that the cables have the same stiffness, k (see [Sultan et al., 2000](#) for details).

For mathematical modeling the bars, top and cabin are considered rigid and the cables massless and linearly elastic. In addition, for robust control design, uncertainties in the system must be taken into account. The uncertainties considered herein are due to changes in the inertial properties of the cabin. Further, the cables are separated into “active” and “passive” cables; the active ones are attached to motors and are used to control the motion of the simulator. Then, the equations of motion can be written as

$$M(q, \dot{q}, \mu)\ddot{q} + C(q, \dot{q}, \mu)\dot{q} + u_0 + A^p(q)T^p + \hat{G}(\mu) = u, \quad (8.1)$$

where $q = [\psi \theta \phi X Y Z]^T$. Here ψ, θ, ϕ are the Euler angles for a 3–1–2 sequence that characterize the orientation of a reference frame attached to the second stage ($\hat{t}_1, \hat{t}_2, \hat{t}_3$ in [Fig. 8.1](#)) with respect to the inertial frame attached to the fixed base, $\hat{b}_1, \hat{b}_2, \hat{b}_3$, and X, Y, Z are the center of mass coordinates of the second stage with respect to the $\hat{b}_1, \hat{b}_2, \hat{b}_3$ frame. Note that the second stage is composed of the

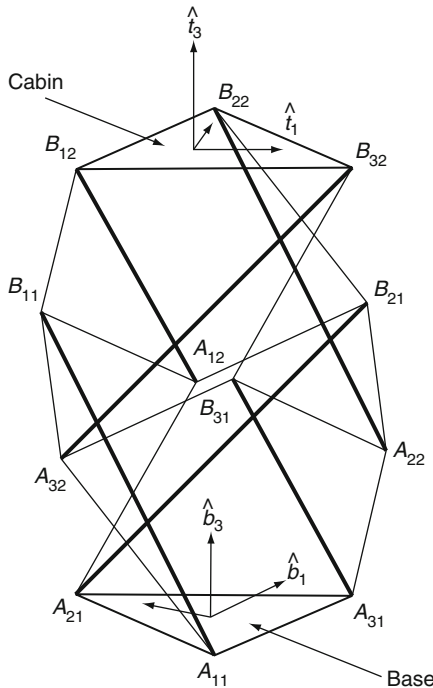


FIG. 8.1 A tensegrity flight simulator.

cabin, top, and the three bars attached to the top. In Eq. (8.1) μ accounts for the uncertainties in the inertial properties of the simulator and takes values in a known bounded set, Δ . In addition, $u_0 = A^a(q_g)T^a$ where q_g is the equilibrium configuration which corresponds to the nominal mass of the second stage, $u = u_0 - A^a(q)T^a$ is the control vector, $\hat{G}(\mu) = [0 \ 0 \ 0 \ 0 \ M_t g]^T$ where M_t is the mass of the second stage, g is the constant gravitational acceleration, whereas superscripts “a” and “p” represent the “active” and “passive” cables, respectively. Note that Eq. (8.1) can be obtained from the general equations of motion, Eq. (6.5), by introducing the constant gravitational field and the uncertainties μ , by splitting the matrix $A(q)$ in the “passive” and “active” components associated with the corresponding cables, and by expressing the quadratic term in generalized velocities as $c(q, \dot{q}, \mu) = L(q, \dot{q}, \mu)\dot{q}$ where

$$L_{ij} = \frac{1}{2} \sum_{n=1}^6 \left(\frac{\partial M_{ij}}{\partial q_n} + \frac{\partial M_{in}}{\partial q_j} + \frac{\partial M_{jn}}{\partial q_i} \right) \dot{q}_n, \quad i = 1, \dots, 6, j = 1, \dots, 6. \quad (8.2)$$

It is important to remark that expressing the equations of motions as in Eqs. (8.1) and (8.2) is essential for the design of robust nonlinear controllers (see Sultan et al., 2000 for details).

In Sultan et al. (2000), detailed analysis of the statics of the simulator has been performed. The prestressability problem, Eq. (5.1), has been solved analytically for symmetrical configurations like the ones defined for the two-stage SVD structure and depicted in Fig. 5.2 and it has been proved that the corresponding stiffness matrix is positive definite. In addition, the two angles that characterize the orientation of the bars, the declination, δ , and the azimuth, α , have been determined from the condition that maximum clearance between bars is obtained. This led to $\delta = \alpha = 60^\circ$. The static response of the simulator when the mass of the second stage varies has also been investigated (i.e., Eq. (8.1) has been solved when the generalized velocities and accelerations are zero and for various values of M_t). For control design six cables have been selected as the “active” cables from the condition that the minimum singular value of matrix $A^a(q_g)$ is maximal over all possible combinations of 6 out of the 12 cables (see Sultan et al., 2000 for details). This procedure led to the conclusion that the best choice for the active cables is represented by the six saddle cables.

The control problem for the flight simulator is described next and its solution is formulated. Let $q_d(t)$ be a desired motion of the simulator. The simulator is equipped with sensors that provide information about its current state represented by $q(t)$ and $\dot{q}(t)$. The control system uses this information to generate the control actions, $u(t)$, that ensure tracking of the desired motion by the simulator. These control actions are implemented using the saddle cables, which are actively controlled by motors attached to the bars. Ideally, the control system must be designed to guarantee that the motion of the system converges to the desired motion exponentially in time, that is, the tracking error converges to zero exponentially. Unfortunately, this stringent requirement generally leads to a discontinuous controller (Corless, 1993), which is not desirable because it may excite high-frequency vibrations in the structure. However, if the requirement is relaxed and only tracking within a given tolerance is required, a continuous controller can be designed (Sultan et al., 2000). To be more specific, let ς be the desired rate of convergence, r the desired tolerance, and $\bar{q}(t) = q(t) - q_d(t)$ the tracking error. Then, the requirement that the tracking error converges exponentially to r is expressed as

$$\|\bar{q}(t)\| \leq (a_1\|\bar{q}(t_0)\| + a_2\|\dot{\bar{q}}(t_0)\|)e^{-\varsigma(t-t_0)} + r, \quad (8.3)$$

where a_1 and a_2 are constant scalars and $\|\cdot\|$ denotes the Euclidean norm. To ensure robustness of the controller, this condition must hold for any value of the uncertainty $\mu \in \Delta$.

A simple continuous nonlinear robust controller which guarantees that Eq. (8.3) is satisfied when it is used to control the system given by Eq. (8.1) is

$$u = -U\eta - \frac{\rho^2}{||\rho\eta|| + e}\eta, \quad (8.4)$$

where

$$\rho = \beta_1||v|| + \beta_2||v|| + \beta_3, \quad v = \dot{q}_d - \Lambda \bar{q}, \quad \eta = \dot{\bar{q}} + \Lambda \bar{q}, \quad \bar{q} = q - q_d. \quad (8.5)$$

The scalars $\beta_1, \beta_2, \beta_3, e$ and matrices Λ, U must be selected to satisfy the following conditions:

$$\begin{aligned} 0 < \beta_0 I \leq M(q, \mu) \leq \beta_1 I, \quad ||C(q, \dot{q}, \mu)|| \leq \beta_2 ||\dot{q}||, \\ ||u_0 + A^P(q)T^P + \hat{G}(\mu)|| \leq \beta_3, \end{aligned} \quad (8.6)$$

$$U > \varsigma \beta_1 I, \quad \Lambda > \varsigma I, \quad 0 < e \leq (\varsigma r)^2 \lambda_{\min}(U) \frac{\beta_0}{\beta_1}, \quad (8.7)$$

where $\lambda_{\min}(U)$ is the minimum eigenvalue of U (see Zenieh & Corless, 1997 for details on the derivation of this controller). Analytical determination of these constants is rarely possible, hence they are usually computed numerically as shown in Sultan et al. (2000).

The ability of the tensegrity simulator equipped with this controller to track motions of an airplane is illustrated next. First, the notion of tracking in this context must be clarified. The main task of a flight simulator is to give the pilot the same sensations as when flying the real aircraft. These sensations are caused by the accelerations and angular velocities the pilot experiences. Then, if the acceleration and angular velocity of the aircraft during a certain maneuver is mimicked by the simulator, the pilot will have the same sensation when ‘‘flying’’ the simulator as when flying the real aircraft.

Consider now that a certain airplane, whose characteristics are given in Sultan et al. (2000), is in rectilinear uniform translational flight at an altitude of 3000 m. This flight condition is dynamically equivalent to an equilibrium configuration of the simulator, which is characterized by q_g . For this example, the following values were considered for the simulator parameters: $l = 5$ m, $b = 3.33$ m, $k = 5000$ N. A pretension coefficient of $P = 2000$ and a gravitational acceleration of $g = 9.81$ m/s² were used. The nominal mass was $M_t = 140$ kg and the corresponding equilibrium $q_g = [302.2 \ 0 \ 0 \ 0 \ 0 \ 3.46]^T$, where the angle is in degrees and the distance in meters. For simplicity the inertia matrix was chosen

diagonal, $I_t = \text{diag}[300 \ 400 \ 500] \text{ kg m}^2$. The controller was designed using the following values (see [Sultan et al., 2000](#) for details on their computation):

$$\begin{aligned}\zeta &= 25, & r &= 0.2, & \beta_0 &= 90, & \beta_1 &= 700, & \beta_2 &= 500, & \beta_3 &= 40,000, \\ e &= 56,252, & \Lambda &= 26I, & U &= 17,501I.\end{aligned}\quad (8.8)$$

When a step elevator command is applied the airplane undergoes a pitching motion that must be tracked by the simulator and the controller. [Figure 8.2](#) shows the time history of the vertical and pitch accelerations of the airplane and simulator when the amplitude of the step command is 2° , whereas the corresponding variations of the controls (the rest lengths of the saddle cables) are given in [Fig. 8.3](#) where the cables have been labeled as follows: 1 = $A_{12}B_{21}$, 2 = $A_{12}B_{11}$, 3 = $A_{22}B_{21}$, 4 = $A_{22}B_{31}$, 5 = $A_{32}B_{11}$, and 6 = $A_{32}B_{31}$. It is clear that the simulator is very effective in tracking the accelerations even through the critical phase, at the onset of the new motion. The cable forces variations are also within an acceptable range. Numerical simulations indicated that all of the cables

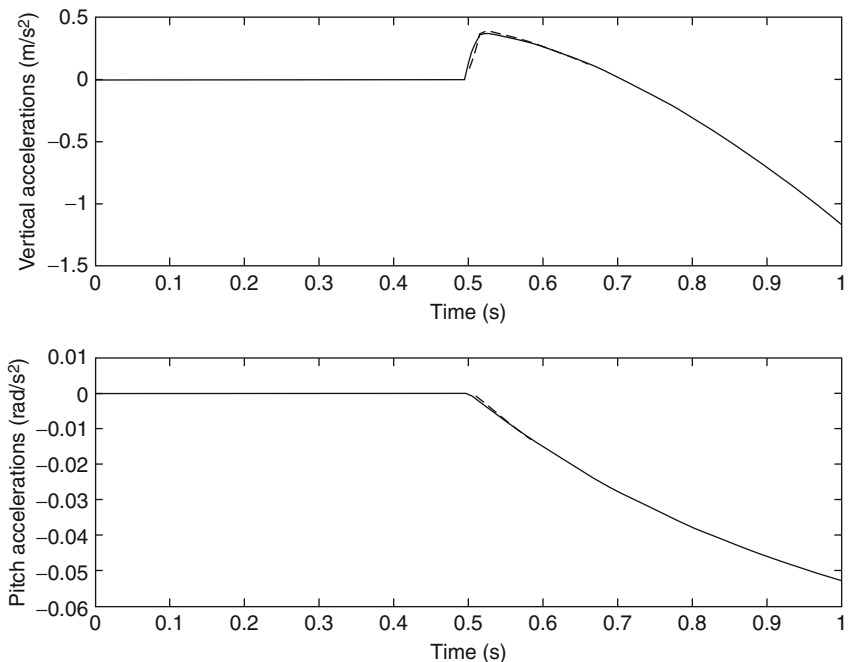


FIG. 8.2 Tensegrity simulator behavior for a step elevator command; desired accelerations (continuous lines) are tracked by the tensegrity simulator.

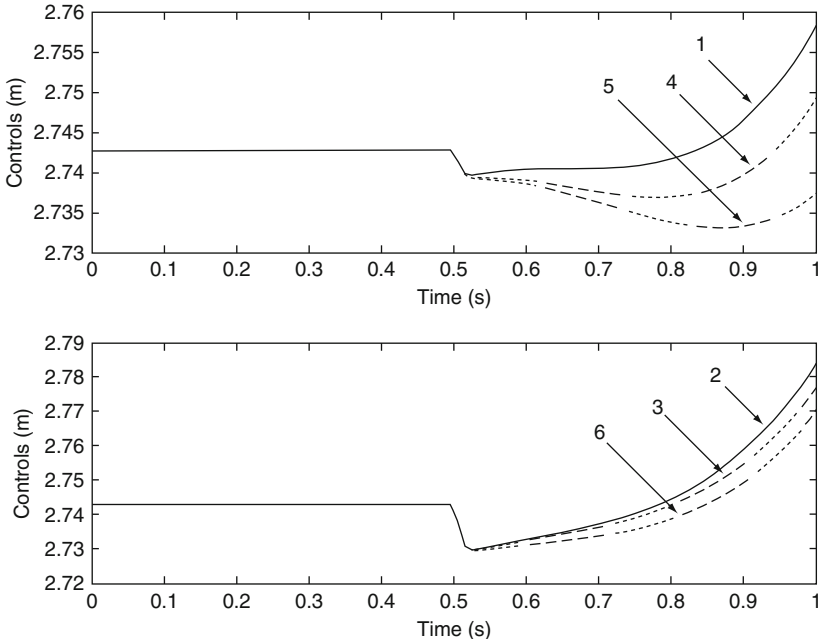


Fig. 8.3 Variation of the controls during the step elevator command.

are in tension throughout the motion and that the tracking is even better for angular velocities and other accelerations (see [Sultan et al., 2000](#)).

The robustness of this controller is illustrated in [Fig. 8.4](#). The robustness has been evaluated as follows: the controller designed for the nominal inertial characteristics, M_t and I_t , was used in numerical simulations on two simulators: one for which M_t and I_t were perturbed by +50%, the second for which these quantities were perturbed by -50%. [Figure 8.4](#) shows the time histories for the vertical accelerations when a step elevator command of 5° is applied for four systems: the airplane (continuous line), the nominal simulator, and the two simulators with perturbed inertial properties (the “+” and “×” curves). One can easily ascertain that the tracking is very good even for these large perturbations (similar results were obtained for other accelerations and angular velocities).

9. Tensegrity Structures in Biology

Early interest in the connection between tensegrity and biology—prompted by the similarity between the architecture of regular viruses and tensegrity structures ([Caspar & Klug, 1962](#))—flourished in the 1990s due to the diligent efforts of

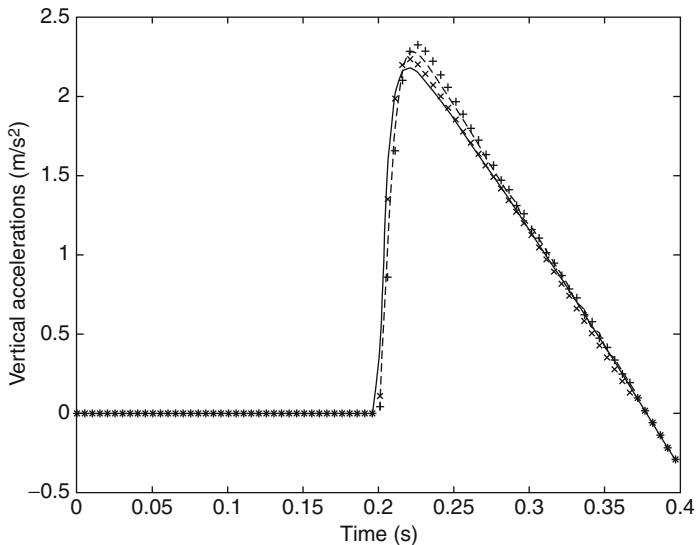


FIG. 8.4 Robustness of the controller: “+” represents the simulator response for 50% perturbations, “×” the response for -50% perturbation, “- - -” the nominal design response and continuous line the airplane response.

several biologists and biomedical engineers, who started to advocate for a model of the cytoskeleton based on tensegrity structures. The cytoskeleton, which is present in all living cells, represents a scaffolding (or skeleton) contained within the cytoplasm. It includes three main kinds of filaments classified as: microtubules, which are hollow cylinders able to carry significant compression, actin filaments, which are elastic components responsible for resisting tension, and intermediate filaments, which are also elastic, highly heterogeneous and connected to all the other elements of the cell. Following observations of the cytoskeleton architecture, the tensegrity cellular model emerged from the necessity to explain mechanotransduction—the process through which cells sense and transduce forces into cellular biochemistry and gene expression changes—by understanding the structure of the cell.

Numerous approaches to understanding the mechanics of the cell focused on the contribution of the membrane, viscous cytoplasm, and individual biopolymers that are found within the cytoskeleton, depicting the cell either as a simple mechanical continuum, a filament gel, or a tensed cortical membrane. Advanced models of the continuum type include a two-compartment model comprised of an elastic cortical membrane and a viscous or viscoelastic cytoplasm (Fung & Liu, 1993). Although useful for the quantification of cell’s

viscoelastic parameters, these models do not take into account the existence of the internal cytoskeleton and its known role in bearing both static ([Shroff, Saner, & Lal, 1995](#)) and dynamic ([Wang et al., 2001](#)) mechanical loads within the cell. On the other hand, the cellular tensegrity model assumes that the actin and intermediate filaments carry a tensile stress within the cytoskeleton that is balanced by internal microtubules and extracellular adhesions. This model differs from continuum models of the cell in that it proposes a critical stabilizing role for cytoskeletal prestress in cell mechanics, and it predicts that specific elements within the cytoskeleton bear either tension or compression.

The first motivation for the tensegrity cellular model was given by the striking resemblance between living cells' cytoskeleton and a tensegrity structure: like a tensegrity structure, the cytoskeleton is composed of "hard" elements (microtubules), and "soft" elements (actin filaments and intermediate filaments) intertwined in a network balanced through internal forces and cellular adhesions (see [Figs. 9.1 and 9.2](#)). As clearly explained by [Ingber \(1998\)](#), the similarities go even further. Inside the cell, a gossamer network of contractile microfilaments extends throughout the cell, exerting tension, in the same manner as cables in a tensegrity structure do. Opposing the tensile forces from the network of microfilaments are two main types of elements: the extracellular matrix, which in a tensegrity cellular model corresponds to the structure's attachments to a surface, and, internal to the cell, microtubules or large bundles of crosslinked microfilaments, which can be assimilated with the bars or, in more complex tensegrity models, with shells or three-dimensional bodies. The intermediate filaments are the

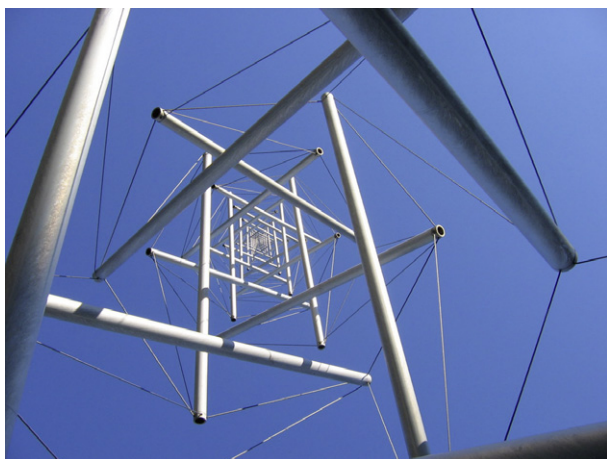


FIG. 9.1 Tensegrity structure built by Snelson.

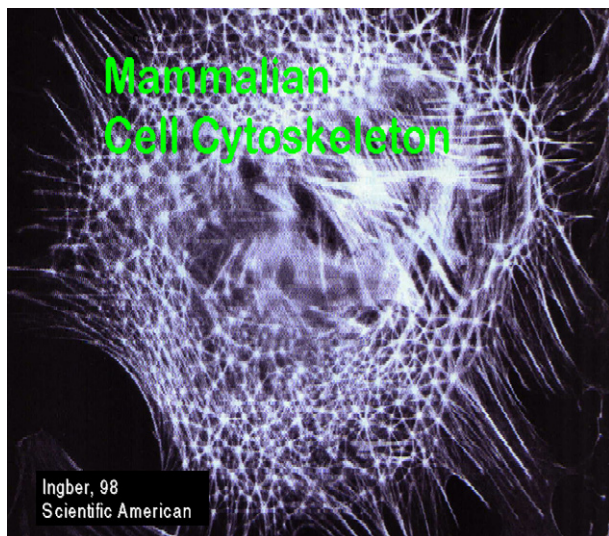


FIG. 9.2 Photo of the cytoskeleton by Kate Nobes.

integrators connecting microtubules to contractile microfilaments, the cell's surface, and the nucleus. Although the cytoskeleton is surrounded by membranes and penetrated by viscous fluid, it is the network of molecular elements that stabilizes the cell, with the tensile elements playing a crucial role in stiffening the cell, exactly as cables in a tensegrity structure do.

Several mathematical formulations of tensegrity cellular models have shown qualitative and quantitative consistencies with *static* experimental results in various cell types (see, e.g., [Coughlin & Stamenovic, 1997, 1998](#); [Stamenovic & Coughlin, 2000](#); [Stamenovic et al., 1996](#); [Wendling, Oddou, & Isabey, 1999](#); [Wendling et al., 2003](#)). For example, tensegrity structures strong anisotropy and emergent behavior observed under static loading is consistent with the experimentally observed behavior in living cells ([Stamenovic et al., 1996](#); [Wendling et al., 1999](#)). The hardening characteristic observed in tensegrity structures models subjected to stretching loads (see Fig. 5.4) was correlated with similar observations in living cells ([Wendling et al., 1999](#)). An important discovery related to the static response of the cell and the behavior of its internal members was obtained using *buckling and postbuckling models* for the bars in tensegrity models. It has been ascertained that such models yield qualitatively *and* quantitatively superior consistencies with experimental observations on living cells (see, e.g., [Coughlin & Stamenovic, 1997](#); [Volokh et al., 2000](#)) than if the bars are considered rigid (see [Stamenovic et al., 1996](#)). These results suggest that

buckling of the microtubules is essential in understanding cell deformability and it may be the mechanism through which cells resist large compression forces (see [Stamenovic & Coughlin, 1999](#)). Moreover, the results are in agreement with measurements on isolated cytoskeleton elements, which indicate that microtubules indeed buckle under compression ([Gittes, Mickey, Nettleton, & Howard, 1993](#)). Tensegrity models were also successful in explaining the observation that the stiffness of the cell increases linearly with the prestress in the cytoskeleton for a relatively large range of prestress ([Stamenovic & Coughlin, 2000](#); [Wang et al., 2001](#)). In addition, the stiffness changes in a simple tensegrity model developed by [Coughlin and Stamenovic \(1998\)](#) to mimic spreading were consistent with experimental observations on cells.

Advances have also been made in using cellular tensegrity models to explain the *dynamics* of living cells. [Canadas et al. \(2002\)](#) used a tensegrity structure with viscoelastic elements as a model of the cytoskeleton to analyze the creep behavior of cells. Their study concluded that the variations of the normalized elasticity and viscous moduli with the internal tension (prestress) and the size of adherent cells are consistent with results provided by models of tensegrity structures in which Voigt elements are used to model the mechanical behavior of the cables and the bars are considered rigid. Later, [Sultan et al. \(2004\)](#) used a modified two-stage SVDT tensegrity structure model in which intermediate filaments were introduced to obtain quantitative and qualitative agreement between experimentally observed frequency responses of cells and numerically computed responses of the tensegrity structure model. In this model, in an attempt to mimic the way intermediate filaments, actin filaments, and microtubules interact within the cytoskeleton, the intermediate filaments were modeled as radial elastic elements connected at the center of the structure and to the end points of the bars. All the bars (i.e., microtubules) were assumed to be rigid and all the cables, corresponding to the actin and intermediate filaments, were modeled as Voigt elements. [Figures 9.3 and 9.4](#), in which G' represents the elastic moduli and G'' the viscous moduli, illustrate the results. Atomic force microscopy revealed that at a fixed external excitation frequency, G' and G'' for cells increase approximately linearly with prestress, whereas at fixed prestress, they increase with frequency according to a power law. As shown in [Figs. 9.3 and 9.4](#), these dependencies are quantitatively matched by *this* particular tensegrity structure model. Interestingly, as discussed in [Sultan et al. \(2004\)](#), radial intermediate filaments proved to be crucial in mimicking these dependencies: when other tensegrity models that did not include these filaments were used, matching the experimental data was not possible. This suggests the importance of including radial elements that mimic the intermediate filaments into the tensegrity model. This study also led to the conclusion that *heterogeneity* within the model is

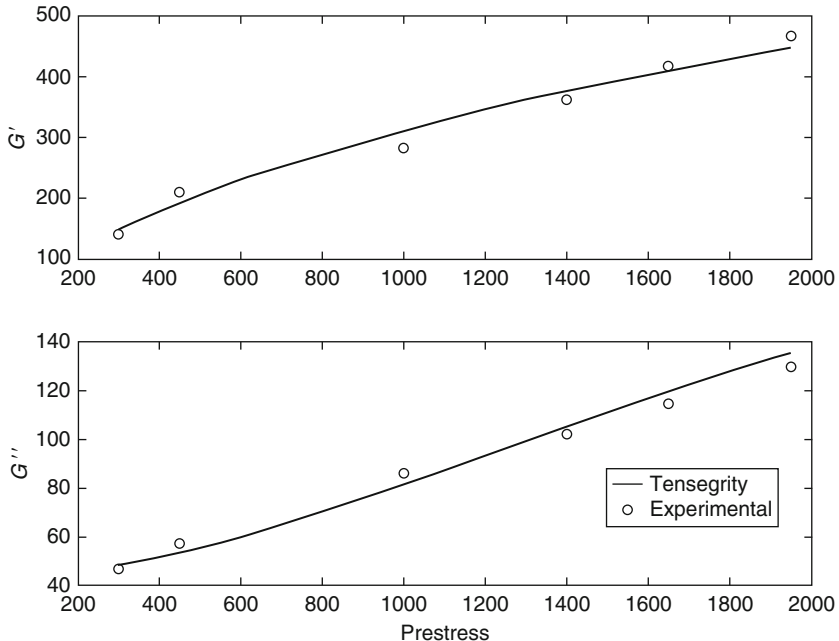


FIG. 9.3 Elastic (G') and viscous moduli (G'') variations with prestress at fixed frequency for a two-stage SVDT tensegrity structure with intermediate filaments (continuous line) match experimental data of a cell (circles).

crucial in *quantitatively* matching the experimentally observed frequency response of the cell. However, the degree of heterogeneity required to obtain agreement between experimental data and model predictions is apparently not realistic (see [Sultan et al., 2004](#)).

Recently, [Canadas, Wendling, and Isabey \(2006\)](#) addressed the role of heterogeneity and the contribution of the internal geometry, via structural rearrangement, on the oscillatory response of a tensegrity model. Their tensegrity structure is *homogeneous*, composed of 24 cables modeled as Voigt elements and six rigid bars, and does not include intermediate filaments. Using numerical simulations of this model's response for low amplitude oscillations, the authors ascertained a specific frequency-dependent contribution of elastic and viscous effects which is responsible for significant changes in the model's dynamical properties. The influence of the spatial rearrangement of the structure's members on the response decreases from low to high frequency as dominant effects are transferred from mainly elastic to mainly viscous. Importantly, the normalized elastic modulus increases with frequency while the normalized viscous modulus decreases, each

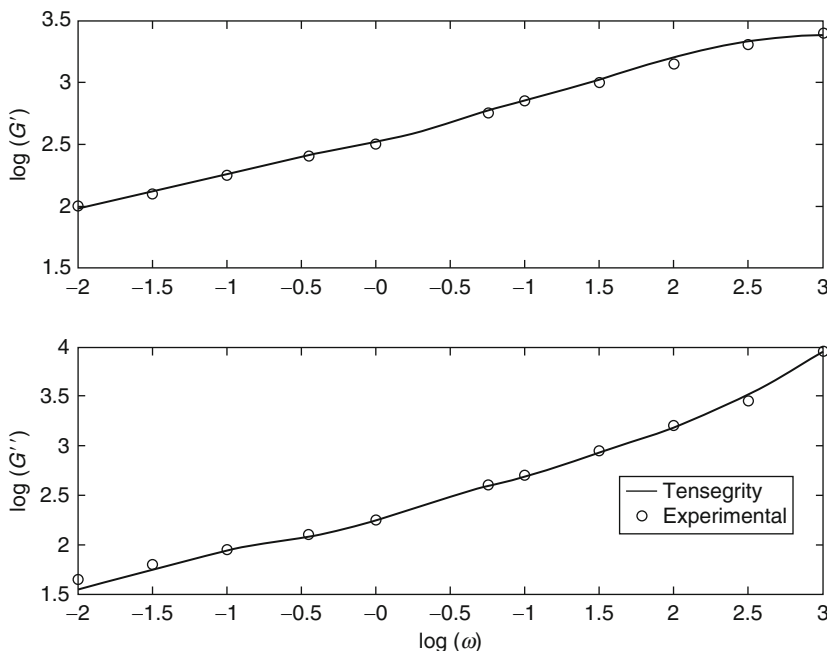


FIG. 9.4 The frequency response of a two-stage SVDT tensegrity structure with intermediate filaments at fixed prestress matches the frequency response of a cell.

dependency corresponding to a specific power law variation over a certain frequency range. Since heterogeneity was eliminated from the model, the satisfactory agreement between the numerical results provided by this tensegrity model and *in vitro* cell experiments led the authors to the conclusion that the frequency-dependent mechanism of spatial rearrangement could play a major role in oscillatory cell dynamics.

These static and dynamic consistencies indicate that a model based on tensegrity can serve as a unifying model of the mechanics of the cell that may help to explain how mechanical behavior emerges through collective interactions among different cytoskeletal filaments and extracellular adhesions in living cells. The major criticism with respect to the existing models and published studies is that current tensegrity cellular models are too simple, accounting only for *some* mechanical effects while ignoring other important and complex interactions of the living cell. This is definitely a challenge that must be addressed by future research. More complex tensegrity models must be developed which should include membranes and effects similar to cytoplasmatic viscosity. Also, more

refined models should take into account the experimentally observed behavior of certain cytoskeletal elements. As it has been remarked previously, microtubules display buckling behavior, which is a major factor in explaining the amazing shape change capabilities of the cell. However, dynamic models of the cell that account for this effect do not exist. Likewise, current tensegrity cellular models consider elastic Voigt elements, whereas it has been experimentally determined that the elastic elements of the cell display nonlinear elastic behaviors. For example, the intermediate filaments are known sources of nonlinear elastic behavior (see, e.g., [Janmey, Eutenauer, Traub, & Schliwa, 1991](#); [Ma, Xu, Coulombe, & Wirtz, 1999](#) and the references therein). Hence, further improvement of the tensegrity cellular model requires nonlinear elastic models for the intermediate filaments (see [Sultan et al., 2004](#) for more discussions). Lastly, some of the observed mechanical behaviors of cells can be explained by other mechanisms than tensegrity, ranging from phase transition phenomena to various discretized mechanical systems. For example, linear lumped spring–dashpot analogues are often used as basic models that are fit to the data obtained from mechanical measurements of living cells ([Bausch, Ziemann, Boulbitch, Jacobson, & Sackman, 1998](#); [Thoumine & Ott, 1997](#)). A more advanced model, which proved valuable in mimicking the mechanical behavior of living cells, includes a two-compartment model comprised of an elastic cortical membrane and a viscous or viscoelastic cytoplasm ([Fung & Liu, 1993](#); [Yeung & Evans, 1989](#)).

In addition to the tensegrity work in cell biology, it is worth to remark that other instantiations of tensegrity structures in life sciences have been recently reported and investigated. For example, [Zanotti and Guerra \(2003\)](#) proposed models based on tensegrity structures to explain protein folding, [Maina \(2007\)](#) used tensegrity for avian lung modeling, while [Frantsevich and Gorb \(2002\)](#) suggested that a prestressed tensegrity structure can be used to describe a certain element of the hornet's leg, namely the arcus. This work is particularly interesting because it reports the natural occurrence of a deployable tensegrity structure. The two authors investigated the hornet's leg attachment pads which give the insect the ability to adhere to a surface. These pads consist of soft deformable structures called aurolia (singular: arolium). The arolium is controlled by a single retractor muscle making it precisely deployable when it is necessary to hold the insect onto a surface. The authors experimentally investigated the mechanical unfolding of the arolium and reached the conclusion that the best model for the crucial element in achieving unfolding, the arcus, is a prestressed tensegrity structure which provides gradual transmission of forces during folding and unfolding.

10. The Future

As Motro pointed out by entitling his book “Tensegrity, the structural systems for the future” (Motro, 2003), it is expected that the future of structural design belongs to these highly flexible, adaptable, and multifunctional structures. Conventional truss structures will most likely fade away as we shall learn how to master the art of building and operating biological-like structures, to which tensegrity have a striking resemblance (see Frantsevich & Gorb, 2002; Ingber, 1998).

Biology and bioengineering will influence research in tensegrity and they will benefit tremendously from the development of more accurate and complex models of tensegrity structures. This interaction will lead to a unified approach to tensegrity structures investigation, in which research in tensegrity as engineering and biological systems will be a two way process. So far, the engineering to biology direction was heavily exploited: models of engineering tensegrity structures were developed and used to explain the behavior of biological systems. Future research will also reverse the process: inspiration from biology will be used to design new tensegrity-based engineering structural systems. For example, by engineering tensegrity structures with membranes to mimic living organisms, morphing structures capabilities will be developed, which will benefit, among other applications, future micro-unmanned air vehicles. Understanding sophisticated tensegrity models will help to better explain how biological organisms interact and function and the resulting knowledge will be leveraged into the emerging field of tissue engineering and organ reconstruction.

It is expected that the first major market for tensegrity structures will be in space structures, because of these structures multiple advantages for such applications: they are lightweight, having a significant strength to mass ratio, can be built as integrated systems with all members capable of carrying actuating, sensing, and information-transmitting functions, and have huge potential for redundant, fault tolerant, easily reconfigurable control. If properly implemented in an integrated design, these characteristics will enable *autonomous, mission adaptive* tensegrity systems. Future generations of space stations, telescopes, robotic manipulators, deployable antennas, and unmanned vehicles will benefit tremendously from tensegrity-based systems.

For applications targeting a mass market (e.g., tensegrity sensors for civil applications such as health monitoring in buildings, bridges, etc.) the situation is different. *Cost-effective manufacturing techniques have to be developed* in order to make tensegrity structures competitive in markets already dominated by other, currently less costly solutions. However, there are several Earth-related civil

applications in which tensegrity structures are prime candidates, like adaptive buildings and energy-harvesting and converting devices. As soon as the adaptive, actively controlled buildings concept gains momentum, these structures will proliferate. Energy-harvesting devices will also find in tensegrity ideal candidates ([Scruggs & Skelton, 2006](#)), because the kinetic energy from the environment can be easily stored in tensegrity structures through the potential elastic field of the elastic elements. [Defossez \(2003\)](#) used similar energy-based considerations to suggest that tensegrity structures can be used as shape memory actuators. He also took the controllable, active tensegrity concept one step further by proposing logical, programmable tensegrity devices ([Defossez, 2004](#)).

Unfortunately, the future does not come at an easy price and many obstacles have to be surmounted to enable tensegrity structures applications. Some of these obstacles are presented next.

11. Challenges for Controllable Tensegrity Structures

As already mentioned, recent advances opened many avenues for tensegrity as controllable structures in applications such as space telescopes, deployable antennas, morphing structures, and autonomous robots, to name only a few. However, crucial challenges lie ahead on the path of controllable tensegrity structures implementation. The biggest barrier is that repeatable, robust *manufacturing capabilities* do not exist even for static tensegrity structures. Kenneth Snelson perfected his art of building instantiations of tensegrity structures but for cost-effective proliferation of these structures, automated manufacturing is crucial. Except for recently developed university laboratory experiments few implementations of controllable tensegrity structures exist. The main reasons for the slow advance in the implementation of controllable tensegrity structures are the challenges their actuation faces. The requirements for tensegrity structures actuation are driven by their specifics, some of which are discussed next (also see [Sultan, 2006](#)):

- Tensegrity structures are generally *lightly damped* (see [Oppenheim & Williams, 2001a,b](#)), which raises several issues with their actuation. On the one hand, this property is desired for dynamical applications because it leads to reduced energy dissipation and hence reduced energy consumption, while also reducing the requirement for complicated cooling mechanisms. On the other hand, the risk of unwanted large amplitude vibrations, which are poorly damped, is high. Hence, first and foremost, the actuators should *avoid inducing resonance* into the structure. Ideally, they should also have adequate bandwidth and be equipped with notch filters. *Vibration reduction devices* should also be installed on tensegrity structures.

- The distribution of the *natural frequencies can be extremely unfavorable by being clustered in a narrow region* ([Murakami & Nishimura, 2001a,b](#); [Nishimura & Murakami, 2001](#); [Sultan, 2009](#)). This fact, coupled with the lightly damped property previously mentioned, may lead to unsatisfactory responses when the structure is subjected to excitation frequencies that are close to the regions of clustered natural frequencies. Thus, the actuators selection process for tensegrity structures is complicated even further. For example, the actuators as well as the filters, which are very often placed on controllable structures, are recommended to be smooth. A filter characterized by a diagonal transfer function $\Gamma(\omega)$ is smooth if

$$\left| \frac{\partial \bar{\sigma}(\Gamma)}{\partial \omega} \right| \ll \left| \frac{\partial \bar{\sigma}(\Pi)}{\partial \omega} \right| \text{ for } \omega = [\omega_i - 0.5\Delta\omega_i, \omega_i + 0.5\Delta\omega_i], \quad (11.1)$$

where $\bar{\sigma}(*)$ denotes the maximum singular value of $*$ and $\Delta\omega_i$ is the half-power frequency at the i th natural frequency of the structure characterized by the transfer function $\Pi(\omega)$ (see [Gawronski, 2004](#)).

- The *range of significant natural frequencies of tensegrity structures can be large* ([Sultan et al., 2002b](#)). This fact raises issues with the actuating as well as with the sensing devices installed on controllable tensegrity structures. For example, to capture the significant dynamics of the structure, the *sampling rate* of the sensors should be at least twice the highest natural frequency of interest.
- Many controllable tensegrity structures applications involve *large displacements*. Hence, actuators capable of *large strokes* are needed to properly cover the large operating range of these structures while avoiding resonance phenomena. Thus, different devices will be necessary to carry out the vibration reduction and actuation tasks.
- Ideally, the actuators should *not alter the mechanical characteristics* of the structure. Hence, their inertial and stiffness properties should be negligible in comparison with those of the structure. This is a demanding, contradictory requirement for *lightweight* and *flexible* structures like tensegrity.

Despite the aforementioned challenges, promising solutions for tensegrity structures actuation are emerging as follows.

11.1. SERVOMOTORS

The progress in microelectronics has made it possible to apply modern control to digital servomotor control. For controllable tensegrity structures brushless servomotors offer several advantages. Firstly, in the case of power failure, they

can apply dynamic braking (Dote, 1990). In a deployment scheme like the one proposed by Sultan and Skelton (1998b, 2003b) and discussed in Section 7, this is especially useful, since the structure will settle down to a neighboring asymptotically stable configuration from which deployment can be later restarted. Secondly, these motors have a low vibration level because they are easy to balance. This will prevent adding to the dynamics of the controlled tensegrity structure, which is very complex in itself. Thirdly, brushless servomotors have long life and high reliability because they do not have brushes or commutators. This makes them especially attractive in controllable tensegrity applications if placed inside the bars, where access is difficult. Lastly, modern servomotors have a high speed of response, a wide range of controlled speed, they are able to provide position, speed, and force control, and their bandwidth is adjustable, which is desirable for the actuation of lightly damped tensegrity structures.

The biggest disadvantage these actuators have is their complexity. For example, their control necessitates, at the minimum, the main motor, current voltage, magnetic flux, temperature sensors, and a power converter/amplifier (Dote, 1990).

11.2. SHAPE MEMORY ALLOYS

Shape memory alloys (SMAs) return to a predetermined shape when heated. When a SMA is below its transformation temperature, it has a low yield strength and can be easily deformed into a new shape. When the material is heated above its transformation temperature it undergoes modification of its crystal structure and this causes it to return to the original shape (Kauffman & Mayo, 1993). If the SMA encounters resistance during this transformation, it generates extremely large forces that may result in large strokes. This phenomenon provides a mechanism for *remote actuation*, especially useful for tensegrity structures in space applications. Moreover, these actuators are generally lightweight and will not affect dramatically the dynamics of the structure.

The major disadvantage of SMAs is the slowness of their cooling cycle. Another inherent problem with SMAs is the precise control of their shape. While standalone SMA actuators are still far from maturity, hybrid systems combining SMAs with servo systems, harvesting the advantages of both actuation mechanisms, may be very useful for future controllable tensegrity applications.

11.3. ELECTROACTIVE POLYMERS

As already mentioned, for controllable tensegrity structures, actuating materials capable of providing *large strokes* are necessary. Since the 1990s, new electroactive polymer (EAP) materials have emerged that exhibit large strains.

Polymers that can be activated chemically, thermally, optically, or magnetically to change shape or size have been available for many years but the convenience and practicality of electrical stimulation made EAPs extremely attractive. These EAPs can be divided into two groups based on their activation mechanism: ionic (involving mobility or diffusion of ions) and electronic (driven by electric fields). Ionic EAP materials such as gels, polymer–metal composites, conductive polymers, and carbon nanotubes require an electrolyte for actuation. Their major advantage is the low drive voltage requirement. However, there is a need to maintain a high level of humidity for their satisfactory operation, and, except for conductive polymers and carbon nanotubes it is difficult to sustain displacements induced by direct current (DC). The electronic polymers (i.e., electrostrictive, electrostatic, piezoelectric, ferroelectric) hold the induced displacement under activation of a DC voltage. These materials have great mechanical energy density but they require a high activation field.

There are several major disadvantages that still prevent the widespread usage of EAP materials such as: EAPs are still exhibiting low conversion efficiency, are not robust, and standard commercial materials are not yet available for consideration in practical applications on a large scale (see [Bar-Cohen, 2004](#) for more details on EAPs).

11.4. PIEZOACTUATORS AND MAGNETOSTRICTIVE ACTUATORS

Certain types of crystals have what is called a piezoelectric property, causing them to expand when electric voltage is applied and return to normal when the electric voltage is cut. A device that harnesses this property and produces movement is called a piezoelectric actuator. Piezoelectric actuators have some particular advantages such as extremely rapid response, ultra-precise movement, and large forces. However, they result in very small strain and displacement, rendering them less appealing for large displacement applications typical of tensegrity structures than servomotors, SMAs, or EPAs. Nevertheless, they may represent efficient active *vibration reduction* devices.

Magnetostriction occurs in ferromagnetic materials, causing them to deform under a magnetic field. One of the most successful magnetostrictive materials is Terfenol-D, which has been used in several high-reliability linear-motor-based actuators ([Ashley, 1998](#)). Terfenol-D produces 5–10 times more strain than piezoceramics as well as a larger force. Terfenol-D also offers a broad range of operating temperatures (-60°F to 160°F) ([Ashley, 1998](#)). The continuous cycling of Terfenol-D through its temperature range has no effect on its magnetostrictive performance. This is a significant advantage over piezoceramics, which experience irreversible losses at only 50% of their Curie temperature and

fully depolarize if the Curie temperature is exceeded (Ashley, 1998). Magnetostrictive actuators also require lower voltage. Like piezoactuators, magnetostrictive actuators may provide good solutions for *vibration reduction* in tensegrity structures. However, to get large strokes complex designs are necessary. For example, magnetostrictive-based stepping motors use an accumulation of small steps produced by quasistatic deformation of the active materials. This concept allows positioning actuators with holding force at rest and long stroke (20–50 mm) (Kottamasu, 1997). A key limiting factor for increased use of these actuating devices is the relatively *high cost*, which is determined predominantly by the rare-earth materials.

12. Conclusions

Tensegrity structures emerged as an *artistic trend* during the early-mid-twentieth century. The interest in these structures gradually migrated from the inspirational world of art to the rigorous world of science, as the necessity for lightweight structures increased with the advent of the space exploration era. Tensegrity structures specifics such as lightness, potential for deployment, and flexibility made them prime candidate solutions for spatial and *dynamic structures* applications. At the same time, advances in computational science and computing power enabled research in tensegrity structures of complexity hardly imagined before. Thus, during the 1990s research in tensegrity diversified and turned into a *multidisciplinary* as well as *interdisciplinary* activity. In the fundamental research area, knowledge reached a level of maturity that prompted the development of revolutionary applications. For example, advances in modern control, digital signal processing, and microelectronics, recently led to successful *controllable tensegrity* structures designs and laboratory implementations in deployable structures and robotics. Furthermore, the observation that many living organisms use as building blocks structures which resemble and have properties similar to tensegrity structures (e.g., prestressability, stiffening under nonzero prestress, large flexibility), established a strong connection between life sciences and tensegrity research. This led to better understanding of the mechanisms responsible for certain static and dynamic behaviors in living cells.

The main challenge for these structures proliferation in engineering is related to the development of repeatable, robust, and cost-effective *manufacturing techniques*. Controllable tensegrity structures face additional challenges, especially due to their damping characteristics and potentially unfavorable natural frequencies distribution, which lead to stringent and conflicting requirements for

actuators, sensors, and control, particularly in applications involving large displacements. However, potential actuation solutions are emerging such as servomotors, shape memory alloys, electroactive polymers, piezoactuators, and magnetostrictive actuators, with the first three categories preferable for large displacement control and the last two for vibration reduction.

In life sciences, existing tensegrity models face a major criticism in that they are too simplistic to accurately describe the ultimate complexity at work, life. Thus, increasingly complex models have to be developed in order to sustain initial success of tensegrity structures models in biology. For example, in cell biology models that account for the existence of membranes and capture known factors which affect cell deformability, such as cytoplasmatic viscosity, turgor (pressure), intermediate filaments, should be developed. Experimentally observed behavior, such as the buckling of microtubules and the nonlinear elastic behavior of cellular filaments should also be included for more realistic representations of the mechanics of the cell using tensegrity-based models.

Once these difficulties are surmounted, the potential for revolutionary advances in engineering and life sciences due to tensegrity structures might surpass even the very optimistic predictions of their most enthusiastic advocate, Buckminster Fuller.

Acknowledgments

The author is grateful to Prof. Erik van der Giessen for the helpful comments made during the preparation of this work.

References

- Adhikari, S. (2004). Optimal complex modes and an index of damping non-proportionality. *Mechanical Systems and Signal Processing*, 18, 1–24.
- Aldrich, J. B., Skelton, R. E., & Kreutz-Delgado, K. (2003). Control synthesis for a class of light and agile robotic tensegrity structures. In: *Proceedings of the American control conference*, Denver, CO.
- Ashley, S. (1998). Magnetostrictive actuators. *Mechanical Engineering Magazine*, 120(6), 68–70.
- Bar-Cohen, Y. (2004). *Electro-active polymer (EAP) actuators as artificial muscles—Reality, potential, and challenges*. Bellingham, WA: SPIE Press.
- Bausch, A. R., Ziemann, F., Boulbitch, A. A., Jacobson, K., & Sackman, E. (1998). Local measurements of viscoelastic parameters of adherent cell surfaces by magnetic bead microrheometry. *Biophysical Journal*, 75, 2038–2049.
- Besseling, J. F., Ernst, L. J., Van der Werff, K., De Koning, A. U., & Riks, E. (1979). Geometrical and physical nonlinearities. Some developments in the Netherlands. *Computer Methods in Applied Mechanics and Engineering*, 17–18, 131–157.
- Calladine, C. R. (1978). Buckminster Fuller's tensegrity structures and Clerk Maxwell's rules for the construction of stiff frames. *International Journal of Solids and Structures*, 14, 161–172.

- Calladine, C. R., & Pellegrino, S. (1991). First order infinitesimal mechanisms. *International Journal of Solids and Structures*, 27(4), 505–515.
- Canadas, P. V., Laurent, M., Oddou, C., Isabey, D., & Wendling, S. (2002). A cellular tensegrity model to analyze the structural viscoelasticity of the cytoskeleton. *Journal of Theoretical Biology*, 218, 155–173.
- Canadas, P. V., Wendling, S., & Isabey, D. (2006). Frequency response of a viscoelastic tensegrity model: structural rearrangement contribution to cell mechanics. *ASME Journal of Biomechanical Engineering*, 128, 487–495.
- Caspar, D. L. D., & Klug, A. (1962). Physical principles in the construction of regular viruses. In: *Proceedings of Cold Spring Harbor symposium on quantitative biology*, Vol. 27 (pp. 1–24).
- Connelly, R. (1980). The rigidity of certain cabled networks and the second order rigidity of arbitrarily triangulated convex surfaces. *Advances in Mathematics*, 37, 272–299.
- Connelly, R. (1982). Rigidity and energy. *Inventiones Mathematicae*, 66, 11–33.
- Connelly, R., & Back, A. (1998). Mathematics and tensegrity. *American Scientist*, 86(2), 453–491.
- Connelly, R., & Whiteley, W. (1992). The stability of tensegrity frameworks. *International Journal of Space Structures*, 7(2), 153–163.
- Connelly, R., & Whiteley, W. (1996). Second-order rigidity and prestress stability for tensegrity frameworks. *SIAM Journal of Discrete Mathematics*, 9(3), 453–491.
- Corless, M. (1993). Control of uncertain nonlinear systems. *Journal of Dynamic Systems, Measurement, and Control*, 115, 471–484.
- Coughlin, M. F., & Stamenovic, D. (1997). A tensegrity structure with buckling compression elements: application to cell mechanics. *Journal of Applied Mechanics*, 64, 480–486.
- Coughlin, M. F., & Stamenovic, D. (1998). A tensegrity model of the cytoskeleton in spread and round cells. *ASME Journal of Biomechanical Engineering*, 120, 770–777.
- Defossez, M. (2003). Shape memory effect in tensegrity structures. *Mechanics Research Communications*, 30, 311–316.
- Defossez, M. (2004). Mechanical response of a tensegrity close to its integrity limit submitted to external constraints. *Mechanics Research Communications*, 31, 569–575.
- Djouadi, S., Motro, R., Pons, J. C., & Crosnier, B. (1998). Active control of tensegrity systems. *ASCE Journal of Aerospace Engineering*, 11(2), 37–44.
- Dote, Y. (1990). *Servomotor and motion control using digital signal processors*. Englewood Cliffs, NJ: Prentice Hall.
- Duffy, J., Roney, J., Knight, B., & Crane, C. D.III, (2000). A review of a family of self-deploying tensegrity structures with elastic ties. *The Shock and Vibration Digest*, 32(2), 100–106.
- Emmerich, D. G. (1988). *Structures Tendues et Autotendants. Monographies de Geometrie Constructive*. La Villette, France: Editions de l'Ecole d'Architecture de Paris.
- Emmerich, D. G. (1996). Emmerich on self-tensioning structures. *International Journal of Space Structures*, 11(1–2), 29–36.
- Estrada, G. G., Bungartz, H. J., & Mohrdieck, C. (2006). Numerical form-finding of tensegrity structures. *International Journal of Solids and Structures*, 43(22–23), 6855–6868.
- Fest, E., Shea, K., & Smith, I. (2004). Active tensegrity structure. *Journal of Structural Engineering*, 130(10), 1454–1465.
- Frantsevich, L., & Gorb, S. (2002). Arcus as a tensegrity structure in the arolium of wasps (Hymenoptera: Vespidae). *Zoology*, 105, 225–237.
- Fuller, R. B. (1962). *Tensile-integrity structures*. U.S. Patent 3,063,521, November 13, 1962.
- Fung, Y. C., & Liu, S. Q. (1993). Elementary mechanics of the endothelium of blood vessels. *ASME Journal of Biomechanical Engineering*, 115, 1–12.
- Furuya, H. (1992). Concept of deployable tensegrity structures in space application. *International Journal of Space Structures*, 7(2), 143–151.
- Gawronski, W. K. (2004). *Advanced structural dynamics and active control of structures*. New York, NY: Springer.

- Gawronski, W. K., & Sawicki, J. T. (1997). Response errors of non-proportionally lightly damped structures. *Journal of Sound and Vibration*, 200(4), 543–550.
- Gittes, F., Mickey, B., Nettleton, J., & Howard, J. (1993). Flexural rigidity of microtubules and actin filaments measured from thermal fluctuations shape. *Journal of Cell Biology*, 120, 923–934.
- Guest, S. D., & Fowler, P. W. (2007). Symmetry conditions and finite mechanisms. *Journal of Mechanics of Materials and Structures*, 2(2), 293–301.
- Hanaor, A. (1988). Prestressed pin-jointed structures—flexibility analysis and prestress design. *Computers & Structures*, 28(6), 757–769.
- Hanaor, A. (1992). Aspects of design of double layer tensegrity domes. *International Journal of Space Structures*, 7(2), 101–113.
- Hanaor, A. (1993). Double-layer tensegrity grids as deployable structures. *International Journal of Space Structures*, 8(1–2), 135–143.
- Ingber, D. E. (1993). Cellular tensegrity: defining new rules of biological design that govern the cytoskeleton. *Journal of Cell Science*, 104, 613–627.
- Ingber, D. E. (1998). The architecture of life. *Scientific American*, 278(1), 48–58.
- Janmey, P. A., Euteneauer, U., Traub, P., & Schliwa, M. (1991). Viscoelastic properties of vimentin compared with other filamentous biopolymer networks. *Journal of Cell Biology*, 113, 155–160.
- Jensen, O., Wroldsen, A. S., Lader, P. F., Fredheim, A., & Heide, M. (2007). Finite element analysis of tensegrity structures in offshore aquaculture installations. *Aquacultural Engineering*, 36, 272–284.
- Juan, S. H., & Tur, J. M. M. (2008). Tensegrity frameworks: static analysis review. *Mechanism and Machine Theory*, 43(7), 859–881.
- Kahla, N. B., & Kebiche, K. (2000). Nonlinear elastoplastic analysis of tensegrity systems. *Engineering Structures*, 23, 1552–1566.
- Kanchanasaratool, N., & Williamson, D. (2002). Modeling and control of class NSP tensegrity structures. *International Journal of Control*, 75(2), 123–139.
- Kauffman, G. B., & Mayo, I. (1993). The metal with a memory. *American Heritage's Invention & Technology*, 9(2), 18–23.
- Kebiche, K., Kazi-Aoual, M. N., & Motro, R. (1999). Geometrical nonlinear analysis of tensegrity systems. *Engineering Structures*, 21(9), 864–876.
- Kenner, H. (1976). *Geodesic math and how to use it*. Berkeley, CA: University of California Press.
- Knight, B., Duffy, J., Crane, C. D., III, & Rooney, J. (2000). Innovative deployable antenna developments using tensegrity design. In: *Proceedings of AIAA/ASME/ASCE/AHS/ASC structures, structural dynamics, and materials conference*, Atlanta, GA.
- Kono, Y., Choong, K. K., Shimada, T., & Kunieda, H. (1999). An experimental investigation of a type of double-layer tensegrity grids. *Journal of the International Association for Shell and Spatial Structures*, 40(130), 103–111.
- Kottamasu, V. (1997). Magnetostrictive elastic wave-type linear motion with Terfenol-D. In: *Proceedings of SPIE symposium on smart structures and materials*, Vol. 3044 (pp. 363–369), San Diego, CA.
- Lazopoulos, K. A. (2004). Stability of an elastic cytoskeletal tensegrity model. *International Journal of Solids and Structures*, 42, 3459–3469.
- Lazopoulos, K. A., & Lazapoulou, N. K. (2005). On the elastica solution of a tensegrity structure: application to cell mechanics. *Acta Mechanica*, 182, 253–263.
- Lazzari, M., Vitaliani, R. V., Majowiecki, M., & Saetta, A. V. (2003). Dynamic behavior of a tensegrity system subjected to follower wind loading. *Computers & Structures*, 81, 2199–2217.
- Ma, L., Xu, J., Coulombe, P. A., & Wirtz, D. (1999). Keratin filament suspensions show unique micromechanical properties. *Journal of Biological Chemistry*, 274, 19145–19151.
- Maina, J. N. (2007). Spectacularly robust! Tensegrity principle explains the mechanical strength of the avian lung. *Respiratory Physiology & Neurobiology*, 115, 1–10.

- Marks, R., & Fuller, R. B. (1973). *The Dymaxion world of Buckminster Fuller*. Garden City, NY: Anchor Books.
- Masic, M., & Skelton, R. E. (2005). Path planning and open-loop shape control of modular tensegrity structures. *Journal of Guidance, Control, and Dynamics*, 28(3), 421–430.
- Masic, M., Skelton, R. E., & Gill, P. E. (2005). Algebraic tensegrity form-finding. *International Journal of Solids and Structures*, 42, 4833–4858.
- Masic, M., Skelton, R. E., & Gill, P. E. (2006). Optimization of tensegrity structures. *International Journal of Solids and Structures*, 43, 4687–4703.
- Maxwell, C. (1864). On the calculation of equilibrium and stiffness of frames. *Philosophical Magazine*, 27, 294–299.
- Medeuil, C. C. (1988). Evolution des simulerurs d'avions civils. *Onde Electrique*, 68(6), 35–41.
- Micheletti, A., Nicotra, V., Podio-Guidugli, P., & Stucchi, S. (2005). The tensegrity footbridge at Tor Vergata University in Rome. In: *Proceedings of footbridge*, Venice, Italy.
- Moored, K. W., & Bart-Smith, H. (2007). The analysis of tensegrity structures for the design of a morphing wing. *Journal of Applied Mechanics*, 74(4), 668–676.
- Motro, R. (1984). Forms and forces in tensegrity systems. In: *Proceedings of the third international conference on space structures*, Amsterdam, Holland.
- Motro, R. (1990). Tensegrity systems and geodesic domes. *International Journal of Space Structures*, 5(3–4), 341–351.
- Motro, R. (1992). Tensegrity structures. The state of the art. *International Journal of Space Structures*, 7(2), 75–83.
- Motro, R. (1996). Structural morphology of tensegrity systems. *International Journal of Space Structures*, 11(1–2), 25–32.
- Motro, R. (2003). *Tensegrity: Structural systems for the future*. London: Kogan Page Science.
- Motro, R., Najari, S., & Jouanna, P. (1986). Static and dynamic analysis of tensegrity systems. In: *Proceedings of ASCE international symposium on shells and spatial structures: Computational aspects*, New York: Springer-Verlag.
- Murakami, H. (2001a). Static and dynamic analyses of tensegrity structures. Part I. Nonlinear equations of motion. *International Journal of Solids and Structures*, 38, 3599–3613.
- Murakami, H. (2001b). Static and dynamic analyses of tensegrity structures. Part II. Quasi-static analysis. *International Journal of Solids and Structures*, 38, 3615–3629.
- Murakami, H., & Nishimura, Y. (2001a). Static and dynamic characterization of regular truncated icosahedral and dodecahedral tensegrity modules. *International Journal of Solids and Structures*, 38(50–51), 9359–9381.
- Murakami, H., & Nishimura, Y. (2001b). Initial shape-finding and modal analyses of cyclic right-cylindrical tensegrity modules. *Computers & Structures*, 79, 891–917.
- Nishimura, Y., & Murakami, H. (2001). Initial shape-finding and modal analyses of cyclic frustum tensegrity modules. *Computer Methods in Applied Mechanics and Engineering*, 190, 5795–5818.
- Oppenheim, I. J., & Williams, W. O. (2000). Geometric effects in an elastic tensegrity structure. *Journal of Elasticity*, 59(1–3), 51–65.
- Oppenheim, I. J., & Williams, W. O. (2001a). Vibration and damping in tensegrity structures. *ASCE Journal of Aerospace Engineering*, 14(3), 85–91.
- Oppenheim, I. J., & Williams, W. O. (2001b). Vibration of an elastic tensegrity structure. *European Journal of Mechanics A/Solids*, 20(6), 1023–1031.
- Park, S., Kim, I., & Ma, F. (1994). Characteristics of modal decoupling in non-classically damped systems under harmonic excitation. *Journal of Applied Mechanics*, 61, 77–83.
- Paul, C., Valero-Cuevas, F., & Lipson, H. (2006). Design and control of tensegrity robots for locomotion. *IEEE Transactions on Robotics*, 22(5), 944–956.
- Pellegrino, S. (1986). *Mechanics of kinematically indeterminate structures*. Cambridge, UK: University of Cambridge, Ph.D. Thesis.

- Pellegrino, S. (1992). A class of tensegrity domes. *International Journal of Space Structures*, 7(2), 127–142.
- Pellegrino, S., & Calladine, C. R. (1986). Matrix analysis of statically and kinematically indetermined frameworks. *International Journal of Solids and Structures*, 22(4), 409–428.
- Pugh, A. (1976). *An introduction to tensegrity*. Berkeley, CA: University of California Press.
- Quirant, J., Kazi-Aoul, M. N., & Motro, R. (2003). Designing tensegrity systems: the case of a double layer grid. *International Journal of Solids and Structures*, 25, 1121–1130.
- Roth, B., & Whiteley, W. (1981). Tensegrity frameworks. *Transactions of the American Mathematical Society*, 265, 419–446.
- Sadao, S. (1996). Fuller on tensegrity. *International Journal of Space Structures*, 11(1–2), 37–42.
- Schenk, M., Guest, S. D., & Herder, J. L. (2007). Zero stiffness tensegrity structures. *International Journal of Solids and Structures*, 44(20), 6569–6583.
- Scruggs, J. T., & Skelton, R. E. (2006). Regenerative tensegrity structures for energy harvesting applications. In: *Proceedings of the conference on decision and control*, San Diego, CA.
- Shea, K., Fest, E., & Smith, I. (2002). Developing intelligent tensegrity structures with stochastic search. *Advanced Engineering Informatics*, 16, 21–40.
- Shroff, S. G., Saner, D. R., & Lal, R. (1995). Dynamic micromechanical properties of cultured rat arterial myocytes measured by atomic force microscopy. *American Journal of Physiology: Cell Physiology*, 269, C268–C292.
- Skelton, R. E., Pinaud, J. P., & Mingori, D. L. (2001). Dynamics of the shell class of tensegrity structures. *Journal of the Franklin Institute*, 338, 255–320.
- Skelton, R. E., & Sultan, C. (1997). Controllable tensegrity, a new class of smart structures. In: *Proceedings of SPIE symposium on smart structures and materials*, Vol. 3039 (pp. 166–177), San Diego, CA.
- Snelson, K. (1965). *Continuous tension, discontinuous compression structures*. U.S. Patent 3,169,611.
- Snelson, K. (1996). Snelson on the tensegrity invention. *International Journal of Space Structures*, 11 (1–2), 43–48.
- Stamenovic, D., & Coughlin, M. F. (1999). The role of prestress and architecture of the cytoskeleton and deformability of cytoskeletal filaments in mechanics of adherent cells: a quantitative analysis. *Journal of Theoretical Biology*, 201, 63–74.
- Stamenovic, D., & Coughlin, M. F. (2000). A quantitative model of cellular elasticity based on tensegrity. *Journal of Theoretical Biology*, 122, 39–43.
- Stamenovic, D., Fredberg, J. J., Wang, N., Butler, J. P., & Ingber, D. E. (1996). A microstructural approach to cytoskeletal mechanics based on tensegrity. *Journal of Theoretical Biology*, 181, 125–136.
- Sultan, C. (1999). *Modeling, design, and control of tensegrity structures with applications*. West Lafayette, IN: Purdue University, Ph.D. Thesis.
- Sultan, C. (2006). Tensegrity structures: from avant-garde art to next generation controllable structures. In: *Proceedings of the world conference on structural control*, San Diego, CA.
- Sultan, C. (2008). Simple conditions for arbitrarily close equilibrium and deployment paths and quasistationary deployment. In: *Proceedings of the IEEE control and decision conference*, Cancun, Mexico.
- Sultan, C. (2009). Designing structures for dynamic properties via natural frequencies separation. Application to tensegrity structures design. *Mechanical Systems and Signal Processing*, 23(4), 1112–1122.
- Sultan, C., Corless, M., & Skelton, R. E. (1999). Peak to peak control of an adaptive tensegrity space telescope. In: *Proceedings of SPIE symposium on smart structures and materials*, Vol. 3667 (pp. 190–201), San Diego, CA.
- Sultan, C., Corless, M., & Skelton, R. E. (2000). Tensegrity flight simulator. *Journal of Guidance, Control, and Dynamics*, 23, 1055–1064.

- Sultan, C., Corless, M., & Skelton, R. E. (2001). The prestressability problem of tensegrity structures. Some analytical solutions. *International Journal of Solids and Structures*, 38–39, 5223–5252.
- Sultan, C., Corless, M., & Skelton, R. E. (2002a). Symmetrical reconfiguration of tensegrity structures. *International Journal of Solids and Structures*, 39(8), 2215–2234.
- Sultan, C., Corless, M., & Skelton, R. E. (2002b). Linear dynamics of tensegrity structures. *Engineering Structures*, 26(6), 671–685.
- Sultan, C., Stamenovic, D., & Ingber, D. E. (2004). A computational tensegrity model explains dynamic rheological behaviors of living cells. *Annals of Biomedical Engineering*, 32(4), 520–530.
- Sultan, C., & Skelton, R. E. (1997). Integrated design of controllable tensegrity structures. In: *Proceedings of the ASME international mechanical engineering congress and exposition*, Vol. 54 (pp. 27–37), Dallas, TX.
- Sultan, C., & Skelton, R. E. (1998a). Force and torque smart tensegrity sensor. In: *Proceedings of SPIE symposium on smart structures and materials*, Vol. 3323 (pp. 357–368), San Diego, CA.
- Sultan, C., & Skelton, R. E. (1998b). Tendon control deployment of tensegrity structures. In: *Proceedings of SPIE symposium on smart structures and materials*, Vol. 3323 (pp. 455–466), San Diego, CA.
- Sultan, C., & Skelton, R. E. (2003a). Tensegrity structures prestressability investigation. *International Journal of Space Structures*, 18(1), 15–30.
- Sultan, C., & Skelton, R. E. (2003b). Deployment of tensegrity structures. *International Journal of Solids and Structures*, 40(18), 4637–4657.
- Sultan, C., & Skelton, R. E. (2004). A force and torque tensegrity sensor. *Sensors and Actuators Journal A: Physical*, 112(2–3), 220–231.
- Tarnai, T. (1980). Simultaneous static and kinematic indeterminacy of space trusses with cyclic symmetry. *International Journal of Solids and Structures*, 16(4), 347–359.
- Thoumine, O., & Ott, A. (1997). Time scale dependent viscoelastic and contractile regimes in fibroblasts probed by microplate manipulation. *Journal of Cell Science*, 110, 2109–2116.
- Libert, G., & Pellegrino, S. (2002). Deployable tensegrity reflectors for small satellites. *Journal of Spacecraft and Rockets*, 39(5), 701–709.
- Libert, G., & Pellegrino, S. (2003a). Review of form-finding methods for tensegrity structures. *International Journal of Space Structures*, 18(4), 209–223.
- Libert, G., & Pellegrino, S. (2003b). Deployable tensegrity masts. In: *Proceedings of AIAA/ASME/ASCE/AHS/ASC structures, structural dynamics, and materials conference and exhibit*, Norfolk, VA.
- Vassart, N., Laporte, R., & Motro, R. (2000). Determination of mechanism's order for kinematically and statically indeterminate systems. *International Journal of Solids and Structures*, 37, 3807–3839.
- Vassart, N., & Motro, R. (1999). Multiparametered form-finding method: application to tensegrity systems. *International Journal of Space Structures*, 14(2), 147–154.
- Volokh, K., Vilnay, O., & Belsky, M. (2000). Tensegrity architecture explains linear stiffening and predicts softening of living cells. *Journal of Biomechanics*, 33(12), 1543–1549.
- Wang, B. B. (1998). Cable-strut systems: part I—tensegrity. *Journal of Construction Steel Research*, 45(3), 281–289.
- Wang, B. B. (2004). *Free-standing tension structures: From tensegrity systems to cable-strut systems*. New York: Taylor & Francis.
- Wang, B. B., & Liu, X. L. (1996). Integral tension research in double layer tensegrity grids. *International Journal of Space Structures*, 11(4), 349–355.
- Wang, N., Naruse, K., Stamenovic, D., Fredberg, J. J., Mijailovich, S. M., Tolic-Nørrelykke, I. M., et al. (2001). Mechanical behavior in living cells consistent with the tensegrity model. *Proceedings of the National Academy of Sciences of the United States of America*, 98, 7765–7770.

- Wendling, S., Canadas, P. V., & Chabrand, P. (2003). Towards a generalized tensegrity model describing the mechanical behaviour of the cytoskeleton structure. *Computer Methods in Biomechanics and Biomedical Engineering*, 6(11), 45–52.
- Wendling, S., Oddou, C., & Isabey, D. (1999). Stiffening linear response of a cellular tensegrity model. *Journal of Theoretical Biology*, 196, 309–325.
- Yeung, A., & Evans, E. (1989). Cortical shell-liquid core model for passive flow of liquid-like spherical cells into micropipettes. *Biophysical Journal*, 56, 139–149.
- Zanotti, G., & Guerra, C. (2003). Is tensegrity a unifying concept of protein folds? *FEBS Letters*, 534 (1–3), 7–10.
- Zenieh, S., & Corless, M. (1997). Simple robust $r - \alpha$ tracking controllers for uncertain fully actuated mechanical systems. *Journal of Dynamic Systems, Measurement, and Control*, 119, 821–825.
- Zhang, L., Maurin, B., & Motro, R. (2006). Form-finding of nonregular tensegrity systems. *Journal of Structural Engineering*, 132(9), 1435–1440.
- Zhang, J. Y., & Ohsaki, M. (2006). Adaptive force density method for form-finding problem of tensegrity structures. *International Journal of Solids and Structures*, 43, 5658–5673.
- Zhang, J. Y., Ohsaki, M., & Kanno, Y. (2006). A direct approach to design of geometry and forces of tensegrity systems. *International Journal of Solids and Structures*, 43, 2260–2278.

Skin Biothermomechanics: Modeling and Experimental Characterization

F. XU^a and T. J. LU^b

^aDepartment of Engineering, Cambridge University, Cambridge CB2 1PZ,
United Kingdom

^bMOE Key Laboratory for Strength and Vibration, School of Aerospace, Xi'an Jiaotong University,
Xi'an 710049, People's Republic of China

Abstract.....	148
1. Introduction.....	148
1.1. Skin Biothermomechanics.....	149
1.2. Aims and Structure.....	150
2. Review of Related Studies.....	152
2.1. Skin Structure.....	152
2.2. Skin Bioheat Transfer and Thermal Damage.....	155
2.3. Skin Biomechanics.....	158
2.4. Skin Biothermomechanics.....	159
3. Modeling of Skin Biothermomechanics and Thermal Pain.....	162
3.1. Modeling of Skin Bioheat Transfer.....	162
3.2. Modeling of Skin Biothermomechanics.....	167
3.3. Modeling of Skin Thermal Pain.....	176
4. Experimental Methodology.....	180
4.1. Experimental Characterization of Skin Mechanical Properties.....	181
4.2. Experimental Characterization of Skin Thermal Denaturation.....	182
4.3. Sample Preparation Techniques.....	182
4.4. Differential Scanning Calorimetry Tests.....	186
4.5. Hydrothermal Tensile Tests.....	187
4.6. Hydrothermal Compressive Tests.....	194
4.7. Dynamic Mechanical Analysis.....	195
5. Biothermomechanical Behavior of Skin Tissue.....	196
5.1. Thermal Denaturation of Collagen in Skin Tissue.....	197
5.2. Tensile Behavior of Skin Tissue.....	200
5.3. Compressive Behavior of Skin Tissue.....	204
5.4. Relaxation Behavior of Skin Tissue.....	214
5.5. Dynamic Viscoelasticity of Skin Tissue.....	227

6. Conclusions	229
6.1. Summary	231
6.2. Limitations	231
6.3. Future Work	233
Acknowledgments	234
References	234

Abstract

The development and widespread use of thermal therapies for skin diseases and injuries with advances in laser, microwave, and similar technologies have not been built upon the detailed understanding of the biothermomechanical–neurophysiological behavior of skin tissue. The emerging studies on skin biothermomechanics are therefore important for it attempts to understand macroscale tissue response to heat-induced microstructural transformations. Skin biothermomechanics is highly interdisciplinary, involving bioheat transfer, burn damage, biomechanics, and physiology. This chapter presents firstly the various theoretical approaches for determining the thermal, thermomechanical, and thermal pain response in skin tissue induced by transient heating. Given the complicated microstructure of skin tissue and its relatively lengthy thermal relaxation time, both Fourier and non-Fourier bioheat transfer models are employed. While insightful, the predictive capability of the current theoretical modeling is, nonetheless, limited by the comparatively few relative experimental studies on temperature-dependent properties of the skin tissue. To better understand the variation in skin properties with temperature and the corresponding collagen denaturation, focus is then placed upon the experimental characterization of the thermomechanical behavior of skin tissue. Uniaxial and biaxial hydrothermal tensile testing systems as well as hydrothermal compressive testing system are purposely designed and built which, together with a commercially available dynamic mechanical analyzer, are employed to obtain suitable data to quantify the influence of temperature and the corresponding thermal damage on the mechanical performance of skin tissue, including tensile, compressive, and viscoelastic behaviors.

1. Introduction

As the protecting interface between the outside environment and the inside body, skin plays a variety of important roles including thermoregulation, sensation, and host defense. Among these roles, thermoregulation is of particular significance: acting as a generator, absorber, transmitter, radiator, conductor, and vaporizer of heat, skin serves an important barrier for the human body to various outside conditions. However, the skin fails to protect the body when the temperature moves out of the normal physiological range, as uncomfortable feeling, or even pain is often induced in extreme hot or cold environment. On the other hand, advances in laser, microwave and similar technologies in

medicine have led to recent developments of thermal treatments for disease and injury, involving skin tissue. In spite of the widespread use of thermal therapies in dermatology, they do not draw upon the detailed understanding of the biothermomechanical–neurophysiological behavior, for none exists to date, even though each behavioral facet is somewhat established and understood. In view of this dilemma, a new research area—skin biothermomechanics and thermal pain—has recently emerged, which is the subject of this study.

1.1. SKIN BIOTHERMOMECHANICS

1.1.1. Schematic of Skin Biothermomechanics and Thermal Pain

The study of skin biothermomechanics and thermal pain is a highly interdisciplinary area involving engineering (e.g., heat transfer and mechanics), biology, and neurophysiology, as schematically shown in Fig. 1.1. The skin is characterized by its biological structure and state, such as its constituent components, blood flow, metabolism, and so on, and properties, such as thermal, mechanical, optical, and dielectric properties. When thermal loading (either as contact heating, electromagnetic energy or acoustic energy) and/or mechanical loading (either as force or deformation) are applied to skin tissue, then there exist different skin states, including temperature, thermal damage/inflammation, and stress/strain distributions. These states then decide the level of pain sensation through the neural system. A better understanding of skin properties, skin bioheat transfer and the thermal damage kinetics, skin biomechanics, skin biothermomechanics and pain sensation, promise to contribute to the continuing advancement of study of thermal pain in general.

1.1.2. Importance of Skin Thermomechanics

With advances in laser, microwave, radiofrequency, and similar technologies, a variety of thermal methods have been developed and applied to the treatment of disease/injury involving skin tissue, such as the removal of port-wine stains (Asahina et al., 2006; Kono et al., 2006; Shafirstein et al., 2003), pigmented and cutaneous lesions (Hamilton, 2004; Kauvar, Rosen, & Khrom, 2006; Pustovalov & Jean, 2007) and tattoos (Diette, Bronstein, & Parrish, 1985). These thermal treatment methods normally involve either raising or lowering the temperature in a precise area of skin tissue, in order to kill or thermally denaturize the necrotic cells; the precise monitoring of the spatial and temporal distribution of temperature, damage, and stress in the tissue is therefore required. Meanwhile, the remaining healthy tissue is kept at a safe temperature level by adopting selective cooling techniques on the skin surface during the treatment. In spite of these important and widely used medical applications, an understanding of the responsible thermomechanical–neurophysiological mechanism remains limited, which can

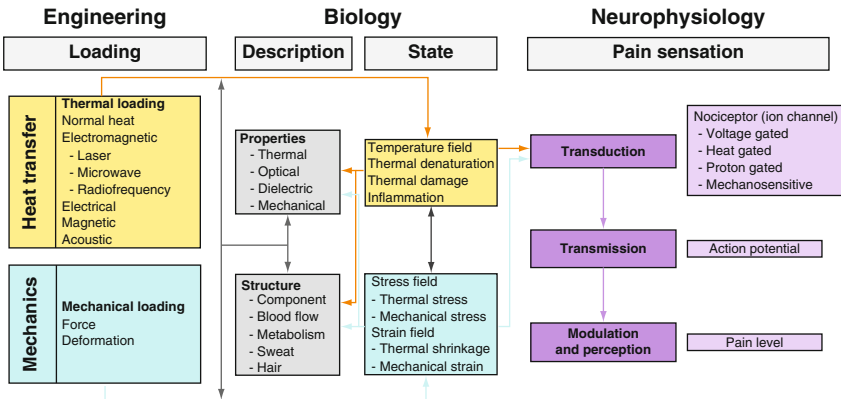


FIG. 1.1 Schematic of skin biothermomechanics and thermal pain.

restrict further refinement and innovation. In addition, a noxious thermal stimulus, hot or cold, applied to human skin, is one of the three main causes of pain.¹ Thermally induced damage plays an important role in causing thermal pain, for example, burn damage has been found to induce severe pain that is difficult to manage (Choinière, Melzack, Girard, Rondeau, & Paquin, 1990; Perry, 1984) and contribute to sensory problems (Gallagher, Rae, & Kinsella, 2000; van Loey & van Son, 2003), all of which commonly reduce quality of life after burn damage. Therefore, the research on skin biothermomechanics and related pain sensation is important and contributes to medical applications for it attempts to understand the macroscale tissue response to heat-induced microstructural transformations.

Besides biomedical applications, space and military missions can also benefit from the proposed study. Extreme environments encountered in space travel and in some military activities make it necessary to provide astronauts and military personnel with sophisticated garments for thermal protection. Challenges are also posed by the need to understand possible thermal effects on military personnel exposed to irradiation.

1.2. AIMS AND STRUCTURE

The specific objectives of the study on skin biothermomechanics are to theoretically model and to experimentally investigate the biothermomechanical behavior of skin tissue under different thermomechanical loadings which are then combined to provide a predictive framework for treating diseased tissue. In one

¹ The other two are mechanically and chemically caused pain.

of our previous studies ([Xu, Seffen, & Lu, 2008](#)), we have described the development of two types of skin bioheat transfer models, based on Fourier and non-Fourier theories, which provide a comprehensive description of the thermal behavior in skin tissue. A theoretical analysis is carried out and closed-form solutions for a simple one-layer Fourier bioheat transfer model of skin tissue are obtained. In view of the lengthy thermal relaxation time of skin tissue, non-Fourier bioheat transfer models have been developed. In another study ([Xu, Wen, Seffen, & Lu, 2008](#)), we have developed a scheme for characterizing the skin biothermomechanical behavior to examine the heat transfer process, thermal damage and the heat-induced mechanical response. A general closed-form solution for thermal stress for a multilayer skin model is derived, while a numerical method (finite element method) is employed for more complicated cases. Two types of case studies are then performed with Fourier and non-Fourier models: the first type of case studies is explored to understand the working mechanism of the clinically applied thermal therapies and to quantify the differences among these thermal therapies; the second type of case studies is explored to investigate the relationship between the thermal relaxation time and the thermo-mechanical response of skin tissue. In a third study ([Xu, Lu, & Seffen, 2008](#)), we have developed a holistic mathematical model for quantifying skin thermal pain to build up a direct correlation between the parameters of thermal stimulation and the level of the corresponding thermal pain sensation, by using the thermomechanical models developed in [Xu, Seffen, et al. \(2008\)](#) and [Xu, Wen, Seffen, et al. \(2008\)](#) and by considering the current biophysical and neurophysiological mechanisms of pain sensation. In the first part of this review, the mathematical approaches introduced in all the studies described above are presented.

While insightful, the present theoretical modeling has some limitations, where the main deficiency is that the skin tissue is assumed to have constant properties due to the comparatively few relative experimental studies. More experiments are thus needed to better understand the variation in properties with temperature and the corresponding collagen denaturation, so that these properties can be reliably used in future, more sophisticated models. However, it is technically very difficult to measure experimentally the biothermomechanical behavior of skin tissue in physiological conditions. As a substitute, analytical and numerical simulations are used, where the quantification of the temperature-dependent skin mechanical properties is an essential step toward building reliable computer simulations. So far, the mechanical properties alone of skin tissue have been studied experimentally, both *in vivo* and *in vitro*. But, most of these studies are performed under normal physiological temperature and little has been done on the characterization of the effect of temperature and corresponding thermal damage. These are addressed in the second part of this study, which specially aims to design and

build experimental systems and to obtain suitable data to quantify the influence of the temperature and the corresponding thermal damage on the mechanical behavior of skin tissue, including tensile, compressive, and viscoelastic behaviors.

This chapter is outlined as follows. [Section 2](#) reviews the literature pertinent to the current research, which is composed of four parts, including skin structure, skin bioheat transfer and thermal damage, skin biomechanics, and skin biothermomechanics. This underpins the theoretical and experimental frameworks for investigating the thermomechanical behavior of skin tissue in this review. [Section 3](#) summarizes the modeling efforts on skin biothermomechanics and thermal pain sensation. [Section 4](#) provides detailed information on the preparation technique of skin samples, the design of two novel experimental systems and measurement techniques, and two commercial items of equipment employed in the current experimental study: differential scanning calorimetry (DSC) and dynamic mechanical analyzer (DMA). [Section 5](#) presents results and corresponding discussions from the experimental characterization of skin biothermomechanics, using the experimental apparatus described in [Section 4](#). The tensile, compressive, and viscoelastic behaviors of skin tissue under different temperatures are examined and the effects of temperature and corresponding collagen denaturation on the mechanical properties of skin tissue are characterized. The main conclusions are given in [Section 6](#), where limitations of current theoretical and experimental methodology are also discussed and future work is proposed.

2. Review of Related Studies

The study of skin biothermomechanics is an interdisciplinary problem, involving heat transfer, mechanics, and biology. Accordingly, this section briefly reviews the literature pertinent to the current research, which is composed of four parts: skin structure, skin bioheat transfer and thermal damage, skin biomechanics, and skin biothermomechanics.

2.1. SKIN STRUCTURE

Skin tissue makes up approximately 14–16% of the human adult body weight and plays a variety of important roles. It generally consists of three layers: the epidermis, the dermis, and the subcutaneous tissue, as shown in [Fig. 2.1A and B](#). The thickness of these layers varies, depending on the bodily location. The dermis makes up the bulk of the human skin tissue and its components are introduced below.

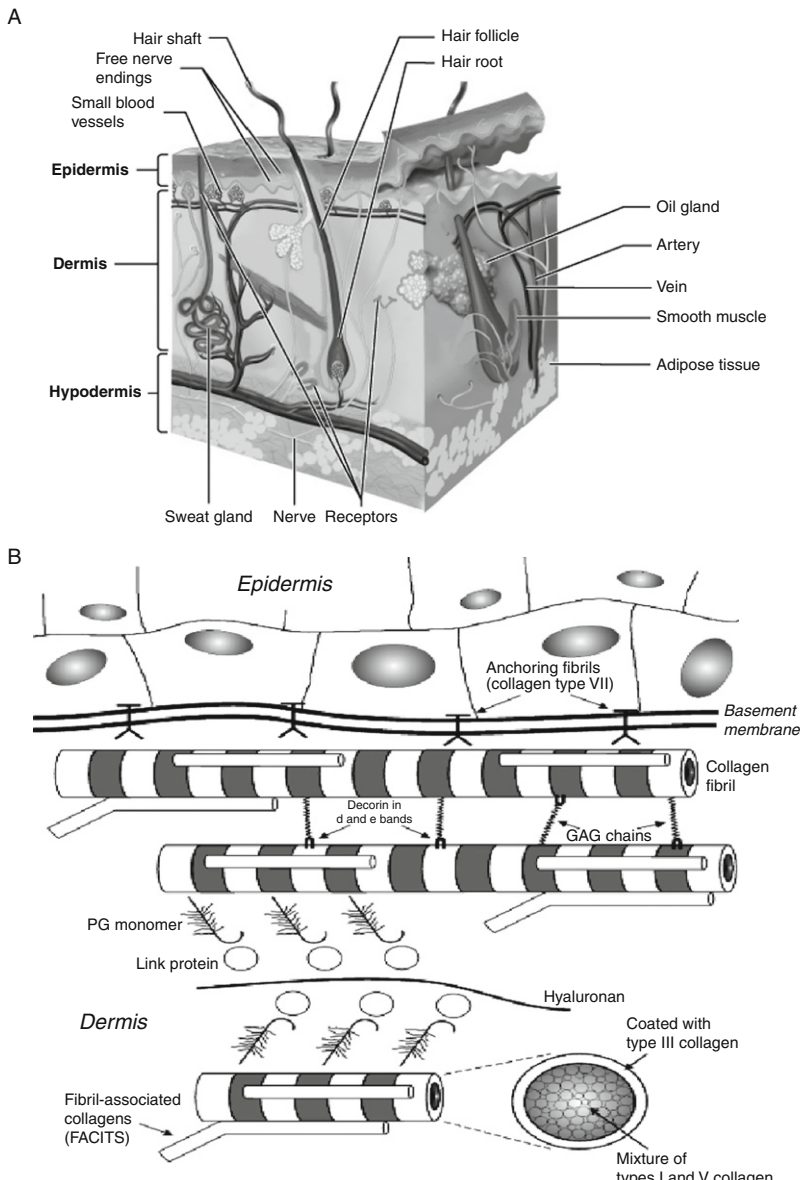


FIG. 2.1 (A) Structure of human skin tissue, see [Whitton and Everall \(1973\)](#). (B) Macromolecular components of skin tissue, see [Silver, Siperko, and Seehra \(2003\)](#).

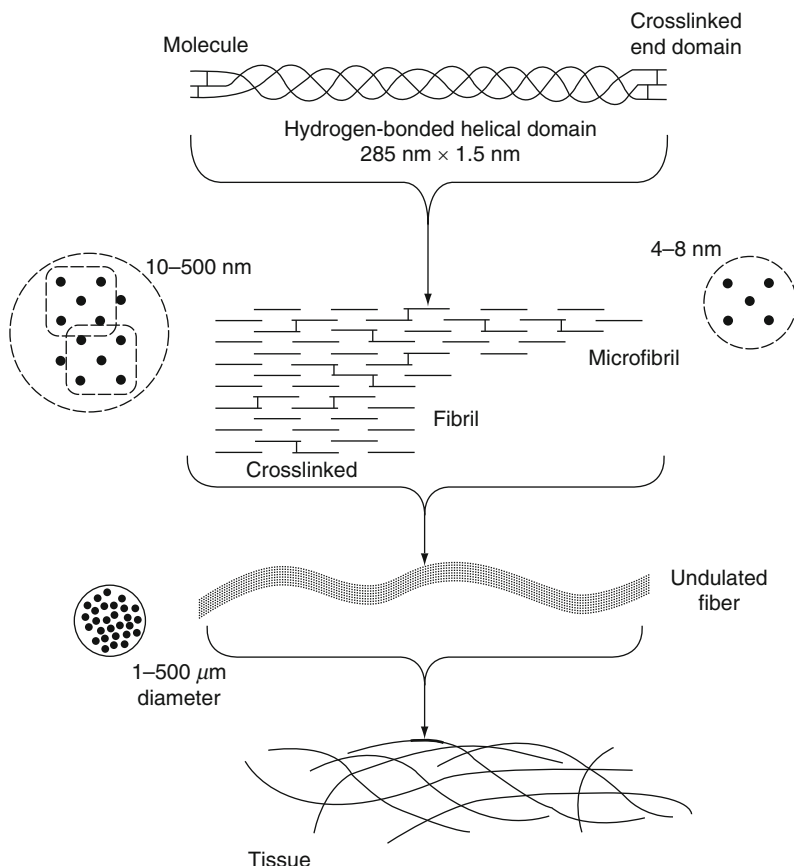


FIG. 2.2 Molecular/fibrillar configuration of type I collagen, see [Wright and Humphrey \(2002\)](#).

2.1.1. Collagen in Dermis

Collagen is the major dermal constituent and accounts for approximately 60–80% of the dry weight of fat-free skin tissue and 18–30% of the volume of dermis ([Ebling, Eady, & Leigh, 1992](#); [Reihsner, Balogh, & Menzel, 1995](#)). The collagen in human dermis is mainly the periodically banded, interstitial collagen (types I, III, and IV),² where about 80–90% is type I collagen and 8–12% is type III collagen. Three polypeptide chains make up the type I collagen molecule and are stabilized in a triple-helix arrangement by intramolecular crosslinks, as shown in [Fig. 2.2](#). These molecules are, in turn, aggregated into a parallel pattern to form

² Collagen occurs in many places throughout the body and there are 28 types of collagen reported in literature ([Myllyharju & Kivirikko, 2004](#)).

collagen fibrils, which are maintained by intermolecular crosslinks and provide the tissue with its tensile properties. Type IV collagen codistributes and assembles into fibrils with types I and III collagen in which it assists in regulating fibril diameter. The wavy and unaligned collagen fiber bundles form an irregular planar network, which allows considerable deformation in all directions without requiring elongation of the individual fibers and provides both tensile strength and elasticity (Finlay, 1969; Wegst & Ashby, 2004).

2.1.2. Elastin in Dermis

Elastin is a minor structural component of the dermis structure, accounting for about 4% of the dermis dry weight and 1% of the volume of dermis (Ebling et al., 1992; Hult & Goltz, 1965). Elastin fibers are considerably thinner and more convoluted than collagen fibers. The base unit of elastin is a long protein chain that is crosslinked by lysine molecules, and four elastin chains are joined at each crosslink by the covalent bonding of a lysine molecule from each elastin chain. Although direct connections between elastin and collagen fibers have not been shown, collagen fibrils appear to wind around the elastin cores.

2.1.3. Ground Substance

The amorphous ground substance can be considered as a highly viscous, thixotropic liquid whose fluid properties are determined by a low concentration (0.05% wet weight of human dermis) of mucopolysaccharides, proteoglycans, and glycoproteins (Tregear, 1966). The most important mucopolysaccharides in ground substance is hyaluronic acid, which is analogous to the polymer molecules found within rubbers. The hyaluronic acid chain has a proteoglycans side chain, which in turn is crosslinked by glycoproteins to additional structures within dermis, such as collagen or elastin fibrils. It is this crosslinking function that is responsible for forming fibers from the collagen fibrils and providing the dermis with its rubber-like behavior. Together they form a gel which does not leak out of the dermis, even under high pressure.

2.2. SKIN BIOHEAT TRANSFER AND THERMAL DAMAGE

2.2.1. Skin Bioheat Transfer

The thermal behavior of skin tissue, or heat transfer in skin tissue, is a heat conduction process coupled with complicated physiological processes, including blood circulation, sweating, metabolic heat generation, and, sometimes, heat dissipation via hair or fur above the skin surface. The thermal properties of skin tissue vary among different layers; even within the same layer, there exists large nonhomogeneity and anisotropy due to the presence of blood vessels and

structural anisotropy. Both the physiological processes and thermal properties of skin tissue are influenced by a variety of factors such as temperature, damage, pressure, age, and so on. To complicate matters, skin is an active, self-regulating system: heat transfer through the skin tissue dramatically affects the state of skin tissue, which can lead to the redistribution of skin blood flow over the cutaneous vascular network, thereby influencing the thermal response of the tissue.

Since the appearance of Pennes bioheat equation³ in 1947 (Pennes, 1948), a variety of models on the heat transfer in different tissues of human body have been proposed, where the body tissue may be represented as a homogeneous continuum material with an embedded hierarchical vascular network (Lubashevsky & Gafychuk, 2004). Based on how the influence of blood flow in the vascular network is considered, these models can be classified into four categories (Arkin, Xu, & Holmes, 1994; Charny, 1992; Crezee, Mooibroek, Lagendijk, & van Leeuwen, 1994; Khaled & Vafai, 2003; Stanczyk & Telega, 2002): continuum models, vascular models, hybrid models, and models based on porous media theory. Since the effect of blood vessels on heat transfer is strongly related to their sizes (Abramson, 1967; Chato, 1980; Lemons, Chien, Crawshaw, Weinbaum, & Jiji, 1987; Weinbaum, Jiji, & Lemons, 1984), a thermal equilibration length of blood vessels, L_{eq} , is defined as the length at which the difference between the blood and the tissue temperatures decreases to $1/e$ of the initial value ($e = \exp 1 = 2.718$). The ratio of L_{eq} to the actual vessel length demonstrates the distinction of thermal significance, $\varepsilon = L_{eq}/L$, where if $\varepsilon \ll 1$, that is, L_{eq} is much shorter than the characteristic length of the blood vessel length, L , the blood exits the vessel at, essentially, the tissue temperature; if $\varepsilon \gg 1$, the blood temperature does not change and leaves the tissue at the same inflow temperature (Chato, 1980; Chen & Holmes, 1980). It was found that, for skin tissue, L_{eq} lies in the range of 3×10^{-5} – 2×10^{-4} mm while $L \sim 1.2$ mm (Creeze & Lagendijk, 1992), therefore, the blood in the skin tissue exits the vessel at essentially the tissue temperature. Thus, many researchers use the Pennes equation to describe skin heat transfer because it is simple and can be solved analytically and can be programmed into finite difference and finite element models. The equation is taken directly from Shih, Kou, Liauh, and Lin (2005) as

³ Pennes measured the radial temperature distribution in the forearm, from which he developed a bioheat transfer model in basic terms of the local rate of tissue heat production and volume flow of blood (Pennes, 1948). In the Pennes model, the microscopic thermal energy balance for perfused tissue is linear, which enables analytical solutions of the heat conduction equation by various methods commonly used. Consequently, it has been adopted by many authors to develop mathematical models of heat transfer in different human tissues (Wissler, 1998).

$$\rho c \frac{\partial T}{\partial t} = k \nabla^2 T + \varpi_b \rho_b c_b (T_a - T) + q_{\text{met}} + q_{\text{ext}}, \quad (2.1)$$

where ρ , c , and k are the density, specific heat, and thermal conductivity of skin tissue, respectively; ρ_b and c_b are the density and specific heat of blood; ϖ_b is the blood perfusion rate; T_a and T are the temperatures of blood and skin tissue, respectively; q_{met} is the metabolic heat generation in the skin tissue and q_{ext} is the heat generation due to external heating sources.

2.2.2. Skin Thermal Damage

When the skin temperature rises above a critical value (~ 43 °C), thermal damage will be induced. Presently, the Arrhenius burn integration, proposed by [Henriques and Moritz \(1947\)](#) and [Moritz and Henriques \(1947\)](#), is widely used for quantifying thermal damage. They assert that skin damage can be represented as a chemical rate process, which is calculated by using a first-order Arrhenius rate equation, whereby damage is related to the rate of protein denaturation, k :

$$k(T) = d\Omega/dt = A \exp(-E_a/RT) \quad (2.2)$$

or, equivalently:

$$\Omega = \int_0^t A \exp(-E_a/RT) dt, \quad (2.3)$$

where A is a material parameter equivalent to a frequency factor,⁴ E_a is the activation energy, and $R = 8.314$ J/mol K is the universal gas constant. [Equation \(2.2\)](#) indicates that a reaction proceeds faster with larger values of T or A for the same E_a , or with smaller values of E_a for the same A . The constants A and E_a are obtained experimentally as will be discussed in some detail in [Section 5.1](#). It should be noted here that the Arrhenius equation is a simple empirical, but remarkably accurate, formula for the temperature dependence of the rate of a chemical reaction ([Connors, 1990](#)).

Many researchers have proposed other similar models. The main differences between these models are the coefficients used in the burn damage integral, arising from the different experimental databases used to define the models and the different emphasis when analyzing the burn process. The available Arrhenius parameters (A , E_a) used to calculate thermal damage for skin tissue from the literature has been reviewed in our previous study (Xu, Wen, Seffen, et al., 2008)

⁴ The units of A are identical to those of the rate constant and vary depending on the order of the reaction. If the reaction is first order, it has the unit of s^{-1} and for that reason it is often called the frequency factor.

and is fitted with the method used by Wright (2003). The results clearly suggest a linear relationship, after a least-squares fit, between the Arrhenius parameters for skin tissue, given by:

$$E_a = 21149.324 + 2688.367 \ln A \quad (2.4)$$

2.3. SKIN BIOMECHANICS

The mechanical properties of the skin tissue have been experimentally studied both *in vivo* and *in vitro* in relation to clinical and cosmetic applications, since the first work of Langer in 1861. *In vivo* measurements are affected by both the skin tissue itself and other structures to which it is attached, leading to a nonuniform strain field in the sample; for better control of the experiment, *in vitro* tests are often used. The mechanical behavior of skin tissue is found to be heterogeneous, anisotropic, nonlinear, and viscoelastic *in vivo* because of its highly nonhomogeneous structure and composition. It is affected by many factors such as age, gender, site, hydration, and so on. Furthermore, the classical constitutive models for engineering materials are not suitable to describe the complicated mechanical behavior of skin tissue.

2.3.1. Skin Behavior Under Stretch

The tensile behavior of skin tissue has been studied widely, as discussed by several good reviews (Edwards & Marks, 1995; Larrabee, 1986; Pierard, 1999; Vogel, 1994). Typical stress–strain relationships of skin tissue under uniaxial and biaxial tension are shown in Fig. 2.3A and B, respectively. Three regimes of behavior can be observed: at low modulus portion, there is a gradual straightening of an increasing fraction of the wavy collagen fibers and stretching of elastic fibers; a linear region at higher modulus where there is stretching and slippage of collagen molecules within crosslinked collagen fibers and collagen fibril slippage; the final softening region in which defibrillation of the collagen fibrils results in a loss of fibrillar structure. Compared with uniaxial stretching, the stress–strain curve for biaxial stretching is shifted to the left for there is a bidirectional stretch of the collagen fibers, as shown in Fig. 2.3B.

2.3.2. Skin Behavior Under Compression

In vivo, skin tissue is regularly compressed by contact with chairs and shoes, and even in the sockets of prosthetic limbs. Although there is abundant experimental data for the tensile behavior of skin tissue, the compressive performance has been rarely studied. Compression of skin tissue is resisted by solid tissue and

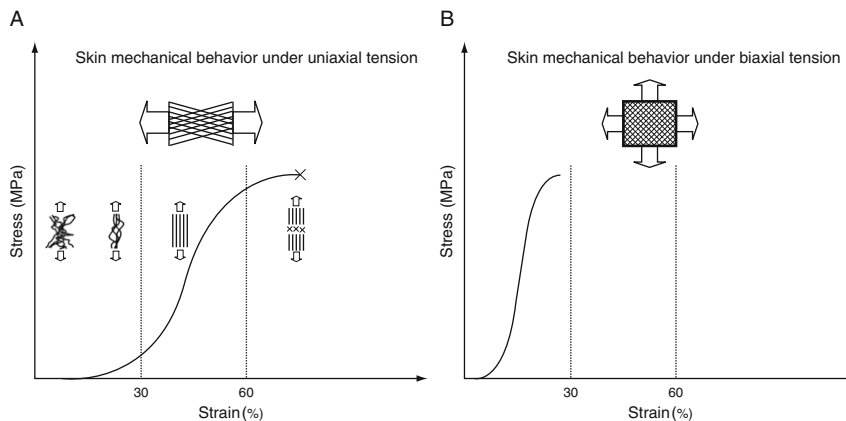


FIG. 2.3 Schematic of skin mechanical behavior under (A) uniaxial and (B) biaxial tension. The curve in (B) is shifted to the left because it is stiffer due to pulling in two directions.

interstitial fluid pressure (Dinnar, 1970). The first effect is due to solid elements in the tissue and is the main cause of the tendency to occlude blood vessels; the second effect determines the motion of tissue fluid and the diffusion coefficient of blood into the capillaries. This point has also been proved by Oomens, van Campen, and Grootenboer (1987), who found good agreement between experimental results of skin response under compression and finite element calculations with “mixture” elements comprising solid and fluid types. The compressive response of skin tissue is also highly viscoelastic and nonlinear (Daly, 1982; Oomens, Van Campen, Grootenboer, & De Boer, 1984; Shergold, Fleck, & Radford, 2006). Both the viscous and the nonlinear aspects were found to diminish greatly under preloading (Ziegert & Lewis, 1978), and they depend on many factors (Daly) such as age, sex, site, hydration, obesity, and so on.

2.4. SKIN BIOTHERMOMECHANICS

Skin biothermomechanics here is defined as the response of skin tissue under thermomechanical loading, which leads to damage—the thermal denaturation of collagen. As noted, skin tissue also contains a small amount of elastin which is very thermally stable (Davidson et al., 1990) (e.g., elastin can survive boiling for several hours with no apparent change), and hence does not need attention here.

The collagen in human dermis is mainly type I collagen, which has a domain within the triple helix that is completely devoid of hydroxyproline. Since hydroxyproline readily forms hydrogen bonds that stabilize the molecule, its

absence makes this domain particularly susceptible to thermal damage (Miles & Bailey, 2001). There are two levels of organization where breakdown is thermodynamically significant (Young, 1998): one is the collagen molecule itself, in which three peptide chains are twisted around each other to form a helical, rod-shaped molecule; the other is the semicrystalline fibril in which collagen molecules are assembled side by side in a staggered manner with the long axis of each molecule aligned with the axial orientation of the fibril. When collagen is heated, the heat-labile intramolecular crosslinks are broken, as shown in Fig. 2.4, and the collagen undergoes a transition from a highly organized crystalline structure to a random, gel-like state, which is the denaturation process (Flory & Garrett, 1958). Collagen shrinkage occurs through the cumulative effect of the unwinding of the triple helix, due to the destruction of the heat-labile intramolecular crosslinks, and the residual tension of the heat-stable intermolecular crosslinks (Allain, Le Lous, Cohen-Solal, Bazin, & Maroteaux, 1980; Arnoczky & Aksan, 2000; Flory & Garrett, 1958).

The effects of heating on collagen can be reversible or irreversible (Hormann & Schlebusch, 1971; Stoop et al., 1999) and the precise heat-induced behavior of collagenous tissue and shrinkage depend on several factors, including the collagen content (Chvapil & Jenovsky, 1963), the maximum temperature reached and exposure time (Allain et al., 1980), the mechanical stress applied to the tissue during heating (Chen, Wright, & Humphrey, 1998a), and aging (Chvapil & Jenovsky, 1963; Le Lous, Cohen-Solal, Allain, Bonaventure, & Maroteaux, 1985).

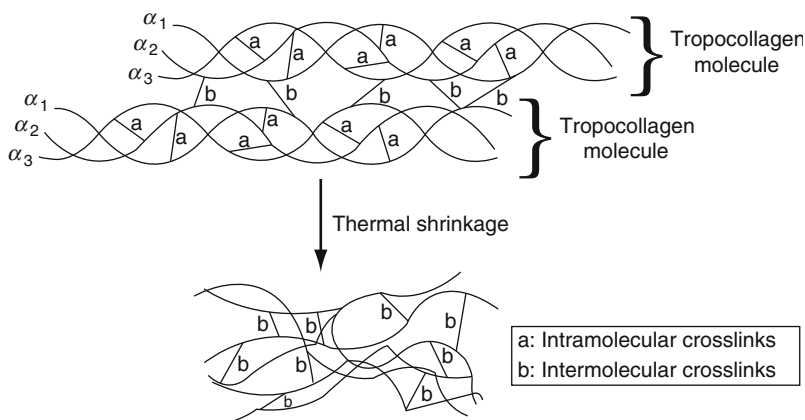


FIG. 2.4 Schematic of thermal denaturation of collagen, see [Arnoczky and Aksan \(2000\)](#).

Different metrics have been used to characterize the thermal denaturation and heat-induced damage of collagen and collagenous tissues, including biological metrics such as enzyme deactivation (Bhowmick & Bischof, 1998) and extravasation of fluorescent-tagged plasma proteins (Green & Diller, 1978), thermal metrics such as changes in enthalpy (Jacques, 2006; Miles, 1993), mechanical metrics such as thermal shrinkage (Chen et al., 1998a,b; Kondo et al., 2005; Lin et al., 2006), and optical metrics such as thermally induced loss of birefringence (de Boer, Srinivas, Malekafzali, Chen, & Nelson, 1998; Pearce, Thomsen, Vijverberg, & McMurray, 1993; Srinivas et al., 2004; Thomsen, 1991). Although the shrinkage of collagen due to thermal denaturation has been widely used and has been suggested as a convenient continuum metric of thermal damage (Diller & Pearce, 1999; Fung, 1990; Wells, Harris, & Humphrey, 2004) pointed out that shrinkage may not be a universal metric to measure thermal damage. Rather, there is a need to identify an independent metric by which one can determine the extent of thermal damage (Baek, Wells, Rajagopal, & Humphrey, 2005).

Diller and Pearce (1999) point out that Ω can be calculated as the logarithm of the relative concentration of “reactants,” or undenatured collagen, in the collagen denaturation process, where Ω can be considered as

$$\Omega(t) = \ln \left[\frac{C(0)}{C(t)} \right], \quad (2.5)$$

where $C(0)$ and $C(t)$ are the initial concentration and the concentration remaining at time t of undenatured collagen, respectively. The degree of thermal denaturation, defined as the fraction of denatured collagen, and denoted by Deg , can be calculated by

$$\text{Deg}(t) = \frac{C(0) - C(t)}{C(0)} = 1 - \exp[-\Omega(t)]. \quad (2.6)$$

Denaturation of collagen occurs as the temperature of the tissue increases. As well as structural changes, the hydration level of collagen also changes, which may involve an initial liberation and subsequent absorption of water (Humphrey, 2003). Not surprisingly, thermal denaturation of a collagenous tissue can result in marked changes in its thermal (Davis, Doss, Humphrey, & Wright, 2000), mechanical (Aksan & McGrath, 2003; Chae, Aguilar, Lavernia, & Wong, 2003; Chao, Burden, & Wong, 2001; Chen & Humphrey, 1998; Chen, Wright, & Humphrey, 1997, 1998a,b; Diaz et al., 2001), and optical properties (Agah, Gandjbakhche, Motamedi, Nossal, & Bonner, 1996; Bosman, 1993; Jun, Harris, Humphrey, & Rastegar, 2003; Lin, Motamedi, & Welch, 1996). For example, increased extensibility of soft tissues (e.g., pericardium and epicardium) due to

thermal treatment has been observed in both uniaxial (Chachra, Gratzer, Pereira, & Lee, 1996; Chen & Humphrey; Lennox, 1949) and biaxial studies (Harris, Wells, & Humphrey, 2003; Wells et al., 2004). However, none of these studies are for skin tissue and there are only few studies focused on the thermal denaturation process of the tissue (Le Lous, Flandin, Herbage, & Allain, 1982; Le Lous et al., 1985; McHugh et al., 1997; Melling et al., 2000; Pierce, Sheridan, Park, Cense, & De Boer, 2004; Reihnsner, Melling, Pfeiler, & Menzel, 2000), despite skin dermis being mainly composed of collagen.

3. Modeling of Skin Biothermomechanics and Thermal Pain

3.1. MODELING OF SKIN BIOHEAT TRANSFER

From a therapeutic viewpoint, a heating scheme with high-energy intensity and short duration can efficiently produce an appropriate and precise dose of heat during thermal therapies. In addition, reducing the overall treatment time is important, especially when the treatment target volume is large. A rapid heating scheme with a good strategy is therefore essential for an effective thermal therapy. However, the possible non-Fourier nature of heat transfer⁵ in living tissue may play an important role during rapid heating, such as thermal ablation when a high-intensity thermal source (e.g., focused laser, ultrasound, or radio-frequency) is used. For example, it has been shown that the non-Fourier behavior of tissue will delay the appearance of peak temperature during thermal treatments, leading to a lower thermal dose level (Shih et al., 2005). Furthermore, damage to human tissue from thermal agitation is an exponential function of temperature (see Eq. (2.3)), so even small improvements in the prediction of temperature can strongly influence the prediction of damage. Knowledge of temperature distribution in skin tissue is also essential for the understanding of the corresponding thermomechanical behavior.

This section aims to provide a comprehensive description of the thermal behavior in skin tissue, and is organized as follows. First, a skin bioheat transfer model based on classical Fourier theory is presented. A theoretical analysis is carried out and closed-form solutions for a simple one-layer skin model are

⁵ In classic Fourier's law, it is assumed that the propagation speed of thermal disturbance is infinite. However, in particular thermal conditions or heat conduction media, the heat conduction behavior shows a non-Fourier feature such as thermal wave phenomenon or hyperbolic heat conduction.

obtained using the Green's Function method⁶ (Ozisik, 1993). Afterward, different non-Fourier bioheat transfer models including thermal wave model and dual-phase-lag (DPL) model are presented.

3.1.1. Pennes Model

As is well known, the conduction term in the traditional Pennes bioheat transfer equation (Pennes, 1948) is based on the classical Fourier's law, which has been known since the publication of French mathematical physicist Joseph Fourier's studies concerning heat conduction:

$$\mathbf{q}(\vec{r}, t) = -k \nabla T(\vec{r}, t), \quad (3.1)$$

where \mathbf{q} is the heat flux vector representing heat flow per unit time, per unit area; k is the thermal conductivity which is a positive, scalar quantity; ∇T is the temperature gradient; and \vec{r} stands for the position vector. The general bioheat transfer equation is given as

$$\rho c \frac{\partial T}{\partial t} = -\nabla \cdot \mathbf{q} + \varpi_b \rho_b c_b (T_a - T) + q_{\text{met}} + q_{\text{ext}}, \quad (3.2)$$

Note that Eq. (3.2) is different from Eq. (2.1) in that it has a term of “ $-\nabla \cdot \mathbf{q}$ ” instead of “ $k \nabla^2 T$. ” From Eqs. (3.1) and (3.2), the Pennes bioheat transfer equation can be derived, and is duplicated here from Eq. (2.1) as

$$\rho c \frac{\partial T}{\partial t} = k \nabla^2 T + \varpi_b \rho_b c_b (T_a - T) + q_{\text{met}} + q_{\text{ext}}. \quad (3.3)$$

Using the Pennes equation (3.3), one can carry out theoretical analysis to obtain closed-form solutions for a simple one-layer Fourier model: the skin tissue is considered as a perfect, infinitely wide/long plate of thickness, H , according to its anatomical structure, where the Cartesian coordinates are embedded at the center of the plate, as shown in Fig. 3.1. This is a good approximation when heat mainly propagates in the direction perpendicular to the skin surface (e.g., in the case of laser heating). Closed-form analytical solutions of Eq. (3.3) have been obtained for different boundary conditions. Since the metabolic heat generation q_{met} is several orders less than that of external heat generation q_{ext} (Gordon, Roemer, & Howarth, 1976), it is neglected in the derivation of the solutions without loss of accuracy. For example, for a one-layer one-dimensional skin

⁶ The method uses Greens's function to solve inhomogeneous differential equations subject to boundary conditions.

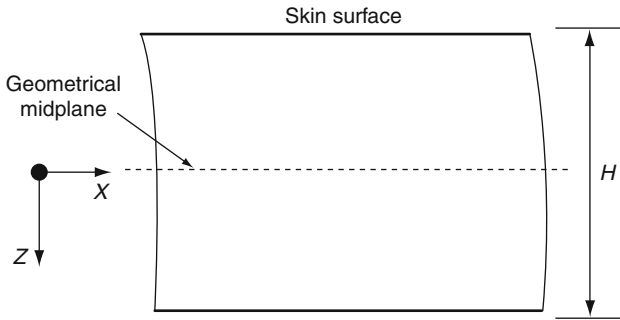


FIG. 3.1 Schematic of the one-layer skin model.

model under surface contact heating, the closed-form solution of temperature at the location z (along the depth H of skin) is given by

$$\begin{aligned} T(z, t) = T_0(z) + \frac{2\alpha}{H} & \left[T_\infty - k \frac{dT_0(z)}{dz} \Big|_{x=0} \right] \\ & \times \sum_{m=1}^{\infty} \beta_m \sin[\beta_m(z+H)] \frac{1}{\alpha \beta_m^2 + \frac{\varpi_b \rho_b c_b}{\rho c}} \left(1 - \exp \left(-\alpha \beta_m^2 t - \frac{\varpi_b \rho_b c_b}{\rho c} t \right) \right) \end{aligned} \quad (3.4)$$

where $T_0(z)$ is the initial temperature field in the tissue and $\beta_m = m\pi/H$, $m = 1, 2, 3, \dots$

In view of the lengthy thermal relaxation time of skin tissue, non-Fourier bioheat transfer models have been developed, as described below.

3.1.2. Thermal Wave Model

In many situations, heat conduction has been treated according to the classical Fourier's law (Eq. (3.1)), which assumes that any thermal disturbance on a body is instantaneously felt throughout the body or, equivalently, the propagation speed of thermal disturbance is infinite. This assumption is reasonable in the majority of practical applications. However, in particular thermal conditions or heat conduction media, where the thermal behavior shows a non-Fourier feature such as thermal wave phenomenon,⁷ or hyperbolic heat conduction as defined mathematically, it fails. Since the experimental observation of a finite thermal

⁷ Temperature jumps are observed which can be regarded as the wave front.

wave speed in liquid helium (Peshkov, 1944), the fundamental wave behavior in heat conduction has been argued from various physical viewpoints (Cattaneo, 1958; Morse & Feshbach, 1953; Vernotte, 1958). Using the concept of a finite heat propagation velocity, Cattaneo (1958) and Vernotte (1958) independently formulated a modified unsteady heat conduction equation, which is a linear extension of the unsteady Fourier equation, where a time scale τ_q is added to Eq. (3.1) to account for the thermal wave behavior:

$$q(\vec{r}, t + \tau_q) = -k\nabla T(\vec{r}, t) \quad (3.5)$$

where $\tau_q = \alpha/C_t^2$ is the thermal relaxation time with α being the thermal diffusivity and C_t being the speed of thermal wave in the medium (Mitra, Kumar, Vedavarz, & Moallemi, 1995; Tzou, 1997). The first-order Taylor expansion of Eq. (3.5) gives

$$q(\vec{r}, t) + \tau_q \partial q(\vec{r}, t)/\partial t = -k\nabla T(\vec{r}, t), \quad (3.6)$$

Due to its similarity in formulation compared to an acoustic wave, the proposed propagation mode of thermal signals is also termed the “second sound wave” by some researchers (Chester, 1963; Peshkov, 1944). Upon substitution of the bioheat conduction Eq. (3.2) into the thermal wave equation, Eq. (3.6), the governing equation of the thermal wave model of bioheat transfer is obtained as

$$\begin{aligned} \tau_q \rho c \frac{\partial^2 T}{\partial t^2} &= k \nabla^2 T - \varpi_b \rho_b c_b T - (\tau_q \varpi_b \rho_b c_b + \rho c) \frac{\partial T}{\partial t} \\ &+ \left(\varpi_b \rho_b c_b T_b + q_{\text{met}} + q_{\text{ext}} + \tau_q \frac{\partial q_{\text{met}}}{\partial t} + \tau_q \frac{\partial q_{\text{ext}}}{\partial t} \right). \end{aligned} \quad (3.7)$$

The above equation is known as a hyperbolic bioheat equation because there appears a double-derivative term ($\tau_q \rho c \partial^2 T / \partial t^2$, called the wave term) that modifies the parabolic Fourier heat equation (Tang & Araki, 1996) into a hyperbolic partial differential equation.

Problems with the Thermal Wave Model Although the thermal wave model has explained many interesting phenomena (Tzou, 1992) and the relaxation behavior has been shown to be admissible within the framework of the second law of extended irreversible thermodynamics (Tzou, 1993), its validity can be questionable. For example, it is not based on the details of energy transport in the material; material properties may not be regarded as constant, for example, the relaxation time, τ_q , is generally temperature dependent (Tzou, 1993); although the thermal wave model can capture the microscale response in time (Ozisik &

(Tzou, 1994; Tzou, 1997), the wave concept does not capture the microscale response in space (Bayazitoglu & Peterson, 1992; Tzou, Ozisik, & Chiffelle, 1994) and the thermal wave model introduces some unusual physical solutions (Godoy & García-Colín, 1997; Koerner & Bergmann, 1998; Taitel, 1972); due to the assumption of a macroscopic behavior averaged over many grains, the validity of the thermal wave model becomes debatable in view of the fast-transient response with microstructural interaction effects (Tzou, 1995a).

To account for deviations from the classical approach involving Fourier conduction and to consider the effect of microstructural interactions in the fast-transient process of heat transport—an effect absent in the thermal wave model—the DPL model has been employed to study bioheat transfer in skin tissue, as described below.

3.1.3. Dual-Phase-Lag Model

In the DPL model, a phase lag for temperature gradient, τ_T , is introduced (Ozisik & Tzou, 1994; Tzou, 1995a, 1997). Together with τ_q , the corresponding governing equation of heat transfer is called the DPL equation and is stated as

$$q(\vec{r}, t + \tau_q) = -k \nabla T(\vec{r}, t + \tau_T), \quad (3.8)$$

where τ_q and τ_T can be interpreted as periods arising from “thermal inertia” and “microstructural interaction,” respectively (Tzou, 1995b). Specifically, τ_q is the phase lag in establishing the heat flux and associated conduction through a medium, while τ_T accounts for the diffusion of heat ahead of sharp wave front that would be induced by τ_q , and is the phase lag in establishing the temperature gradient across the medium during which conduction occurs through its small-scale structures. Through the first and second-order Taylor expansions, the DPL model can be developed into several pertinent models. For example, the simplest example of the DPL model is its first-order expansions for both q and T , given as

$$q(\vec{r}, t) + \tau_q \frac{\partial q(\vec{r}, t)}{\partial t} = -k \left[\nabla T(\vec{r}, t) + \tau_T \frac{\partial \nabla T(\vec{r}, t)}{\partial t} \right]. \quad (3.9)$$

Substituting the Eq. (3.2) into this equation, one obtains the so-called type 1 DPL model of bioheat transfer:

$$\begin{aligned} \tau_q \rho c \frac{\partial T^2}{\partial t^2} &= k \nabla^2 T + \tau_T k \nabla^2 \frac{\partial T}{\partial t} - \varpi_b \rho_b c_b T - (\tau_q \varpi_b \rho_b c_b + \rho c) \frac{\partial T}{\partial t} \\ &+ \left(\varpi_b \rho_b c_b T_a + q_{\text{met}} + q_{\text{ext}} + \tau_q \frac{\partial q_{\text{met}}}{\partial t} + \tau_q \frac{\partial q_{\text{ext}}}{\partial t} \right). \end{aligned} \quad (3.10)$$

An in-depth description of the thermal behavior of skin tissue has thus far been presented where different heat transfer models for skin tissue have been developed based on both Fourier' and non-Fourier' theories. Associated issues of thermal stresses and thermal damage are addressed in the following section. The aim is to develop a computational approach to examine the heat transfer process, thermal damage and the heat-induced mechanical response, so that the underlying mechanism of clinically applied thermal therapies can be understood and that the differences among these thermal therapies can be quantified.

3.2. MODELING OF SKIN BIOTHERMOMECHANICS

Based on the above study on heat transfer, we present in this section the scheme for characterizing the skin biothermomechanical behavior to examine the heat transfer process, thermal damage, and the heat-induced mechanical response. A general closed-form solution for thermal stress for a multilayer skin model is derived, while numerical method (finite element method) is employed for more complicated cases. Two types of case studies are then performed with Fourier and non-Fourier models.

3.2.1. Model Development

As previously discussed, skin tissue has a complicated multilayer structure (see [Fig. 2.1](#)). The thermal properties of different layers have the same order of magnitude ([Table 3.1](#)), but the mechanical properties vary greatly by up to three orders of magnitude from one layer to another. A one-layer continuum model for heat transfer may be assumed; while, to obtain the distribution of heat-induced stresses, the skin tissue must be treated as a laminated composite structure, with each layer assumed to be uniform with linear, orthotropic thermoelastic properties, as shown in [Fig. 3.2](#). The thermomechanical behavior of skin tissue is simplified to be a “sequentially coupled” problem; in other words, the mechanical behavior has no influence on the thermal behavior. The temperature field in skin tissue obtained from solving the governing equations of bioheat transfer is used as the input of the thermomechanical model, from which the corresponding thermal stress field is obtained.

In multilayer models, skin is regarded as a multilayer structure, each having a thickness, t_k , and material properties of Young's modulus, E_k , and Poisson's ratio, ν_k , where $k = 1, 2, \dots, N$ with N being total number of layers.

TABLE 3.1

Thermophysical properties of skin tissue for three-layer model.

Parameters		Value	References
Thermal expansion coefficient ($\times 10^{-4} \text{ K}^{-1}$)	Epidermis	1	Assumption ^a
	Dermis	1	Assumption ^a
	Subcutaneous fat	1	Assumption ^a
Poisson's ratio (-)	Epidermis	0.48	Delalleau et al. (2006)
	Dermis	0.48	Delalleau et al. (2006)
	Subcutaneous fat	0.48	Delalleau et al. (2006)
Young's modulus (MPa)	Epidermis	102	Hendriks et al. (2006)
	Dermis	10.2	Hendriks et al. (2006)
	Subcutaneous fat	0.0102	Hendriks et al. (2006)
Skin density (kg/m^3)	Epidermis	1190.0	Duck (1990)
	Dermis	1116.0	Duck (1990)
	Subcutaneous fat	971.0	Duck (1990)
Skin thermal conductivity (W/mK)	Epidermis	0.235	Elkins and Thomson (1973)
	Dermis	0.445	Elkins and Thomson (1973)
	Subcutaneous fat	0.185	Elkins and Thomson (1973)
Skin specific heat (J/kg K)	Epidermis	3600.0	Henriques and Moritz (1947)
	Dermis	3300.0	Henriques and Moritz (1947)
	Subcutaneous fat	2700.0	Henriques and Moritz (1947)
Metabolic heat generation (W/m ³)	Epidermis	368.1	Roetzel and Xuan (1998)
	Dermis	368.1	Roetzel and Xuan (1998)
	Subcutaneous fat	368.3	Roetzel and Xuan (1998)
Thickness (mm)	Epidermis	0.1	Sejrsen (1972)
	Dermis	1.5	Dahan, Lagarde, Turlier, Courrech, and Mordon (2004)
	Subcutaneous fat	4.4	Assumption

^a There is no reported data on the thermal expansion coefficient of epidermis and dermis layer of skin tissue, but available data for stratum corneum of neonatal rat (Humphries & Wildnauer, 1971) and human fat (Fidanza, Keys, & Anderson, 1953) show that thermal expansion coefficient of skin tissue is on the order of 10^{-4} K^{-1} .

The in-plane extensional ([A]), coupling ([B]), and bending ([D]) stiffnesses of the overall laminate of structure are given by, respectively (Kollar & Springer, 2003)

$$A_{ij} = \sum_{k=1}^N (\bar{Q}_{ij})_k (z_k - z_{k-1}), \quad B_{ij} = \frac{1}{2} \sum_{k=1}^N (\bar{Q}_{ij})_k (z_k^2 - z_{k-1}^2), \quad (3.11)$$

$$D_{ij} = \frac{1}{3} \sum_{k=1}^N (\bar{Q}_{ij})_k (z_k^3 - z_{k-1}^3),$$

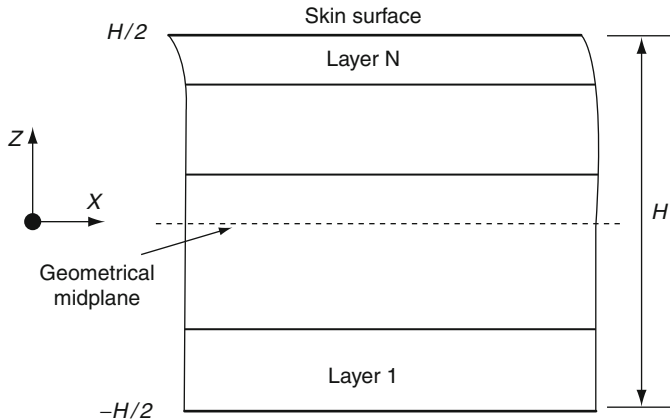


FIG. 3.2 Schematic of the multilayer skin tissue.

where z_k is the coordinate of k th layer along depth; A_{ij} , B_{ij} , and D_{ij} ($i, j = 1, 2, 6$)⁸ are separately assembled into the elements of 3×3 stiffness matrices $[A]$, $[B]$, and $[D]$; $[\bar{Q}]$ is the stiffness matrix of the layered skin structure, defined by

$$[\bar{Q}] = \begin{bmatrix} \bar{Q}_{11} & \bar{Q}_{12} & \bar{Q}_{16} \\ \bar{Q}_{12} & \bar{Q}_{22} & \bar{Q}_{26} \\ \bar{Q}_{16} & \bar{Q}_{26} & \bar{Q}_{66} \end{bmatrix},$$

$$\left\{ \begin{array}{l} (\bar{Q}_{11})_k = (\bar{Q}_{22})_k = \frac{E_k}{1 - v_k^2}, \quad (\bar{Q}_{16})_k = (\bar{Q}_{26})_k = 0, \\ (\bar{Q}_{12})_k = \frac{v_k E_k}{1 - v_k^2}, \quad (\bar{Q}_{66})_k = \frac{E_k}{2(1 + v_k)}. \end{array} \right. \quad (3.12)$$

Due to the combined thermal and mechanical loading, the vector of strains, $\{\varepsilon\}_k$, at a point in each layer under plane-strain conditions are

$$\{\varepsilon\}_k = [\bar{S}]_k \{\sigma\}_k + \{\lambda\}_k \Delta T, \quad (3.13)$$

where ΔT is the temperature difference at a point relative to a reference temperature, $\{\lambda\}_k$ is the vector of the thermal expansion coefficient, and $[\bar{S}]_k$ is the compliance matrix. It should be noted here that the vectors of stresses, $\{\sigma\}_k$, and strains, $\{\varepsilon\}_k$, refer to in-plane strain and stress. By inverting the above equation, the vector of stresses, $\{\sigma\}_k$, can be obtained as

$$\{\sigma\}_k = [\bar{Q}]_k [\{\varepsilon\}_k - \{\lambda\}_k \Delta T]. \quad (3.14)$$

⁸ ij means the directions of orthotropic material in plane stress state.

In a lamina, the total strains over the whole depth generally do not vanish, but are given as

$$\{\varepsilon\}_k = \{\varepsilon^0\} + z\{\kappa\}. \quad (3.15)$$

The resulting stresses are

$$\{\sigma\}_k = [\bar{Q}]_k (\{\varepsilon^0\} + z\{\kappa\} - \{\lambda\}_k \Delta T), \quad (3.16)$$

where $\{\varepsilon^0\}$ and $\{\kappa\}$ are the strain and curvature at the geometrical midplane. The resultant in-plane laminate forces per unit length, $\{N\}$, are found by integrating through the thickness of the laminate:

$$\begin{aligned} \{N\} &= \int \{\sigma\}_k dz \\ &= \int [\bar{Q}]_k (\{\varepsilon^0\} + z\{\kappa\} - \{\lambda\}_k \Delta T) dz, \\ &= [A]\{\varepsilon^0\} + [B]\{\kappa\} - \{N^T\}, \end{aligned} \quad (3.17)$$

where

$$\begin{aligned} [A] &= \begin{bmatrix} A_{11} & A_{12} & A_{16} \\ A_{12} & A_{22} & A_{26} \\ A_{16} & A_{26} & A_{66} \end{bmatrix}, \quad [B] = \begin{bmatrix} B_{11} & B_{12} & B_{16} \\ B_{12} & B_{22} & B_{26} \\ B_{16} & B_{26} & B_{66} \end{bmatrix}, \\ \text{and } \{N^T\} &= \int [\bar{Q}]_k \{\lambda\}_k \Delta T dz. \end{aligned}$$

Similarly, the resultant in-plane moments per unit length are found to be

$$\begin{aligned} \{M\} &= \int \{\sigma\}_k z dz \\ &= \int [\bar{Q}]_k (\{\varepsilon^0\} + z\{\kappa\} - \{\lambda\}_k \Delta T) z dz, \\ &= [B]\{\varepsilon^0\} + [D]\{\kappa\} - \{M^T\}, \end{aligned} \quad (3.18)$$

where

$$[D] = \begin{bmatrix} D_{11} & D_{12} & D_{16} \\ D_{12} & D_{22} & D_{26} \\ D_{16} & D_{26} & D_{66} \end{bmatrix} \quad \text{and } \{M^T\} = \int [\bar{Q}]_k \{\lambda\}_k \Delta T dz$$

From Eqs. (3.17) and (3.18) and by defining

$$\begin{cases} \{N^E\} = \{N\} + \{N^T\}, \\ \{M^E\} = \{M\} + \{M^T\}, \end{cases}$$

it is found

$$\begin{aligned} \begin{cases} \{N\} + \{N^T\} = [A]\{\varepsilon^0\} + [B]\{\kappa\} \\ \{M\} + \{M^T\} = [B]\{\varepsilon^0\} + [D]\{\kappa\} \end{cases} &\Rightarrow \begin{cases} \varepsilon^0 \\ \kappa \end{cases} = \begin{cases} A' & B' \\ B' & D' \end{cases} \begin{cases} N^E \\ M^E \end{cases} \\ &\Rightarrow \begin{cases} \varepsilon^0 = A'N^E + B'M^E, \\ \kappa = B'N^E + D'M^E, \end{cases} \end{aligned} \quad (3.19)$$

where

$$\begin{aligned} [A'] &= [A^*] - [B^*][D^*]^{-1}[C^*] = \begin{bmatrix} a'_{11} & a'_{12} & 0 \\ a'_{12} & a'_{11} & 0 \\ 0 & 0 & a'_{66} \end{bmatrix}, \\ [C'] &= [B'] = \begin{bmatrix} c'_{11} & c'_{12} & 0 \\ c'_{12} & c'_{11} & 0 \\ 0 & 0 & c'_{66} \end{bmatrix}, \\ [B'] &= [B^*][D^*]^{-1} = \begin{bmatrix} b'_{11} & b'_{12} & 0 \\ b'_{12} & b'_{11} & 0 \\ 0 & 0 & b'_{66} \end{bmatrix}, \\ [D'] &= [D^*]^{-1} = \begin{bmatrix} d'_{11} & d'_{12} & 0 \\ d'_{12} & d'_{11} & 0 \\ 0 & 0 & d'_{66} \end{bmatrix}, \end{aligned}$$

$$[A^*] = [A]^{-1}, \quad [B^*] = -[A]^{-1}[B], \quad [C^*] = [B][A]^{-1}, \text{ and } [D^*] = [D] - [B][A]^{-1}[B].$$

Thus, the in-plane stresses parallel to the skin surface, σ_{xx} , in each layer (Fig. 3.2) can be obtained as

$$\{\sigma_{xx}\}_k = \bar{E}_k \begin{pmatrix} -\bar{\lambda}_k \Delta T + \left[(a'_{11} + a'_{12})(1 + v_k) \left(\sum_{i=1}^N \int_{z_{i-1}}^{z_i} \bar{E}_i \bar{\lambda}_i \Delta T dz \right) \right. \\ \left. + (b'_{11} + b'_{12})(1 + v_k) \left(\sum_{i=1}^N \int_{z_{i-1}}^{z_i} \bar{E}_i \bar{\lambda}_i \Delta T z dz \right) \right] \\ + z(1 + v_k) \left[(b'_{11} + b'_{12}) \left(\sum_{i=1}^N \int_{z_{i-1}}^{z_i} \bar{E}_i \bar{\lambda}_i \Delta T dz \right) \right. \\ \left. + (d'_{11} + d'_{12})(1 + v_k) \left(\sum_{i=1}^N \int_{z_{i-1}}^{z_i} \bar{E}_i \bar{\lambda}_i \Delta T z dz \right) \right] \end{pmatrix}, \quad (3.20)$$

where $\bar{E} = E/(1 - v^2)$, $\bar{\lambda} = (1 + v)\lambda$, and N is the total number of skin layers.

3.2.2. Case Study

Description of the Problem The skin is initially cooled by natural convection by environmental air ($T_e = 25^\circ\text{C}$, $h = 7 \text{ W/m}^2\text{K}$). At $t = 0$, the skin surface is suddenly taken into contact with a hot source of constant temperature 100°C

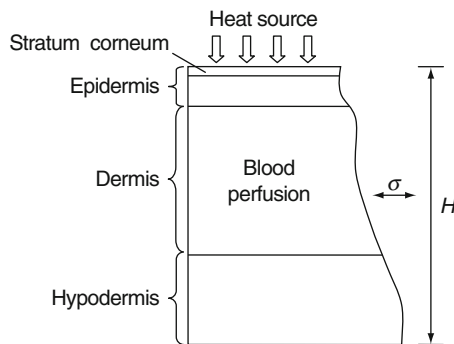


FIG. 3.3 Idealized skin model according to the real structure of skin as shown in Fig. 2.1.

such as boiling water; after contacting for 15 s, the hot source is removed and the skin is cooled by use of water/ice mixture of 0 °C for 30 s (the heating/cooling is uniform along the surface). A three-layer skin model is used, which is composed of epidermis, dermis and fat layer, as shown in Fig. 3.3. The relevant parameters used are given in Tables 3.1 and 3.2.

Results The above problem is solved by using different bioheat transfer models: Pennes model, thermal wave model and DPL model. For the multilayer skin model, predictions from different models are shown in Fig. 3.4 for temperature, in Fig. 3.5 for thermal damage, and in Fig. 3.6 for thermal stress. The temperature, thermal damage, and thermal stress distributions in the skin tissue at the end of heating ($t = 15$ s) and cooling ($t = 45$ s) are shown separately in Figs. 3.4C–D, 3.5C–D, and 3.6C–D, while Figs. 3.4A – B and 3.5A – B plot the corresponding temperature and burn damage at the epidermis–dermis (ED) interface and dermis–fat (DF) interface of skin as functions of time, respectively. Since the nociceptors⁹ emerge from superficial dermis running into epidermis (Patapoutian, Peier, Story, & Viswanath, 2003) as low as 50 μm from the skin surface (Kruger, Perl, & Sedivec, 1981), attention is focused on thermal stress at the skin surface and ED interface, as shown in Fig. 3.6A and B.

Figure 3.4A–D demonstrates that the tissue temperature calculated from different models deviates substantially under constant surface temperature heating. With the thermal wave model, the tissue temperature inside the body is undisturbed during the initial stage of heating, which is attributed to the non-thermally consumption related biological activities¹⁰ (Liu, Chen, & Xu, 1999);

⁹ Special receptor for pain sensation.

¹⁰ Activities like driving a water particle or an ion, changing electrical potentials of cell membranes, or triggering a biochemical process.

TABLE 3.2

Thermophysical properties of skin tissue for one-layer model.

Parameters	Value	References
Thermal expansion coefficient ($\times 10^{-4} \text{ K}^{-1}$)	1	Assumption
Poisson's ratio (-)	0.48	Delalleau, Josse, Lagarde, Zahouani, and Bergheau (2006)
Young's modulus (MPa)	102	Hendriks, Brokken, Oomens, Bader, and Baaijens (2006)
Skin density (kg/m^3)	1190.0	Duck (1990)
Skin thermal conductivity (W/mK)	0.235	Elkins and Thomson (1973)
Skin specific heat (J/kg K)	3600.0	Henriques and Moritz (1947)
Metabolic heat generation (W/m ³)	368.1	Roetzel and Xuan (1998)
Thickness (mm)	6.0	Sejrsen (1972)

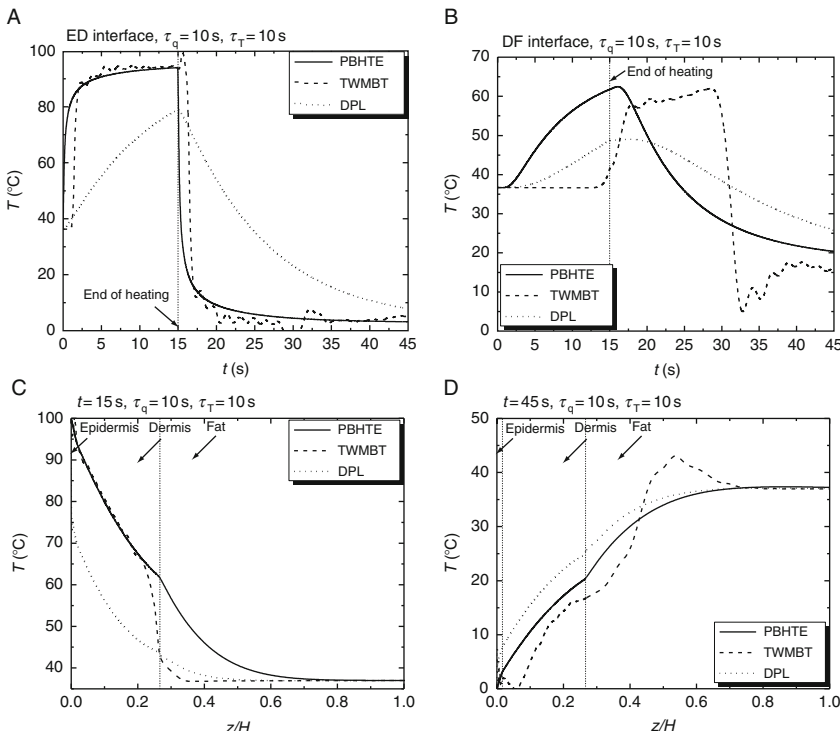


FIG. 3.4 Comparison of predictions of temperature from different models: (A) variation with time at ED interface, (B) variation with time at DF interface, (C) distribution along skin depth at $t = 15 \text{ s}$, and (D) distribution along skin depth at $t = 45 \text{ s}$ (PBHTE, Pennes model; TWMBT, thermal wave model; DPL, dual-phase-lag model).

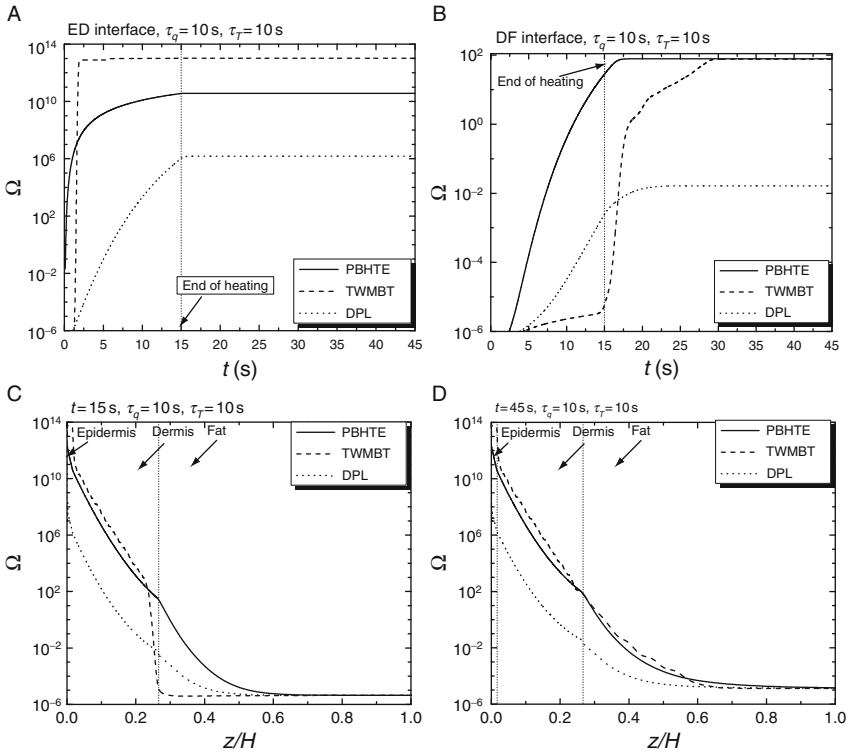


FIG. 3.5 Comparison of predictions of thermal damage from different models for the case of surface contact heating in non-Fourier analysis: (A) variation with time at epidermis–dermis, (ED) interface, (B) variation with time at DF interface, (C) distribution along skin depth at $t = 15$ s, and (D) distribution along skin depth at $t = 45$ s (PBHTE, Pennes model; TWMBT, thermal wave model; DPL, dual-phase-lag model). Note that $z/H = 0.0167$ and 0.267 indicate the epidermis–dermis (ED) and dermis–fat (DF) interfaces, respectively.

followed by a instantaneous jump, which may be viewed as the wave-front emerging from the finite propagation of the thermal wave or the existence of the relaxation time τ_q . Unlike the thermal wave model, no wave behavior is observed in the DPL model as expected, but a non-Fourier diffusion-like behavior exists due to the second thermal relaxation time, τ_T , whose effect is to weaken the thermal wave effect, thereby to destroy the sharp wave front. Additionally, a sudden temperature drop for heating or a step for cooling at the skin surface is associated with the DPL model, as shown in Fig. 3.4C and D.

The large differences among the predicted temperatures of different models cause significant deviations in thermal damage evaluations. For example, the thermal damage predicted by the thermal wave model at the end of heating for the

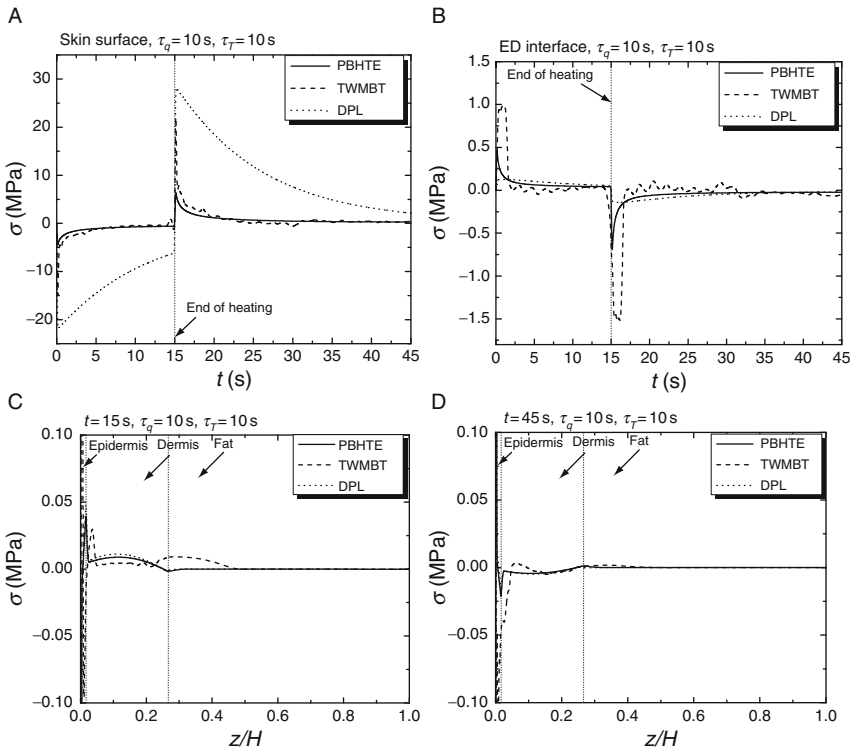


FIG. 3.6 Comparison of predictions of thermal stress from different models for the case of surface contact heating in non-Fourier analysis: (A) variation with time at skin surface, (B) variation with time at epidermis–dermis (ED) interface, (C) distribution along skin depth at $t = 15\text{ s}$, and (D) distribution along skin depth at $t = 45\text{ s}$ (PBHTE, Pennes model, TWMBT, thermal wave model; DPL, dual-phase-lag model). Note that $z/H = 0.0167$ and 0.267 indicate the epidermis–dermis (ED) and dermis–fat (DF) interfaces, respectively.

ED interface is the largest, about three orders larger in magnitude than that from the Pennes model, and about seven orders larger than those from the DPL model. A wave front for thermal damage is also observed for the thermal wave model, which appears in Fig. 3.5B as a steep profile. As for the thermal damage distribution along the skin depth, the Pennes and the thermal wave models give similar results, which are much larger in magnitude than the DPL model.

The thermal stresses developed due to nonuniform temperature distributions are confined near the skin surface, see Fig. 3.6C and D and both the skin surface and ED interface are subjected to large tensile stresses ($>10\text{ MPa}$), see Fig. 3.6A

and B, during both heating and cooling processes. This implies higher thermal damage occurring in these locations, consistent with the results of Fig. 3.5A and B. Furthermore, the magnitude of stress at the skin surface obtained with the DPL model is much larger than that with other models, although the same boundary condition is applied. This is caused by the sudden temperature drop at skin surface, see Fig. 3.4C. It should be noted here that the mean mechanical threshold of nociceptors in the skin tissue lies in the range of about 0–0.6 MPa and mainly between 0.1 and 0.2 MPa (James & Richard, 1996), which suggests that, in addition to heating, thermal stress may also contribute to thermal pain. Other supporting evidence shows that, for the same level of nociceptor activity, a heat stimulus evokes more pain than a mechanical stimulus and that tissue deformation due to heating and cooling may explain the origins of pain (Reuck & Knight, 1966; Van Hees & Gybels, 1981).

3.3. MODELING OF SKIN THERMAL PAIN

3.3.1. Model Development

When the skin temperature rises above a critical value, an uncomfortable feeling or pain sensation is induced. In this section, the current understanding of the mechanisms for thermal pain and its relation to skin biothermomechanics is described.

Pain sensation has been studied extensively for a long time over a range of scales, from the molecular level to the entire human neural system level. Thermal stimulation is one of the three main causes of pain, the others being mechanical and chemical stimulations, and has been widely used in the study of pain (Arendt-Nielsen & Chen, 2003). However, the understanding of the underlying mechanisms of thermal pain sensation is still far from clear due to the influence of many factors, both physiological and psychological.

Although the utilization of computational models in the field of pain has been very limited and attempts at modeling pain have generally focused on acute pain,¹¹ there are strong arguments for the mathematical modeling of pain (Britton & Skevington, 1996; Picton, Campbell, & Turner, 2001): it can handle extremely complex processes; the model can be used to predict behavior which has perhaps gone unnoticed; the method is noninvasive. So far several models have been developed to capture effects at the molecular and cellular levels, up

¹¹ Acute pain usually refers to the pain sensation caused by soft tissue damage, infection, and/or inflammation among other causes (Fink, 2005).

to the level of network of neurons (Britton & Skevington; Haeri, Asemani, & Gharibzadeh, 2003). However, none of these models have considered morphological plausibility (i.e., the structural reality) and the biothermomechanical response of skin tissue, or correlated the external stimulus parameters directly with the pain sensation level, and no transmission process has been considered. We have therefore developed a holistic mathematical model for quantifying skin thermal pain to build up a direct correlation between the parameters of thermal stimulation and the level of the corresponding thermal pain sensation, by using the thermomechanical models developed above and by considering the current biophysical and neurophysiological mechanisms of pain sensation. Both the transduction process within the skin tissue and the transmission process along the neural fibers are addressed by the model.

For simplicity, the present holistic mathematical model only attempts to model superficial nociceptive acute pain; neuropathic pain and chronic pain¹² are not considered. Additionally, psychological factors that may influence pain are not modeled, such as distraction, empathy, and so on. It is known that classical descriptions of pain typically include four processes (as described below): transduction, transmission, perception, and modulation. Due to the interaction between perception and modulation, the holistic model is thus composed of three models: model of transduction, model of transmission, and model of perception and modulation, as schematically shown in Fig. 3.7. Details of the model can be found in our previous study (Xu, Lu, et al., 2008). Here we only present results from a case study.

3.3.2. Case Study

Description of Problem The skin tissue is initially kept at constant temperature of 37 °C, when at $t = 0$, its surface is suddenly taken into contact with a hot source at a constant temperature, T_s for 5 s. The depth of nociceptor in the skin tissue is assumed to vary in the range of $25 \mu\text{m} \leq z_{\text{noci}} \leq 200 \mu\text{m}$. Using the skin thermomechanical model described in the previous section, the temperature history of nociceptor is obtained first, which is then used as the input for the neural model. The nociceptors are assumed to be C fibers¹³ with a conduction

¹² Chronic pain was originally defined as pain that has lasted 6 months or longer. More recently it has been defined as pain that persists longer than the temporal course of natural healing, associated with a particular type of injury or disease process (Shipton & Tait, 2005).

¹³ Peripheral nerves include myelinated afferent $A\delta$, $A\alpha$, and $A\beta$ fibers, as well as unmyelinated afferent C fibers. However, $A\beta$ fibers only respond to nonnoxious, low density mechanical stimuli. Most nociceptors are either $A\delta$ or C fibers, while thermal pain sensations are mediated by both thin myelinated $A\delta$ and unmyelinated C fibers (Meyer, Campbell, & Raja, 1994).

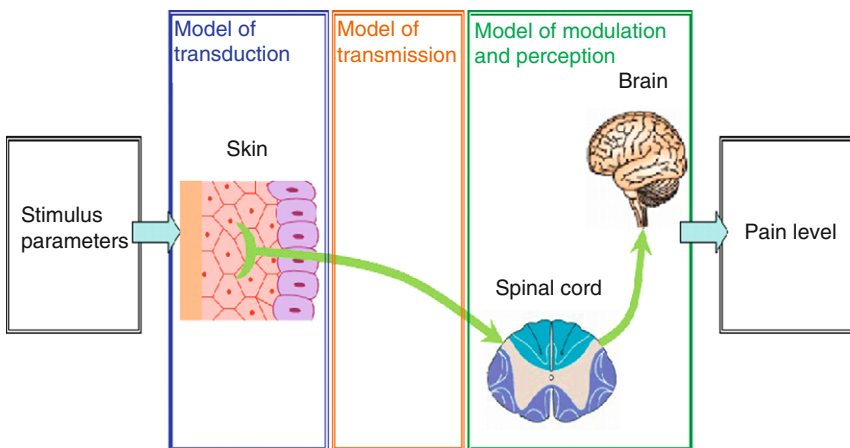


FIG. 3.7 Schematic of the holistic skin thermal pain model.

TABLE 3.3

Thermophysical properties of blood.

Parameters	Value	References
Blood density (kg/m^3)	1060.0	Duck (1990)
Blood specific heat (J/kg K)	3770.0	Torvi and Dale (1994)
Arterial blood temperature ($^\circ\text{C}$)	37	
Core temperature ($^\circ\text{C}$)	37	

velocity of 1 m/s. The one-dimensional, three-layer skin model is used where the effect of blood perfusion is only considered in the dermis layer. The relevant parameters of skin tissue used are summarized in Tables 3.1 and 3.3.

Influence of Nociceptor Depth As described before (Xu, Wen, Lu, & Seffen, 2008), thermal pain is decided by stimuli at the location of nociceptor, which varies over different parts of the body, and from person to person. For example, Tillman, Treede, Meyer, and Campbell (1995a) found that the heat threshold for a C fiber mechanoheat nociceptor was determined by its depth of location. In the present case study, nociceptors located at different depths are considered with a stimulus at the skin surface of $T_s = 55^\circ\text{C}$: four depths, $z_{\text{noci}} = 25, 50, 100, 200 \mu\text{m}$, are chosen which are in the range

reported in literature. The predicted temperature history at the location of nociceptor is given in Fig. 3.8A, while the corresponding neural responses and pain level are shown in Fig. 3.8B–D, respectively. From Fig. 3.8A, it can be seen that the temperature at the location of the nociceptor increases exponentially in the early stages of heating, before tending toward a constant value with time. The temperature at the nociceptor located closer to skin surface is higher, for example, at $t = 5$ s, the temperature at $z_{\text{noci}} = 25 \mu\text{m}$ is almost 5 °C higher than at $z_{\text{noci}} = 200 \mu\text{m}$. The variation of membrane voltage with time¹⁴ is plotted in Fig. 3.8B. The frequency of the action potential impulses increases with time and, similar to that of temperature, it tends to a constant value. The frequency also increases as the nociceptor depth is reduced, which can be better seen from the frequency history shown in Fig. 3.8C. Therefore, it can be seen from the results that the pain level, as shown in Fig. 3.8D, is higher if the nociceptor is located closer to the surface of skin tissue under the same stimulus intensity. This may be used to explain why different pain thresholds were obtained by different studies for the same stimulus (Tillman et al., 1995a,b).

It should be noted here that there is a clear latency of about 1 s between the start of stimulation and the response of T cell as shown in Fig. 3.8D due to the transmission process. Similar results have also been experimentally observed. For example, Campbell and LaMotte (1983) found that, the time for detecting temperature stimuli in the range of 39–51 °C was between 0.7 and 1.1 s for the finger tip and between 0.4 and 1.1 s for the arm.

¹⁴ The essential function of nociceptors (pain receptor) depends on ion channels (Caterina & Julius, 1999; McCleskey & Gold, 1999), which mediate the selective passage of specific ions or molecules across a cell membrane (Alberts et al., 1994). Ion channels belonging to nociceptors include heat activated channels (Cesare & McNaughton, 1996; Dittert et al., 1998; Kirschstein, Büsselberg, & Treede, 1997; Nagy & Rang, 1999), capsaicin receptor (Caterina, Rosen, Tominaga, Brake, & Julius, 1999; Nagy & Rang, 1999), ATP-gated channels (Burnstock, 1996; Burnstock & Wood, 1996; Hamilton, 2002; Hilliges et al., 2002), proton-gated channels or acid-sensing channels (Krishtal & Pidoplichko, 1980, 1981; Waldmann, 2001), nociceptor-specific voltage-gated Na^+ channels (Waxman, Dib-Hajj, Cummins, & Black, 1999), and mechanosensitive channels, amongst others. These channels are generally converted from closed to open states, or “gated,” by three types of stimuli: thermal (hot or cold), mechanical, and chemical stimuli, with thresholds of 43 °C and $\sim 0.2 \text{ MPa}$ for the first two. There is another important class of ion channels, which are gated by changes in transmembrane voltage rather than the above-mentioned stimuli. These voltage-gated channels respond to membrane depolarization or hyperpolarization, and are central to the generation and transmission of electrical signals (action potential) along nerve fibers (Elmore, 2004).

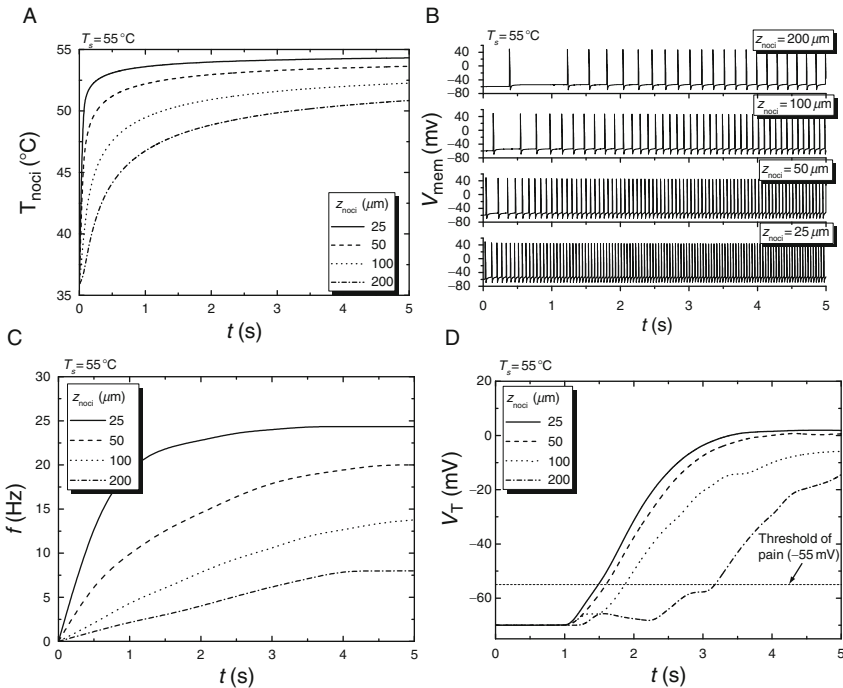


FIG. 3.8 Influence of nociceptor location on transduction: (A) temperature, (B) membrane voltage variation, (C) frequency response, and (D) pain level.

4. Experimental Methodology

In all the studies described above, a mathematical approach has been introduced for determining the thermomechanical response in skin tissue induced by heating and the corresponding skin thermal pain sensation, where the main deficiency is that the skin tissue is assumed to have thermally independent properties due to the comparatively few relative studies. These are addressed in the following two sections, which specially aims to design and build experimental systems and to obtain suitable data to quantify the influence of the temperature and the corresponding thermal damage on the mechanical behavior of skin tissue, including tensile, compressive, and viscoelastic behaviors. This section presents the experimental methodology adopted to quantify the thermal denaturation and mechanical behavior of skin tissue under thermal agitations. In particular, it describes the methodology for obtaining and preparing the skin samples; the methodology of thermal analysis with the DSC; the design and

manufacture of the hydrothermal tensile system and the hydrothermal compressive system; and the thermodynamic analysis of skin viscoelasticity with dynamic mechanical analyzer.

4.1. EXPERIMENTAL CHARACTERIZATION OF SKIN MECHANICAL PROPERTIES

The only truly reliable method to determine skin mechanical properties is through *in vivo* testing since the deformation of skin may be strongly dependent on active biological processes while, with *in vitro* testing, the tissue has been removed from collateral processes such as blood perfusion, lymphatic drainage, metabolism, nervous, and hormonal controls. For example, during compression, the deformation of skin tissue has been found to be largely a function of fluid interchange with the surrounding unstressed skin tissue (Daly, 1982). The skin tissue used for *in vitro* experiments is not perfused and thus, it lacks restorative fluidic pressures, which can potentially reduce the visible compression of the tissue after application of pressure (Bonilla, Massanet, & Almodóvar, 2005). However, *in vivo* measurements are affected by both the skin tissue itself and other structures to which it is attached, which prevents a controllability of loading.

Most of the *in vitro* experiments on skin mechanical properties employ a tensile approach, where it is now accepted that biaxial testing can mimic the sorts of deformation experienced *in vivo*. However, there are many difficulties in performing such experiments on soft biological tissues (Sacks & Sun, 2003): for example, the edges must be able to expand freely in the lateral direction, and in the central target region, the stress and strain states should be uniform so that data analysis can be performed simply. In view of these problems, an unconfined compression¹⁵ test through the thickness of tissue has been suggested since it results in an approximate in-plane biaxial behavior (Hepworth, Steven-fountain, Bruce, & Vincent, 2001; Shergold et al., 2006). If the compressibility of skin tissue is small, as has been reported in the literature, or in other words, skin tissue deforms under constant volume (e.g., the Poisson ratio is 0.5), the compression introduces equivalent biaxial extensions in the plane of the skin tissue. For example, Shergold (2004) found that the Ogden model evaluated from his compression tests of pig skin tissue provided a reasonable approximation to the tensile orthotropic constitutive behavior measured by Ankersen, Birkbeck, Thomson, and Vanezis (1999). However, the unconfined compression test is

¹⁵ Compression in which there is free expansion in the lateral direction of the sample.

very dependent on the friction characteristics between the skin sample and the compression platens, which can restrict lateral expansion. Fortunately, this problem can be overcome in a number of ways: by covering the moving platen with a polytetrafluoroethylene (PTFE) sheet (Miller & Chinzei, 1997); by using platens of polished stainless steel (Miller-Young, Duncan, & Baroud, 2002); by removing the epidermis layer from skin sample (Hepworth et al.); by coating smooth compression platens with lubricant or grease (margarine) (Hepworth et al.; Shergold et al.); by using lubricated squeezing flow (Nasseri, Bilston, & Tanner, 2003), and so on.

4.2. EXPERIMENTAL CHARACTERIZATION OF SKIN THERMAL DENATURATION

As for characterizing thermal denaturation of collagenous tissues, in spite of the different metrics used (as described in [Section 2](#)), there are generally two types of heating protocols used in most experiments (Wright & Humphrey, 2002), namely, the temperature-jump protocol and the controlled heating-rate protocol. In the first case, the specimen is heated quickly to a specified hyperthermal temperature, where the time needed for the temperature rise is very short and can be neglected, and the temperature is maintained isothermally during the test period. In the case of controlled heating-rate protocol, the temperature of the specimen is raised, usually at a constant rate, to a specified hyperthermal temperature over time.

However, most of the studies using the above two heating protocols, such as hydrothermal isometric tension (HIT) testing, are mainly aimed at the denaturation process, while our study focuses on the temperature, thermal denaturation, and their influence on the mechanical behavior of skin tissue. Therefore, the two methodologies on mechanical response and thermal denaturation as described above will be combined together below to characterize the thermomechanical behavior of skin tissue.

4.3. SAMPLE PREPARATION TECHNIQUES

4.3.1. Selection of Samples

The ethical and immunological issues associated with human skin tissue testing require us to find a substitute tissue. Pig skin tissue is chosen due to its structural and functional efficacy compared to human skin tissue (Douglas, 1972; Johnson et al., 2001; Meyer, Schwarz, & Neurand, 1978; Shergold & Fleck, 2005; Shergold et al., 2006), including the histology, morphology, cell

kinetics, density of hair, etc. Furthermore, repetitive tests can be realized for the same animal because of its large size, reducing the variation in results (Middelkoop et al., 2004).

Pig skin tissue varies in thickness by site; however, there appears to be a good concordance in thickness among age-matched donors. Therefore, skin samples from the cheek, ear, back, belly, and flank areas are used. Specifically, pig ear skin tissue taken from the center auricle is used for tensile tests, which has been shown to be very similar to human skin tissue (Meyer, Kacza, Zschemisch, Godynicki, & Seeger, 2007), while skin tissue from the back of pig is chosen for compression tests in consideration of its large thickness and low anisotropy (Ankersen et al., 1999). In the present experiments, skin samples from domestic British breeds of pigs are used, which are obtained from a local slaughter house near Cambridge, UK.

4.3.2. Sample Procurement

Samples of pig skin tissue to a depth of the subcutaneous fat at different body sites are procured daily, 10-min postmortem by block dissection. The skin sample is excised with sharp scissors and a single-edged razor blade, taking care to minimize the mechanical strain applied to the tissue. They are then fast-chilled following the standard tissue procurement protocol to 4 °C in a pregassed Krebs–Henseleit Ringer (KHR, pH 7.4). Samples are transported to the laboratory immediately afterward, where the samples are separated from subcutaneous fat by wet/fast dissection in KHR at 4 °C and the epidermal layers are not removed to prevent the death of cells caused by mechanical trauma. The skin samples are tested within a few hours of slaughter, in order to minimize degradation of the tissue structure. In all, efforts have been placed on keeping the cellular component of the samples viable. Any storage of test samples at room temperature has been avoided, and only samples that have been stored at 4 °C are used. This routine has been shown to best preserve the samples (Meyer, Zschemisch, & Godynicki, 2003; Meyer et al., 2007), permitting fibroblasts to remain viable for long periods (Wright, Wiig, Winlove, Bert, & Reed, 2003).

It should be pointed out that biological tissues, such as skin here, swell when in contact with physiological solution, due to the osmotic pressure difference induced by the fixed charges of the proteoglycans (Urban, Maroudas, Bayliss, & Dillon, 1979). In our experimental study, all specimens were allowed to swell more than 4 h before data was collected to eliminate the possibility of different effects of swelling on the results, in view that most of the swelling of excised skin tissue takes place within 3–4 h after immersion (Lanir & Fung, 1974).

4.3.3. Sample Preparation

Sample Cutting Before cutting, any hair on the skin tissue is closely clipped with electric clippers. The outline geometry of the sample is marked on the skin tissue with surgical skin marker prior to excision. Skin samples of different shapes are prepared in KHR at 4 °C by use of tissue punches immediately prior to mounting in the experimental apparatus. For tensile and relaxation tests, a rectangular specimen, approximately 20 × 20 mm for biaxial tests (20 × 2.5 mm for uniaxial tests), is cut from the excised skin tissue with a press-knife constructed from disposable razor blades held in a block of perspex. A dumbbell shape is not selected due to technical difficulty and potential tissue damage, although it may have been preferable to use on strictly mechanical grounds due to the uniform distribution of load in the central region of sample and the avoidance of end effects (Wright et al., 2003). For compression tests, cylindrical specimens¹⁶ are cut from pig skin tissue, using a 10-mm diameter leather die punch mounted on a hand press in KHR at 4 °C. The punch is straight internally and tapered externally, and has a sharp edge.

Sample Measurements For tensile tests, the thickness of each rectangular strip is measured using a micrometer after stretching the samples to their original size as measured before excision,¹⁷ accurate to 0.01 mm, and its width is measured using digital slide calipers, accurate to 0.01 mm. Five sets of measurements are performed at different locations and the average set is taken for the size of sample. Any errors in sample size measurement due to penetration of the micrometer probe into the skin tissue are observed to be less than 0.1 mm by comparing with direct measurements using a microscope. Precise measurement of the length of sample in tensile tests is not performed since an optical method is used for the displacement/strain measurement, where the length can be optically recorded instead. For compressive tests, both the thickness (height) and diameter of each sample are measured using a micrometer, accurate to 0.01 mm, after placing the sample between glass slides in the undeformed state.

Predamage of Samples To study the influence of thermal denaturation/damage on skin properties, selected skin samples are thermally denatured before testing by wrapping them in water-tight aluminum foil packets and submerging in a KHR bath with prescribed heating histories (Essenpreis,

¹⁶ Compression of specimen during cutting produces a curved rather than straight edge to specimen. The curved shape is induced due to tissue expansion resulted from compression during cutting.

¹⁷ This is aimed to remove the effect of shrinkage induced during cutting.

1992; Lin, Motamedi, & Welch, 1996). Care is taken during this process to minimize dehydration.

Mechanical Preconditioning of Samples Preconditioning¹⁸ is often applied to mechanical testing of skin tissue both *in vitro* and *in vivo*. Compared to tensile preconditioning, in which the samples are typically loaded/unloaded for more than 20 cycles, compressive preconditioning requires fewer cycles (Wu, Cutlip, Andrew, & Dong, 2007; Wu, Dong, Smutz, & Schoppe, 2003): Wu et al. (2003) found that repeatable mechanical behavior is observed after 3–4 cycles of compressive loading, irrespective of the loading rate and loading configurations. Although preconditioning has been routinely applied in soft tissue tests, the exact mechanism responsible for the improved replicability remains unclear (Wu et al., 2003, 2007). From a microstructural point of view, uniaxial tensile preconditioning serves to orient the originally randomly distributed collagen fibers to a more straight and uniform pattern (Lanir, 1987); in compression, preconditioning does not significantly affect the orientation of the collagen fibers, rather, it improves the contact conditions between the sample and the compression platens or chamber walls (Wu et al., 2003).

In the present study, mechanical preconditioning of skin samples in KHR solution at 37 °C is applied before each test, to obtain reproducible responses. The skin sample is subjected to a displacement controlled sinusoidal excitation at a specific frequency (0.05 Hz), and the loading/unloading curves are examined to determine if repeatable stress–strain curves are achieved. The test data are discarded if the loading/unloading curves fail to converge to a repeatable stress–strain relationship. After preconditioning, the samples are preloaded to a stress state of 10 kPa, which is a reasonable initial stress *in vivo* (Diridollou et al., 2001), to mimic its *in vivo* condition. Enough time is allowed, prior to starting the test, for the skin sample to get to the equilibrium state, which is chosen as the reference configuration. It should be noted here that the mechanical preconditioning may have some effect on the following viscoelastic measurements. This effect, however, can be neglected here since preconditioning recovery has a much longer time constant (hours) compared with the duration of several minutes test period.

¹⁸ Viscoelasticity is readily evident in many soft tissues, where there is energy dissipation, or hysteresis, between the loading and unloading of the tissue during mechanical tests. Some soft tissues can be preconditioned by repetitive cyclic loading to the extent where the stress–strain curves for the loading and unloading portions of the tests nearly overlap.

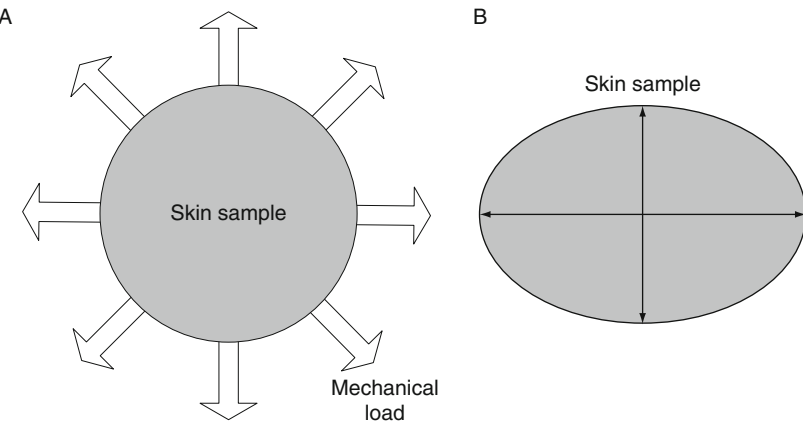


FIG. 4.1 Identification of material axis. A circular skin specimen has opposing pairs of small clamps placed on its perimeter (A): each pair is separately preloaded, and two markers are made, and aligned to the stretch axes. For several positions on the perimeter, the markers produce an ellipsoidal pattern whose semi-axes are aligned to the material axes (B). For uniaxial tensile tests, the sample is cut along the minor semi-axes, while for biaxial tests, the square sample is cut with adjacent sides parallel to the semi-axes, respectively.

Identification of Material Axis The thermal and mechanical behaviors of skin tissue are anisotropic; therefore, the material axis¹⁹ of test samples should be first identified. Generally, identification of the material axis is based on observations of the gross specimen shape or the fiber architecture. However, in skin tissue, the fibers are too small to be observed visually. The equal-load method (Choi & Vito, 1990) is therefore used where the material axis is identified by determining which direction, when loaded to the same stress, demonstrates the greatest and least strain values, (Fig. 4.1).

4.4. DIFFERENTIAL SCANNING CALORIMETRY TESTS

The thermal metric is used in this study to characterize the thermal denaturation and heat-induced damage of skin tissue by using DSC, which has been used extensively to characterize the thermal behavior of collagenous tissues including skin tissue (Schiller, Funke, & Gunther, 2004; Young, 1998). DSC detects thermodynamic changes by measuring the flow of heat between a sample and a reference, whereby the variation of enthalpy or apparent specific heat²⁰ of skin samples with temperature is recorded during the heating and the parameters for

¹⁹ Direction of collagen fiber orientation in skin tissue.

²⁰ Representing the combined effects of specific and latent heats.

describing thermal denaturation process are then calculated based on the assumed reaction model of first-order kinetics (Eq. (2.2) in Section 2.2).

The thermal stability of collagen in pig skin sample is assessed with a TA Instruments DSC of type Q1000 T_{zero} , scanning from 20 to 100 °C at four different heating rates ($r_h = 2, 5, 10, \text{ and } 20 \text{ }^{\circ}\text{C/min}$). The skin sample, of about 8 mg in weight, is put inside a hermetically sealed pan, which is kept away from all contamination. The pan is then placed in a differential scanning calorimetric cell and heating is applied at a constant rate, r_h . The controlled heating-rate protocol is chosen for it needs comparatively much fewer specimens than temperature-jump tests (Wright & Humphrey, 2002).

4.5. HYDROTHERMAL TENSILE TESTS

4.5.1. System Design

A hydrothermal tensile system²¹ has been designed and built, which can be either force or displacement controlled, enabling a variety of uniaxial and biaxial tensile tests under hydrothermal conditions, such as HIT tests and hydrothermal isotonic tests. Biaxial mechanical testing is chosen in the present system for the following reasons: (1) *in vivo*, skin tissue is loaded biaxially; (2) as the fibers in skin tissue are multidirectional, the orientation of the fibers with respect to the load axis must be taken into account; (3) for incompressible or nearly incompressible materials, biaxial mechanical testing can be used to obtain the material parameters needed for 3D constitutive models; (4) pursuit of a multiaxial analysis is of clinical importance to surgeons for if the orientation of maximum extensibility is known, the excision can be planned to optimize wound closure; and (5) uniaxial test can also be performed with a biaxial testing system by loading in only one direction.

To perform accurate tensile experiments on soft biological tissues, the following should be considered. Small specimen sizes should be used for otherwise it becomes difficult to precisely identify material axes. Correct gripping is needed to avoid damage to the specimen and to assure a uniform distribution of forces along the specimen edges. Biological degradation can be avoided by testing quickly, and testing should aim for homogeneous deformation within the specimen. Compared to the uniaxial test, biaxial testing needs to address additional requirements: the edges must be able to expand freely in the lateral direction; in the central target region, the stress and strain states should be uniform so that data analysis can be performed simply; and the target region must be small and located

²¹ A tensile system in a temperature controlled fluid environment.

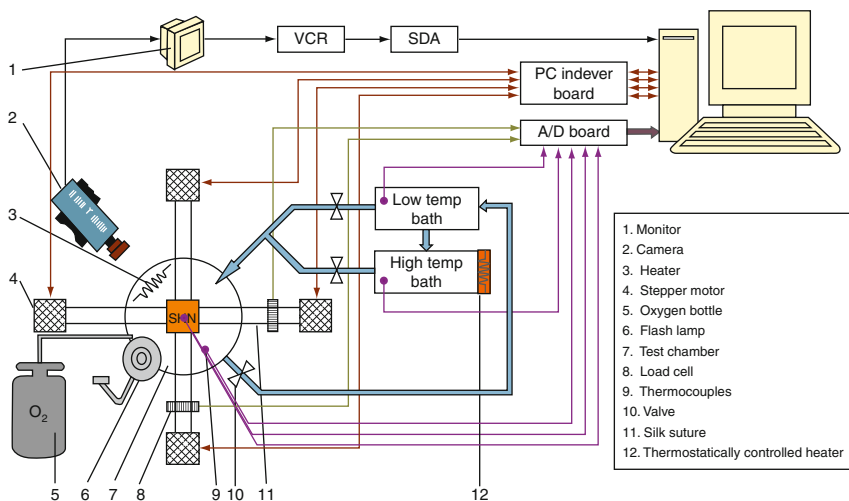


FIG. 4.2 Schematic design of the hydrothermal tensile experimental system.

far away enough from the outer edges to avoid the effects of specimen grips or tethers.

Based on the above requirements, the designed experimental system composes of four main subsystems, as schematically shown in Fig. 4.2, which are now described.

Testing Chamber The environmental chamber applies a specific thermal boundary condition to the specimen and allows testing of the sample in air or liquid under user-defined thermal conditions, for example, nearly constant temperatures (a temperature-jump test) or constant heating rates. The top plate of the chamber has a central port that allows the optical strain measurement with a charge-coupled device (CCD) camera. The bottom plate has drains to remove liquid from the chamber. The temperature of the fluid in the test bath is controlled by means of fluid exchange via a pump with thermally controlled reservoirs and maintained at a prescribed level using a heat insulation method²²: there are two reservoirs, one with a high temperature, which is controlled by a thermostatic immersion heater up to temperatures of 100 °C, and the other has a low temperature. The temperatures of both reservoirs are monitored by a T-type thermocouple. Another T-type thermocouple is immersed into the KHR solution and placed very near the tissue²³ to monitor the temperature of the KHR solution.

²² Minimization of heat loss by use of heat insulation material around the testing chamber.

²³ Approximately 0.5 mm from the surface of the sample.

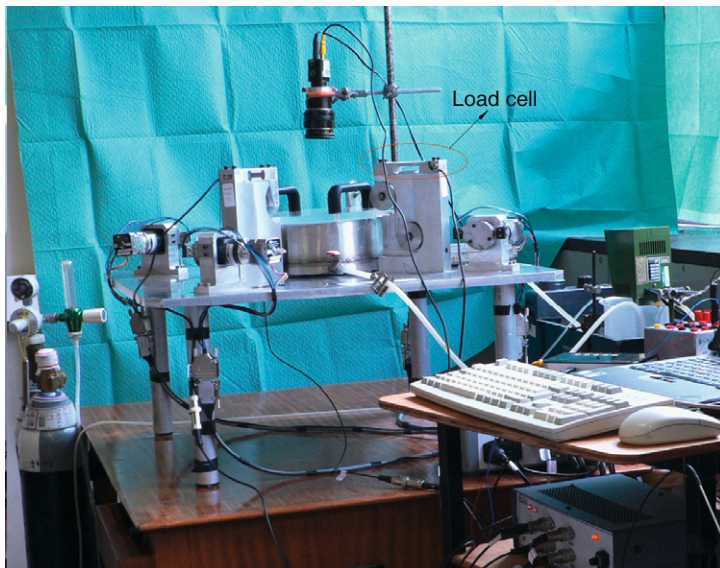


FIG. 4.3 Loading subsystem of the hydrothermal tensile testing system: user-defined loading, such as isometric tension tests and isotonic tension tests, can be achieved through the pulley system.

Loading System The loading system applies either a uniaxial or a biaxial set of forces or deformations to the specimen, Fig. 4.3. It is mounted on a square, custom machined, aluminum plate. A circular watertight specimen chamber is mounted centrally on the top plate and the loading assemblies are aligned at the four ends of the chamber with two perpendicular loading axes.

Nearly uniformly distributed in-plane biaxial forces/deformations are applied to the square specimen through four load carriages. The load can be applied in each of the four carriage assemblies independently by use of a pulley system. Part of the pulley system is connected to stepper motors, which impose deformations on the skin being tested and allows computer-controlled loading in orthogonal directions. The stepper motors are individually controlled using custom-designed motor controller, which is modified from a four-axis indexer card. A pair of motors is used to stretch the specimen in opposing directions to keep the specimen located nearly at center of test chamber in order to improve video strain resolution. The other part of the pulley/weight system is to apply isotonic loads (equal loading): pairs of identical weights are placed at the ends of the pulley system so that equal forces are applied along each axis.

One of the major challenges is the design of the holding system of connecting the tissue to the load cell: the specially designed clamp for the current system has

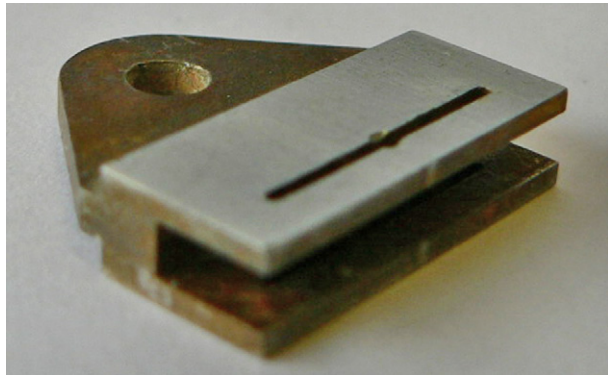


FIG. 4.4 Clamp designed for the tensile tests.

a slot in each clamp, and the skin sample is fixed in the clamp by putting five pins through the slot. In this way, the sample can be able to expand freely in the lateral direction during tensile test, Fig. 4.4. The clamp is connected to the pulley system by using inextensible string.

Another problem is that the density of skin tissue ($\sim 1200 \text{ kg/m}^3$) is larger than that of the liquid ($\sim 1000 \text{ kg/m}^3$), which results in the sinking of tissue sample in the liquid during the test. To solve this, small pieces of polystyrene foam are placed on the underside of the tissue to render it nearly neutrally buoyant, as used by other researchers (Wells, 2005).

Strain/Displacement and Stress/Force Measurement System Two force transducers (load cells), which are watertight and temperature compensated, are mounted outside of the specimen chamber on two orthogonal load carriages, as shown in Fig. 4.3. In-plane finite strains and deformations in the tissue are measured optically by tracking the position histories of contrasting markers on the surface of the specimen, based on the method of Downs, Halperin, Humphrey, and Yin (1990): the strain and deformation are traced between different deformation states by performing a two-dimensional cross-correlation on subsets of the images (Malcolm, Nielsen, Hunter, & Charette, 2002), which are recorded with a CCD camera at 30 Hz. The image is captured to video file for detailed off-line analysis, although in-time analysis can also be achieved via a video frame grabber board. The accuracy of the cross-correlation relies on high-contrast, high-frequency information within the images, which is provided by staining the tissue sample with a surgical marker pen before each experiment and

by self-holding surface feature²⁴ of skin tissue. The deformation field is obtained by comparing the current marker positions, given by pixel coordinates, to the reference positions. It should be noted here that the bidirectional tissue strain is measured only in a central region so that the effects of local stress concentrations of the gripping attachments are avoided. To keep the interested region within the field of view of the CCD, the two motors are set to the same speed. Force measurements are synchronized with CCD images by a LED in shot at the beginning of each sequence.

Due to the large deformations, stretch ratio, instead of strain, is used in this study, which is defined as $\lambda = l/l_0$ with l and l_0 being the current and initial marker distance on the sample as measured by the optical method. As for the stress, since we were unable to precisely describe the sample thickness during testing to determine true stress in a sample, engineering stress was calculated from the applied force, F , divided by the initial cross-sectional area, A_0 , as $\sigma = F/A_0$.

Data Acquisition System The current system uses two computers to acquire the data: one for recording the video and the other for recording the force and temperature. Analog signals from the load cells and thermocouples are transmitted to a custom-made amplifier, and later to an A/D converter. The A/D conversion board employed has eight signal channels, where two channels are reserved for analog signals from the thermocouples and another two are occupied by analog signals from the load cells, which are connected to a signal conditioner. The data acquisition from the load cells and thermocouples and the motor control are all performed using an integrated software system developed purposely with LabView, which allows the user to operate the rig and perform experiments through a single graphical user interface. This software supports motor control in either position or force feedback modes, allowing deformation states to be specified in terms of stress or stretch.

4.5.2. Validation of the System

Before being used to test skin samples, the system is calibrated and validated, as described below.

Heat Transfer Analysis The system is aimed at testing the mechanical behavior of skin samples under different heating conditions, as needed by the theoretical modeling of skin biothermomechanics described in previous sections.

²⁴ Some natural feature of skin surface can also be used as marker, such as wrinkle.

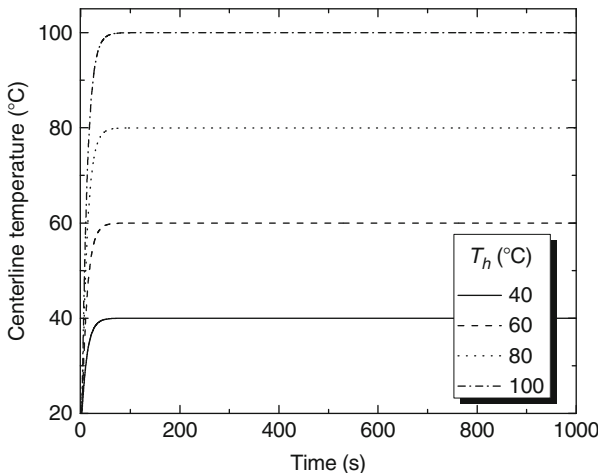


FIG. 4.5 Validation of the heating condition of the current system: centerline temperature of the skin sample (with maximum thickness of 2.4 mm) reaches the target temperature T_h very quickly as compared to the duration of the tests.

It is thus important to analyze the heat transfer in the sample during the tests. The Pennes equation (Eq. (2.1)) without blood perfusion term²⁵ is used here for the heat transfer analysis, where the skin sample is assumed to be thin and flat, and to experience on its two surfaces a step change in temperature from a uniform room temperature to an immersion fluid temperature up to 100 °C. The unloaded thickness of skin sample is in the range of 1.6–2.4 mm and the maximum value of 2.4 mm is used to estimate the maximum time required for the samples to reach the target temperature. Thermal properties are obtained from published data in the literature as given in Table 3.2. Using the closed-form solution of skin heat transfer obtained in our previous study (Xu, Wen, Seffen, et al., 2008), the centerline temperature history of the skin sample under heating of different temperatures can be obtained, as shown in Fig. 4.5. For example, with heating of 100 °C, the centerline temperature of the skin sample rises to 90 °C within 10 s, which is very short compared to the whole duration of the test (10 min). Analyses for other temperatures reveal similar results (see Fig. 4.5).

Tissue-Like Phantom Experiment for System Validation Since the response and stretch-rate sensitivity of silicone rubber is close to that of skin (Shergold, 2004), it is considered as an *in vitro* model for skin for the purpose of validating

²⁵ In view that the samples are tested *in vitro*.

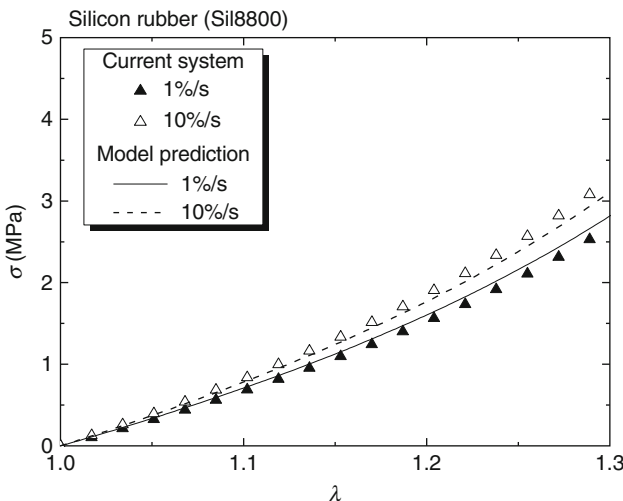


FIG. 4.6 Validation of the current system: comparison of biaxial tensile results with the prediction of model from Shergold et al. (2006).

the system. Silicon rubber Sil8800 is used here since its response has been obtained by the previous study in our lab (Shergold et al., 2006). The system can thus be validated by comparing the measured results from the current system with the predictions of the constitutive model. Square specimens of similar dimensions as the skin samples to be tested (approximately 20×20 mm and thickness 2.0 mm) are cut from silicone rubber sheets using a leather die punch mounted onto a hand press. The biaxial tensile stress versus stretch responses are measured at two stretch rates of 1%/s and 10%/s. Three tests are conducted for each silicone rubber sample and the average response is calculated. The measured tensile stress versus stretch responses of Sil8800 silicone rubber are shown in Fig. 4.6 and a good agreement has been achieved between the measurement and model prediction, which indicates the validity of the current test system.

4.5.3. Hydrothermal Tensile Test Procedure

In tensile testing, a square specimen (rectangular for uniaxial tests) is attached to each of the four loading assemblies (two for uniaxial test) by a self-designed holding system, across two perpendicular axes to allow physiological movement. The applied thermal and mechanical loads are recorded, along with the time of measurement, relative to the start of the experiment.

4.5.4. Hydrothermal Relaxation Test Procedure

The viscoelastic properties of skin tissue are usually characterized by two classic experimental tests, either a stress relaxation test or a creep test. A uniaxial stress–relaxation test is adopted in this study, where the stress relaxation test is conducted with two protocols. First, the stress relaxation is performed for different stretch levels (1.1, 1.3, and 1.5) with a high loading speed ($\gamma = 50\%/\text{s}$) in order to study the effect of stain level on relaxation: at low levels of stretch, the mechanical behavior is mainly due to the role of elastin (Alexander & Cook, 1976; Silver, Kato, Ohno, & Wasserman, 1992) which has been shown to be temperature-stable (Davidson et al., 1990); but the loads are too small relative to the noise level (Baek et al., 2005; Eshel & Lanir, 2001), and high stretch levels are adopted. In the second protocol, the tissue samples are stretched to 1.5 times their initial length (a stretch of 1.5) at a low loading speed of $1\%/\text{s}$, and the displacements of the samples are then kept constant while the time histories of the force are recorded for a time period of 500 s. As before, each test is repeated three times with three different samples and the averaged values are used.

4.6. HYDROTHERMAL COMPRESSIVE TESTS

4.6.1. Hydrothermal Compressive System

A hydrothermal compressive system has been designed and built to study the thermomechanical behavior of skin tissue under compression and is schematically shown in Fig. 4.7. The cylindrical skin sample is placed at the bottom of a cylindrical test chamber filled with KHR solution. The chamber temperature is

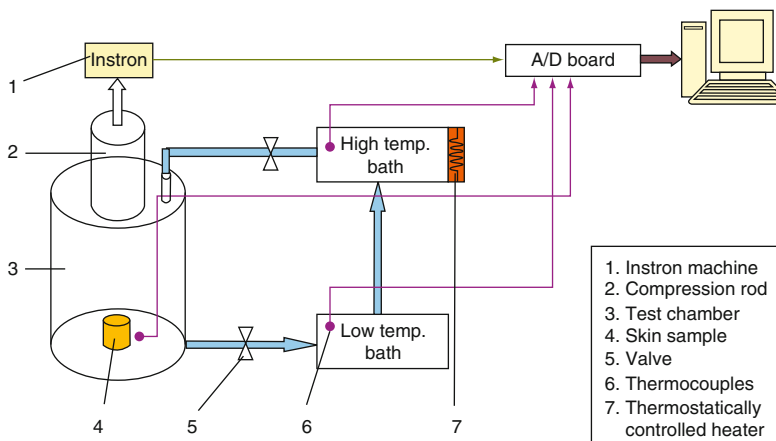


FIG. 4.7 Schematic of the hydrothermal compressive experimental system.

controlled by a circulation system similar to the hydrothermal tensile system. The temperature of the KHR solution in the test chamber is measured by a T-type thermocouple, which is placed approximately 0.5 mm away from the skin sample surface. An axial compressive load is applied to the sample through a compression indentor that is connected to an InstronTM materials testing machine (5500R), operating under the MerlinTM software. Longitudinal stretch measurements are made with a linear variable displacement transducer (LVDT) and an Electronic Instrument Research Ltd laser extensometer (LE-05) using two strips of retroreflective material glued in the compression platens. All load cells, thermocouples and laser extensometer signals are logged by a PC using an ADC board, as before.

4.6.2. Hydrothermal Compressive Test Procedure

Only when friction is negligible, the sample expands uniformly during compression so that the state of deformation within the sample is orthogonal. Therefore, a lubricant (Vaseline) is applied to the faces of the specimen before loading to reduce friction between the specimen and the compression platens. In the unconfined compression tests, the cylindrically shaped samples, of diameter 10 mm and thickness 2–5 mm, are compressed between two impermeable, smooth platens (with diameter of 20 mm), allowing the samples to expand laterally during compression. The top platen is driven down until it just touches the top surface of the specimen. Similar to tensile testing, the liquid in the high temperature reservoir is heated to a chosen temperature, while the low temperature reservoir contained cold liquid. A valve in the test chamber is opened to allow the hot or cold liquid to fill the test chamber until the sample is fully immersed in the liquid, while a thermocouple near the sample is used to inform the software of the exact time at which the experiment started. A force is applied to the skin sample by the compression indentor and the applied displacement, stretch, and loads are recorded. As before, each test is repeated three times with three different samples and the averaged values are used.

4.7. DYNAMIC MECHANICAL ANALYSIS

Various techniques have been used to characterize the viscoelastic behaviors of engineering materials, including dynamic mechanical analysis (DMA), the resonant method (Madigosky & Lee, 1983; Oyadji & Tomlinson, 1985), the nonresonant method (Ahn & Kim, 1994; Nielsen, Wismer, & Gade, 2000), and the wave propagation method (Arbogast et al., 1997; Mossberg, Hillström, & Söderström, 2001; Pereira, Mansour, & Davis, 1991). Among these, DMA is the most commonly used due to its commercial availability and its popularity for

investigating the viscoelastic properties of polymers over a wide range of temperatures and mechanical loading frequencies (Ferry, 1980; McCrum, Read, & Williams, 1991). The dynamic viscoelasticity of the skin tissue is investigated in this study by a dynamic mechanical analyzer (DMA Q800). During each DMA test, the storage modulus, E'' , loss modulus, E'' , and loss factor, $\tan \delta$, are all measured as functions of temperature history. The storage modulus is analogous to the stiffness measured from a monotonic test. The loss factor is defined as the ratio between the amount of mechanical energy lost and stored during a cycle ($\tan \delta = E''/E'$), representing the damping capability of skin tissue.

The measurements are carried out with a single cantilever bending testing mode at a fixed frequency of 1 Hz and different heating rates ($r_h = 2, 5, 10\text{ }^{\circ}\text{C/min}$), with a temperature range of $25\text{--}80\text{ }^{\circ}\text{C}$. In this study, the measurements are performed within the linear elastic region.²⁶ Deformation of a cantilevered specimen produces a combination of both flexural and shear forces. In short, thick specimens, shear forces are dominant while in long, thin specimens, flexural deformation is the dominant mode. In the present tests, the length to thickness ratio of skin samples is greater than 10 which leads to pure flexure (Chae et al., 2003).

The specimen is clamped between two clamps, one movable and the other stationary, and then enclosed in a thermal chamber filled with air. The frequency, amplitude, and a temperature range appropriate for the material being tested are input into the analyzer, which applies an oscillation to the specimen while slowly moving through the specified temperature range. All the tests are performed at a fixed frequency of 1 Hz.

5. Biothermomechanical Behavior of Skin Tissue

The experimental characterization of the thermomechanical behavior of skin tissue is presented in this section. The objective is to test the hypothesis that collagen is a significant determinant of the thermally induced change in the mechanical properties of skin tissue. For this purpose, DSC analysis is used to detect the denaturation of collagen in skin tissue and to measure its thermal stability. The integrity of the collagen network is analyzed using the thermal damage integration (Eqs. (2.3) and (2.6) in Section 2). Hydrothermal tensile and

²⁶ To accurately determine the mechanical properties, the deformation of skin sample must be based on displacement amplitudes within the linear viscoelastic region to ensure that the material behavior is independent of the magnitude of deformation (Chae et al., 2003). The nonlinear stress-strain curve can be seen as being composed of several linear sections, for example, as a bilinear curve as shown in Fig. 5.11.

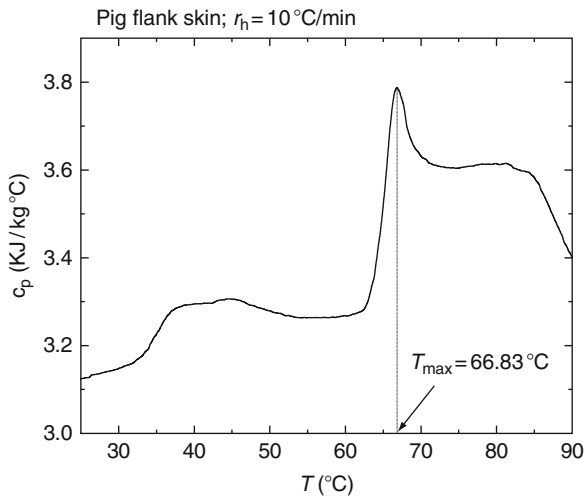


FIG. 5.1 Characteristic DSC thermogram, that is, variation of specific heat with temperature, of a skin tissue sample: the temperature corresponding to the peak is $66.83\text{ }^{\circ}\text{C}$.

compressive experiments are then performed to assess the thermal dependency of skin mechanical behavior. To characterize the viscoelastic properties of skin tissue as a function of temperature and collagen denaturation, stress relaxation tests under tension and DMA versus temperature are also performed.

5.1. THERMAL DENATURATION OF COLLAGEN IN SKIN TISSUE

A typical DSC thermogram of a skin sample from pig flank is shown in Fig. 5.1. The measured specific heat capacity falls in a range comparable to published data in the literature (Henriques & Moritz, 1947; Young, 1998). The result of Fig. 5.1 demonstrates that, for a stress-free skin sample subjected to temperatures in the range of $30\text{--}90\text{ }^{\circ}\text{C}$, a broad endothermal²⁷ peak appears: denaturation is characterized by a sudden increase in the energy absorption, which immediately precedes this peak, starting at about $60\text{ }^{\circ}\text{C}$. With further heating, the endotherm reaches its maximum value at the denaturation temperature of $66.83\text{ }^{\circ}\text{C}$ and then decreases. It is known that the temperature of thermal denaturation strongly depends on the water content in collagen (e.g., it has been found that there is an increase of the rate of shrinkage, and hence denaturation,

²⁷ In thermodynamics, endothermal describes a process or reaction that absorbs energy in the form of heat.

with increased hydration at a given temperature (Weir, 1949), and on the degree of crosslinking between the chains (Pietrucha, 2005). The peak in Fig. 5.1 is connected with the transition of collagen structure from the ordered triple helix form to a randomly coiled conformation in the domains between crosslinks.

It has also been observed that the characteristics of denaturation are heating-rate dependent (not shown here for brevity), where the maximum value of the peak at higher heating rates moves toward higher temperatures. If a collagenous tissue is heated from an initial value at a constant heating rate, r_h , the rate of the decline in the number of native molecules with time follows the first order kinetics, given by Miles (1993), Miles, Burjanadze, and Bailey (1995), and Ozawa (1970):

$$T = T_i + r_h t, \quad (5.1)$$

$$\frac{dN}{dt} = -k(T)N, \quad (5.2)$$

where T_i is the initial tissue temperature, N is the molecules of native, or undenatured, collagen in the tissue, T is the current tissue temperature, and $k(T)$ is the usual reaction rate. Combining Eqs. (5.1) and (5.2) results in

$$\frac{1}{N} \frac{dN}{dT} = -\frac{k(T)}{r_h}. \quad (5.3)$$

This equation predicts that the maximum of $(-dN/dT)$ can be obtained when

$$\frac{d^2N}{dT^2} = 0 \Rightarrow \frac{d}{dT} \left[\frac{k(T)}{r_h} N \right] = 0 \Rightarrow N \frac{dk(T)}{dT} + k(T) \frac{dN}{dT} = 0. \quad (5.4)$$

When combined with the Arrhenius equation (Eq. (2.2) from Section 2)

$$k(T) = A \exp \left(-\frac{E_a}{RT} \right), \quad (5.5)$$

the relation between Arrhenius parameters (E_a , A) and the peak temperature of thermal denaturation (T_{max}) is obtained as

$$\frac{r_h E_a}{A R T_{max}^2} = \exp \left(-\frac{E_a}{R T_{max}} \right). \quad (5.6)$$

Equation (5.6) can be rewritten as

$$\ln \left(\frac{r_h}{T_{max}^2} \right) = -\frac{E_a}{R} \frac{1}{T_{max}} - \ln \left(\frac{E_a}{R} \right) + \ln A. \quad (5.7)$$

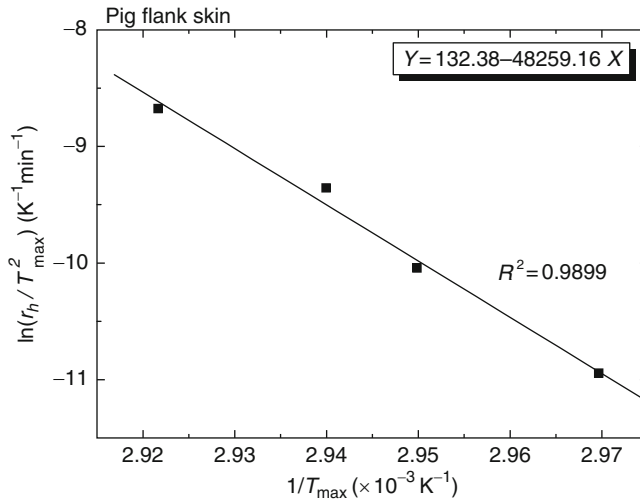


FIG. 5.2 Characteristic plot of $\ln(r_h/T_{\max}^2)$ versus $1/T_{\max}$ for pig flank skin tissue: dots (black) are experimental data; line (red) is the best fit line by least squares; also indicated is the equation of fitted line with X for $1/T_{\max}$ and Y for $\ln(r_h/T_{\max}^2)$. R^2 value represents the scatter of data along the line of best fit.

The activation energy E_a can be obtained from a log–log plot of $\ln(r_h/T_{\max}^2)$ versus $1/T_{\max}$, while A can be derived through the intercept. With these results, the thermal damage and the degree of thermal denaturation of skin collagen for a given heating history can be quantified with Eqs. (2.3) and (2.6), respectively. It should be noted here that the thermal denaturation of a collagenous tissue depends not only on the temperature history but also on the stress state during heating (Humphrey, 2003), which, however, is very difficult to quantify due to the lack of corresponding research. Therefore, in the following calculation of thermal damage, the parameters obtained from DSC measurements in the absence of mechanical loading are used.

A characteristic plot of $\ln(r_h/T_{\max}^2)$ versus $1/T_{\max}$ for a pig flank skin sample is presented in Fig. 5.2. Tests with belly, back, ear, and face skin samples have also been performed and the results of the derived Arrhenius parameters are presented in Table 5.1. As shown in Section 2, there is a linear relationship between the published experimental results of Arrhenius parameters $\ln A$ and E_a for skin tissue, as given by Eq. (2.4). The comparison of the results here for different pig skin samples with results calculated from Eq. (2.4) has been presented in Fig. 5.3, where it can be seen that a very good agreement has been achieved.

TABLE 5.1
Experimental results of Arrhenius parameters (E_a , A).

Sample	E_a ($\times 10^5$ J/mol)	A (s^{-1})
Back skin	5.255	2.126×10^{81}
Belly skin	3.935	1.151×10^{61}
Ear skin	5.867	5.240×10^{91}
Face skin	4.710	4.575×10^{72}
Flank skin	4.012	1.501×10^{61}

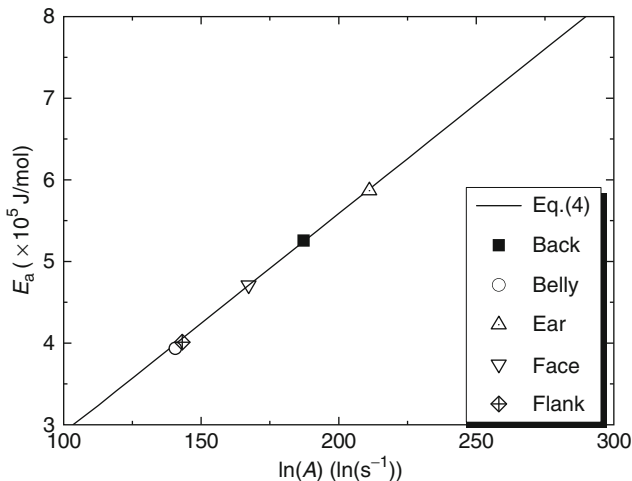


FIG. 5.3 Comparison of the results of Arrhenius parameters of this study with literature results.

5.2. TENSILE BEHAVIOR OF SKIN TISSUE

Hydrothermal tensile tests, which enable the variation of temperature during mechanical tests, are performed to quantify the effects of temperature and corresponding thermal denaturation on the tensile behavior of skin tissue.

5.2.1. Uniaxial Tensile Behavior

A typical uniaxial tensile behavior of pig ear skin sample measured at $T = 37$ °C is shown in Fig. 5.4 (black dots). Note that skin has a low stiffness at low stretch but undergoes significant stretch hardening at high stretch level. This J-shaped stress–stretch curve is typical for mammalian skin, although the stretch hardening characteristic varies from specie to specie. In Fig. 5.4, the uniaxial tensile stress–stretch responses of human chest skin (Dunn, Silver, &

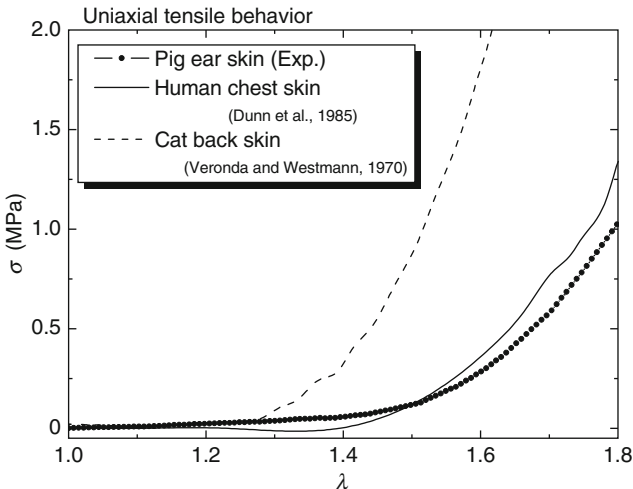


FIG. 5.4 Comparison of the uniaxial tensile behavior of pig ear skin measured at $T = 37^\circ\text{C}$ with reported data on human chest skin (Dunn et al., 1985) and cat back skin (Veronda & Westmann, 1970).

Swann, 1985) and cat back skin (Veronda & Westmann, 1970) are also shown for comparison. It is interesting to find that the uniaxial tensile behavior of pig ear skin obtained in this study agrees well with that of human skin. This is, however, not unexpected since pig ear skin is selected purposely because of its similarity with human skin (Meyer et al., 2007) as described in Section 3. Compared with pig ear skin and human chest skin, cat back skin stretches faster.

Uniaxial tensile tests of pig ear skin samples under different temperatures have been performed and the stress–stretch relationships are given in Fig. 5.5: a good repeatability has been noted for three same tests and a single averaged response is shown. As described above, there are two behavior regimes for all the curves. First, when $\varepsilon < \sim 50\%$, the curves almost overlap. This low modulus region is thermally very stable due to the dominance of elastin in the skin behavior and the gradual straightening of an increasing fraction of the wavy collagen fibers and stretching of elastic fibers. When $\varepsilon > \sim 50\%$, the stress increases almost linearly with stretch; and the slopes under different temperatures are different and reduce with increasing temperature. This effect is due to the stretching and slippage of collagen molecules within crosslinked collagen fibers and to collagen fibril slippage: with an increase in temperature, the highly organized crystalline structure of collagen changes to a random, gel-like state, which results in the corresponding decrease in stiffness. Furthermore, the hydration change with temperature may also make a contribution. Water plays a significant role in

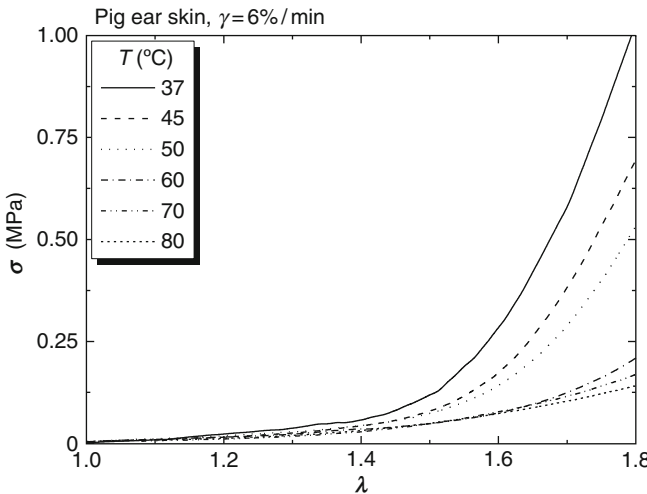


FIG. 5.5 Stress–stretch relation of uniaxial hydrothermal tensile tests under different temperatures: γ is the stretch rate at which tests are performed.

governing the gross properties of skin tissue (Auriol, Vaillant, Machet, Diridollou, & Lorette, 1993; Hoffman, Robichaud, & Grigg, 2003), which consist primarily of water. However, due to heating, the level of hydration may vary, for example, Luescher, Ruegg, and Schindler (1974) suggested that primary hydration water is set free during the process of thermal denaturation. It should be noted that when $T \geq 60$ °C, there is relatively little change in the modulus with temperature, which can be explained by the thermal damage process: when the stretch rate and temperature are given, the relationship between the stretch and thermal denaturation degree (Deg) calculated according to the heating history can be obtained, as shown in Fig. 5.6. Figure 5.6 shows that when $T \geq 60$ °C, the collagen is fully denaturized, while at $T = 45$ and 50 °C, denaturation is much slower.

5.2.2. Biaxial Tensile Behavior

The biaxial tensile behaviors of pig skin samples is tested at 37 and 60 °C. The stress–stretch relationships measured for samples from different body sites are given in Fig. 5.7. An interesting result can be observed from the figure: only the skin tissue from porcine cheek appears to be abnormal in the fact that the curves for the two different axes overlap each other. This means that it has an equal distribution of collagen/elastin fibers across both axes of a square, independent of

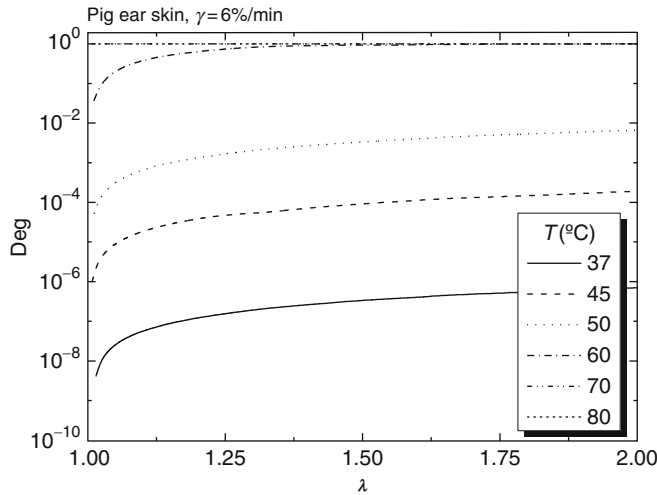


FIG. 5.6 Stretch-thermal damage degree (Deg) relation of hydrothermal tensile tests under different temperatures: Deg is obtained from Eq. (2.6) with given heating condition and stretch rate.

the cutting angle. This discovery may allow the series of experiments on skin tissue to come to fruition since a uniform stress distribution in the tissue can be easily achieved even in biaxial tests. However, this observation is abnormal since it is well known that clear Langer's lines²⁸ have been observed for face skin tissue (Rubin, 1948). Relative to that at body temperature, the stiffness of skin tissue under hyperthermal temperature decreases considerably. This feature is due to the similar reasons as those in uniaxial results described above.

In Fig. 5.7, the uniaxial tensile behaviors of pig ear skin samples (dots) obtained under the same stretch rate and heating conditions have also been given for comparison. Consistent with the observation in the literature, as described in Section 2.3, biaxial tensile loading, compared with uniaxial stretch, results in lateral narrowed stress–stretch curve and the reduction in the stretch before entry into the linear region occurs, which is due to the two-directional stretch of collagen fibers.

²⁸ “Langer's lines,” sometimes also called cleavage lines, are a term used to define the direction within the human skin along which the skin has the least flexibility. These lines correspond to the alignment of collagen fibers within the dermis (Cox, 1942).

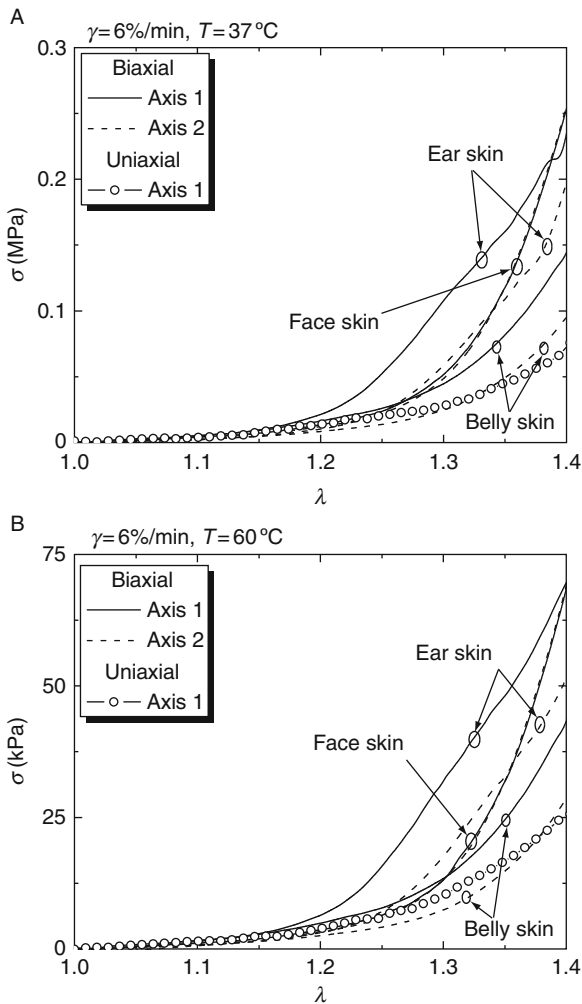


FIG. 5.7 Stress–stretch relation of biaxial hydrothermal tensile tests for samples from different sites at (A) $T = 37^\circ\text{C}$ and (B) $T = 60^\circ\text{C}$: axis 1 (solid lines) and axis 2 (dashed lines) are material axes identified with the equal-load method as described in Section 4.1; scattered points are experimental results from uniaxial tests.

5.3. COMPRESSIVE BEHAVIOR OF SKIN TISSUE

Almost all of the previously published mechanical models of skin tissue are based on experimental data under tension, although *in vivo*, skin tissue is often subjected to compressive loading by different agents. The goal of the present

section is to study the relationship between temperature, thermal damage, and the corresponding change in the compressive behavior of skin tissue.

5.3.1. Typical Example of Compressive Behavior

A representative compressive stress–stretch response obtained at a stretch rate $\gamma = 24\%/\text{min}$ ²⁹ is presented in Fig. 5.8A. The relationship exhibits a consistent three-stage hardening of a toe region with low stiffness at low stretch levels, a transition region from low to high stiffness, and a high stiffness region at large stretch levels. The results are comparable to the published compressive behavior of pig back skin tissue obtained at similar stretch rate ($\gamma = 25\%/\text{min}$) (Shergold et al., 2006), as shown in Fig. 5.8A.

Compared with the mechanical characteristics of skin tissue in uniaxial tension, the compressive stress/stretch curves are similar in trend; however, the transition from low to high stiffness in uniaxial tension occurs mostly at a stretch level of 1.4–1.6 (Dunn et al., 1985; Lanir & Fung, 1974; Wan, 1994), which is much larger than that in compression (about 1.2–1.3) as observed in the results here (Fig. 5.8B). Similar results have also been reported elsewhere for pig back skin tissue (Shergold et al., 2006; Wu et al., 2003, 2007). Wu et al. (2003, 2007) observed a transition at an even lower stretch level of 1.04–1.05 for confined compression and 6–7% for unconfined compression: the difference is because the fat layer is removed in this study. However, compared with the biaxial tensile behavior of pig back skin obtained by Ankersen et al. (1999), the compressive behavior obtained in this study shows a slower rate of stretch hardening, as shown in Fig. 5.8B. This is mainly due to the different testing environments adopted: in the current study all the tests were performed in liquid (KHR), while the tests of Ankersen et al. were performed in air environment. Testing in air will induce the decrease of the hydration and humidity of the samples, which have been shown to increase the stiffness of skin tissue (Bert & Reed, 1997; Jemec, Jemec, Jemec, & Serup, 1990; Overgaard & Jemec, 1993).

5.3.2. Temperature-Dependent Compressive Behavior

The hydrothermal compressive tests of back skin tissue under different temperatures have been performed and the results are given in Fig. 5.9. It is interesting to see that, contrary to the tensile tests, the compressive stiffness increases with increasing temperature although the thermal damage degree also increases, as shown in Fig. 5.10. One key difference is that the compressive tests are performed in a direction normal to the principal orientation of collagen and

²⁹ This strain rate is chosen for a better comparison with data reported in the literature.

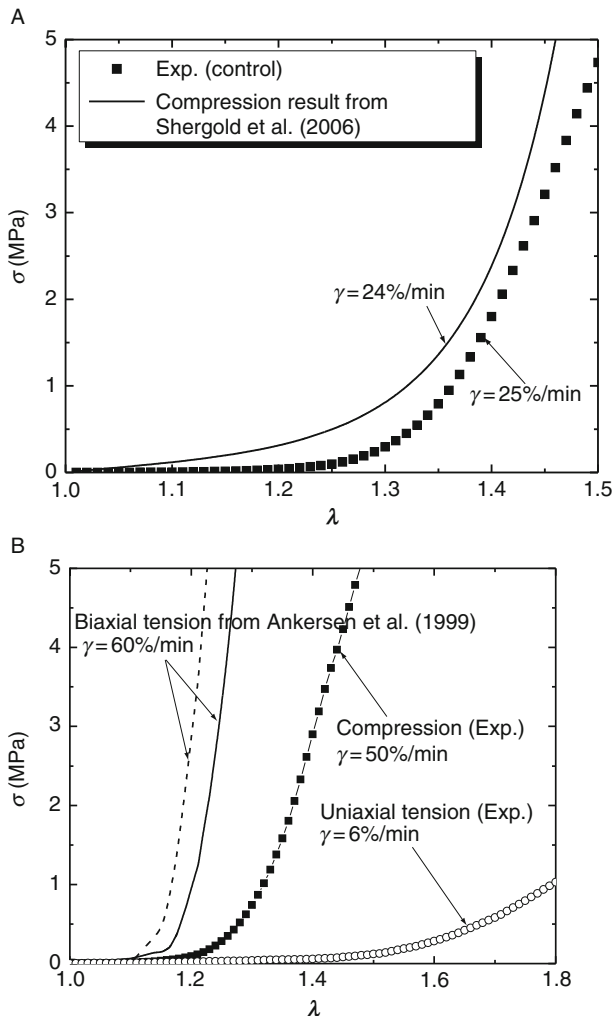


FIG. 5.8 Representative stress–stretch responses from a compressive test (black solid dots) and comparison between the compression results (A) with published compressive behavior (Shergold et al., 2006) and (B) with uniaxial tensile behavior (red circle dots) obtained in this study and published biaxial tensile behavior of pig back skin tissue (Ankersen et al., 1999).

elastin fibers. Even though there exists denaturation of collagen, which appears in the tensile tests, the compressive behavior is governed by the mechanical properties of the gel-like ground substance, inside which the fibers are located (Dikstein & Hartzstark, 1983; Tregear & Dirnhuber, 1965). Very little is known about the

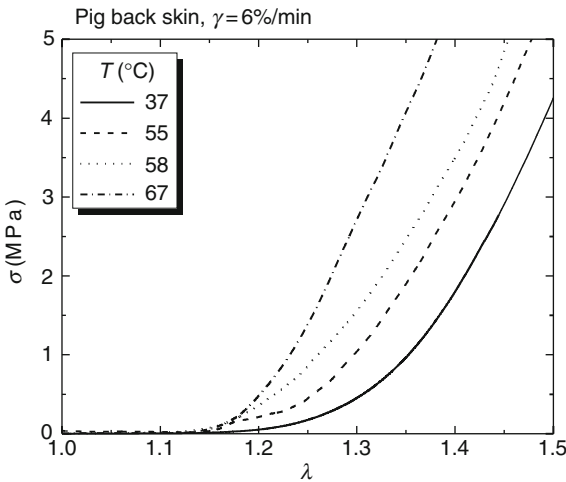


FIG. 5.9 Stress–stretch relation of hydrothermal compressive tests under different temperatures.

mechanical properties of this substance; it can only be speculated that its stiffness increases with increasing temperatures.

To characterize the temperature effect on skin mechanical behavior and compare their characteristics under different testing methods, a procedure is proposed here to obtain the modulus of skin sample at low (E_l) and high (E_h) stretch levels, as shown in Fig. 5.11: the stretch–stress curve is treated as a bilinear line, the tangents at low and high stretch levels are then obtained, and E_l and E_h are defined as the slope of the two tangents. The variations of E_l and E_h with temperatures for tensile and compressive behaviors are given in Fig. 5.12A and B, respectively. While E_l for tensile behavior of skin tissue does not change much with temperature, E_h decreases almost linearly with increasing temperature until about 60 °C, after which it decreases little. E_h for tensile behavior obtained here (0.3–4.5 MPa) also agrees well with the published *in vitro* measurements of Young's modulus for animal skin tissue, for example, cat skin (0.5 MPa) (Veronda & Westmann, 1970) and rat skin (1.18–4.62 MPa) (Ranu, Burlin, & Hutton, 1975; Vogel, 1971). Compared with that for tensile behavior, E_h for compressive behavior increases with temperature and is much higher (28–54 MPa). This is due to (1) different mechanisms of tensile and compressive behaviors as discussed above and (2) different skin samples used for tensile (pig ear skin) and compressive (pig back skin) testing, and the regional difference of skin mechanical behavior has been observed by many researchers (Elsner, Wilhelm, & Maibach, 1990; Jansen & Rottier, 1958a,b; Pierard, Letawe,

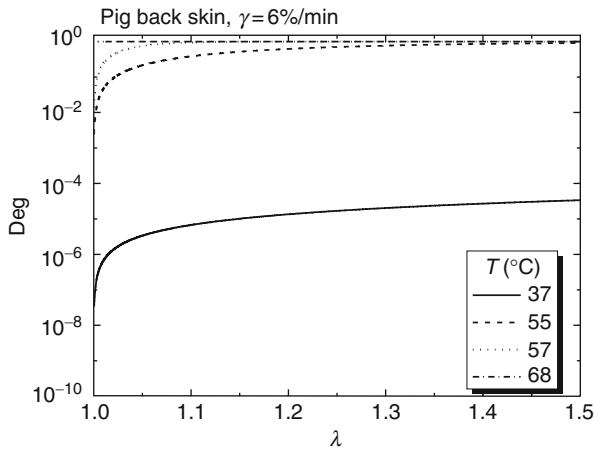


FIG. 5.10 Stretch-thermal damage degree relation of hydrothermal compressive tests under different temperatures.

Dowlati, & Pierard-Franchimont, 1995; Pierard, Nikkels-Tassoudji, & Pierard-Franchimont, 1995; Smalls, Wickett, & Visscher, 2006).

5.3.3. Thermal-Damage-Induced Changes in Compressive Behavior

To separate reversible changes from irreversible ones and to study the influence of thermal denaturation on skin properties, selected skin samples are thermally denatured before testing (i.e., predamaged). Using the Arrhenius parameters (E_a, A) of pig skin tissue obtained from the DSC analysis, different heating temperatures, T_h , and durations, t_h , are chosen to induce damage in skin sample to a specified degree. In all, 22 groups of samples are prepared, with groups 1–4 having no predamage and used as control groups. Details of each group are given in Table 5.2.

Figure 5.13A–C presents the thermal-damage-induced changes in skin compressive behavior at three different stretch rates ($\gamma = 25, 50, 125\text{%/min}$). The results at all three stretch rates exhibit a clear trend of curve shifting toward the right with increasing damage. When the damage degree (Deg) has a value near unity, implying that the collagen is fully denaturized, there is little difference between curves: the stiffness of skin tissue decreases with increasing degree of thermal damage, which is reasonable; and increased extensibility of soft tissues due to thermal treatment has been observed in both uniaxial (Chachra et al., 1996;

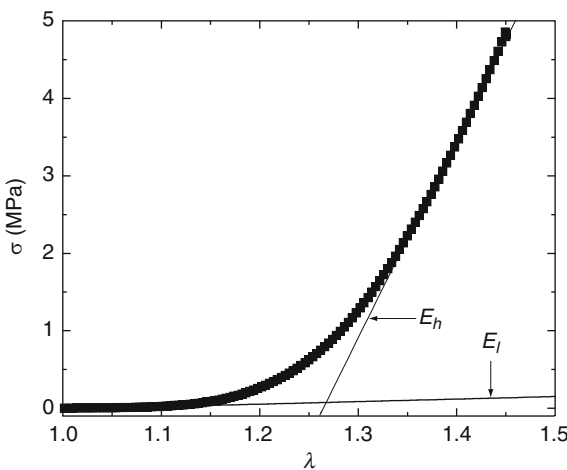


FIG. 5.11 Method for calculating the moduli at low (E_l) and high (E_h) stretch levels.

Chen & Humphrey, 1998; Lennox, 1949) and biaxial tensile testing (Harris et al., 2003; Wells et al., 2004) of skin tissue.

There are several possible mechanisms for explaining why the thermal damage changes the compressive behavior of skin tissue. The first one is the hyperthermal-temperature-induced thermal denaturation of dermal collagen. It has been suggested that collagen may play an important role in determining the overall mechanical properties of skin tissue (Lanir, 1987), and thus it seems reasonable to assume that collagen would also play a major role in the compressive behavior of skin tissue. However, this cannot be the principal reason since the compressive tests are performed normal to the principal orientation of collagen. Another possible mechanism is the dehydration change accompanying thermal damage as well as rehydration during the thermal recovery process after heating. It is known that there can be either an inward or outward flux of interstitial fluid due to the heating of a soft tissue (Humphrey, 2003), and the compressive behavior is governed by the mechanical properties of the gel-like ground substance, inside which the fibers are located (Dikstein & Hartshtark, 1983; Oomens et al., 1987; Tregear & Dirnhuber, 1965). Hormann and Schlebusch (1971) and Luescher et al. (1974) suggested that renaturation, or reformation of some of the triple-helix structures, occurs after heating, which involves the slow rebounding of primary hydration water to the amorphous protein and the formation of additional water bridges within the more disorganized molecule. A third possible mechanism is the viability of cells in the skin tissue, where

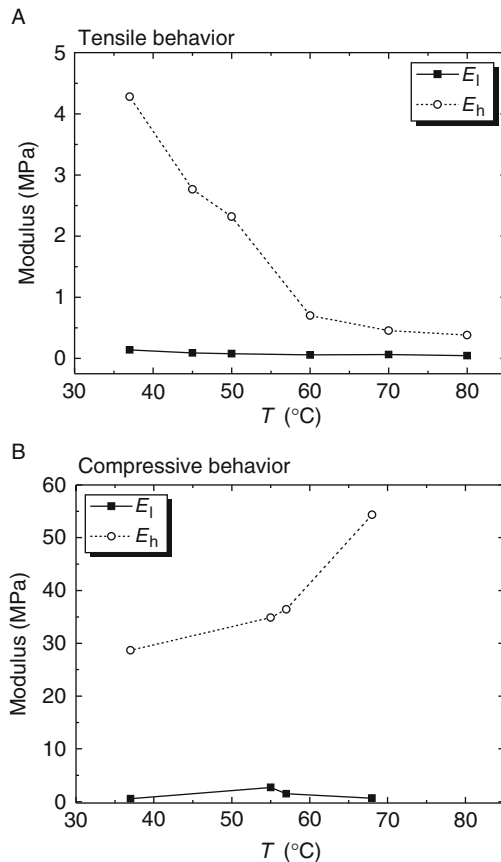


FIG. 5.12 Variations of the moduli at low (E_l) and high (E_h) stretch levels with temperatures for (A) tensile behavior and (B) compressive behavior.

specifically, Yip, Walker, Fernlund, and Pinder (2007) found that the *in situ* fibroblast viability has great influence on the mechanical properties of rat back skin tissue.

It is interesting to note that Fig. 5.13, compared to Fig. 5.9, exhibits contradictory results: in Fig. 5.9, the compressive stiffness increases with increasing temperature even though the thermal damage and the degree of thermal denaturation also increase. It has been shown by others that the stiffness of skin tissue increases progressively in dehydration and decreases in over hydration under compression (Bert & Reed, 1997). In Fig. 5.9, all the tests are performed with fresh samples at hyperthermal temperatures where only heat-induced dehydration

TABLE 5.2

Details of predamaged samples.

Sample Group No.	T_h (°C)	T_h (s)	Ω	Deg	γ (%/min)
1	37	0	0	0	25
2	37	0	0	0	50
3	37	0	0	0	125
4	37	0	0	0	250
5	55	12	0.0579	0.0563	25
6	55	12	0.0579	0.0563	50
7	55	12	0.0579	0.0563	125
8	55	12	0.0579	0.0563	250
9	65	1	1.44	0.762	25
10	65	1	1.44	0.762	50
11	65	1	1.44	0.762	125
12	65	3	4.31	0.987	25
13	65	3	4.31	0.987	50
14	65	3	4.31	0.987	125
15	65	30	86.2	1	25
16	65	30	86.2	1	50
17	70	10	219	1	25
18	70	10	219	1	50
19	70	5	109	1	25
20	70	5	109	1	50
21	70	18.5	405	1	25
22	75	10	3081	1	25

occurs, while tests in Fig. 5.13 are performed with predamaged samples at body temperature where the samples are rehydrated during the thermal recovery process of predamage procedure.

5.3.4. Stretch-Rate Sensitivity at Different Thermal Damage Levels

The stretch-rate sensitivity of pig skin tissue at four different damage levels is presented in Fig. 5.14A–D for uniaxial compressive loads. A clear sensitivity emerges for all damage levels, where the skin tissue stiffens and strengthens with increasing stretch rates. This feature mirrors results in the literature. For example, it has been observed by others that, under stretch-controlled tests, the overall stiffness of skin tissue decreases with decreasing stretch rates (Arumugam, Naresh, & Sanjeevi, 1994; Giles, Black, & Bischoff, 2007; Jamison, Marangoni, & Glaser, 1968; Lanir & Fung, 1974; Shergold et al., 2006; Vogel & Hilgner, 1979a,b).

Since collagen fibers comprise bundles of collagen fibrils aligned parallel to a hyaluronic acid chain, and linked to the hyaluronic acid by proteoglycan side chains, it is likely that the stretch-rate sensitivity of skin tissue is attributable to viscous losses due to the interaction of ground substance with collagen fibers at

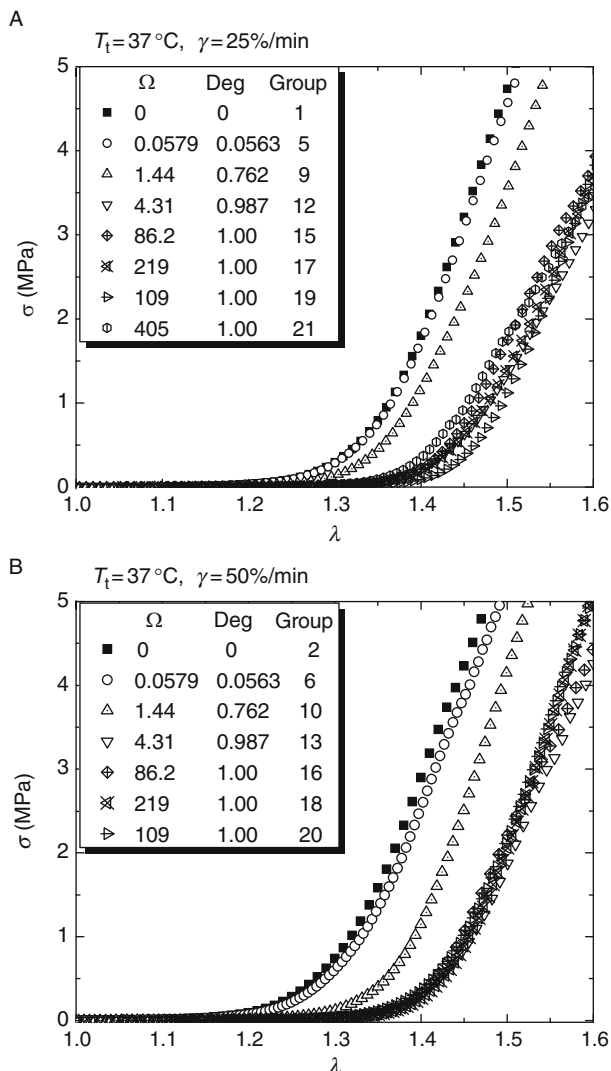


FIG. 5.13 (Continued)

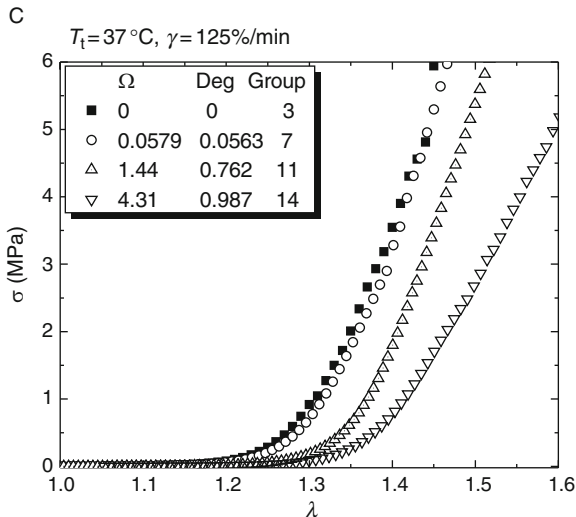


FIG. 5.13 Effect of thermal denaturation on skin compressive behavior at different stretch rates of (A) $\gamma = 25\%/\text{min}$, (B) $\gamma = 50\%/\text{min}$, and (C) $\gamma = 125\%/\text{min}$.

the macroscopic scale (Cohen, Hooley, & McCrum, 1976) as well as with collagen fibers at the microscopic scale (Haut, 1983). For example, much of the sensitivity to stretch rate has been attributed to the uncoiling and aligning movement of collagen (Lanir, 1979), and Daly (1982) suggested that the stretch-rate sensitivity of skin tissue occurred at all structure levels of collagen and was due in part to bonds between fibrils and fibers. However, the uncoiling and aligning movement of collagen should not be the main mechanism for the case here, since the compressive tests are performed through the skin thickness direction and a similar stretch sensitivity has been observed at all damage levels. Thus the stretch-rate sensitivity may be attributed to the variation of viscous interaction between collagen fibers and ground substance induced by hydration change accompanying thermal damage. For example, the stretch-rate sensitivity was well modeled by Shergold et al. (2006) by increasing the shear modulus with increasing stretch rate, with no attendant change in the stretch hardening exponent. Arumugam et al. (1994) also attributed the higher stress to higher frictional force at higher stretch rates. The movement of fluid in the hydrated matrix may also play an important role (Li, Armstrong, & Mow, 1983).

5.4. RELAXATION BEHAVIOR OF SKIN TISSUE

Skin tissue is a viscoelastic material. However, to the authors' best knowledge, there is no published study on the temperature dependency of skin viscoelasticity, although other collagenous tissues such as cartilage (Chae et al., 2003;

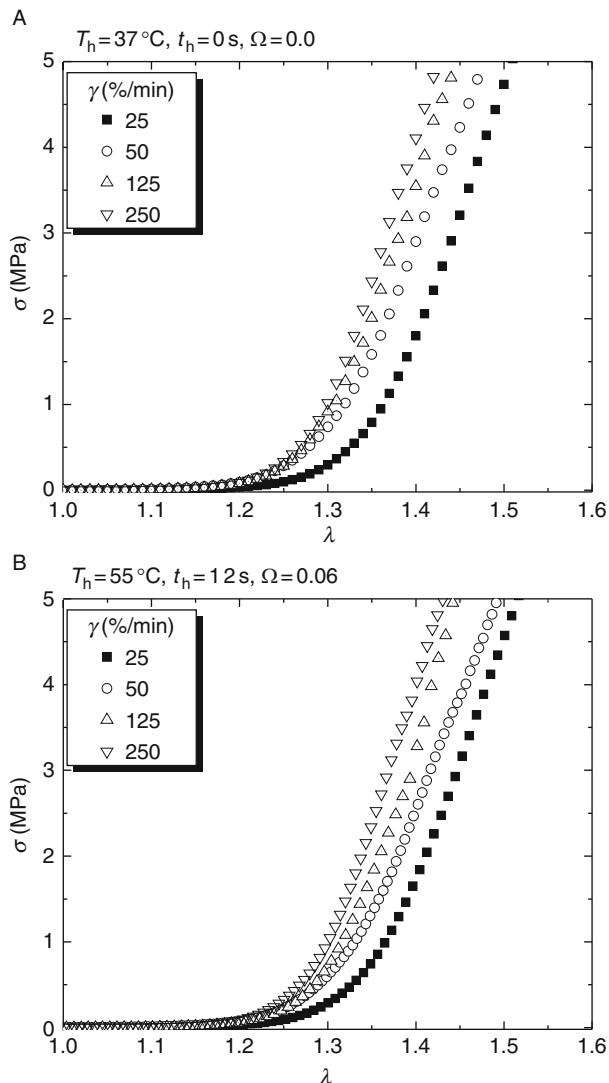


FIG. 5.14 (Continued)

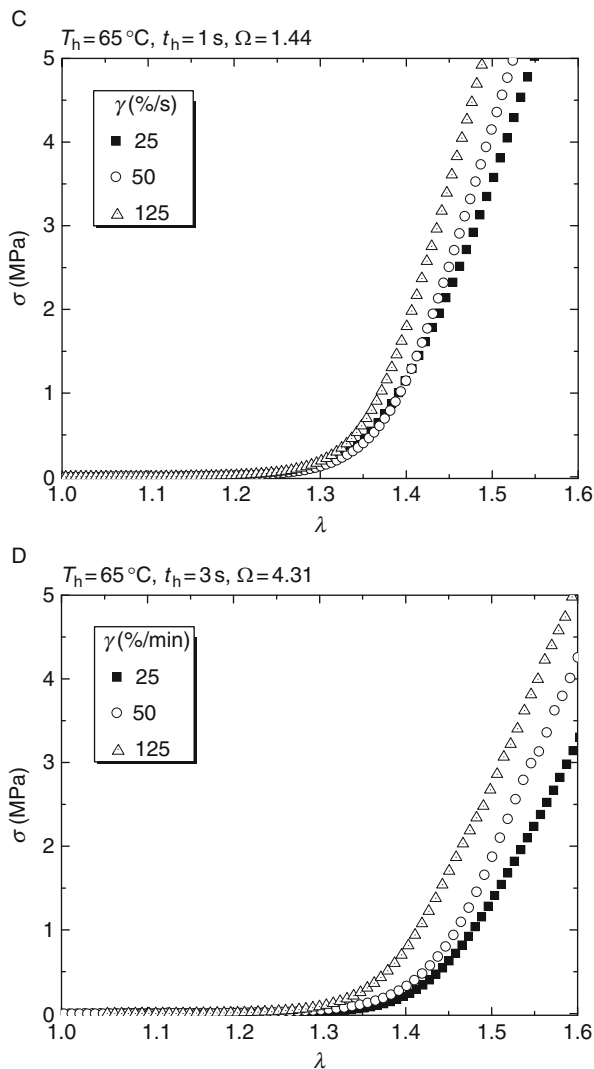


FIG. 5.14 Stain-rate sensitivity at damage levels of (A) $\Omega = 0$, (B) $\Omega = 0.06$, (C) $\Omega = 1.44$, and (D) $\Omega = 4.31$. T_h and t_h are heating temperature and duration, respectively.

Chao et al., 2001) and bone (Mano, 2005; Yamashita et al., 2002) have been studied in detail. The aim of the present section is therefore to characterize the temperature-dependent relaxation behavior of skin tissue. Stress relaxation tests under different temperatures are then performed, and results and discussion are presented.

5.4.1. Modeling of Skin Viscoelastic Behavior

Quasilinear Viscoelastic Theory The time-dependent mechanical behavior of soft tissues can be formulated using Boltzmann hereditary integrals (Fung, 1993; Lakes, 1998), whereby the stress histories $\sigma(t)$ are related to the strain histories $\epsilon(t)$ according to

$$\sigma(t) = \int_0^t G(t - \tau, \epsilon) \dot{\epsilon}(\tau) d\tau, \quad (5.8)$$

where t is the time, τ is the dummy variable for time, and $G(t, \epsilon)$ is the relaxation modulus.

For the quasilinear response of tissue, it is assumed that the relaxation function $G(t, \epsilon)$ can be further separated into a strain-dependent part and a time-dependent part, as

$$G(t) = g(t)E(\epsilon) \quad (5.9)$$

where $g(t)$ is the normalized relaxation function that only depend on time, and $E(\epsilon)$ is the elastic modulus. This form is also called the quasilinear viscoelastic (QLV) theory, which was formulated by Fung (1971) and has been proved useful for describing the viscoelastic behavior of different soft tissues such as skin tissue (Decraemer, Maes, Vanhuyse, & Vanpeperstraete, 1980; Ledoux & Blevins, 2007; Wu, Cutlip, Welcome, & Dong, 2006), ligament (Defrate & Li, 2006; Funk, Hall, Crandall, & Pilkey, 2000; Moon, Woo, Takakura, Gabriel, & Abramowitch, 2006), cartilage (Simon, Coats, & Woo, 1984; Woo, Simon, Kuei, & Akeson, 1980), and tendon (Defrate & Li; Johnson et al., 1994; Sarver et al., 2003).

Insertion of Eq. (5.9) into Eq. (5.8) leads to the following nonlinear separable integral formulations:

$$\sigma(t) = \int_0^t g(t - \tau) \frac{d\sigma_e[\epsilon(\tau)]}{d\epsilon} \frac{d\epsilon(\tau)}{d\tau} d\tau, \quad (5.10)$$

where $\sigma_e(\tau)$ is the elastic stress response.

The QLV theory was developed on the basis that the reduced relaxation function describes the normalized stress response of a sample in response to a step increase in strain such that the tissue has no time to relax during this loading process. This, however, is experimentally impossible to realize. To isolate the nonlinear elastic properties of tissue from its viscous properties, relatively high rates have been used. However, with a high stretch rate, it is technically difficult to obtain reliable instantaneous material parameters due to inertial effects and,

thus, greater technical challenges must be overcome in the design of the testing machine and data acquisition system, especially for small tissue samples (Wu et al., 2007). Although several methods have been proposed to modify the analysis where finite ramp times are considered in order to better approximate the solutions (Carew, Talman, Boughner, & Vesely, 1999; Dortmans, Sauren, & Rousseau, 1984; Kwan, Lin, & Woo, 1993; Lin, Kwan, & Woo, 1987; Myers, McElhaney, Nightingale, & Doherty, 1991; Nigul & Nigul, 1987), these methods are still dependent on fast ramp rates, and therefore, may be affected by the associated errors. One of the main problems is overshoot, followed by a rebound back to the target stretch under high rates due to limitations in the mechanical testing equipment. This has been shown to have a considerable effect on the measured forces (Ledoux & Blevins, 2007) and to introduce an unwanted bias into the estimation of QLV parameters (Doehring, Carew, & Vesely, 2004; Gimbel, Sarver, & Soslowsky, 2004). For example, during stress relaxation of tendon, Gimbel et al. found that there was an average overshoot magnitude of 7.5% of the intended stretch, causing an error as large as 30% of the estimation of QLV parameters when the overshoot is not accounted for in the data fitting process.

It has been recommended that a slow stretch rate should be used in stress-relaxation tests (Abramowitch & Woo, 2004; Gimbel et al., 2004), since at low stretch rate the actual strain history (variation of strain with time) can be well approximated by a linear ramp followed by holding at constant stretch. Thus, the errors associated with fast stretch rates (e.g., overshoot, vibration, poorly approximated strain histories) can be reduced or avoided (Abramowitch & Woo; Funk et al., 2000; Gimbel et al.). For instance, recent studies have shown that a slow ramp rate (0.15%/s) in conjunction with a direct fit for the ramp and stress-relaxation portions can provide an accurate estimation of parameters, avoiding thus the errors associated with fast stretch rates (Abramowitch & Woo). In view of these, comparatively low stretch rates have been used in the tests performed in this study.

Skin Model Development of Based on QLV Theory An exponential approximation has often been chosen to describe the nonlinear elastic behavior of skin tissue under tension. Here, the following expression is used to describe the instantaneous elastic response:

$$\sigma_e(\varepsilon) = A(e^{B\varepsilon} - 1), \quad (5.11)$$

where A is a linear factor having the same units as stress and B is a nondimensional parameter representing the nonlinearity of elastic response (rate of stress stiffening). The product of A and B represents the initial slope of the elastic stress-strain curve.

The combination of exponentials has been shown to provide a good fit to viscoelastic behavior of soft tissues with efficient computational implementation (Puso & Weiss, 1998) and has been used satisfactorily to describe the viscoelastic behavior of skin tissue (Kenedi, Gibson, Evans, & Barbenel, 1975; Wu et al., 2006), given as

$$g(t) = k_0 + \sum_{i=1}^n k_i e^{-t/\tau_i}, \quad (5.12)$$

where k_0 represents the percentage of stress at the equilibrium state of relaxation process, and $\sum_{i=0}^n k_i = 1$. The preliminary investigation demonstrates that the sum of three exponentials is sufficient to correlate well with the experimental data in this study:

$$g(t) = k_0 + k_1 e^{-t/\tau_1} + k_2 e^{-t/\tau_2}, \quad (5.13)$$

where τ_i ($i = 1, 2$) are the long- and short-term time constants.

With the elastic and viscous components described above, a model based on the QLV theory is developed. For a linear ramp in strain followed by holding at constant strain, the strain history of this “ramp-and-hold” relaxation can be described as

$$\varepsilon(t) = \gamma(t - t_0), \text{ for } t_0 \leq t \leq t_R(\text{ramp}), \quad (5.14)$$

$$\varepsilon(t) = \gamma(t_R - t_0) = \varepsilon_{\max}, \text{ for } t_R \leq t \leq t_\infty(\text{hold}), \quad (5.15)$$

where γ is the stretch rate, ε_{\max} is the maximum strain, and t_0 , t_R , and t_∞ denote moments in time at the start of ramp, the end of ramp, and the end of relaxation, respectively.

The stress resulting from a ramp phase over time period $t_0 \leq t \leq t_R$ can be expressed by substituting Eqs. (5.11), (5.13)–(5.15) into Eq. (5.10). Specifically for the case of $t_0 = 0$, the following expressions can be obtained:

$$\begin{aligned} \sigma(t, A, B, k_0, k_1, k_2) = & Ak_0(e^{B\gamma t} - 1) + \sum_{i=1}^2 \frac{AB\gamma k_i}{B\gamma + (1/\tau_i)} \\ & \times (e^{B\gamma t} - e^{-t/\tau_i}), \quad 0 \leq t \leq t_R(\text{ramp}), \end{aligned} \quad (5.16)$$

$$\begin{aligned}\sigma(t, A, B, k_0, k_1, k_2) = & Ak_0(e^{B\gamma t_R} - 1) + \sum_{i=1}^2 \frac{AB\gamma k_i}{B\gamma + (1/\tau_i)} \\ & \times \left(e^{B\gamma t_R} - e^{-t_R/\tau_i} \right) e^{-t/\tau_i}, \quad t_R \leq t \leq t_\infty(\text{hold}).\end{aligned}\quad (5.17)$$

From Eq. (5.17) the stress during relaxation can be considered as the sum of three components, an equilibrium stress at t_R and the other two being long- and short-term decay components, respectively.

5.4.2. Relaxation Behavior of Skin Tissue

Typical Example of Skin Stress–Relaxation Behavior A representative uniaxial stress–time response from a relaxation test performed at body temperature ($T = 37^\circ\text{C}$) is presented in Fig. 5.15, which shows the response of pig ear skin tissue during both the ramp and relaxation phases of the test. In the ramp region ($0\text{s} \leq t \leq 50\text{s}$), the response is concave due to the nonlinearity caused by an increasing recruitment of collagen fibers with increasing stretch. In the relaxation region, the stress–relaxation curve is characterized by a sharp decrease in stress, followed by a gradual reduction up to 550 s. The uniaxial tensile relaxation results of pig ear skin tissue obtained here are comparable with those of human skin tissue (Barbenel & Evans, 1977) and rat skin tissue (Purslow, Wess, & Hukins, 1998) under tension, and pig foot skin tissue under compression (Wu et al., 2006) both qualitatively and quantitatively.

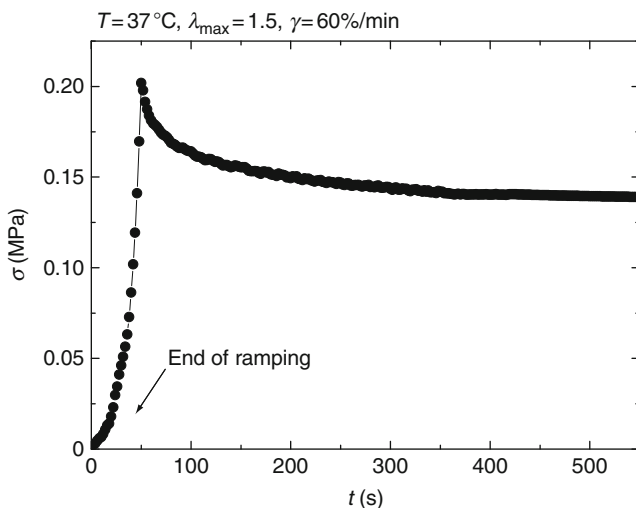


FIG. 5.15 Representative uniaxial tensile stress–relaxation response of pig ear skin tissue.

Verification of the QLV Theory The model developed in Section 5.4.1 is based on the QLV theory, which is built upon the assumption that the stress relaxation function can be separated into one time-dependent portion and one stretch-dependent portion. In other words, the normalized stress relaxation function, $g(t)$, should be independent of the stretch/stress level. Different trends in viscous-elastic separability have been observed in soft biological tissues. For example, the validity of the assumption has been justified for relaxation behavior of a variety of soft tissues including ligament, tendon and esophagi, both qualitatively (Haut & Little, 1972; Lanir, 1980) and quantitatively (Pioletti & Rakotomanana, 2000; Yang, Fung, Chian, & Chong, 2006) and has been argued to be reasonable for other soft tissues composed mainly of collagen (Pioletti & Rakotomanana). But in some other studies, it has been also shown that the relaxation behavior of collagenous tissues is dependent on stretch level (Bonifasi-Lista, Lake, Ellis, Rosenberg, & Weiss, 2002; Haut & Little; Hingorani, Provenzano, Lakes, Escarcega, & Vanderby, 2004; Komatsu, Sanctuary, Shibata, Shimada, & Botsis, 2007; Lakes & Vanderby, 1999; Lanir, 1980; Oyen et al., 2005; Provenzano, Lakes, Keenan, & Vanderby, 2001; Thornton, Oliynyk, Frank, & Shrive, 1997), which demonstrates the limits of Fung's QLV approach.

To verify the hypothesis of variables separation in QLV theory for skin tissue, stress relaxation tests of pig skin samples at three different stretch levels ($\lambda_{\max} = 1.1, 1.3, 1.5$ with rate $\gamma = 50\%/s$) at $T = 37$ °C are performed. The normalized relaxation response, calculated as $g(t) = \sigma_t/\sigma_{t_R}$, from different values of ε_{\max} is plotted in Fig. 5.16. The results show that the normalized relaxation of skin tissue is significant at all stretch levels. According to the QLV model, the normalized responses, $g(t)$, should have an identical shape, regardless of ε_{\max} , which is a direct result of the stretch-relaxation function separability (Eq. (5.10)). However, the experimental results of Fig. 5.16 show that $g(t)$ depends strongly on the ε_{\max} , which is inconsistent with the QLV modeling approach. This inconsistency can also be shown by the strong dependence of the elastic (equilibrium) stress fraction, $\text{Frac}_E = \sigma_\infty/\sigma_{t_R}$, as proposed by Oyen et al. (2005), on ε_{\max} : $\text{Frac}_E = 0.69, 0.65, 0.57$ for $\varepsilon_{\max} = 50\%, 30\%, 10\%$, respectively. Similar results with an increasing elastic fraction at larger stretch levels have also been observed elsewhere for skin tissue (Dunn & Silver, 1983) and human amnion (Oyen et al.).

The QLV approach is applicable only to tissues for which the separation of viscous and elastic energy is independent of stretch level. All the results here show that this model is not applicable to skin tissue tested in this study. A different model is therefore needed, but this is beyond the scope of this work.

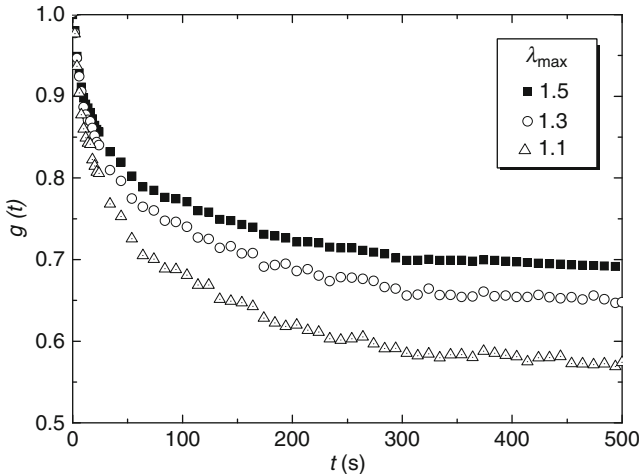


FIG. 5.16 Normalized relaxation responses, $g(t) = \sigma_t/\sigma_{t_R}$, from three experimental uniaxial relaxation tests demonstrate differences in shape for the time-dependent responses.

Relaxation Behavior Under Hyperthermal Temperatures The uniaxial tensile tests of pig ear skin tissue under four hyperthermal temperatures ($T = 50, 60, 70$, and 80 °C) have been performed. Together with the results obtained at body temperature, the normalized function of $g(t) = \sigma_t/\sigma_{t_R}$ is given in Fig. 5.17. Within physiological temperature ranges, it has been shown that the viscoelastic behavior of collagenous tissues is independent of temperature history (Cohen et al., 1976; Rigby, Hirai, Spikes, & Eyring, 1959). However, in the hyperthermal range, the stress-relaxation responses of skin tissue at a higher temperature relax faster and reach an equilibrium state much sooner than those at temperatures closer to body temperature, as shown in Fig. 5.17. This observation is in agreement with those reported in the open literature. For example, the stress in thermally treated collagenous tissue was found to relax faster and to a larger degree for a similar loading (Baek et al., 2005). The acceleration of stress relaxation due to thermal heating in mechanically deformed tissue was also observed in the laser reshaping of cartilage (Chao, Ho, & Wong, 2003; Gaon & Wong, 2000; Karamzadeh et al., 1999; Sobol et al., 2000; Wong et al., 1998, 1999), and laser thermokeratoplasty of corneal (Brinkmann et al., 2000).

Variation of Elastic Fraction with Temperature The elastic (equilibrium) stress fraction, $\text{Frac}_E = g(\infty) = \sigma_\infty/\sigma_{t_R}$, under different temperatures has been obtained from Fig. 5.17, as shown in Fig. 5.18. It can be seen that Frac_E depends

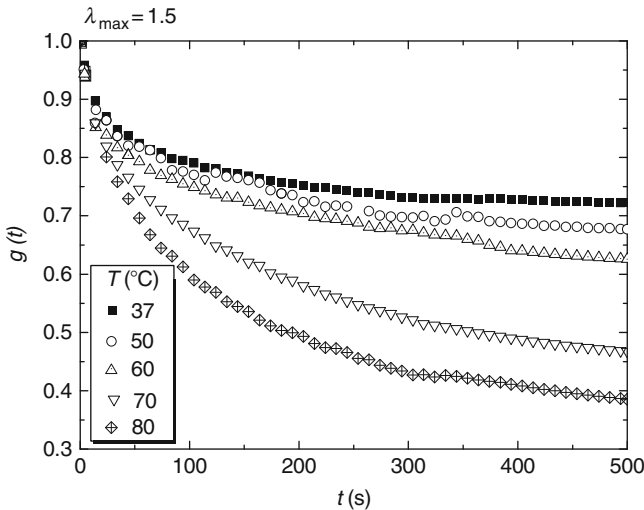


FIG. 5.17 The normalized relaxation function, $g(t) = \sigma(t)/\sigma_{t_R}$, under different hyperthermal temperatures.

strongly on the temperature: it decreases with increasing temperature over the whole temperature range, but decreases much faster in the hyperthermal range ($T = 50\text{--}80$ °C). In other words, as the temperature decreases, the energy dissipation decreases and the mechanical energy is increasingly elastic.

5.4.3. Discussion on Skin Relaxation Behavior

In this section, the possible roles played by different tissue components in skin viscoelasticity and the thermally induced changes in these factors are discussed.

Effect of Different Components Histological examination reveals that the viscoelastic response of skin tissue was mainly caused by the dermis, and not the epidermis in nature (Tsubouchi et al., 2006); Silver, Freeman, and DeVore (2001) also found the removal of epidermis does not change the viscoelastic properties of the tissue. Therefore, the following discussion is relative to the roles of different components of skin dermis.

Skin tissue is composed of cellular and extracellular compartments. The extracellular compartment consists of dominant collagen fibers embedded in ground substance. The mechanical response of skin tissue to applied loads involves two components as noted previously: a viscous component associated with energy dissipation by molecular and viscous sliding of collagen fibrils

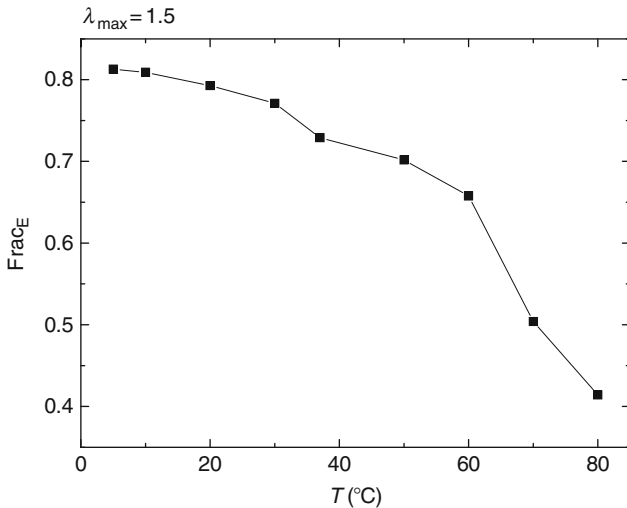


FIG. 5.18 The effect of temperature on the elastic fraction, $Frac_E = \sigma_\infty / \sigma_{t_R}$, for skin tissue.

during alignment with the force direction (Silver et al., 1992); and an elastic component associated with energy storage as a result of stretching of flexible regions in the collagen triple helix (Silver, Christiansen, Snowhill, & Chen, 2000; Silver, Horvath, & Foran, 2001; Silver et al., 2001). The viscous nature of collagenous tissues arises from the inherent viscoelasticity of the solid phase as well as fluid movement, resulting in viscous drag between the solid and fluid phases during loading (Huang, Chang, Aggarwal, Lee, & Ehrlich, 1993).

Effect of Elastic Components The extent to which a tissue exhibits stress relaxation has been shown to be directly related to the elastic content: elastin and collagen (Fung, 1981). However, in the study here of pig ear skin tissue, the elastin should not play an important role in the temperature-induced variation of viscoelastic behavior, for a high stretch level ($\epsilon_{\max} = 50\%$) has been chosen. At this level, the mechanical behavior of skin tissue is dominated by the response of collagen fibers (Silver et al., 1992).

The collagen fiber component plays a major role in the stress–stretch response of skin tissue, especially at high stretch levels ($\lambda \geq 1.3$) (Potts & Breuer, 1981; Silver et al., 2000; Silver, Horvath, et al., 2001). Collagen is intrinsically viscoelastic (Haut & Little, 1972; Sanjeevi, Somanathan, & Ramaswamy, 1982), implying that collagen viscoelasticity may be the source leading to the viscoelastic behavior of skin tissue (Purslow et al., 1998). For example, a

correlation between collagen content and the viscoelastic behavior of rat skin has been established (Vogel, 1988). An increase in collagen crosslinking was found to increase both the viscoelastic storage and loss moduli of guinea pig skin tissue under dynamic loading (Mansour, Davis, Srour, & Theberge, 1991). Furthermore, upon loading the initially crimped collagen fibers in dermis undergo reorientation, suggesting that the time-dependent reorientation of collagen fibers may be responsible for skin viscoelasticity. For example, the increase of elastic fraction³⁰ with increasing stretch in the skin stress-relaxation response was attributed to the rearrangement of individual collagen fiber orientations, resulting in an aligned collagen network at high stretch levels (Dunn & Silver, 1983). Structural reorganization was also recognized to be important in tendon viscoelasticity (Sasaki, Shukunami, Matsushima, & Izumi, 1999). However, Purslow et al. found no involvement of collagen fiber rotation in skin viscoelastic stress relaxation.

Role of Ground Substance The ground substance is a gel like substance containing a class of chemicals including proteoglycans (PG) and glycoproteins. The ground substance has been found to play an important role in the viscoelastic behavior of dermis. According to Wilkes, Brown, and Wildnauer (1973), the time-dependent behavior of dermis can be related to the viscous resistance that fibers experience while moving through the ground substance. Minns, Soden, and Jackson (1973) showed that the removal of ground substance in tendon, aorta and ligamentum nuchae induced a decrease in relaxation hysteresis and other time-dependent effects. Vogel (1976) found a correlation between the relaxation and the content of glycosaminoglycans (GAG) in skin tissue, which constitute a part of the PG. Purslow et al. (1998) also suggested that the viscoelastic effects of skin tissue arise from molecular relaxations within the proteoglycan matrix surrounding the collagen fibers or within the collagen fibers themselves. Eshel and Lanir (2001) found that the absence of proteoglycans influenced the low stretch relaxation patterns and deteriorated the viscoelastic mechanisms.

In summary, the skin viscoelasticity at high stretch level is decided by the collagen and ground substance tissue while the component of elastin should not play an important role. The temperature effect is discussed below.

³⁰ Equivalent to the ratio of equilibrium force to initial force.

Effect of Temperature and Thermal Denaturation Results from thermomechanical tests on collagenous tissues can be difficult to interpret due to the simultaneous occurrence of thermal damage, thermoelastic, and thermoviscoelastic processes, the least understood being the altered viscoelastic behaviors during and after heating (Baek et al., 2005).

As discussed in previous sections, three possible mechanisms exist for why temperature effects change the viscoelastic behavior of skin tissue. The first one is the thermal denaturation of dermis collagen and it seems reasonable to assume that collagen plays a major role in the viscoelastic nature of skin tissue subjected to thermal loading. For example, the acceleration of stress relaxation in laser reshaping of cartilage was partly attributed to the temperature-dependent, bound-free water transition in the cartilage matrix and selective collagen denaturation (Chao et al., 2003; Gaon & Wong, 2000; Karamzadeh et al., 1999; Sobol et al., 2000; Wong et al., 1998, 1999). Wells, Langille, Lee, and Adamson (1999) found a correlation between the relaxation rate of ovine aortic collagen and the concentration of thermally stable collagen crosslinks: if more crosslinking is present, the slippage of adjacent chain fragments will be inhibited, and the observed load relaxation will be slower. To check the role of collagen denaturation, the heat-induced thermal damage degree (Deg) of pig ear skin tissue under hyperthermal temperatures has been plotted as functions of time, as shown in Fig. 5.19. These results clearly show that collagen in skin tissue is damaged to a higher degree with increasing time and temperature. This explains the abrupt change in the elastic fraction around 60 °C in Fig. 5.18.

Another possible mechanism is the temperature-induced change in hydration. It has been shown that the viscoelastic behavior of soft tissues are related to the interactions among collagen, proteoglycans, and water molecules (Nishimura et al., 1998; Rochdi, Foucat, & Renou, 1999). There can be an inward or outward flux of interstitial fluid due to heating a soft tissue (Humphrey, 2003) and the viscoelastic properties of a tissue can be changed by altering its water content (Chimich, Shrive, Frank, Marchuk, & Bray, 1992). Baek et al. (2005) speculated that a loss of water causes the stress to relax, and the faster relaxation in thermally treated tissues is caused by the faster and greater water loss.

The third possible mechanism is the temperature-changed cell viability in skin tissue. From Fig. 5.19, it can be seen that collagen in skin tissue is almost fully damaged (Deg is near unity), indicating that fibroblast viability decreases with heating duration and temperature. Using poison (2-deoxy-D-glucose), Yip et al. (2007) studied the effect of *in situ* fibroblast viability on the mechanical properties of rat back skin tissue. They found that there is greater stress relaxation

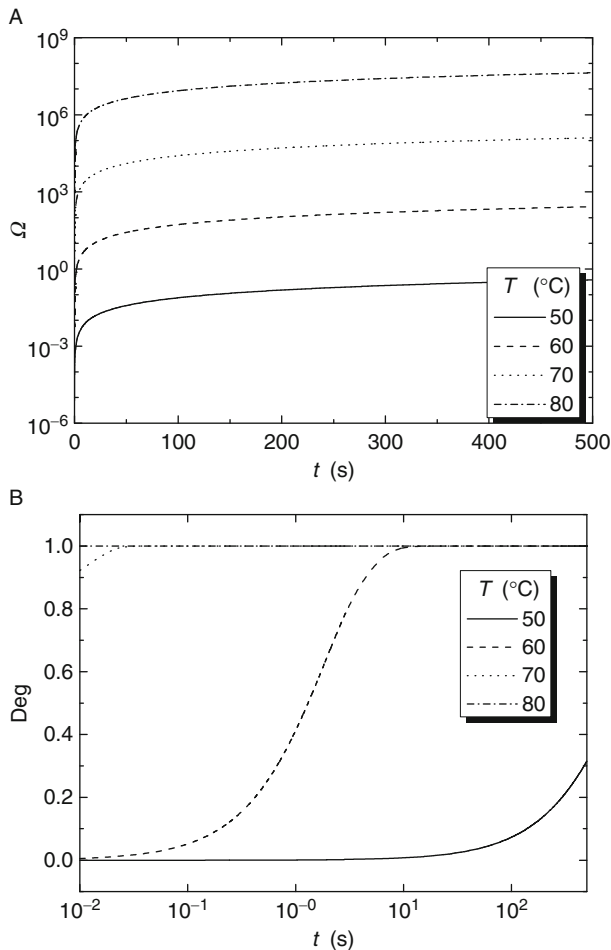


FIG. 5.19 (A) Thermal damage and (B) damage degree due to temperature increase during the relaxation tests.

in skin tissue stretched in normal Kreb's solution than that in Kreb's solution with poison, and that there exists a correlation between the amount of stress relaxation and the number of viable fibroblasts in the tissue: tissues with more viable fibroblasts have lower stress relaxation.

In summary, temperature has significant effect on the viscoelastic behavior of skin tissue; in the hyperthermal temperature range, the effect is caused by thermal denaturation of collagen as well as heating-induced hydration and cell viability changes.

5.5. DYNAMIC VISCOELASTICITY OF SKIN TISSUE

Most studies on the viscoelasticity of skin tissue have been performed under static experimental conditions. Although the understanding of mechanical behavior under static loading is truly beneficial, it is also very important to understand the mechanical behavior of skin tissue under dynamic loading. A few researchers have described the viscoelastic properties of skin tissue under dynamic loading (Dawes-Higgs, Swain, Higgs, Appleyard, & Kossard, 2004; Jacquemoud, Bruyere-Garnier, & Coret, 2007; Pereira et al., 1991), but none has considered temperature-dependent skin dynamic viscoelasticity. This is addressed in this section.

Figure 5.20A–C plots, the measured storage modulus, loss modulus and loss factor, respectively, of flank skin as functions of temperature. It is found that the storage modulus has a value ranging from 0.5 to 10 MPa, consistent with the data at room temperature reported in the literature (Pereira et al., 1991). The storage modulus of pig skin tissue increases as the temperature increases, almost linearly, implying that the skin tissue becomes stiffer with increasing temperature. The loss factor, however, is practically independent of temperature, suggesting that the viscous property of skin tissue is unaltered, that is, the damping capability of pig skin tissue does not change with varying temperature. The loss factor has a value of about 0.14, similar to that measured by the method of surface wave propagation at room temperature (Kirkpatrick, Duncan, & Fang, 2004). The results show no obvious variation in the slope of $\tan \delta$ as the DMA scan rate is varied. However, the storage modulus appears to increase with increasing heating rate.

To compare the dynamic results here with the previously obtained static results, the storage modulus can be used as the corresponding Young's modulus in view of the comparably low testing frequency (1 Hz). By comparing the modulus for the tensile behavior of pig ear skin sample under different temperatures (Fig. 5.12A) with the storage modulus, as given in Fig. 5.21, it can be found that the magnitudes of the moduli agree well, but the storage modulus increases with temperature, contrary to that of the tensile behavior. This is because the dynamic testing was performed in a thermal chamber filled with air, which resulted in the dehydration of the skin sample during heating, while the tensile testing was performed in a chamber filled with liquid (KHR).

The storage modulus, loss modulus, and loss factor of pig skin tissue are plotted as functions of thermal damage and thermal denaturation degree in Fig. 5.22. These results show that the effects of thermal damage and thermal denaturation degree on the viscoelastic properties of pig skin tissue are similar to that of temperature. This means that the changes of collagen triple-helix structure

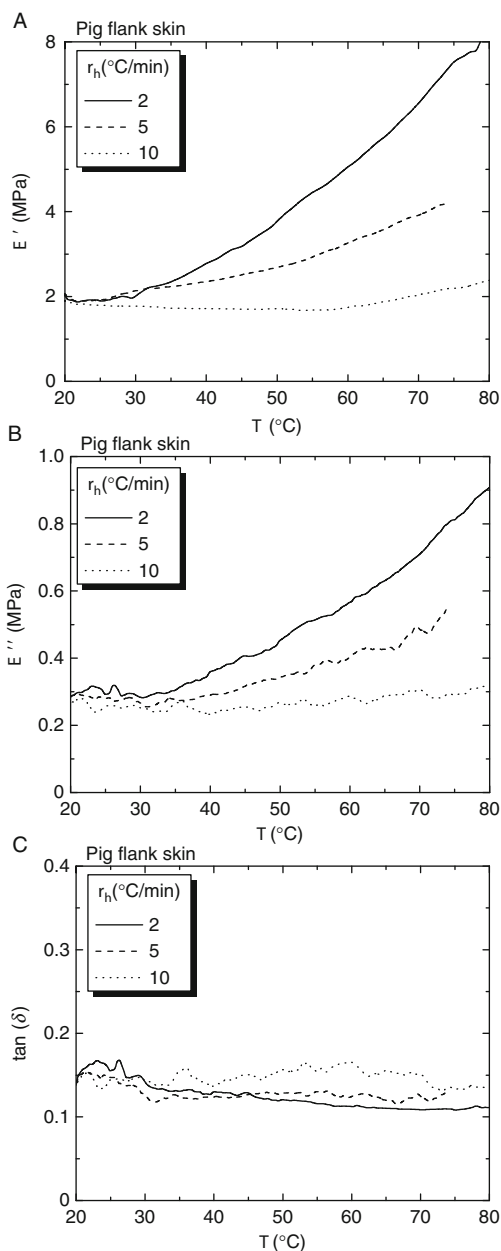


FIG. 5.20 Variations of (A) storage modulus, E' , (B) loss modulus, E'' , and (C) loss factor, $\tan \delta$, with temperature for flank skin sample.

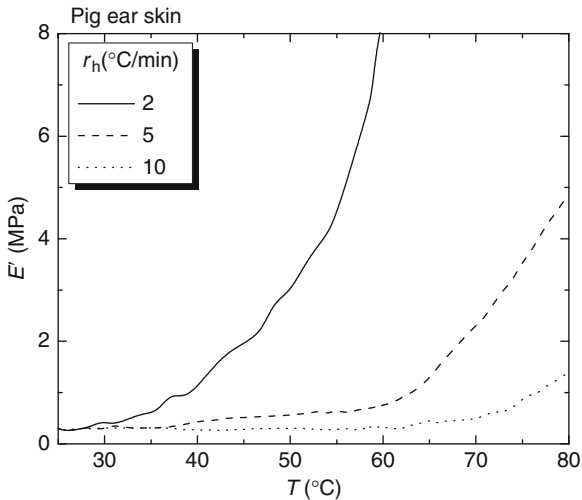


FIG. 5.21 Variations of storage modulus, E' , with temperature for ear skin sample.

during thermal denaturation process may not be a major factor in deciding the storage modulus and loss factor of tissue, at least at the test frequency used in this study. It has been postulated that the mechanical changes observed using DMA are the result of a combination of water loss and changes in the intrinsic molecular structure of tissue with heating (Chae et al., 2003). In the present investigation, the heat treatment causes collagen denaturation as well as dehydration, and weight loss of the skin samples has also been observed during the test. Thus, the variations in the tests here may be attributed to the release of bound water during heating. This is supported by the fact that heat stabilization is enhanced by the formation of strong interchains bonds as a result of condensation reactions, making the collagen matrices stiffer with a higher resistance to deformation (Pietrucha, 2005).

6. Conclusions

The widespread use of thermal therapies for skin disease treatments requires the corresponding understanding of the biothermomechanical behavior of skin tissue. In this chapter, a variety of mathematical approaches have been first developed to examine the heat transfer process, thermal damage, and the heat-induced mechanical response. Detailed analyses are then performed with both Fourier and non-Fourier heat transfer models. For accurate modeling, the

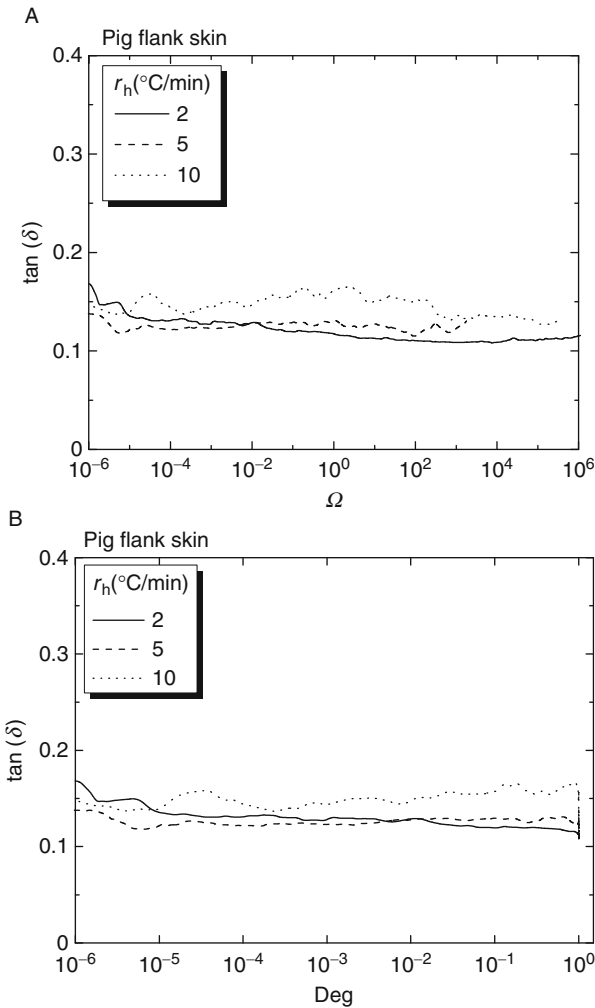


FIG. 5.22 Variations of loss factor, $\tan \delta$, with (A) thermal damage and (B) damage degree.

experimental characterization of the thermomechanical behavior of skin tissue is necessary. Although the mechanical properties of skin tissue under normal physiological conditions have been studied extensively, experimentally, both *in vivo* and *in vitro*, there has been little characterization of the changes in the mechanical properties of skin tissue due to temperature rising and the corresponding thermal damage. These are thus addressed as the emphasis of this study. The main summaries, limitations, and future work are described below.

6.1. SUMMARY

The tensile, compressive, and viscoelastic behaviors of skin tissue under different temperatures and thermal damage levels have been examined, to characterize the effect of temperature variations and corresponding collagen denaturation on the mechanical properties of skin tissue. The results have been discussed together with the corresponding thermal damage process. Comparisons of the experimental results with reported results in literature have been performed, and a good agreement has been achieved. Internal comparisons of results obtained from different methods have also been made. The following conclusions can be drawn.

DSC results show that the transition temperature of collagen in pig flank skin samples is about 66.8 °C, and from the DSC results the Arrhenius parameters can be obtained for skin samples from different locations. Under tensile loading, the modulus at high stretch level of the tested skin samples decreases with increasing temperature due to the thermal denaturation of skin collagen: compressive loading, however, showed quite the opposite due to the different underlying mechanisms between tensile and compressive behaviors of skin tissue. Biaxial tests at 37 and 60 °C show that the skin tissue from porcine cheek appears to be abnormal in the fact that it has an equal tensile response across both axes of a square independent of cutting angle. This discovery has allowed the series of experiments on skin tissue to come to fruition since a uniform stress distribution in the tissue can be easily achieved even in biaxial tests. Compared with uniaxial stretching, biaxial tensile loading results in the lateral narrowed stress–stretch curve and the reduction in the stretch before entry into the linear region occurs under all temperatures tested, which is due to the two-directional stretch of collagen fibers. Under compression, the stiffness of skin tissue decreases with increasing thermal damage degree. A stretch-rate sensitivity is observed at different damage levels, and the stiffness of skin tissue decreases with thermal damage. Temperature has a significant effect on the static viscoelasticity of skin tissue. As for the dynamic skin viscoelasticity, DMA results showed that the storage modulus is highly temperature dependent; however, the loss factor did not show a significant dependency on either temperature or thermal denaturation.

6.2. LIMITATIONS

There are several limitations to the present study, as described below:

1. The thermal denaturation of a collagenous tissue depends on not only the temperature history but also the stress state during heating ([Humphrey, 2003](#)), which is, however, very difficult to quantify due to the lack of

corresponding research. Therefore, in the calculation of thermal damage the parameters obtained from DSC measurements in the absence of applied tractions were used.

2. It is well known that the mechanical properties of skin tissue are in general nonlinearly elastic and viscoelastic. In the tensile and compressive testing of the present study, however, we concentrated only on the nonlinear elasticity of the tissue. The data of compressive behavior were fit with the Odgen model with the assumption of incompressivity. However, it was found that pigskin under compression is compressible; even in unconfined compression, the volume of specimens varies with increasing compressive deformation ([Wu et al., 2003](#)).
3. Engineering stretch/strain and stress are used in this chapter. Most mechanical models including Kelvin–Maxwell model and integrate model use this kind of definitions and a good agreement with the experiment results has been achieved. However, these are linear elastic definitions, which have been pointed out to be inappropriate for studies of large deformation and nonlinear solid mechanics should be used in the future study.
4. The viscoelastic behavior of skin was only tested for uniaxial loading and, thus, biaxial loading needs to be studied in the future for skin *in vivo* experiences multiaxial natural tension. The stretch applied in the present relaxation test was 1.5, but a previous study found that after a 1.2 stretch the fibroblasts were apoptotic or necrotic ([Martel, Walker, Reed, & Bert, 2001](#)).
5. The dynamic testing in this study was performed in a chamber filled with air, and the mechanical changes observed were induced by a combination of effects that include both water loss and changes in the intrinsic molecular structure of tissue with heating. Further studies should focus on identifying the relative contribution of water loss and thermal denaturation. Another limitation of the dynamic testing is that all the tests were performed at a fixed frequency of 1 Hz and it is expected that the loading frequency would also play a role.
6. In our previous studies (Xu, Wen, Seffen, et al., 2008), a mathematical approach has been developed for determining the thermomechanical response in skin tissue, where temperature/damage independent linear elastic mechanical properties of skin tissue have been used. The assumptions used are reasonable in view that (1) the stretch level considered in that case is purely induced by thermal loads and is thus comparatively small (< 1.01) and (2) the results in the present study have shown that temperature/damage has little effect at this low stretch level (see [Figs. 5.12 and 5.16](#)).

However, in medical applications, deformation of skin at high stretch level also occurs, for example, skin indentation during laser-skin treatment (Basinger, Aguilar, & Nelson, 2004; Klavuhn, 2001). For these cases, it can be expected that the incorporation of the temperature/damage dependent mechanical properties in the thermomechanical model will have a great effect on the predicted thermomechanical behavior of skin tissue.

6.3. FUTURE WORK

The approach developed in this study provides a platform to study the thermal and mechanical behaviors, and corresponding pain sensation. This method introduces engineering to the fields of biology and neurophysiology, opening the door to future advancements at the interface of these fields.

First, the full suite of models and experimental results can be used for development of a thermal therapy model with a user-friendly interface. The therapy model can be validated by comparing it with the response from the clinical patients. Once validated, the model can then be used for (1) characterization of present strategies for delivering thermal therapies by considering patient's pain feeling as an additional factor; (2) optimization of thermal treatments by maximizing the therapeutic effect while minimizing unwanted side effects such as pain sensation; and (3) design of new and better treatment strategies, to assert novel heat treatments in view of productive commercial exploitation.

Second, it can be used for improving artificial skin, for example, robot skin. Robot has wider applications in different environments, especially in space. Robotic skin is needed to respond to work more efficiently in highly unstructured environments and facilitate human–robot interactions for both work and entertainment purposes. The approach developed in this study can help the design of new robot skin which can detect pressure, temperature, moisture/humidity, hardness of objects, and electrical conductivity of objects.

Third, the approach developed in this study can be helpful for the transdermal drug delivery, for example, needle-free injection. Needle-free injection has been used for more than 50 years with excellent bioavailability. However, pain and bruising have limited its wider applications. The holistic skin pain model considering both skin mechanical and neural response can help to better understand the physical mechanisms of jet penetration into skin and to improve the current injectors by minimizing the pain sensation felt by patients.

Acknowledgments

This work was supported by the Overseas Research Studentship (ORS) and Overseas Trust Scholarship of Cambridge University, the National Natural Science Foundation of China (10572111, 10632060), the National Outstanding Youth Foundation of China, the National 111 Project of China (B06024), and the National Basic Research Program of China (2006CB601202).

References

- Abramowitch, S. D., & Woo, S. L. (2004). An improved method to analyze the stress relaxation of ligaments following a finite ramp time based on the quasi-linear viscoelastic theory. *Journal of biomechanical engineering*, 126(1), 92–97.
- Abramson, D. I. (1967). *Circulation in the extremities*. New York: Academic.
- Agah, R., Gandjbakhche, A. H., Motamed, M., Nossal, R., & Bonner, R. F. (1996). Dynamics of temperature dependent optical properties of tissue: Dependence on thermally induced alteration. *IEEE Transactions on Bio-medical Engineering*, 43(8), 839–846.
- Ahn, T.-K., & Kim, K.-J. (1994). Sensitivity analysis for estimation of complex modulus of viscoelastic materials by non-resonance method. *Journal of Sound and Vibration*, 176, 543–561.
- Aksan, A., & McGrath, J. J. (2003). Thermomechanical analysis of soft-tissue thermotherapy. *Journal of Biomechanical Engineering*, 125(5), 700–708.
- Alberts, B., Bray, D., Lewis, J., Raff, M., Roberts, K., & Watson, J. D. (1994). *Molecular biology of the cell*. New York: Garland.
- Alexander, H., & Cook, T. H. (1976). Variations with age in the mechanical properties of human skin *in vivo*. In R. M. Kennedy (Ed.), *Bedsore biomechanics* (pp. 109–118). Bath: McMillan Press.
- Allain, J. C., Le Lous, M., Cohen-Solal, L., Bazin, S., & Maroteaux, P. (1980). Isometric tensions developed during the hydrothermal swelling of rat skin. *Connect Tissue Research*, 7, 127–133.
- Ankersen, J., Birkbeck, A. E., Thomson, R. D., & Vanezis, P. (1999). Puncture resistance and tensile strength of skin simulants. *Proceedings of the Institution of Mechanical Engineers. Part H*, 213(6), 493–501.
- Arbogast, K. B., Thibault, K. L., Scott Pinheiro, B., Winey, K. I., & Margulies, S. S. (1997). A high-frequency shear device for testing soft biological tissues. *Journal of biomechanics*, 30(7), 757–759.
- Arendt-Nielsen, L., & Chen, A. C. N. (2003). Lasers and other thermal stimulators for activation of skin nociceptors in humans. *Neurophysiologie Clinique/Clinical Neurophysiology*, 33(6), 259–268.
- Arkin, H., Xu, L. X., & Holmes, K. R. (1994). Recent developments in modeling heat transfer in blood perfused tissues. *IEEE Transactions on Biomedical Engineering*, 41(2), 97–107.
- Arnoczky, S. P., & Aksan, A. (2000). Thermal modification of connective tissues: Basic science considerations and clinical implications. *The Journal of the American Academy of Orthopaedic Surgeons*, 8(5), 305–313.
- Arumugam, V., Naresh, M. D., & Sanjeevi, R. (1994). Effect of strain rate on the fracture behaviour of skin. *Journal of Bioscience*, 19(3), 307–313.
- Asahina, A., Watanabe, T., Kishi, A., Hattori, N., Shirai, A., Kagami, S., et al. (2006). Evaluation of the treatment of port-wine stains with the 595-nm long pulsed dye laser: A large prospective study in adult Japanese patients. *Journal of the American Academy of Dermatology*, 54(3), 487–493.
- Auriol, F., Vaillant, L., Machet, L., Diridollou, S., & Lorette, G. (1993). Effects of short-time hydration on skin extensibility. *Acta Dermato-Venereologica*, 73(5), 344–347.

- Baek, S., Wells, P. B., Rajagopal, K. R., & Humphrey, J. D. (2005). Heat-induced changes in the finite strain viscoelastic behavoir of a collaagenous tissue. *Journal of Biomechanical Engineering*, 127(4), 580–586.
- Barbenel, J. C., & Evans, J. H. (1977). The time-dependent mechanical properties of skin. *The Journal of Investigative Dermatology*, 69(3), 318–320.
- Basinger, B., Aguilar, G., & Nelson, J. S. (2004). Effect of skin indentation on heat transfer during cryogen spray cooling. *Lasers in Surgery and Medicine*, 34(2), 155–163.
- Bayazitoglu, Y., & Peterson, G. P. (1992). Fundamental issues in hyperbolic heat conduction. *ASME HTD*, 227.
- Bert, J. L., & Reed, R. K. (1997). Pressure-volume relationship for rat dermis: Compression studies. *Acta physiologica Scandinavica*, 160(1), 89–94.
- Bhowmick, S., & Bischof, J. C. (1998). Supraphysiological thermal injury in dunning AT-1 Prostate tumor cells. *Advances in Heat and Mass Transfer in Biotechnology*, 77–78. ASME HTD-Vol. 362/BED-40.
- Bonifasi-Lista, C., Lake, S., Ellis, B., Rosenberg, T., & Weiss, J. A. (2002). Strain- and rate-dependent viscoelastic properties of human MCL in tension. *Transactions of the Orthopaedic Research Society*, 27, 609.
- Bonilla, C. M. A., Massanet, A. R. F., & Almodóvar, N. V. (2005). Mechanics of biomaterials: Skin repair and grafts. In: *Proceedings of applications of engineering mechanics in medicine*. Mayaguez: University of Puerto Rico.
- Bosman, S. (1993). Heat-induced structural alterations in myocardium in relation to changing optical properties. *Applied Optics*, 32(4), 461–463.
- Brinkmann, R., Radt, B., Flamm, C., Kampmeier, J., Koop, N., & Birngruber, R. (2000). Influence of temperature and time on thermally induced forces in corneal collagen and the effect on laser thermokeratoplasty. *Journal of Cataract and Refractive Surgery*, 26, 744–754.
- Britton, N. F., & Skevington, S. M. (1996). On the mathematical modelling of pain. *Neurochemical Research*, 21(9), 1133–1140.
- Burnstock, G. (1996). A unifying purinergic hypothesis for the initiation of pain. *Lancet Neurol*, 347, 1604–1605.
- Burnstock, G., & Wood, J. N. (1996). Purinergic receptors: Their role in nociception and primary afferent neurotransmission. *Current Opinion in Neurobiology*, 6, 526–532.
- Campbell, J. N., & LaMotte, R. H. (1983). Latency to detection of first pain. *Brain Research*, 266, 203–208.
- Carew, E. O., Talman, E. A., Boughner, D. R., & Vesely, I. (1999). Quasi-linear viscoelastic theory applied to internal shearing of porcine aortic valve leaflets. *Journal of Biomechanical Engineering Transactions ASME*, 121(4), 386–392.
- Caterina, M. J., & Julius, D. (1999). Sense and specificity: A molecular identity for nociceptors. *Current opinion in neurobiology*, 9, 525–530.
- Caterina, M. J., Rosen, T. A., Tominaga, M., Brake, A. J., & Julius, D. (1999). Capsaicin-receptor homologue with a high threshold for noxious heat. *Nature*, 398(6726), 436–441.
- Cattaneo, C. (1958). A form of heat conduction equation which eliminates the paradox of instantaneous propagation. *Compute Rendus*, 247, 431–433.
- Cesare, P., & McNaughton, P. A. (1996). A novel heat-activated current in nociceptive neurons and its sensitization by bradykinin. *Proceedings of the National Academy of Sciences of the USA*, 93(26), 15435–15439.
- Chachra, D., Gratzer, P. F., Pereira, C. A., & Lee, J. M. (1996). Effect of applied uniaxial stress on rate and mechanical effects of cross-linking in tissue-derived biomaterials. *Biomaterials*, 17(19), 1865–1875.
- Chae, Y., Aguilar, G., Lavernia, E. J., & Wong, B. J. (2003). Characterization of temperature dependent mechanical behavior of cartilage. *Lasers in Surgery and Medicine*, 32(4), 271–278.

- Chao, K. K. H., Burden, M. A., & Wong, B. J. F. (2001). *Dynamic changes in the elastic modulus of lagomorph nasal septal cartilage during Nd:YAG ($\lambda = 1.32 \mu\text{m}$) laser irradiation* (pp. 247–254). San Jose, CA: Society of Photo-Optical Instrumentation Engineers.
- Chao, K. K., Ho, K. H., & Wong, B. J. (2003). Measurement of the elastic modulus of rabbit nasal septal cartilage during Nd:YAG ($\lambda = 1.32 \mu\text{m}$) laser irradiation. *Lasers in Surgery and Medicine*, 32(5), 377–383.
- Charny, C. K. (1992). Mathematical models of bioheat transfer. *Advances in Heat Transfer*, 22, 19–155.
- Chato, J. C. (1980). Heat transfer to blood vessels. *Journal of Biomechanical Engineering, Transactions of the ASME*, 102(2), 110–118.
- Chen, M. M., & Holmes, K. R. (1980). Microvascular contributions in tissue heat transfer. *Annals New York Academy Science*, 335, 137–150.
- Chen, S. S., & Humphrey, J. D. (1998). Heat-induced changes in the mechanics of a collagenous tissue: Pseudoelastic behavior at 37 degrees C. *Journal of Biomechanics*, 31(3), 211–216.
- Chen, S. S., Wright, N. T., & Humphrey, J. D. (1997). Heat-induced changes in the mechanics of a collagenous tissue: Isothermal free shrinkage. *Journal of Biomechanical Engineering*, 119(4), 372–378.
- Chen, S. S., Wright, N. T., & Humphrey, J. D. (1998a). Heat-induced changes in the mechanics of a collagenous tissue: Isothermal, isotonic shrinkage. *Journal of Biomechanical Engineering*, 120(3), 382–388.
- Chen, S. S., Wright, N. T., & Humphrey, J. D. (1998b). Phenomenological evolution equations for heat-induced shrinkage of a collagenous tissue. *IEEE Transactions on Biomedical Engineering*, 45(10), 1234–1240.
- Chester, M. (1963). Second sound in solid. *Physical Reviews*, 131, 2013–2015.
- Chimich, D., Shrive, N., Frank, C., Marchuk, L., & Bray, R. (1992). Water content alters viscoelastic behavior of the normal adolescent rabbit medial collateral ligament. *Journal of Biomechanics*, 25, 831–837.
- Choi, H. S., & Vito, R. P. (1990). Two-dimensional stress-strain relationship for canine pericardium. *Journal of Biomechanical Engineering, Transactions of the ASME*, 112, 153–159.
- Choinière, M., Melzack, R., Girard, N., Rondeau, J., & Paquin, M. J. (1990). Comparisons between patients' and nurses' assessment of pain and medication efficacy in severe burn injuries. *Pain*, 40, 143–152.
- Chvapil, M., & Jensovsky, L. (1963). The shrinkage temperature of collagen fibres isolated from the tail tendons of rats of various ages and from different places of the same tendon. *Gerontologia*, 1, 18–29.
- Cohen, R. E., Hooley, C. J., & McCrum, N. G. (1976). Viscoelastic creep of collagenous tissue. *Journal of Biomechanics*, 9(4), 175–184.
- Connors, K. A. (1990). *Chemical kinetics*. Wiley-VCH: The Study of Reaction Rates in Solution.
- Cox, H. (1942). The cleavage lines of the skin. *The British Journal of Surgery*, 29, 234–240.
- Crezee, J., & Lagendijk, J. J. (1992). Temperature uniformity during hyperthermia: The impact of large vessels. *Physics in Medicine and Biology*, 37, 1321–1337.
- Crezee, J., Mooibroek, J., Lagendijk, J. J., & van Leeuwen, G. M. (1994). The theoretical and experimental evaluation of the heat balance in perfused tissue. *Physics in Medicine and Biology*, 39(5), 813–832.
- Dahan, S., Lagarde, J. M., Turlier, V., Courrech, L., & Mordon, S. (2004). Treatment of neck lines and forehead rhytids with a nonablative 1540-nm Er:glass laser: A controlled clinical study combined with the measurement of the thickness and the mechanical properties of the skin. *Dermatologic Surgery*, 30(6), 872–879.
- Daly, C. H. (1982). Biomechanical properties of dermis. *The Journal of Investigative Dermatology*, 79(Suppl. 1), s17–s20.

- Davidson, J. M., Giro, M., Sutcliffe, M., Zoia, O. D. Q., Liu, J. J. M., Perkett, E., et al. (1990). Regulation of elastin synthesis. In A. M. Tamburro & J. M. Davidson (Eds.), *Elastin: Chemical and biological aspects*. Galatina, Italy: Congedo Editore.
- Davis, E. D., Doss, D. J., Humphrey, J. D., & Wright, N. T. (2000). Effects of heat-induced damage on the radial component of thermal diffusivity of bovine aorta. *Journal of Biomechanical Engineering*, 122(3), 283–286.
- Dawes-Higgs, E. K., Swain, M. V., Higgs, R. J. E. D., Appleyard, R. C., & Kossard, S. (2004). Accuracy and reliability of a dynamic biomechanical skin measurement probe for the analysis of stiffness and viscoelasticity. *Physiological Measurement*, 25(1), 97–105.
- de Boer, J. F., Srinivas, S. M., Malekafzali, A., Chen, Z. P., & Nelson, J. S. (1998). Imaging thermally damaged tissue by polarization sensitive optical coherence tomography. *Optics Express*, 3, 212–218.
- Decraemer, W. F., Maes, M. A., Vanhuyse, V. J., & Vanpeperstraete, P. (1980). A non-linear viscoelastic constitutive equation for soft biological tissues based upon a structural model. *Journal of Biomechanics*, 13, 559–564.
- Defrate, L. E., & Li, G. (2006). The prediction of stress-relaxation of ligaments and tendons using the quasi-linear viscoelastic model. *Biomechanics and Modeling in Mechanobiology*, 6, 245–251.
- Delalleau, A., Josse, G., Lagarde, J. M., Zahouani, H., & Bergheau, J. M. (2006). Characterization of the mechanical properties of skin by inverse analysis combined with the indentation test. *Journal of Biomechanics*, 39(9), 1603–1610.
- Diaz, S., Lavemia, E., & Wong, B. J. F. (2001). *Mechanical behavior of cartilage during laser irradiation* (pp. 192–197). San Jose, CA: Society of Photo-Optical Instrumentation Engineers.
- Diette, K. M., Bronstein, B. R., & Parrish, J. A. (1985). Histologic comparison of argon and tunable dye lasers in the treatment of tattoos. *The Journal of Investigative Dermatology*, 85(4), 368–373.
- Dikstein, S., & Hartzshark, A. (1983). What does low-pressure indentometry measure. *Ärztlische Kosmetologie*, 16, 327–328.
- Diller, K. R., & Pearce, J. A. (1999). Issues in modeling thermal alterations in tissues. *Annals New York Academy of Science*, 888, 153–164.
- Dinnar, U. (1970). A note on theory of deformation in compressed skin tissues. *Mathematical Bioscience*, 8, 71–82.
- Diridollou, S., Vabre, V., Berson, M., Vaillant, L., Black, D., Lagarde, J. M., et al. (2001). Skin ageing: Changes of physical properties of human skin *in vivo*. *International Journal of Cosmetic Science*, 23, 353–362.
- Dittert, I., Vlachova, V., Knotkova, H., Vitaskova, Z., Vyklicky, L., Kress, M., et al. (1998). A technique for fast application of heated solutions of different composition to cultured neurones. *Journal of Neuroscience Methods*, 82, 195–201.
- Doehring, T. C., Carew, E. O., & Vesely, I. (2004). The effect of strain rate on the viscoelastic response of aortic valve tissue: A direct-fit approach. *Annals of Biomedical Engineering*, 32(2), 223–232.
- Dortmans, L. J., Sauren, A. A., & Rousseau, E. P. (1984). Parameter estimation using the quasi-linear viscoelastic model proposed by Fung. *Journal of Biomechanical Engineering, Transactions of the ASME*, 106(3), 198–203.
- Douglas, W. R. (1972). Of pigs and men and research: A review of applications and analogies of the pig, Sus scrofa, in human medical research. *Space and Life Sciences*, 3, 226–234.
- Downs, J., Halperin, H. R., Humphrey, J. D., & Yin, F. C. P. (1990). An improved video-based computer tracking system for soft-biomaterials testing. *IEEE Transactions on Bio-medical Engineering*, 37, 903–907.
- Duck, F. A. (1990). *Physical properties of tissue: A comprehensive reference book*. New York: Academic Press.
- Dunn, M. G., & Silver, F. H. (1983). Viscoelastic behavior of human connective tissues: Relative contribution of viscous and elastic components. *Connective Tissue Res.*, 12(1), 59–70.

- Dunn, M. G., Silver, F. H., & Swann, D. A. (1985). Mechanical analysis of hypertrophic scar tissue: Structural basis for apparent increased rigidity. *The Journal of Investigative Dermatology*, 84(1), 9–13.
- Ebling, F., Eady, R., & Leigh, I. (1992). Anatomy and organization of human skin. In R. H. Champion, J. L. Burrington & F. J. G. Ebling (Eds.), *Textbook of dermatology*. New York: Blackwell Scientific Publications.
- Edwards, C., & Marks, R. (1995). Evaluation of biomechanical properties of human skin. *Clinics Dermatology*, 13(4), 375–380.
- Elkins, W., & Thomson, J. G. (1973). Instrumented thermal manikin. *Acurex Corporation, Aerotherm Division Report AD-781*, 176.
- Elmore, D. E. (2004). *Investigations of ion channel structure-function relationships using molecular modeling and experimental biochemistry*. California: California Institute of Technology.
- Elsner, P., Wilhelm, D., & Maibach, H. I. (1990). Mechanical properties of human forearm and vulvar skin. *British Journal of Dermatology*, 122(5), 607–614.
- Eshel, H., & Lanir, Y. (2001). Effects of strain level and proteoglycan depletion on preconditioning and viscoelastic responses of rat dorsal skin. *Annals of Biomedical Engineering*, 29, 164–172.
- Essenpreis, M. (1992). *Thermally induced changes in optical properties of biological tissues*. London: University College London.
- Ferry, J. D. (1980). *Viscoelastic properties of polymers*. New York: Wiley.
- Fidanza, F., Keys, A., & Anderson, J. T. (1953). Density of body fat in man and other mammals. *Journal of Applied Physiology*, 6, 252–256.
- Fink, W. A. Jr. (2005). The pathophysiology of acute pain. *Emergency Medicine Clinics of North America*, 23(2), 277–284.
- Finlay, B. (1969). Scanning electron microscopy of the human dermis under uni-axial strain. *Bio-medical Engineering*, 4, 322–327.
- Flory, P. J., & Garrett, R. R. (1958). Phase transition in collagen and gelatin systems. *Journal of American Chemical Society*, 80, 4836–4845.
- Fung, Y. C. (1971). Stress-strain history relations of soft tissues in simple elongation. In Y. C. Fung, N. Perrone & M. Anliker (Eds.), *Biomechanics: Its foundations and objectives* (pp. 181–208). Englewood Cliffs, NJ: Prentice-Hall, Inc.
- Fung, Y. C. (1981). *Biomechanics: Mechanical properties of living tissue*. New York: Springer.
- Fung, Y. C. (1990). *Biomechanics: Motion, flow, stress, and growth*. New York: Springer.
- Fung, Y. C. (1993). *Biomechanics: Mechanical properties of living tissues*. New York: Springer.
- Funk, J. R., Hall, G. W., Crandall, J. R., & Pilkey, W. D. (2000). Linear and quasi-linear viscoelastic characterization of ankle ligaments. *Journal of Biomechanical Engineering, Transactions of the ASME*, 122(1), 15–22.
- Gallagher, G., Rae, C. P., & Kinsella, J. (2000). Treatment of pain in severe burns. *American Journal of Clinical Dermatology*, 1, 329–335.
- Gaon, M. D., & Wong, B. J. F. (2000). Measurement of the elastic modulus of porcine septal cartilage specimens following Nd:YAG laser treatment. *Proceedings—Society of Photo-Optical Instrumentation Engineers*, 3907, 370–379.
- Giles, J. M., Black, A. E., & Bischoff, J. E. (2007). Anomalous rate dependence of the preconditioned response of soft tissue during load controlled deformation. *Journal of Biomechanics*, 40(4), 777–785.
- Gimbel, J. A., Sarver, J. J., & Soslowsky, L. J. (2004). The effect of overshooting the target strain on estimating viscoelastic properties from stress relaxation experiments. *Journal of Biomechanical Engineering, Transactions of the ASME*, 126(6), 844–848.
- Godoy, S., & García-Colín, L. S. (1997). Nonvalidity of the telegrapher's diffusion equation in two and three dimensions for crystalline solids. *Physical Reviews E*, 55, 2127–2131.

- Gordon, R. G., Roemer, R. B., & Howarth, S. M. (1976). A mathematical model of the human temperature regulatory system—Transient cold exposure responses. *IEEE Transactions on Biomedical Engineering*, 23(6), 434–444.
- Green, D. M., & Diller, K. R. (1978). Measurement of burn induced leakage of macromolecules in living tissue. *Transactions of the ASME, Journal of Biomechanical*, 100, 153–158.
- Haeri, M., Asemani, D., & Gharibzadeh, S. (2003). Modeling of pain using artificial neural networks. *Journal of Theoretical Biology*, 220(3), 277–284.
- Hamilton, M. M. (2004). Laser treatment of pigmented and vascular lesions in the office. *Facial Plastic Surgery*, 20(1), 63–69.
- Hamilton, S. G. (2002). ATP and pain. *Pain Practice*, 2(4), 289–294.
- Harris, J. L., Wells, P. B., & Humphrey, J. D. (2003). Altered mechanical behavior of epicardium due to isothermal heating under biaxial isotonic loads. *Journal of Biomechanical Engineering*, 125, 381–388.
- Haut, R. C. (1983). *The sensitivity of skin to strain rate of loading*. 7th Annual meeting of the american society of biomechanics, Rochester, Minn.
- Haut, R. C., & Little, R. W. (1972). A constitutive equation for collagen fibers. *Journal of Biomechanics*, 5(5), 423–430.
- Hendriks, F. M., Brokken, D., Oomens, C. W., Bader, D. L., & Baaijens, F. P. (2006). The relative contributions of different skin layers to the mechanical behavior of human skin *in vivo* using suction experiments. *Medical Engineering and Physics*, 28(3), 259–266.
- Henriques, F. C., & Moritz, A. R. (1947). Studies of thermal injury, I. The conduction of heat to and through skin and the temperatures attained therein. A theoretical and an experimental investigation. *American Journal of Pathology*, 23, 531–549.
- Hepworth, D. G., Steven-fountain, A., Bruce, D. M., & Vincent, J. F. (2001). Affine versus non-affine deformation in soft biological tissues, measured by the reorientation and stretching of collagen fibres through the thickness of compressed porcine skin. *Journal of Biomechanics*, 34(3), 341–346.
- Hilliges, M., Weidner, C., Schmelz, M., Schmidt, R., Orstavik, K., Torebjork, E., et al. (2002). ATP responses in human C nociceptors. *Pain*, 98(1–2), 59–68.
- Hingorani, R. V., Provenzano, P. P., Lakes, R. S., Escarcega, A., & Vanderby, R. J. (2004). Nonlinear viscoelasticity in rabbit medial collateral ligament. *Annals of Biomedical Engineering*, 32, 306–312.
- Hoffman, A. H., Robichaud, D. R., & Grigg, P. (2003). *The effect of hydration upon the compliance properties of rat skin* (pp. 633–634). *Proceedings of the 2003 summer bioengineering conference*, Key Biscayne, FL.
- Hormann, H., & Schlebusch, H. (1971). Reversible and irreversible denaturation of collagen fibers. *Biochemistry*, 10(6), 932–937.
- Huang, D., Chang, T. R., Aggarwal, A., Lee, R. C., & Ehrlich, H. P. (1993). Mechanisms and dynamics of mechanical strengthening in ligament-equivalent fibroblast-populated collagen matrices. *Annals of Biomedical Engineering*, 21, 289.
- Hult, A. M., & Goltz, R. W. (1965). The measurement of elastin in human skin and its quantity in relation to age. *Journal of Investigative Dermatology*, 44, 408–412.
- Humphrey, J. D. (2003). Continuum thermomechanics and the clinical treatment of disease and injury. *Applied Mechanics Reviews*, 56(2), 231–260.
- Humphries, W. T., & Wildnauer, R. H. (1971). Thermomechanical analysis of stratum corneum. I. Technique. *The Journal of Investigative Dermatology*, 57(1), 32–37.
- Jacquemoud, C., Bruyere-Garnier, K., & Coret, M. (2007). Methodology to determine failure characteristics of planar soft tissues using a dynamic tensile test. *Journal of Biomechanics*, 40(2), 468–475.
- Jacques, S. L. (2006). Ratio of entropy to enthalpy in thermal transitions in biological tissues. *Journal of Biomedical Optics*, 11(4), 041108.

- James, N. C., & Richard, A. M. (1996). *Neurobiology of nociceptors*. Oxford: Oxford University Press.
- Jamison, C. E., Marangoni, R. D., & Glaser, A. A. (1968). Viscoelastic properties of soft tissue by discrete model characterization. *Journal of Biomechanics*, 1(1), 33–36.
- Jansen, L. H., & Rottier, P. B. (1958a). Comparison of the mechanical properties of strips of human abdominal skin excised from below and from above the umbilic. *Dermatologica*, 117(4), 252–258.
- Jansen, L. H., & Rottier, P. B. (1958b). Some mechanical properties of human abdominal skin measured on excised strips: A study of their dependence on age and how they are influenced by the presence of striae. *Dermatologica*, 117(2), 65–83.
- Jemec, G. B., Jemec, B., Jemec, B. I., & Serup, J. (1990). The effect of superficial hydration on the mechanical properties of human skin *in vivo*: Implications for plastic surgery. *Plastic and Reconstructive Surgery*, 85(1), 100–103.
- Johnson, T. E., Mitchell, M. A., Rico, P. J., Fletcher, D. J., Eurell, T. E., & Roach, W. P. (2001). Corneal and skin laser exposures from 1540 nm laser pulses, laser-tissue interactions XI: Photochemical, photothermal, and photomechanical. In D. D. Duncan, J. O. Hollinger & S. L. Jacques (Eds.), *SPIE* (pp. 222–229).
- Johnson, G. A., Tramaglini, D. M., Levine, R. E., Ohno, K., Choi, N.-Y., & Woo, S. L.-Y. (1994). Tensile and viscoelastic properties of human patellar tendon. *Journal of Orthopedic Research*, 12, 796–803.
- Jun, J. H., Harris, J. L., Humphrey, J. D., & Rastegar, S. (2003). Effect of thermal damage and biaxial loading on the optical properties of a collagenous tissue. *Journal of Biomechanical Engineering*, 125(4), 540–548.
- Karamzadeh, A. M., Wong, B. J. F., Milner, T. E., Dao, X., Tanenbaum, B. S., & Nelson, J. S. (1999). Temperature distributions in Nd:YAG (=1.32 mm) laser-irradiated cartilage grafts accompanied by cryogen spray cooling. *Proceedings—Society of Photo-Optical Instrumentation Engineers*, 3601, 422–433.
- Kauvar, A. N., Rosen, N., & Khrom, T. (2006). A newly modified 595-nm pulsed dye laser with compression handpiece for the treatment of photodamaged skin. *Lasers in Surgery and Medicine*, 38(9), 808–813.
- Kenedi, R. M., Gibson, T., Evans, J. H., & Barbenel, J. C. (1975). Tissue mechanics. *Physics in Medicine and Biology*, 20(3), 699–717.
- Khaled, A. R. A., & Vafai, K. (2003). The role of porous media in modeling flow and heat transfer in biological tissues. *International Journal of Heat and Mass Transfer*, 46(26), 4989–5003.
- Kirkpatrick, S. J., Duncan, D. D., & Fang, L. (2004). Low-frequency surface wave propagation and the viscoelastic behavior of porcine skin. *Proceedings of SPIE*, 5474, 127.
- Kirschstein, T., Büsselfberg, D., & Treede, R. D. (1997). Coexpression of heat-evoked and capsaicin-evoked inward currents in acutely dissociated rat dorsal root ganglion neurons. *Neuroscience Letters*, 231, 33–36.
- Klavuhn, K. G. (2001). *Epidermal protection: A comparative analysis of sapphire contact and cryogen spray cooling*. Lumenis Inc.
- Koerner, C., & Bergmann, H. W. (1998). Physical defects of the hyperbolic heat conduction equation. *Applied Physics A: Materials Science & Processing*, 67(4), 397–401.
- Kollar, L. P., & Springer, G. S. (2003). *Mechanics of composite structure*. Cambridge: Cambridge University Press.
- Komatsu, K., Sanctuary, C., Shibata, T., Shimada, A., & Botsis, J. (2007). Stress-relaxation and microscopic dynamics of rabbit periodontal ligament. *Journal of biomechanics*, 40(3), 634–644.
- Kondo, E., Yasuda, K., Kitamura, N., Kudoh, T., Minami, A., & Tohyama, H. (2005). The effect of electrothermal shrinkage on the biomechanical properties of the anterior cruciate ligament: An experimental study. *Arthroscopy*, 21(4), 448–456.

- Kono, T., Groff, W. F., Sakurai, H., Takeuchi, M., Yamaki, T., Soejima, K., et al. (2006). Evaluation of fluence and pulse-duration on purpuric threshold using an extended pulse pulsed-dye laser in the treatment of port wine stains. *The Journal of Dermatology*, 33(7), 473–476.
- Krishtal, O. A., & Pidoplichko, V. I. (1980). A receptor for protons in the nerve cell membrane. *Neuroscience*, 5, 2325–2327.
- Krishtal, O. A., & Pidoplichko, V. I. (1981). A receptor for protons in the membrane of sensory neurons may participate in nociception. *Neuroscience*, 6, 2599–2601.
- Kruger, L., Perl, E. R., & Sedivec, M. J. (1981). Fine structure of myelinated mechanical nociceptor endings in cat hairy skin. *The Journal of Comparative Neurology*, 198(1), 137–154.
- Kwan, M. K., Lin, T. H., & Woo, S. L. (1993). On the viscoelastic properties of the anteromedial bundle of the anterior cruciate ligament. *Journal of Biomechanics*, 26, 447–452.
- Lakes, R. S. (1998). *Viscoelastic solids*. New York: CRC Press.
- Lakes, R. S., & Vanderby, R. (1999). Interrelation of creep and relaxation: A modeling approach for ligaments. *Journal of Biomechanical Engineering, Transactions of the ASME*, 121, 612–615.
- Lanir, Y. (1979). The rheological behavior of the skin: Experimental results and a structural model. *Biorheology*, 16(3), 191–202.
- Lanir, Y. (1980). A microstructure model for the rheology of mammalian tendon. *Journal of Biomechanical Engineering, Transactions of the ASME*, 102, 332–339.
- Lanir, Y. (1987). Skin mechanics. In R. Skalak & S. Chien (Eds.), *Handbook of bioengineering* (pp. 11.11–11.25). New York: McGraw-Hill.
- Lanir, Y., & Fung, Y. C. (1974). Two-dimensional mechanical properties of rabbit skin. II. Experimental results. *Journal of Biomechanics*, 7(2), 171–182.
- Larrabee, W. F.Jr, (1986). A finite element model of skin deformation. I. Biomechanics of skin and soft tissue: A review. *Laryngoscope*, 96(4), 399–405.
- Ledoux, W. R., & Blevins, J. J. (2007). The compressive material properties of the plantar soft tissue. *Journal of Biomechanics*, 40, 2975–2981. doi:10.1016/j.biomech.2007.02.009.
- Le Lous, M., Cohen-Solal, L., Allain, J. C., Bonaventure, J., & Maroteaux, P. (1985). Age related evolution of stable collagen reticulation in human skin. *Connect Tissue Research*, 13, 145–155.
- Le Lous, M., Flandin, F., Herbage, D., & Allain, J.-C. (1982). Influence of collagen denaturation on the chemorheological properties of skin, assessed by differential scanning calorimetry and hydrothermal isometric tension measurement. *Biochimica et Biophysica Acta (BBA)—General Subjects*, 717(2), 295–300.
- Lemons, D. E., Chien, S., Crawshaw, L. I., Weinbaum, S., & Jiji, L. M. (1987). Significance of vessel size and type in vascular heat transfer. *The American Journal of Physiology*, 253(1 Pt 2), R128–135.
- Lennox, F. G. (1949). Shrinkage of collagen. *Biochimica et Biophysica Acta*, 3, 170–187.
- Li, J. T., Armstrong, C. G., & Mow, V. C. (1983). The effect of strain rate on mechanical properties of articular cartilage in tension. *Biomechanics Symposium ASME*, 117–120.
- Lin, H. C., Kwan, M. K., & Woo, S. L.-Y. (1987). On the Stress relaxation properties of anterior cruciate ligament (ACL). *Proceedings, ASME Adv Bioengineering*, 5–6.
- Lin, S. J., Lo, W., Tan, H. Y., Chan, J. Y., Chen, W. L., Wang, S. H., et al. (2006). Prediction of heat-induced collagen shrinkage by use of second harmonic generation microscopy. *Journal of Biomedical Optics*, 11(3), 34020.
- Lin, W., Motamedi, M. M., & Welch, A. J. (1996). Dynamics of tissue optics during laser heating of turbid media. *Applied Optics*, 35(19), 3413–3420.
- Liu, J., Chen, X., & Xu, L. X. (1999). New thermal wave aspects on burn evaluation of skin subjected to instantaneous heating. *IEEE Transactions on Biomedical Engineering*, 46(4), 420–428.
- Lubashevsky, I. A., & Gafiychuk, V. V. (2004). *Mathematical description of the heat transfer in living tissue (Part I)*. adap-org/9911001.
- Luescher, M., Ruegg, M., & Schindler, P. (1974). Effect of hydration upon the thermal stability of tropocollagen and its dependence on the presence of neutral salts. *Biopolymers*, 13(12), 2489–2503.

- Madigosky, W. M., & Lee, G. F. (1983). Improved resonance technique for materials characterization. *Journal of Acoustical Society of America*, 73, 1374–1377.
- Malcolm, D. T. K., Nielsen, P. M. F., Hunter, P. J., & Charette, P. G. (2002). Strain measurement in biaxially loaded inhomogeneous, anisotropic elastic membranes. *Biomechanics and Modeling of Mechanobiology*, 1, 197–210.
- Mano, J. F. (2005). Viscoelastic properties of bone: Mechanical spectroscopy studies on a chicken model. *Materials Science and Engineering C*, 25, 145–152.
- Mansour, J. M., Davis, B. R., Srour, M., & Theberge, R. (1991). Effects of ribose on the tensile behavior of skin: Application to a theory of aging. *Proceedings 1991 Biomechanics Symposium, ASME*, 299–302.
- Martel, H., Walker, D. C., Reed, R. K., & Bert, J. L. (2001). Dermal fibroblast morphology is affected by stretching and not by C48/80. *Connective Tissue Research*, 42, 235–244.
- McCleskey, E. W., & Gold, M. S. (1999). Ion Channels of Nociception. *Annual Review of Physiology*, 61, 835–856.
- McCrum, N. G., Read, B. E., & Williams, G. (1991). *Anelastic and dielectric effects in polymer solids*. New York: Dover Publications.
- McHugh, A. A., Fowlkes, B. J., Maeovsky, E. I., Smith, D. J., Jr., Rodriguez, J. L., & Garner, W. L. (1997). Biomechanical alterations in normal skin and hypertrophic scar after thermal injury. *The Journal of Burn Care & Rehabilitation*, 18(2), 104–108.
- Melling, M., Pfeiler, W., Karimian-Teherani, D., Schnallinger, M., Sobal, G., Zangerle, C., et al. (2000). Differential scanning calorimetry, biochemical, and biomechanical analysis of human skin from individuals with diabetes mellitus. *The Anatomical Record*, 59, 327–333.
- Meyer, R. A., Campbell, J. N., & Raja, S. N. (1994). Peripheral neural mechanisms of nociception. In P. D. Wall & R. Melzack (Eds.), *Textbook of pain* (pp. 13–44). London: Churchill Livingstone.
- Meyer, W., Kacza, J., Zschemisch, N. H., Godynicky, S., & Seeger, J. (2007). Observations on the actual structural conditions in the stratum superficiale dermidis of porcine ear skin, with special reference to its use as model for human skin. *Annals of Anatomy*, 189(2), 143–156.
- Meyer, W., Schwarz, R., & Neurand, K. (1978). The skin of domestic mammals as a model for the human skin, with special reference to the domestic pig. *Current Problems in Dermatology*, 7, 39–52.
- Meyer, W., Zschemisch, N. H., & Godynicky, S. (2003). The porcine ear skin as a model system for the human integument: Influences of storage conditions on basic features of epidermis structure and function—A histological and histochemical study. *Pol. J. Vet. Sci*, 6, 17–28.
- Middelkoop, E., Van den Bogaerd, A. J., Lamme, E. N., Hoekstra, M. J., Brandsma, K., & Ulrich, M. M. W. (2004). Porcine wound models for skin substitution and burn treatment. *Biomaterials*, 25(9), 1559–1567.
- Miles, C. A. (1993). Kinetics of collagen denaturation in mammalian lens capsules studied by differential scanning calorimetry. *International Journal of Biological Macromolecules*, 15(5), 265–271.
- Miles, C. A., & Bailey, A. J. (2001). Thermally labile domains in the collagen molecule. *Micron*, 32(3), 325–332.
- Miles, C. A., Burjanadze, T. V., & Bailey, A. J. (1995). The kinetics of the thermal denaturation of collagen in unrestrained rat tail tendon determined by differential scanning calorimetry. *Journal of Molecular Biology*, 245(4), 437–446.
- Miller, K., & Chinzei, K. (1997). Constitutive modelling of brain tissue: Experiment and theory. *Journal of Biomechanics*, 30(11–12), 1115–1121.
- Miller-Young, J. E., Duncan, N. A., & Baroud, G. (2002). Material properties of the human calcaneal fat pad in compression: Experiment and theory. *Journal of Biomechanics*, 35, 1523–1531.

- Minns, R. J., Soden, P. D., & Jackson, D. S. (1973). The role of the fibrous components and the ground substance in the mechanical properties of biological tissues: A preliminary investigation. *Journal of Biomechanics*, 6, 153–165.
- Mitra, K., Kumar, S., Vedavarz, A., & Moallemi, M. K. (1995). Experimental evidence of hyperbolic heat conduction in processed meat. *Journal of Heat Transfer, Transactions ASME*, 117(3), 568–573.
- Moon, D. K., Woo, S. L., Takakura, Y., Gabriel, M. T., & Abramowitch, S. D. (2006). The effects of refreezing on the viscoelastic and tensile properties of ligaments. *Journal of Biomechanics*, 39(6), 1153–1157.
- Moritz, A. R., & Henriquez, F. C. (1947). Study of thermal injuries II. The relative importance of time and source temperature in the causation of cutaneous burns. *American Journal of Pathology*, 23, 695–720.
- Morse, P. M., & Feshbach, H. (1953). *Methods of theoretical physics*. New York: McGraw-Hill.
- Mossberg, M., Hillström, L., & Söderström, T. (2001). Non-parametric identification of viscoelastic materials from wave propagation experiments. *Automatica*, 37, 511–521.
- Myers, B., McElhaney, J., Nightingale, R., & Doherty, B. (1991). Experimental Limitations of Quasi-Linear Theory, and a Method for Reducing These Effects. *ASME Advances in Bioengineering, BED-20*, 139–142.
- Myllyharju, J., & Kivirikko, K. I. (2004). Collagens, modifying enzymes and their mutations in humans, flies and worms. *Trends in Genetics*, 20, 33–43.
- Nagy, I., & Rang, H. (1999). Noxious heat activates all capsaicin-sensitive and also a sub-population of capsaicin-insensitive dorsal root ganglion neurons. *Neuroscience*, 88(4), 995–997.
- Nagy, I., & Rang, H. P. (1999). Similarities and differences between the responses of rat sensory neurons to noxious heat and capsaicin. *The Journal of Neuroscience*, 19(24), 10647–10655.
- Nasseri, S., Bilston, L., & Tanner, R. (2003). Lubricating squeezing flow: A useful method for measuring the viscoelastic properties of soft tissues. *Biorheology*, 40, 545–551.
- Nielsen, L. F., Wismer, N. J., & Gade, S. (2000). Improved method for complex modulus estimation. *Journal of Sound and Vibration*, 34, 20–24.
- Nigul, I., & Nigul, U. (1987). On algorithms of evaluation of fung's relaxation function parameters. *Journal of Biomechanics*, 20(4), 343–352.
- Nishimura, M., Yan, W., Mukudai, Y., Nakamura, S., Nakamasu, K., Kawata, M., et al. (1998). Role of chondroitin sulfate-hyaluronan interactions in the viscoelastic properties of extracellular matrices and fluids. *Biochimica et Biophysica Acta*, 1380, 1–9.
- Oomens, C. W., van Campen, D. H., & Grootenhoefer, H. J. (1987). In vitro compression of a soft tissue layer on a rigid foundation. *Journal of Biomechanics*, 20(10), 923–935.
- Oomens, C. W. J., Van Campen, D. H., Grootenhoefer, H. J., & De Boer, L. J. (1984). Experimental and theoretical compression studies on porcine skin.. *Biomechanics: Current interdisciplinary research, selected proceedings of meetings of European society of biomechanics*, 227–232.
- Overgaard, O. L., & Jemec, G. B. (1993). The influence of water, glycerin, paraffin oil and ethanol on skin mechanics. *Acta Dermato-Venereologica*, 73(6), 404–406.
- Oyadji, S. O., & Tomlinson, G. R. (1985). Determination of the complex moduli of viscoelastic structural elements by resonance and non-resonance methods. *Journal of Sound and Vibrations*, 101, 277–298.
- Oyen, M. L., Cook, R. F., Stylianopoulos, T., Barocas, V. H., Calvin, S. E., & Landers, D. L. (2005). Uniaxial and biaxial mechanical behavior of human amnion. *Journal of Materials Research*, 20, 2902–2909.
- Ozawa, T. (1970). Kinetic analysis of derivatives curves in thermal analysis. *Journal of Thermal Analysis and Calorimetry*, 2, 301–324.
- Ozisik, M. N. (1993). *Heat conduction*. New York: John Wiley & Sons, Inc.

- Ozisik, M. N., & Tzou, D. Y. (1994). On the wave theory in heat conduction. *ASME Journal of Heat Transfer*, 116, 526–535.
- Papapoutian, A., Peier, A. M., Story, G. M., & Viswanath, V. (2003). Thermo TRP channels and beyond: Mechanisms of temperature sensation. *Nature Reviews Neuroscience*, 4(8), 529–539.
- Pearce, J., Thomsen, S., Vijverberg, H., & McMurray, T. (1993). Kinetics of birefringence changes in thermally coagulated rat skin collagen. *Proceedings of SPIE*, 180–186.
- Pennes, H. H. (1948). Analysis of tissue and arterial blood temperatures in the resting human forearm. *Journal of Applied Physiology*, 1, 93–122.
- Pereira, J. M., Mansour, J. M., & Davis, B. R. (1991). Dynamic measurement of the viscoelastic properties of skin. *Journal of Biomechanics*, 24(2), 157–162.
- Perry, S. W. (1984). Undermedication for pain on a burn unit. *General Hospital Psychiatry*, 6, 308–316.
- Peshkov, V. (1944). Second sound in helium II. *Journal of Physics*, 8, 381–382.
- Picton, P. D., Campbell, J. A., & Turner, S. J. (2001). Modelling chronic pain: An initial survey. In L. Zhang & F. Gu (Eds.), *Proceedings of 8th international conference on neural information processing* (pp. 1267–1270). Shanghai, China: Fudan University Press.
- Pierard, G. E. (1999). EEMCO guidance to the *in vivo* assessment of tensile functional properties of the skin—Part 1: Relevance to the structures and ageing of the skin and subcutaneous tissues. *Skin Pharmacology and Applied Skin Physiology*, 12(6), 352–362.
- Pierard, G. E., Letawe, C., Dowlati, A., & Pierard-Franchimont, C. (1995). Effect of hormone replacement therapy for menopause on the mechanical properties of skin. *Journal of American Geriatric Society*, 43(6), 662–665.
- Pierard, G. E., Nikkels-Tassoudji, N., & Pierard-Franchimont, C. (1995). Influence of the test area on the mechanical properties of skin. *Dermatology (Basel, Switzerland)*, 191(1), 9–15.
- Pierce, M. C., Sheridan, R. L., Park, B. H., Cense, B., & De Boer, J. F. (2004). Collagen denaturation can be quantified in burned human skin using polarization-sensitive optical coherence tomography. *Burns*, 30, 511–517.
- Pietrucha, K. (2005). Changes in denaturation and rheological properties of collagen-hyaluronic acid scaffolds as a result of temperature dependencies. *International Journal of Biological Macromolecules*, 36(5), 299–304.
- Pioletti, D. P., & Rakotomanana, L. R. (2000). On the independence of time and strain effects in the stress relaxation of ligaments and tendons. *Journal of Biomechanics*, 33(12), 1729–1732.
- Potts, R. O., & Breuer, M. M. (1981). *The low strain viscoelastic properties of skin*. 3rd International symposium bioengineering and the skin, Philadelphia, PA.
- Provenzano, P., Lakes, R., Keenan, T., & Vanderby, J. R. (2001). Nonlinear ligament viscoelasticity. *Annals of Biomedical Engineering*, 29(10), 908–914.
- Purslow, P. P., Wess, T. J., & Hukins, D. W. L. (1998). Collagen orientation and molecular spacing during creep and stress-relaxation in soft connective tissues. *Journal of Experimental Biology*, 201(1), 135–142.
- Puso, M. A., & Weiss, J. A. (1998). Finite element implementation of anisotropic quasilinear viscoelasticity using a discrete spectrum approximation. *ASME Journal of Biomechanical Engineering*, 120, 62–70.
- Pustovalov, V. K., & Jean, B. (2007). Melanin granule models for the processes of laser-induced thermal damage in pigmented retinal tissues. I. Modeling of laser-induced heating of melanosomes and selective thermal processes in retinal tissues. *Bulletin of Mathematical Biology*, 69(1), 245–263.
- Ranu, H. S., Burlin, T. E., & Hutton, W. C. (1975). The effects of x-irradiation on the mechanical properties of skin. *Physics in Medicine and Biology*, 20(1), 96–105.
- Rehsner, R., Balogh, B., & Menzel, E. J. (1995). Two-dimensional elastic properties of human skin in terms of an incremental model at the *in vivo* configuration. *Medical Engineering & Physics*, 17(4), 304–313.

- Reihnsner, R., Melling, M., Pfeiler, W., & Menzel, E. J. (2000). Alterations of biochemical and two-dimensional biomechanical properties of human skin in diabetes mellitus as compared to effects of in vitro non-enzymatic glycation. *Clinical Biomechanics*, 15, 379–386.
- Reuck, A. V. S., & Knight, J. (1966). *Touch, heat and pain*. London: Churchill Ltd.
- Rigby, R. B., Hirai, R., Spikes, J. D., & Eyring, H. (1959). The mechanical properties of rat tail tendon. *Journal of Genetic Physiology*, 43, 265–283.
- Rochdi, A., Foucat, L., & Renou, J. P. (1999). Effect of thermal denaturation on water-collagen interactions: NMR relaxation and differential scanning calorimetry analysis. *Biopolymers*, 50, 690–696.
- Roetzel, W., & Xuan, Y. (1998). Transient response of the human limb to an external stimulus. *International Journal of Heat and Mass Transfer*, 41(1), 229–239.
- Rubin, L. R. (1948). Langer's lines and facial scars. *Plastic and Reconstructive Surgery*, 3, 147–155.
- Sacks, M. S., & Sun, W. (2003). Multiaxial mechanical behavior of biological materials. *Annual Reviews of Biomedical Engineering*, 5, 251–284.
- Sanjeevi, R., Somanathan, N., & Ramaswamy, D. (1982). A viscoelastic model for collagen fibres. *Journal of Biomechanics*, 15(3), 181–183.
- Carver, J. J., Robinson, P. S., & Elliott, D. M. (2003). Methods for quasi-linear viscoelastic modeling of soft tissue: Application to incremental stress-relaxation experiments. *Journal of Biomechanical Engineering*, 125(5), 754–758.
- Sasaki, N., Shukunami, N., Matsushima, N., & Izumi, Y. (1999). Time-resolved X-ray diffraction from tendon collagen during creep using synchrotron radiation. *Journal of Biomechanics*, 32(3), 285–292.
- Schiller, R., Funke, A. P., & Gunther, C. (2004). DSC measurements on full thickness mice skin: An additional tool to investigate permeation enhancement of highly lipophilic drugs. *Journal of Thermal Analysis and Calorimetry*, 77(2), 497–510.
- Sejrsen, P. (1972). Measurement of cutaneous blood flow by freely diffusible radioactive isotopes. *Danish Medical Bulletin*, 18, 1–38.
- Shafirstein, G., Baumler, W., Lapidoth, M., Ferguson, S., North, P. E., & Waner, M. (2003). *Laser tissue interaction modeling for treatment planning of port-wine stain* (pp. 313–315). Tucson, AZ: Institute of Electrical and Electronics Engineers, Inc.
- Shergold, O. A. (2004). *The mechanics of needle-free injection*. Cambridge: University of Cambridge.
- Shergold, O. A., & Fleck, N. A. (2005). Experimental investigation into the deep penetration of soft solids by sharp and blunt punches, with application to the piercing of skin. *Journal of Biomechanical Engineering*, 127(5), 838–848.
- Shergold, O. A., Fleck, N. A., & Radford, D. (2006). The uniaxial stress versus strain response of pig skin and silicone rubber at low and high strain rates. *International Journal of Impact Engineering*, 32(9), 1384–1402.
- Shih, T.-C., Kou, H.-S., Liauh, C.-T., & Lin, W.-L. (2005). The impact of thermal wave characteristics on thermal dose distribution during thermal therapy: A numerical study. *Medical Physics*, 32(9), 3029–3036.
- Shipton, E. A., & Tait, B. (2005). Flagging the pain: Preventing the burden of chronic pain by identifying and treating risk factors in acute pain. *European journal of Anaesthesiology*, 22(6), 405–412.
- Silver, F. H., Christiansen, D. L., Snowhill, P. B., & Chen, Y. (2000). Role of storage on changes in the mechanical properties of tendon and self-assembled collagen fibers. *Connective Tissue Research*, 41(2), 155–164.
- Silver, F. H., Freeman, J. W., & DeVore, D. (2001). Viscoelastic properties of human skin and processed dermis. *Skin Research Technology*, 7(1), 18–23.
- Silver, F. H., Horvath, I., & Foran, D. J. (2001). Viscoelasticity of the vessel wall: The role of collagen and elastic fibers. *Critical Reviews in Biomedical Engineering*, 29(3), 279–301.

- Silver, F. H., Kato, Y. P., Ohno, M., & Wasserman, A. J. (1992). Analysis of mammalian connective tissue: Relationship between hierarchical structures and mechanical properties. *Journal of Long Term Effects of Medical Implants*, 2(2–3), 165–198.
- Silver, F. H., Siperko, L. M., & Seehra, G. P. (2003). Mechanobiology of force transduction in dermal tissue. *Skin Research and Technology*, 9(1), 3–23.
- Simon, B. R., Coats, R. S., & Woo, S. L.-Y. (1984). Relaxation and creep quasilinear viscoelastic models for normal articular cartilage. *ASME Journal of Biomechanical Engineering*, 106, 159–164.
- Smalls, L. K., Wickett, R. R., & Visscher, M. O. (2006). Effect of dermal thickness, tissue composition, and body site on skin biomechanical properties. *Skin Research and Technology*, 12(1), 43–49.
- Sobel, E., Sviridov, A., Omel'chenko, A., Bagratashvili, V., Kitai, M., Harding, S. E., et al. (2000). Laser reshaping of cartilage. *Biotechnology & Genetic Engineering Reviews*, 17, 553–578.
- Srinivas, S. M., de Boer, J. F., Park, H., Keikhanzadeh, K., Huang, H. E., Zhang, J., et al. (2004). Determination of burn depth by polarization-sensitive optical coherence tomography. *Journal of Biomedical Optics*, 9(1), 207–212.
- Stanczyk, M., & Telega, J. J. (2002). Modelling of heat transfer in biomechanics—A review. Part I. Soft tissues. *Acta Bioengineering Biomechanics*, 4(1), 31–61.
- Stoop, R., van der Kraan, P. M., Buma, P., Hollander, A. P., Poole, A. R., & van den Berg, W. B. (1999). Denaturation of type II collagen in articular cartilage in experimental murine arthritis. Evidence for collagen degradation in both reversible and irreversible cartilage damage. *The Journal of Pathology*, 188(3), 329–337.
- Taitel, Y. (1972). On the parabolic, hyperbolic and discrete formulation of the heat conduction equation. *International Journal of Heat and Mass Transfer*, 15(2), 369–371.
- Tang, D. W., & Araki, N. (1996). The wave characteristics of thermal conduction in metallic films irradiated by ultra-short laser pulses. *Journal of Physics D: Applied Physics*, 29, 2527–2533.
- Thomsen, S. (1991). Pathologic analysis of photothermal and photomechanical effects of laser-tissue interactions. *Photochemistry and Photobiology*, 53(6), 825–835.
- Thornton, G. M., Olijnyk, A., Frank, C. B., & Shriven, N. G. (1997). Ligament creep cannot be predicted from stress relaxation at low stress: A biomechanical study of the rabbit medial collateral ligament. *Journal of Orthopaedic Research*, 15(5), 652–656.
- Tillman, D. B., Treede, R. D., Meyer, R. A., & Campbell, J. N. (1995a). Response of C fibre nociceptors in the anaesthetized monkey to heat stimuli: Correlation with pain threshold in humans. *Journal of Physiology*, 485(Pt 3), 767–774.
- Tillman, D. B., Treede, R. D., Meyer, R. A., & Campbell, J. N. (1995b). Response of C fibre nociceptors in the anaesthetized monkey to heat stimuli: Estimates of receptor depth and threshold. *The Journal of Physiology*, 485(Pt 3), 753–765.
- Torvi, D. A., & Dale, J. D. (1994). A finite element model of skin subjected to a flash fire. *Journal of Biomechanics Engineering*, 116(3), 250–255.
- Tregear, R. T. (1966). *Physical functions of the skin*. New York: Academic Press.
- Tregear, R. T., & Dirnhuber, P. (1965). Viscous flow in compressed human and rat skin. *Journal of Investigative Dermatology*, 45, 119–125.
- Tsubouchi, K., Enosawa, S., Harada, K., Okamoto, J., Fujie Masakatsu, G., & Chiba, T. (2006). Evaluation of the relationship between the viscoelastic stress and strain of fetal rat skin as a guide for designing the structure and dynamic performance of a manipulator for fetal surgery. *Surgery Today*, 36(8), 701–706.
- Tzou, D. Y. (1992). Thermal shock phenomena under high-rate response in solids. In C. L. Tien (Ed.), *Annual review of heat transfer* (pp. 111–185). Washington, DC: Hemisphere.
- Tzou, D. Y. (1993). An engineering assessment to the relaxation time in thermal wave propagation. *International Journal of Heat and Mass Transfer*, 36(7), 1845–1851.

- Tzou, D. Y. (1995a). A unified field approach for heat conduction from macro- to micro-scales. *Journal of Heat Transfer, Transactions ASME*, 117(1), 8–16.
- Tzou, D. Y. (1995b). Experimental support for the lagging behavior in heat propagation. *Journal of Thermophysics and Heat Transfer*, 9, 686–693.
- Tzou, D. Y. (1997). *Macro- to micro-scale heat transfer: The lagging behavior*. Washington, DC: Taylor and Francis.
- Tzou, D. Y., Ozisik, M. N., & Chiffelle, R. J. (1994). The lattice temperature in the microscopic two-step model. *Journal of Heat Transfer*, 116, 1034–1038.
- Urban, J. P. G., Maroudas, A., Bayliss, M. T., & Dillon, J. (1979). Swelling pressures of proteoglycans at the concentrations found in cartilagenous tissues. *Biorheology*, 16, 447–464.
- Van Hees, J., & Gybels, J. (1981). C nociceptor activity in human nerve during painful and non painful skin stimulation. *Journal of Neurology, Neurosurgery, and Psychiatry*, 44(7), 600–607.
- van Loey, N. E., & van Son, M. J. (2003). Psychopathology and psychological problems in patients with burn scars: Epidemiology and management. *American Journal of Clinical Dermatology*, 4, 245–272.
- Vernotte, P. (1958). Les paradoxes de la theorie continue de l'équation de la chaleur. *Compute Rendus*, 246, 3154–3155.
- Veronda, D. R., & Westmann, R. A. (1970). Mechanical characterization of skin-finite deformations. *Journal of Biomechanics*, 3(1), 111–124.
- Vogel, H. G. (1971). Antagonistic effect of aminoacetonitrile and prednisolone on mechanical properties of rat skin. *Biochimica et Biophysica Acta*, 252(3), 580–585.
- Vogel, H. G. (1976). Tensile strength, relaxation and mechanical recovery in rat skin as influenced by maturation and age. *Journal of Medicine*, 7, 177–188.
- Vogel, H. G. (1988). Age dependent mechanical and biochemical changes in the skin. *Bioengineering of the Skin*, 4, 75–81.
- Vogel, H. G. (1994). Mechanical measurements of skin. *Acta Dermato-Venereologica. Supplementum (Stockh)*, 185, 39–43.
- Vogel, H. G., & Hilgner, W. (1979a). Influence of age and of desmotropic drugs on the step phenomenon observed in rat skin. *Archives of Dermatological Research*, 264(2), 225–241.
- Vogel, H. G., & Hilgner, W. (1979b). The step phenomenon as observed in animal skin. *Journal of Biomechanics*, 12(1), 75–81.
- Waldmann, R. (2001). Proton-gated cation channels--neuronal acid sensors in the central and peripheral nervous system. *Advances in Experimental Medicine and Biology*, 502, 293–304.
- Wan, A. W. (1994). Biaxial tension test of human skin *in vivo*. *Bio-medical Materials and Engineering*, 4, 473–486.
- Waxman, S. G., Dib-Hajj, S., Cummins, T. R., & Black, J. A. (1999). Sodium channels and pain. *Proceedings of the National Academy of Sciences of the United States of America*, 96, 7635–7639.
- Wegst, U. G. K., & Ashby, M. F. (2004). The mechanical efficiency of natural materials. *Philosophical Magazine*, 84(21), 2167–2181.
- Weinbaum, S., Jiji, L. M., & Lemons, D. E. (1984). Theory and experiment for the effect of vascular microstructure on surface tissue heat transfer—Part I: Anatomical foundation and model conceptualization. *Journal of Biomechanics Engineering*, 106(4), 321–330.
- Weir, C. E. (1949). Rate of shrinkage of tendon collagen-heat, entropy, and free energy of activation of the shrinkage of untreated tendon. Effect of acid, salt, pickle, and tannage on the activation of tendon collagen. *Journal of American Leather Chemical Association*, 44, 108–140.
- Wells, P. B. (2005). *Thermal alteration of collagenous tissue subjected to biaxial isometric constraints*. Texas: Texas A&M University.
- Wells, P. B., Harris, J. L., & Humphrey, J. D. (2004). Altered mechanical behavior of epicardium under isothermal biaxial loading. *Journal of Biomechanical Engineering*, 126, 492–497.

- Wells, S. M., Langille, B. L., Lee, J. M., & Adamson, S. L. (1999). Determinants of mechanical properties in the developing ovine thoracic aorta. *The American Journal of Physiology*, 277(4 Pt 2), H1385–1391.
- Whitton, J. T., & Everall, J. D. (1973). The thickness of the epidermis. *British Journal of Dermatology*, 89, 467–476.
- Wilkes, G. L., Brown, I. A., & Wildnauer, R. H. (1973). The biomechanical properties of skin. *CRC Critical Reviews in Bioengineering*, 1(4), 453–495.
- Wissler, E. H. (1998). Pennes' 1948 paper revisited. *Journal of Applied Physiology*, 85(1), 35–41.
- Wong, B. J. F., Milner, T. E., Anvari, B., Sviridov, A., Omel'chenko, A., Bagratashvili, V., et al. (1998). Measurement of radiometric surface temperature and integrated backscattered light intensity during feedback controlled laserassisted cartilage reshaping. *Lasers Med Sci*, 13, 66–72.
- Wong, B. J. F., Milner, T. E., Kim, H. K., Telenkov, S., Chew, C. F., Sobol, E. N., et al. (1999). Characterization of temperature dependent biophysical properties during laser mediated cartilage reshaping. *IEEE Journal of Selected Top Quantum Electron*, 5, 1095–1102.
- Woo, S. L.-Y., Simon, B. R., Kuei, S. C., & Akeson, W. H. (1980). Quasi-linear viscoelastic properties of normal articular cartilage. *ASME Journal of Biomechanics Engineering*, 102, 85–90.
- Wright, N. T. (2003). On a relationship between the Arrhenius parameters from thermal damage studies. *Journal of Biomechanical Engineering*, 125, 300–304.
- Wright, N. T., & Humphrey, J. D. (2002). Denaturation of collagen via heating: An irreversible rate process. *Annual Review of Biomedical Engineering*, 4, 109–128.
- Wright, D. M., Wiig, H., Winlove, C. P., Bert, J. L., & Reed, R. K. (2003). Simultaneous measurement of interstitial fluid pressure and load in rat skin after strain application in vitro. *Annals of Biomedical Engineering*, 31(10), 1246–1254.
- Wu, J. Z., Cutlip, R. G., Andrew, M. E., & Dong, R. G. (2007). Simultaneous determination of the nonlinear-elastic properties of skin and subcutaneous tissue in unconfined compression tests. *Skin Research and Technology*, 13(1), 34–42.
- Wu, J. Z., Cutlip, R. G., Welcome, D., & Dong, R. G. (2006). Estimation of the viscous properties of skin and subcutaneous tissue in uniaxial stress relaxation tests. *Bio-Medical Materials and Engineering*, 16(1), 53–66.
- Wu, J. Z., Dong, R. G., Smutz, W. P., & Schopper, A. W. (2003). Non-linear and viscoelastic characteristics of skin under compression: Experiment and analysis. *Bio-Medical Materials and Engineering*, 13(4), 373–385.
- Xu, F., Lu, T. J., & Seffen, K. A. (2008). Skin thermal pain modeling: A holistic method. *Journal of Thermal Biology*, 33(4), 223–237.
- Xu, F., Seffen, K. A., & Lu, T. J. (2008). Non-Fourier analysis of skin biothermomechanics. *International Journal of Heat and Mass Transfer*, 51, 2237–2259.
- Xu, F., Wen, T., Lu, T. J., & Seffen, K. A. (2008). Modelling of nociceptor transduction in skin thermal pain sensation. *Journal of Biomechanical Engineering*, 130, 1–13.
- Xu, F., Wen, T., Seffen, K. A., & Lu, T. J. (2008). Biothermomechanics of skin tissue. *Journal of the Mechanics and Physics of Solids*, 56(5), 1852–1884.
- Yamashita, J., Li, X., Furman, B. R., Rawls, H. R., Wang, X., & Agrawal, C. M. (2002). Collagen and bone viscoelasticity: A dynamic mechanical analysis. *J Biomed Mater Res*, 63(1), 31–36.
- Yang, W., Fung, T. C., Chian, K. S., & Chong, C. K. (2006). Viscoelasticity of esophageal tissue and application of a QLV model. *Journal of Biomechanical Engineering, Transactions of the ASME*, 128(6), 909–916.
- Yip, C. P., Walker, D., Fernlund, G., & Pinder, K. (2007). Role of dermal fibroblasts in rat skin tissue biomechanics. *Bio-Medical Materials and Engineering*, 17(2), 109–117.
- Young, G. S. (1998). Thermodynamic characterization of skin, hide and similar materials composed of fibrous collagen. *Studies in Conservation*, 43(2), 65–79.
- Ziegert, J. C., & Lewis, J. L. (1978). *In vivo* mechanical properties of soft tissue covering bony prominences. *Journal of Biomechanical Engineering, Transactions of the ASME*, 100, 194–201.

Subject Index

- A/D conversion, 191
- Armchair CNT
- Brenner potential *vs.* mR/L for, 51–52
 - buckling strain based on Brenner potential for, 54
 - critical external pressure for bifurcation
 - for (*see* Critical external pressure for bifurcation for armchair CNT)
 - critical strain for, 55–56
 - critical twist for bifurcation for, 61–62
 - degree of anisotropy *vs.* radius of, 24
 - energy (per atom) *vs.* radius for, 43
 - Arrhenius burn integration, 157
 - Arrhenius parameters, 157–158, 198–200
 - Atomistic-based shell theory, 6–7, 62–63
 - Axial strain, 43, 51, 53
 - Axisymmetric bifurcation, 50
 - and compression, 54
 - critical strain for, 52–53
 - Bars in tensegrity structure, 81
 - Bending moment/curvature ratio, 49–50
 - Biaxial mechanical testing, 187
 - Bifurcation
 - axisymmetric, 50
 - non-axisymmetric, 52–53
 - onset of, 54
 - Bravais lattice, 12
 - Buckling strain, 53–54
 - Calladine’s analysis, 77
 - Carbon nanotube
 - based on interatomic potential, finite-deformation shell theory for curved surface, 34–35
 - deformation, 36–38
 - membrane strains and curvatures, 35–36
 - membrane stresses and moments, 38–42
 - based on interatomic potential, linear shell theory for
 - constitutive relations, 21–24
 - equilibrium equations, 25
 - membrane strains and curvatures, 18–21
 - bending of, 49
 - buckling
 - critical buckling loads, 32–33
 - external pressure, 32
 - torsion, 31–32
 - uniaxial compression, 31
 - as classical linear elastic isotropic shells, 4
 - continuum models for
 - vs.* constitutive model, 5–6
 - continuum shell modeling of on interatomic potential. (*see* Interatomic potential)
 - shell thickness in prior, 17
 - type-I continuum model, 4–5
 - type-II continuum model, 5
 - defect nucleation in, 5
 - hexagonal lattice structure, 20
 - instability, 49
 - in compression, 53–56
 - subject to external pressure, 58–60
 - subject to internal pressure, 56–58
 - in tension, 50–53
 - in torsion, 60–62
 - linear elastic structural response to
 - bending, 27–30
 - internal/external pressure, 27
 - torsion, 27

- Carbon nanotube (*cont.*)
 uniaxial tension, 26–27
 mechanical behavior, atomistic
 studies of, 3
 pressure of, 45–47
 prior to deformation, 3
 rigidity tensors for, 26
 structural response of, 6
 tension of, 43–45
 torsion of, 47–49
- Cauchy–Born rule, 12
- Cauchy membrane stress tensor, 39–40
- Clamp designed for tensile tests, 190
- CNT. *See* Carbon nanotube
- Collagen
 in dermis, 154–155
 shrinkage of, 161
 thermal denaturation, 160–161
 thermal stability in pig skin
 sample, 187
 Type I, 154, 159
 Type III, 154
 Type IV, 155
- Compressive stress–stretch response, skin tissue, 205
- Constitutive model, 6
- Constrained particle dynamics
 technique, 119
- Constructivist art, 71–72
- Continuum models
 type-I, 4–5
 type-II, 5
- Controllable tensegrity structures,
 85, 119
 challenges for
 electroactive polymer (EAP)
 materials, 136–137
 piezoelectric and magnetostrictive
 actuators, 137–138
 requirement for actuation, 134–135
 shape memory alloys (SMA), 136
 servomotors, 135–136
 control design, 117–118
- Critical external pressure for
 bifurcation for armchair CNT
 based on Brenner potential *vs.* L/(mR),
 58, 60
- based on second-generation interatomic potential, 58–59
- Critical strain
 for axisymmetric bifurcation, 52
 for bifurcation in compression, 55
 for bifurcation in tension based on second-generation potential, 53–54
 for non-axisymmetric bifurcation, 52–53
- Critical twist for bifurcation, 61–62
- Curved surface, general description of, 34–35
- Cytoskeleton, 126
- Data acquisition system, 191
- Defect nucleation in CNT, 5
- Deformed configuration
 constitutive relation for, 40
 moment tensor for, 39–40
 tension, bending, and coupling
 rigidities in, 41
- Deformed surface
 base vectors for, 35
 point on, 36
- Degree of coupling, 22–23
- Dermis, 152–153
 collagen in, 154–155, 159
 elastin in, 155
- Differential scanning calorimetry tests, 186–187
- DMA. *See* Dynamic mechanical analysis
- Dual-phase-lag (DPL) model, 166–167
- Dynamical structures, 85, 117
- Dynamic mechanical analysis, 195–196
- Dynamic viscoelasticity
 for flank skin sample, 227–228
 loss modulus, 227–228
 storage modulus, 227
 and thermal denaturation, 227, 229
- EAP. *See* Electroactive polymers
- Elastic (equilibrium) stress fraction,
 variation of, 221–222
- Elastin in dermis, 155
- Electroactive polymers, 136–137
- Energy-harvesting devices, 71, 134
- Environmental chamber, 188
- Equilibrium equations, 25

- incremental form, 42, 63–64
linear shell theory for CNT, 25
for membrane stress, 39–42
Euler beam buckling, 54
- Finite-deformation shell theory, 5, 34–49
- Flight simulators
control problem for, 122–123
motion base for, 120
statics analysis of, 122
- Force-density method, 94
- Force transducers, 190
- Fourier bioheat transfer model of skin tissue, 151, 163–164
- Frames, equilibrium and stiffness of, 76–77
- Glycoproteins, 155, 224
- Graphene
based on interatomic potential, plate theory for
bending rigidity, 16–17
bond angle, 10–11
bond angle between bonds, 14
bond energy, 14–15
Bravais sublattices, 12–13
in-plane membrane strain and curvature, 12–13
membrane stress, 16
multibody atomistic interactions, 11–12
strain energy density, 15–16
bending rigidity of, 42–43
- Graphene sheet
carbon atoms inside, 2–3
rolling into CNT, 42
wrapped seamlessly to CNT, 4
- Green strain, components of, 36–37
- Ground substance
role in viscoelastic behavior
of dermis, 224
skin structure, 155
- Heat conduction, wave behavior in, 165
- Human skin tissue
- ethical and immunological issues associated with, 182
structure, 152–153
- Hyaluronic acid, 155, 212
- Hydrothermal compressive system, 194–195
- Hydrothermal compressive test procedure, 195
- Hydrothermal isometric tension (HIT) testing, 182
- Hydrothermal relaxation test procedure, 194
- Hydrothermal tensile system
data acquisition system, 191
design, 187–188
loading system, 189–190
testing chamber, 188–189
validation
heating conditions, 191–192
tissue-like phantom experiment for, 192–193
- Hydrothermal tensile test procedure, 193
- Hydroxyproline, 159
- Hyperbolic heat conduction, 164
- Interatomic potential
for carbon
bond angle, 10–11
bond angle between bonds, 14
bond energy, 14–15
bond order, 7–8
Bravais sublattices, 12–13
multibody atomistic interactions, 11–12
second-generation, 8–10
strain energy density, 15–16
- linear shell theory for carbon nanotubes
based on
constitutive relations, 21–24
equilibrium equations, 25
membrane strains and curvature, 18–21
- Internal pressure
and CNT deformation, 45
vs. engineering strain, 46
instability of CNT subject to, 56–58

- Internal pressure (*cont.*)
 limit, 45–46
 and pressure/strain ratio, 46–47
- Joints-free structures, 75
- KHR solution, 188
- Krebs–Henseleit Ringer (KHR), 183
- Linear dynamical feedback controllers, 118
- Linearized dynamical models, 104
- Linear matrix inequalities techniques, 118
- Linear shell theory
 anisotropy effects, 23–24
 bond length and angle, 20–21
 and continuum theory, 19
 curvature terms, 20
 degree of coupling *vs.* CNT radius, 23
 equilibrium equations, 25
 point on CNT, 18–19
 strain energy density, 21–22
- LMIs. *See* Linear matrix inequalities techniques
- Loading system, 189–190
- Magnetostrictive actuators, 137–138
- Mechanical preconditioning of skin samples, 185–186
- Membrane strain tensor, 38
- Membrane stress, 16, 22
 in CNT, 38–39
 equilibrium equations for, 39–42
- Moment tensor, 38–40
- Motion simulation, 118–119
- Mucopolysaccharides, 155
- Needle Tower, 72
- Nociceptors
 stimuli at location, 178, 180
 temperature history, 177, 179
- Nonaxisymmetric bifurcation
 CNT lengths and, 58
 critical strain for, 52–53
- Non-Fourier models, 151, 164
- Nonlinear solvers, prestressable configurations, 94
- Normalized relaxation function, 222
- Ogden model, 181
- One-layer Fourier model, 163–164
 temperature prediction, 173–174
 thermal damage prediction, 174
 thermophysical properties of skin tissue for, 173
- Optimization form-finding method, 119
- Pennes bioheat equation, 156
- Pennes model, 163–164
- Piezoactuators, 137
- Pig skin tissue, 182–183
- Pin-jointed cylindrical truss structures, 80–81
- Piola–Kirchhoff membrane stress tensor, 38
- Pressure/strain ratio, 46–47
- Proteoglycans, 155
- Proto-tensegrity sculpture, 72–73
- Quasilinear viscoelastic (QLV) theory development, 216–217
 skin model development based on, 217–219
 verification, 220–221
- Relaxation behavior, 214
 collagen, 223–224
 components of skin dermis, 222–223
 elastin, 223
 ground substance role in, 224
 under hyperthermal temperatures, 221
 quasilinear viscoelastic theory, 216–217
 skin model development, 217–219
 verification, 220–221
- temperature and thermal denaturation effects, 225
 uniaxial stress–time response, 219
 variation of elastic fraction, 221–222
- Sample preparation techniques
 material axis identification, 186
 mechanical preconditioning, 185–186
 predamage of samples, 184–185
 sample cutting, 184
 sample measurements, 184

- sample procurement, 183
selection of samples, 182–183
- Second-generation interatomic potential
vs. bond length, 8–10
CNT radius in, 23
critical strain for bifurcation in
compression based on, 55
- Servomotors, 135–136
- Shape memory alloys, 136
- Shear rigidity, 16
- Single-wall carbon nanotube
degree of coupling *vs.* radius, 23–24
modeling as thin shell, order of errors, 25
buckling loads, 32–33
external pressure, 32
linear elastic structural response,
26–30
rigidity tensors, 26
torsion, 31–32
uniaxial compression, 31
- radius, 23
structure, 2–3
- Skin bioheat transfer, 155
factors influencing, 156
modeling, 162
dual-phase-lag model, 166–167
Pennes model, 163–164
thermal wave model, 164–166
- models, types, 151
- Skin biothermomechanics
definition, 159
model development
case study, 171–176
in-plane stresses, 171
multilayer models, 167–168
one-layer continuum model, 167
stiffnesses, 168–169
vector of strains, 169
vector of stresses, 169–170
- objectives of, 150
scheme for characterizing, 151
theoretical modeling, 151–152
and thermal pain, schematic, 149–150
- Skin model, idealized, 172
- Skin thermal damage
continuum metric, 161
quantification
- Arrhenius burn integration, 157
Arrhenius parameters, 157–158
- Skin thermal pain
case study
nociceptors, temperature
history, 177, 179
one-dimensional, three-layer skin
model, 178
stimuli at location of
nociceptor, 178, 180
- model development
holistic mathematical model,
176–177
pain sensation, 176
quantification, 151
- Skin thermomechanics, importance,
149–150
- Skin tissue
compressive behavior, 204
effect of thermal denaturation on, 213
stretch-rate sensitivity, 211–215
temperature-dependent, 205–208
thermal-damage-induced changes in,
208–211
- density, 190
- dynamic viscoelasticity
for flank skin sample, 227–228
loss modulus, 227–228
storage modulus, 227
and thermal denaturation, 229
- heat transfer in. (*see* Skin bioheat
transfer)
- layers, 152
- macromolecular components, 153
- mechanical properties of
compressive performance, 158–159
deformation, 181
experimental characterization of,
181–182
factors influencing, 158
tensile behavior, 158
viscoelastic properties, 194
- mechanical response of, 222
- multilayer, 169
- nonlinear elastic behavior, 217
- relaxation behavior, 214
collagen, 223–224

- Skin tissue (*cont.*)
- components of skin dermis, 222–223
 - elastin, 223
 - ground substance role in, 224
 - under hyperthermal temperatures, 221
 - QLV theory, 217–220
 - quasilinear viscoelastic theory, 216–217
 - uniaxial stress–time response, 219
 - variation of elastic fraction, 221–222
- stretch-rate sensitivity, 212–213
- thermal damage for. (*see* Skin thermal damage)
- thermal denaturation, 162
- experimental characterization, 182
- thermomechanical behavior
- biaxial tensile behaviors, 202–204
 - collagen denaturation, 197–200
 - DSC analysis, 196
 - uniaxial tensile behavior, 200–202
- for three-layer model, thermophysical properties, 168
- time-dependent mechanical behavior, 216
- viscoelastic behavior
- effect of temperature and thermal denaturation on, 225–226
 - modeling of, 216–219
- SMA. *See* Shape memory alloys
- Static and kinematic
- indeterminacy, 77–79
- Stochastic search methods, 119
- Strain/displacement system, 190
- Strain energy density
- vs. bending energy density, 17
 - and curvature, 15
 - expression for, 21
 - for infinitesimal deformations, 21–22
 - vs. membrane energy, 16–17
- Stress/force measurement system, 190
- Stress relaxation test, 215
- QLV theory, 217, 220
 - skin viscoelasticity, 194, 197
- Stretch-rate sensitivity, skin tissue, 211–213
- Superstable tensegrity framework, 83
- SVD tensegrity structure, 87
- deployment sequence, 115
- equilibrium manifold, 92–93
- external forces and
- moments, 99–100
- linear friction moments, 101, 104–105
- modified model, 129–131
- natural frequencies, 108, 110
- prestressability, 95–96
- symmetrical configurations, 88–89
- Taylor series expansion
- around point on CNT, 18–19, 34–35
- DPL model, 166
- interatomic potential, 10–12
- Temperature-dependent compressive behavior, skin tissue
- denaturation of collagen, 206–207
 - skin mechanical behavior, 207, 209–210
 - stress–stretch relation, 205, 207
 - stretch-thermal damage, 205, 208
- Tensegrity
- and biology, connection between, 125–126
 - concept, 74–75
 - definition, 73
 - structural engineering research in
 - Calladine’s analysis, 76–77
 - features, pioneers work, 81
 - finite mechanism, 79–80
 - pin-jointed cylindrical truss structures, 80–81
 - state of prestress, 79
 - static and kinematic indeterminacy, 77–79
- Tensegrity cellular model, 126
- actin and intermediate filaments, 127
 - buckling of microtubules in, 128–129
 - dynamical properties, 129–131
 - heterogeneity within, 129–131
 - mathematical formulations of, 128
 - mechanics of cell, 131–132
 - numerical simulations of, 130
 - shape change capabilities, 132
 - static response of, 128, 131

- Tensegrity dynamics
bars and cables, 84
displacement, 83, 85
- Tensegrity flight simulator
controller robustness, 125–126
control problem for, 122–123
equations of motion of, 120–121
mathematical modeling, 120
notion of tracking motion in, 123
statics analysis of, 122
step elevator command
 accelerations, 124
 variation of controls during, 124–125
- Tensegrity structures
actuation
 electroactive polymers, 136–137
 magnetostrictive actuators, 137–138
 piezoactuators, 137
 requirements for, 134–135
 servomotors, 135–136
 shape memory alloys, 136
applications of, 70–71
clustered natural frequencies in
 degree of symmetry and, 106
 design parameters and, 108–109
 fast algorithm to solve, 110
 minimum separation between, 111
 proportional damping approximation
 and, 107, 109–111
 resonance phenomena, 107
 separation of, 108
- control and estimation techniques
 constrained particle dynamics
 technique, 119
 linear dynamical feedback controllers, 118
 LMIs techniques, 118
 motion simulation, 118–119
 optimization form-finding method, 119
 stochastic search methods, 119
- and control design, 117–118
- cost-effective manufacturing techniques
 for, 133
- and cytoskeleton, 127
- deployment of
 difficulty in, 112
- disadvantage associated with, 116
- equilibrium controls, 113–114
- fault tolerant, 114
- variation of controls during, 116
- derived from two-stage SVD type, 92–93
- dynamic properties, analysis of
 damping, 100–101
 nonlinear equations of motion, 97–100
 stiffness, 102–104
- Earth-related civil applications in, 133–134
- history of
 constructivist art, 71–72
 Needle Tower, 72
 proto-tensegrity, 72–73
 Snelson's sculptures, 73–75
 in twentieth century, 75
- homogeneous, 130
- investigation, unified
 approach to, 133
- in life sciences, 132
- literature on, 76
- market for, 133
- mathematics research, 82–83
- numerical form-finding for, 84
- prestressability problem for, 85
 equilibrium manifold, 87
 formulation of, 86
 generalized coordinates, 88
 kinetic friction, 86
 numerical solvers for, 94–95
 symmetrical configurations, 88–90
 two-stage SVD tensegrity structure, 87–88, 92–93
- static response analysis
 load–displacement
 characteristics, 96
 nonlinear, 95
 pretension coefficient, 95
 stiffness, 97
 torque–twist characteristics, 96
- vibration properties of, 104–106
- Tension-integrity principle, 74
- Thermal-damage-induced changes in
 compressive behavior, skin tissue
 compressive stiffness, 210

- Thermal-damage-induced changes in compressive behavior, skin tissue
(*cont.*) mechanisms of, 209
in pig skin tissue, 208
renaturation/reformation, 209
- Thermal equilibration length of blood vessels, 156
- Thermal pain and skin biothermomechanics, schematic of, 149–150
- Thermal signals, propagation mode of, 165
- Thermal wave behavior, 165
- Thermal wave model, 164 of bioheat transfer, 165 problems with, 165–166
- Thermal wave phenomenon, 164
- Thermoregulation, 148
- Tissue-like phantom experiment, 192–193
- Torsion of CNT Green strain and curvature tensors, 47–48 torque *vs.* normalized twist for, 48–49
- Two-compartment model, 126
- Two-stage SVD tensegrity structure components of, 87 deployment path, 112 equilibrium controls, 113 optimal control problem, 114–115
- sequence of intermediate configurations, 115
- equilibrium manifold for, 93 frequency response of, 131 linear friction moments at joints in, 104–105
- linear kinetic damping, 108 load–displacement characteristics, 96
- maximum modal frequency variation for, 105–106
- minimum modal frequency variation for, 105
- simulator obtained from, 120 symmetrical configuration of, 88–92 symmetrical prestressable configuration, 112
- tensegrity structures derived from, 92–93
- torque-twist characteristics, 96
- Vascular network, influence of blood flow in, 156
- Zigzag CNTs bending, 49 Brenner potential *vs.* mR/L, 51–52 energy (per atom) *vs.* radius, 43 instability, 51 internal pressure, 45–47 tension, 43–44 torque, 48